Journal of the Serbian Chemical Society

*e*Version
lectronic

Available on line at

СХД
1897

www.shd.org.rs/JSCS/

CONTENTS*

* For colored figures in this issue please see electronic version at the Journal Home Page:
http://www.shd.org.rs/JSCS/

REVIEW

Cobalt catalyzed defunctionalization reactions

LJILJANA K. KORAČAK[#] and VLADIMIR D. AJDAČIĆ*[#]

Innovative Centre, Faculty of Chemistry, Ltd., Studentski Trg 12–16, 11158 Belgrade, Serbia

Abstract: Catalytic defunctionalization of complex molecules has attracted significant attention in organic synthesis. This reaction enables common functional groups to serve as "traceless handles" for the new bond construction. In this mini-review, we have summarized the latest advances, methodologies and mechanistic insights into the selective cleavage of C–C and C–X bonds catalysed by cobalt complexes, shedding light on their increasing importance in modern chemical synthesis. The content of this review is categorized according to the type of functional group being removed from molecules.

Keywords: decarbonylation; decarboxylation; dehalogenation; desulfurization; deoxygenation.

CONTENTS

1. INTRODUCTION

Transition metal-mediated defunctionalisation through cleavage of C–C or C–X bonds is an essential synthetic approach.[1] Moreover, defunctionalisation reactions exert a direct influence on synthetic organic chemistry by enabling the temporary utilization of functional groups in synthetic transformations.[2] In various contexts, defunctionalised substrates are deemed more advantageous than

their functionalized form. For example, the dehalogenation of polychlorinated aromatic pesticides yields less environmentally hazardous compounds. The deoxygenation of aldehydes, acids and similar molecules derived from natural sources produces compounds suitable for use as biofuels.[3] While highly effective, the typical utilization of the expensive palladium,[4,5] rhodium[6,7] and ruthenium[8,9] complexes might impede the development of this field. On the other hand, cobalt is earth-abundant, inexpensive and less toxic compared to second row transition metals. Over the last two decades, cobalt has garnered significant attention for its applications as a catalyst in bond formation[10] and the bond cleavage[11] processes. In this mini-review, we highlight the development of the cobalt-catalysed defunctionalisation reactions and their applications in synthetic organic chemistry.

2. DEHYDRODECARBOXYLATION

Obtaining the terminal alkenes from carboxylic acids is a significant pursuit in organic chemistry with far-reaching implications in both academic research and industrial applications. Terminal alkenes are versatile building blocks used in the synthesis of various compounds, including pharmaceuticals, agrochemicals, and materials.[12] The practicability of accessing terminal alkenes from carboxylic acids lies in the abundance and accessibility of carboxylic acids as starting material. Carboxylic acids are prevalent in nature, and can be derived from renewable sources such as biomass or waste streams, offering a sustainable alternative to petroleum-derived feedstocks.[13] Moreover, carboxylic acids are relatively inexpensive and can be synthesized through various routes, making them attractive precursors for alkene synthesis.[14] Traditional methods for alkene synthesis often involve multi-step low atom economy processes with the use of toxic and expensive reagents.[15] In contrast, the direct conversion of carboxylic acids to terminal alkenes offers a more atom-efficient and environmentally benign route. In recent years, significant advancements have been made in the development of catalytic systems and reaction methodologies for the selective conversion of carboxylic acids to terminal alkenes. Transition metal catalysis, particularly involving palladium,[16] nickel[17,18] or iron catalysts,[19] has emerged as a powerful tool for this transformation.

Tunge and Cartwright have successfully developed a two-catalyst approach to produce enamides and enecarbamates directly from readily available and affordable *N*-protected amino acids using a photoredox catalyst under blue LED irradiation and a cobaloxime catalyst Co(dmgH)$_2$ClPy.[20] The protocol, despite its success with diverse amino acids, exhibits low selectivity, resulting in the production of significant quantities of both olefin isomers (*E*/*Z*, Scheme 1). Maintaining a slight excess of photo catalyst relative to cobaloxime is essential for the reaction to succeed.
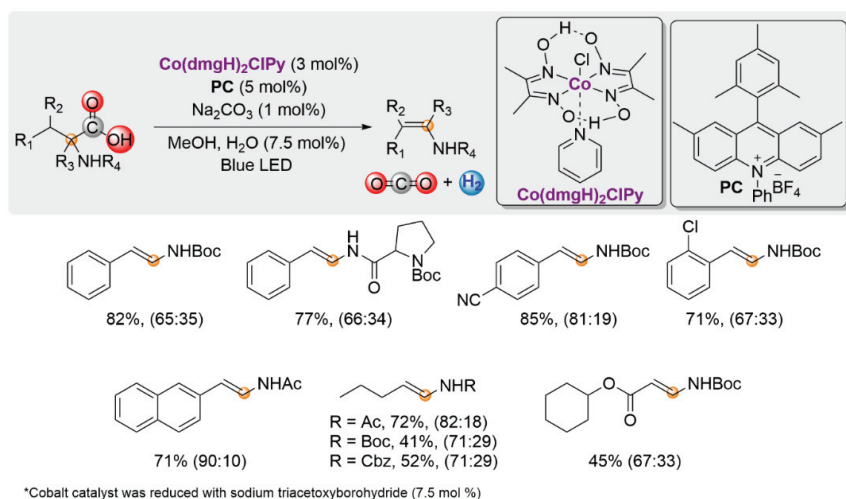
Scheme 1. Scope of *N*-acyl amino acids.

In the reaction mechanism, the olefin formation was initially proposed to occur through oxidative decarboxylation, generating a radical intermediate followed by a hydrogen atom transfer (HAT) reaction (Scheme 2). This process ultimately produces only CO_2 and H_2 as the stoichiometric byproducts.
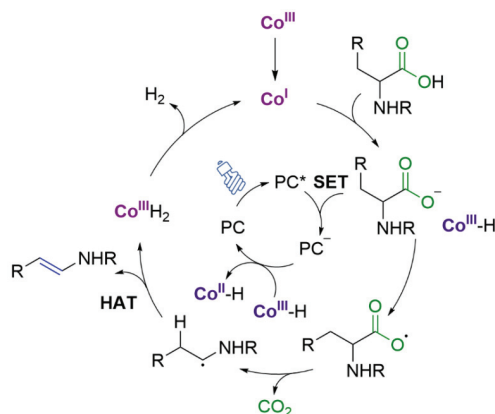
Scheme 2. Proposed mechanism for photoredox/cobalt dual-catalyzed decarboxylative elimination.

Two years later, the same research group reported novel insights into the underlying reaction mechanism. Their experimental studies suggest that the primary catalytic cycle involves Co(II) and Co(III) intermediates rather than an anionic Co(I) species.[21] This proposal is based on thorough experimentation and analysis, providing valuable insights into the mechanistic pathways of the reaction. Based on their research, it was proposed that a proton-coupled electron trans-

fer (PCET) pathway is the preferred route for HAT, and HE by protonation of the Co(III) hydride is the most probable pathway (Scheme 3).
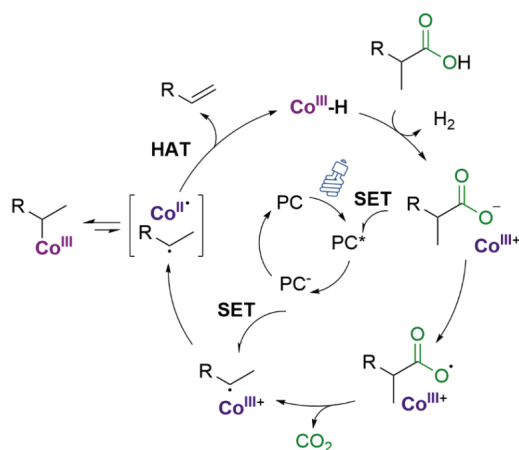
Scheme 3. Hypothetical mechanism for photoredox/cobalt dual-catalyzed decarboxylative elimination.

Under the photochemical conditions, Ritter and co-workers achieved the catalytic dehydrogenative decarboxyolefination of both fatty acids, and structurally complex carboxylic acids, into olefins.[22] They identified the cobaloxime Co(dmgH)$_2$(4-OMe-py)Cl as a proton reduction catalyst and the photoredox catalyst Ir[dF(CF$_3$)ppy]$_2$(dtbpy)PF$_6$, which mediates oxidative decarboxylation, as optimal catalytic system that enables high reaction yields requirement for stoichiometric additives. From their substrate scope study, it is evident that the decarboxyolefination of a large variety of structurally and functionally complex carboxylic acids had been successful (Scheme 4).
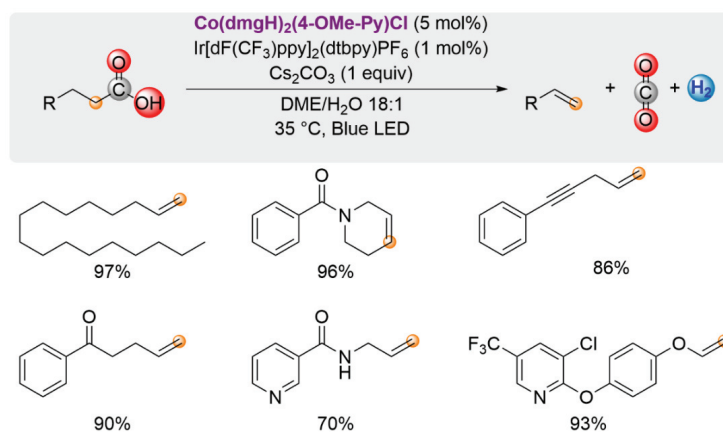
Scheme 4. Substrate scope for dehydrogenative decarboxyolefination.

In this method, the presence of a base is significantly important as it increases the concentration of carboxylate, facilitating the efficient one-electron oxidation to form the neutral carboxyl radical by the iridium catalyst (Scheme 5).
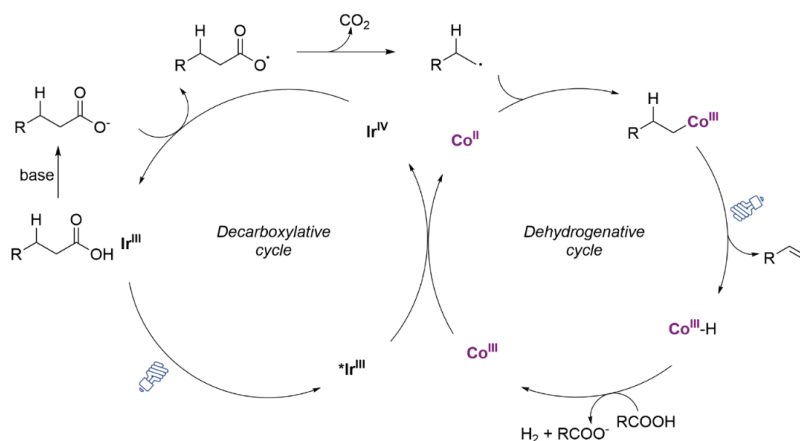
Scheme 5. Proposed mechanism for catalytic dehydrogenative decarboxyolefination of carboxylic acid.

Larionov and coworkers also applied a photoinduced dual catalytic dehydro-decarboxylation strategy to carboxylic acids using acridine as a photocatalyst and cobaloxime in a mixture of dichloromethane and methanol under Blue LED irradiation, in order to obtain alkenes.[23] From their comprehensive substrate scope study, it was observed that the developed method exhibits a broad substrate scope, encompassing various carboxylic acids, and demonstrated high tolerance towards diverse functional groups, thereby showcasing its versatility and potential applicability (Scheme 6).
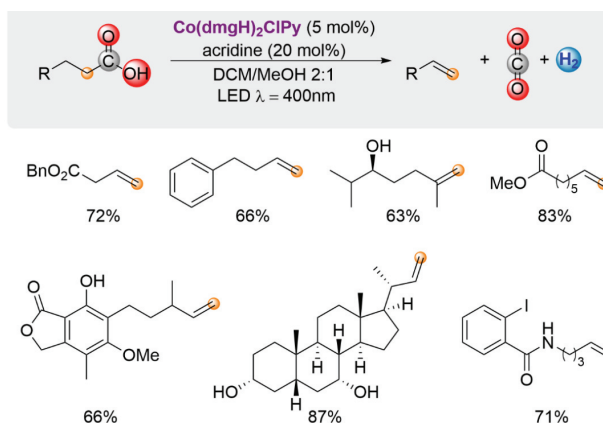
Scheme 6. Substrate scope of photoinduced dehydrodecarboxylation.

They also discovered an efficient chemoenzymatic synthesis (LACo, lipase-acridine-cobaloxime method) of long-chain alkenes from triglycerides and unrefined biomass. Amano lipase PS from *Burkholderia cepacia* was used to achieve enhanced conversion in the hydrolysis of triglycerides (Scheme 7).
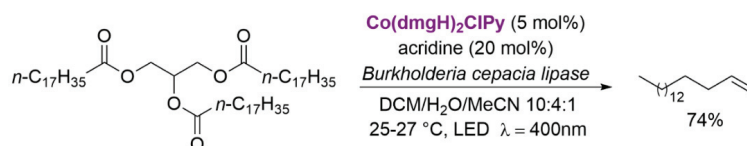
Scheme 7. Cooperative chemoenzymatic LACo process.

3. DECARBONYLATION

The aldehyde decarbonylation reaction is among the most important transformations both in biological systems and in a synthetic laboratory. Various organisms possess the ability to convert long-chain aldehydes into alkanes or alkenes *via* a group of enzymes known as aldehyde decarbonylases.[24] This process is accomplished by the release of small molecules such as formic acid, carbon dioxide and carbon monoxide. Numerous methods have been identified for the decarbonylation of aldehydes catalysed by transition metals and their complexes.[25,26] Given the ubiquity of the aldehyde group, selective decarbonylation can serve as an important synthetic strategy, using the aldehyde groups as "traceless handles" in various transformations such as the Diels–Alder (DA) reaction, C–H activation, and others.[2]

Li and coworkers in 2016 reported the first example of the Co-catalyzed decarbonylation.[27] It was exemplified only on one substrate, 2,4,5-trifluorobenzaldehyde. They demonstrated catalytic decarbonylation reaction of 2,4,5-trifluorobenzaldehyde to afford 1,2,4-trifluorobenzene with $CoMe(PMe_3)_4$ as a catalyst, and with 1.2 eq. of triethylsilane as a hydrogen source (Scheme 8).
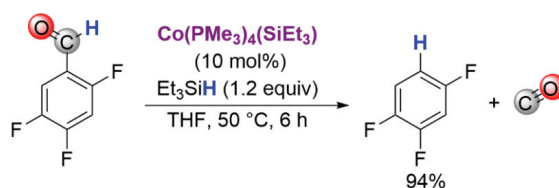
Scheme 8. Decarbonylation of 2,4,5-trifluorobenzaldehyde catalyzed by $CoMe(PMe_3)_4$.

Dehydroformylation of α-quaternary aldehydes that involves a decarbonylation step was achieved by Sorensen and coworkers using the dual catalytic system (Scheme 9).[28] Tetrabutylammonium decatungstate (TBADT) and cobaloxime pyridine chloride (COPC) were used as catalysts and upon UV irradiation

at room temperature olefinic products were obtained as regioisomeric mixtures in low yields (Scheme 9).
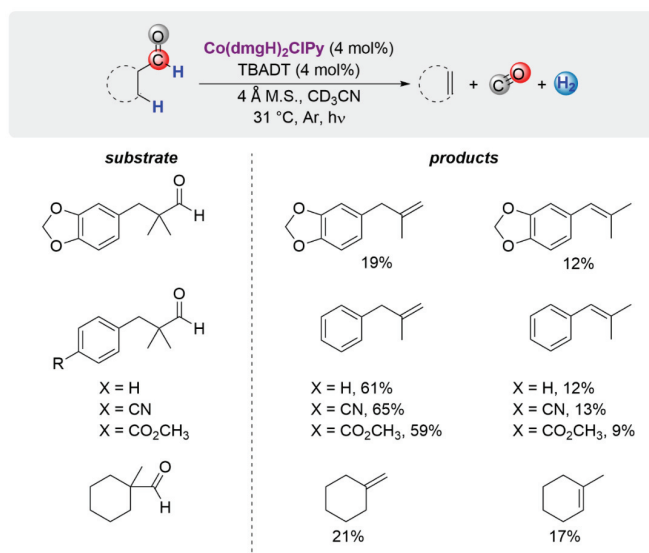
Scheme 9. Dehydroformylation of α-quaternary aldehydes.

Next year, Tonzetich and colleagues successfully conducted the decarbonlyation of aromatic and aliphatic aldehydes using cobalt(I) pincer complexes as catalyst.[29] However, a drawback of this method is the necessity for a stoichiometric amount of the catalyst. As depicted in the reaction mechanism illustrated in Scheme 10, following the formation of the product, the cobalt carbonyl complex **A** is unable to undergo further substitution to complete the catalytic cycle.
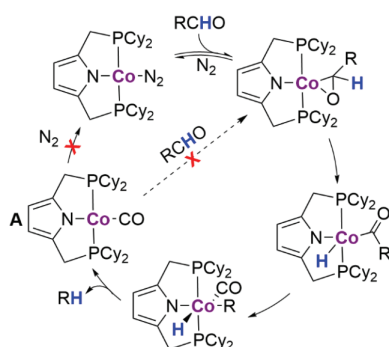
Scheme 10. Proposed mechanism for aldehyde decarbonylation.

Based on the previous observations of Sorensen and colleagues, König *et al.* reported a photocatalytic method for the decarbonylation of benzaldehydes in short reaction time.[30] Their method uses thioxanthone (TX) as an inexpensive

hydrogen atom transfer (HAT) agent, cobalt(II) acetylacetonate (Co(acac)$_2$) as the cobalt source, and 4,4'-di-*tert*-butyl-2,2'-dipyridyl (bbbpy) as the ligand (Scheme 11). The limitations of this methodology include the weak reactivity of substrates bearing hydroxy, thioether, nitro and carboxylic acid groups, the degradation of amino and bromo substituted derivatives, and the limited success with aliphatic aldehydes.
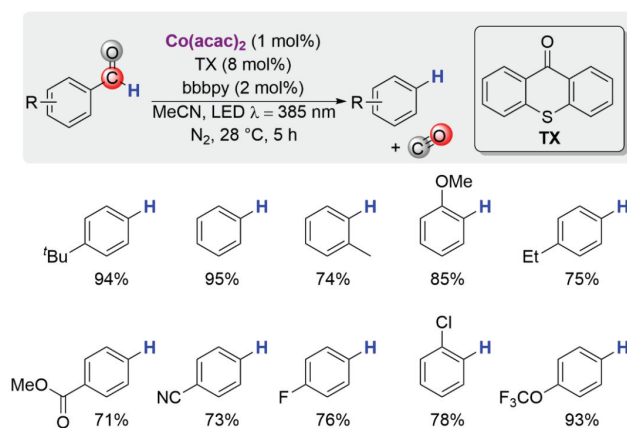
Scheme 11. Decarbonylation of benzaldehydes.

Initially, when the photocatalyst (PC) is excited to its triplet state (PC*), a hydrogen atom transfer (HAT) occurs with benzaldehyde (**I**), resulting in the formation of an acyl radical (**II**). This intermediate can then combine with the cobalt(II) complex (**III**) to produce a cobalt(III) complex (**IV**). This acyl complex (**IV**) is likely to undergo decarbonylation, releasing carbon monoxide and forming organocobalt complex **V** which can interact with the reduced form of the photocatalyst (PC–H), restoring it to its ground state (PC) through HAT. Con-
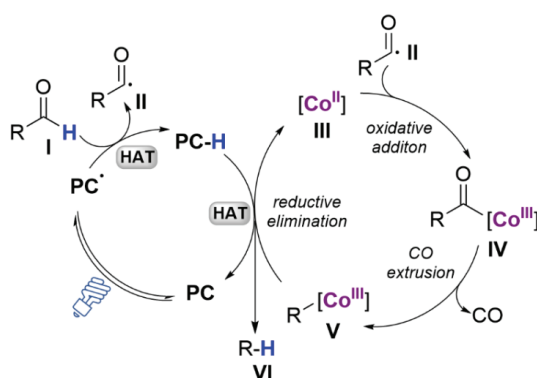
Scheme 12. Proposed reaction mechanism.

comitantly, the final product, decarbonylated arene (**VI**), is formed in this last step, and active cobalt species is regenerated (Scheme 12). To confirm the evolution of carbon monoxide, CO produced from the decarbonylation of 4-*t*-butylbenzaldehyde is used in the palladium-catalysed aminocarbonylation reaction, resulting in the synthesis of the anxiolytic drug moclobemide in good yield (Scheme 13).
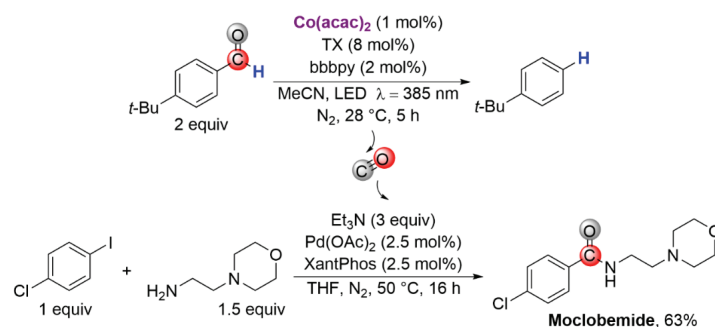
Scheme 13. Test reaction for confirming CO evolution.

Following their research on the photocatalytic method for the decarbonylation of benzaldehydes, König *et al*. reported a photocatalytic dehydroformylation.[31] This process integrates the dehydrogenation of benzyl alcohols into benzaldehydes, followed by the decarbonylation to produce arenes in a one-pot two-step protocol. It enables the efficient conversion of the diverse benzyl alcohols under mild photocatalytic conditions. The combination of tetrabutylammonium decatungstate as photoexcitable HAT-agent and cobaloxime pyridine chloride as co-catalyst was found to be highly effective (Scheme 14).
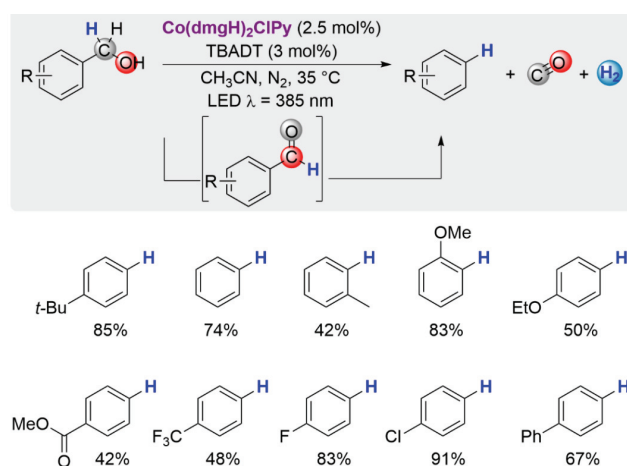
Scheme 14. Substrate scope for benzylalcohols.

4. DEHALOGENATION

The use of halides as blocking/protecting groups is an intriguing concept. For this purpose, it is essential to develop efficient dehalogenation strategies.[32,33] Additionally, the dehalogenation processes are crucial for eliminating toxic halogenated compounds, like chlorinated arenes, which persist in the environment and resist natural degradation, and a few examples of them are depicted in Fig. 1.[34] The efficient reductive dehalogenation methods, often involving transition metals and hydride sources, have been explored extensively.[35]
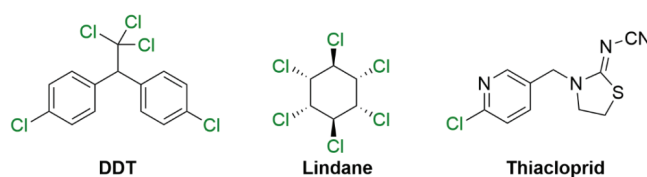
Fig. 1. Halogen-containing pesticides.

Based on their previous research related to selective C–F/C–H bond activation of fluoroarenes by cobalt complexes, Li *et al*. reported the selective hydrodefluorination of aryl fluorides catalysed by Co(PMe$_3$)$_4$.[36] In this method, sodium formate was applied as a reducing agent, and the reaction can be conducted in either acetonitrile or DMSO (Scheme 15).
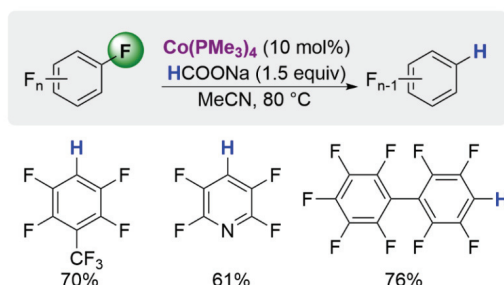
Scheme 15. Cobalt-catalyzed hydrodefluorination of polyfluoroarenes.

Based on the proposed mechanism, the process begins with the oxidative addition of the C–F bond of the aryl fluoride to the cobalt(0) centre, forming intermediate **I**, followed by substitution of fluoride ligand by a formate anion to yield complex **II**. Decarboxylation of **II** generates the hydrido cobalt(II) intermediate **III**. Subsequent ligand exchange between the hydrido H atom and the F atom of the perfluoroarenes produces the hydrodefluorination product, regenerating the starting Co(II) fluoride (Scheme 16).

Hydrodehalogenation of aryl bromides in the presence of cobalt porphyrin catalyst was achieved by Chan and coworkers.[37] The optimized reaction condit-

ions, encompassing cobalt porphyrin catalyst and 50 equiv of KOH, at 200 °C in THF under nitrogen, were applied for hydrodehalogenation of few electron-rich and electron-poor aryl bromides (Scheme 17). Although the yields were moderately good, the substrate scope was mainly limited. Conducting the reaction in air using 2-propanol as the solvent and 4-bromoanisole as the model substrate resulted in the formation of anisole, only slightly lower yield than that obtained under a nitrogen atmosphere.
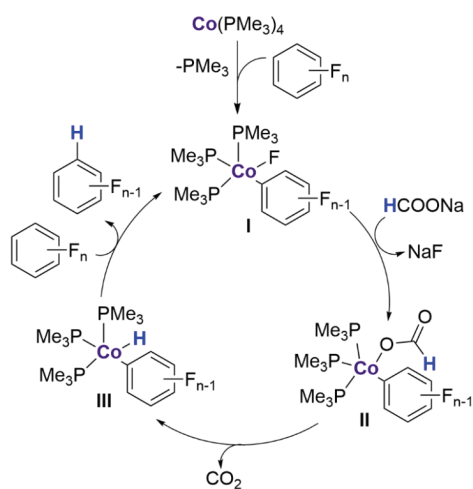
Scheme 16. Proposed mechanism of the catalytic hydrodefluorination.
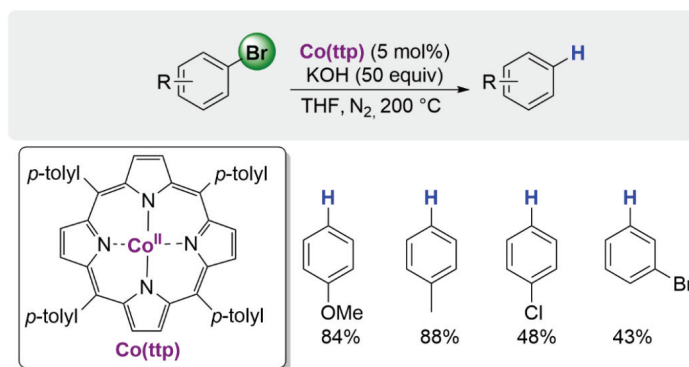
Scheme 17. Substrate scope of aryl-bromides.

The reaction starts with Co^{II}(ttp) abstracting a bromine atom from ArBr, leading to the formation of aryl radical and Co^{III}(ttp)Br. Subsequently, the aryl radical abstracts a hydrogen atom from the solvent to produce ArH and Co^{III}(ttp)Br intermediate undergoes ligand substitution with KOH, yielding KBr and Co^{III}(ttp)OH. The Co^{III}(ttp)OH species then generates H_2O_2 and regenerate Co^{II}(ttp) *via* reductive elimination (Scheme 18).
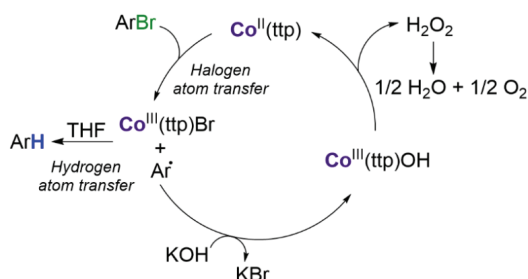
Scheme 18. Proposed reaction mechanism.

A few years later, the same group improved their method for the catalytic hydrodebromination reaction of aryl bromides in the presence of a cobalt porphyrin catalyst.[38] Replacing Co^{II}(ttp) with more electron rich Co^{II}(tbp) at lower temperature, in the less reactive hydrogen donating solvent (EtOH) resulted in a higher yield and broader scope. The limited reactivity is observed for the C–Cl bond suggests that aryl chlorides exhibit inertness towards hydrodechlorination under the optimized reaction conditions (Scheme 19).
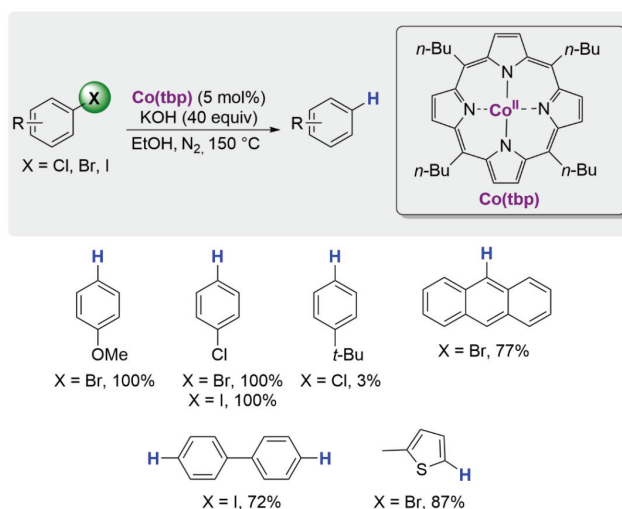
Scheme 19. Substrate scope of Co(tbp) catalyzed hydrodehalogenation.

They have also proposed a revised mechanism, that is based on single electron transfer. In strongly basic conditions, Co^{II}(tbp) coordinates with OH^- to form $[Co^{II}(tbp)(OH)]^-$, which transfers one electron to an aryl bromide, generating an aryl bromide radical anion. This radical anion undergoes rapid carbon––bromide bond cleavage to produce an aryl radical and a bromide anion. The aryl radical can abstract a hydrogen atom from EtOH, yielding the corresponding arene as the final product. Alternatively, the Co(tbp)aryl intermediate can undergo

hydrolysis to yield the corresponding arene and Co^{III}(tbp)OH. The resullting Co^{III}(tbp)OH then undergoes reductive dimerization to regenerate Co^{II}(tbp) (Scheme 20).
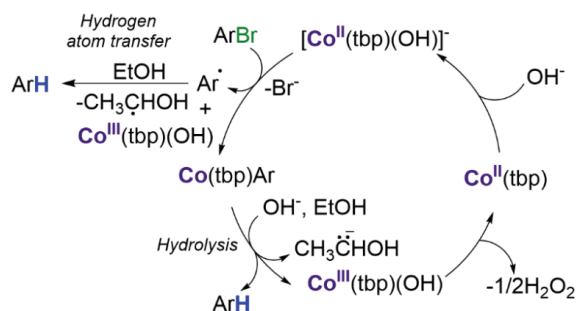
Scheme 20. Catalytic cycle for Co^{II}(tbp) catalyzed hydrodebromination.

In 2015, Liao and co-workers proposed the reaction mechanism of debromination, catalysed by the B_{12}-dependent reductive dehalogenase (NpRdhA), elucidated using the quantum chemical cluster approach with 2,6-dibromophenolate as a model substrate (Scheme 21).[39] According to the proposed mechanism, the reaction proceeds through Co^I-initiated concerted dehalogenation for the reductive dehalogenase NpRdhA. They also demonstrated that reactivity in the dehalogenation reaction changes with various halogen substitutions (F, Cl, Br, I) and indicated the enzyme's inability to catalyse the defluorination of 2,6-difluorophenolate.

Using molecular hydrogen as a green reducing agent, Beller and coworkers reported a method for hydrodehalogenation of alkyl and (hetero)aryl-halides in the presence of heterogeneous cobalt catalyst.[40] Synthesis of novel sustainable catalyst was based on the complexation of cobalt salt Co(OAc)$_2$ by chitosan (a polymer of D-glucosamine) followed by pyrolysis. The substrate scope was very broad; a range of alkyl, aryl, heteroaryl halides successfully underwent hydrodehalogenation in the presence of this new cobalt catalyst from cheap and readily available biowaste with good chemoselectivity (Scheme 22).

They demonstrated the utility of this method in the multistep synthesis of ($\pm$)-peronatin B alkaloid (Scheme 23) and in degradation of halogen containing pesticides (Metazachlor, Benodanil).

Dehalogenation of bromo- and chloro-aryl and -alkyl derivatives in the presence of CoBr$_2$, manganese as reductant, and bipyridine ligand, in acetonitrile at 50 °C, and isopropanol as hydrogen donor, was explored by Gosmini and co-workers in 2021.[41] A range of aryl halides featuring both electron-withdrawing and electron-donating functional groups underwent successful dehalogenation (Scheme 24).
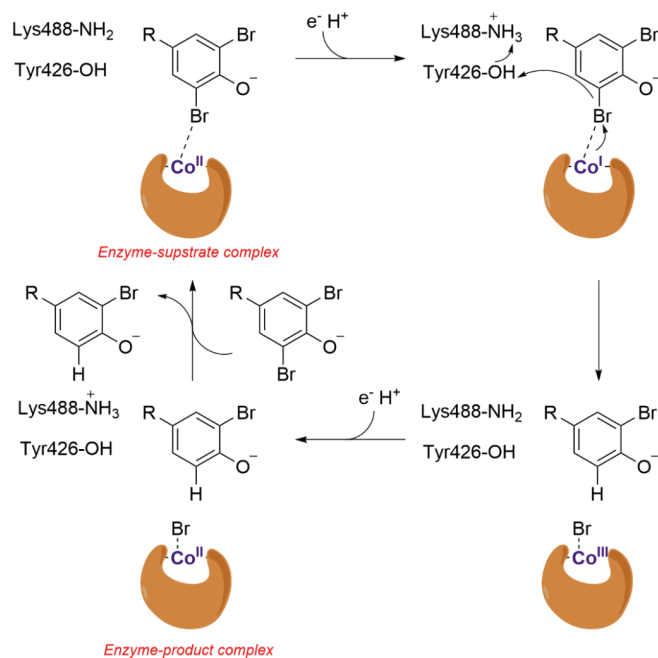
Scheme 21. Suggested reductive debromination mechanisms for NpRdhA.
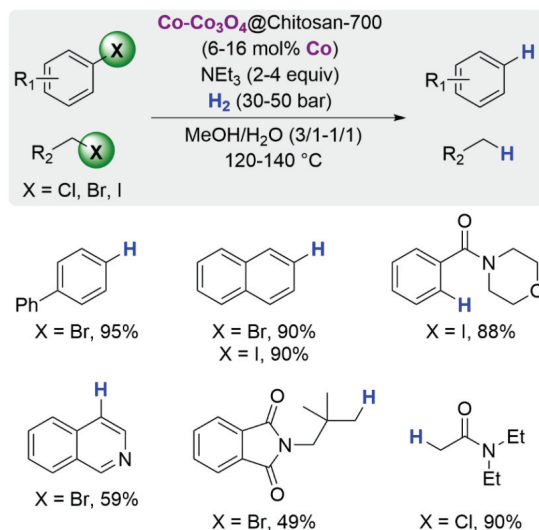
Scheme 22. Hydrodehalogenationof alkyl and aryl halides.

In addition to the classic methods described previously, there have also been developments in the utilization of vitamin B_{12} and related bioinspired complexes as efficient catalysts for dehalogenation reactions. These compounds undergo

chemical,[42] photochemical[43] or electrochemical[44] reduction to form supernuc-leophilic cobalt species, which then reacts with alkyl and aryl halides to produce alkyl/aryl complexes, by the cleavage of C-X bond (Fig. 2).[45]
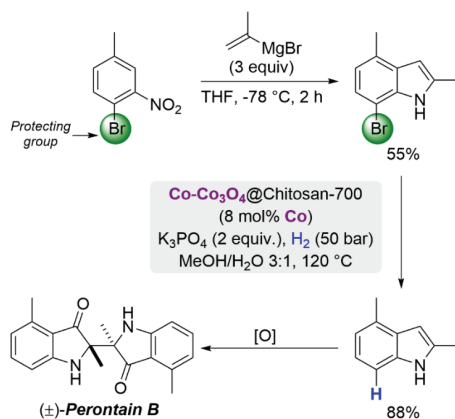
Scheme 23. Application in (±)-peronatin B alkaloid synthesis.
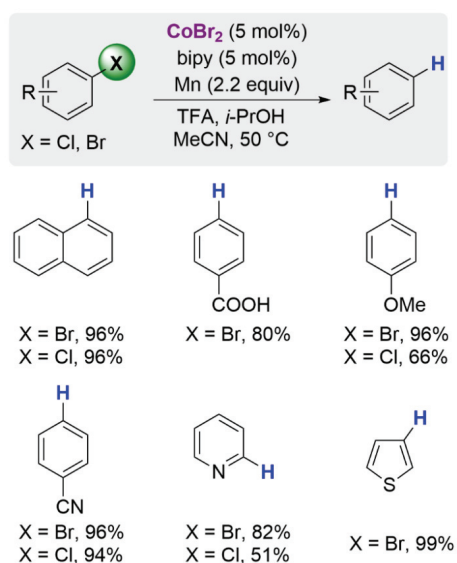
Scheme 24. Reactivity of aryl electrophiles.

5. DEOXYGENATION

Over the past few decades, the increasing costs associated with petroleum and other fossil fuels, both in financial, environmental, and societal terms, have underscored the need to turn to renewable resources for fuel and chemicals production. Biomass-derived materials have emerged as prime contenders for renewable chemical sources due to their abundance and ease of handling.[3] However, these materials are typically rich in oxygen, necessitating efficient deoxygenation processes. Therefore, it is necessary to continually develop new meth-

odologies and catalytic systems for removing oxygen-containing functional groups (hydroxy[46], alkoxy[47], *etc.*).
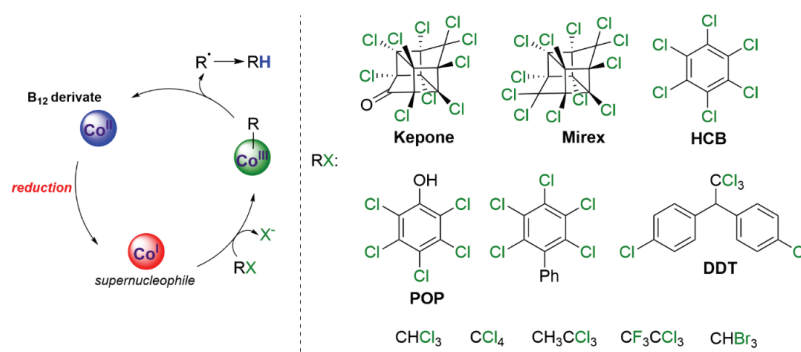
Fig. 2. Vitamin B_{12} derivatives as efficient catalysts for dehalogenation.

5.1. Dehydroxylation

In 1978, Funabiki and coworkers reported the use of the cobalt complex $HCo(CN)_5^{-3}$, formed *in situ* from cobalt(II) chloride and potassium cyanide under hydrogen atmosphere, as a catalyst for the deoxygenation of allylic alcohols.[48] According to the proposed concerted reaction mechanism, the hydrogenation of the C=C bond was followed by elimination of the hydroxy group. However, the occurrence of double bond transposition is contingent upon the ratio of cyanide to cobalt, leading to the formation of a mixture of products (Scheme 25).
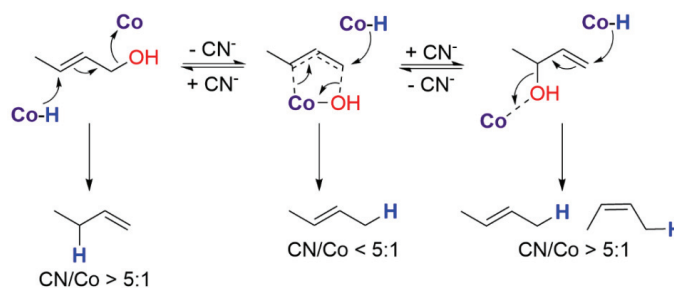
Scheme 25. Direct deoxygenation of allylic alcohols with *in situ* formed $HCo(CN)_5^{-3}$.

Later, in 1990 Jong-Tae Lee and Howard Alper demonstrated the deoxygenation of allylic alcohols using *β*-cyclodextrin as a phase transfer catalyst and hydridopentacyanocobaltate anion as a catalyst.[49] The catalytic deoxygenation of primary and secondary allylic alcohols was achieved in good yields affording olefins, however the tertiary allylic alcohols did not undergo the reaction under these reaction conditions (Scheme 26).

Scheme 26. Hydrogenolysis of allylic alcohols using $HCo(CN)_5^{-3}$ and β-cyclodextrin.

The advantage of this method is evident as no hydrogenation or shift of the double bond was observed. According to the proposed mechanism, the reaction of the adduct of β-cyclodextrin (β-CD) and $HCo(CN)_5^{-3}$ with the σ-allyl complex **VI** would yield the product and regenerate **II** (Scheme 27).

Scheme 27. Proposed reaction mechanism.

Mebane and co-workers in 2001 reported a novel method for the deoxygenation of aromatic alcohols using Raney catalysts.[50] Raney cobalt was first used in this kind of transformation and demonstrates its effectiveness exclusively in catalysing the deoxygenation of α-substituted alcohol (Scheme 28). Compared to

Scheme 28. Deoxygenation of α-substituted alcohols.

Raney nickel, Raney cobalt is less reactive in transfer hydrogenolysis reactions. However, its advantage is reflected in the absence of ring reduction encountered during the deoxygenation of *α*-substituted alcohols containing two or more aromatic rings, which can occur with Raney nickel.

5.2. Deoxygenation of phenol ether

In 2014, Wang and co-workers demonstrated an efficient cobalt-catalysed method for the reductive cleavage of inert aromatic C–O bonds with high selectivity.[51] The desired products were obtained in good to moderate yields using airstable Co(acac)$_2$ as a catalyst (Scheme 29).
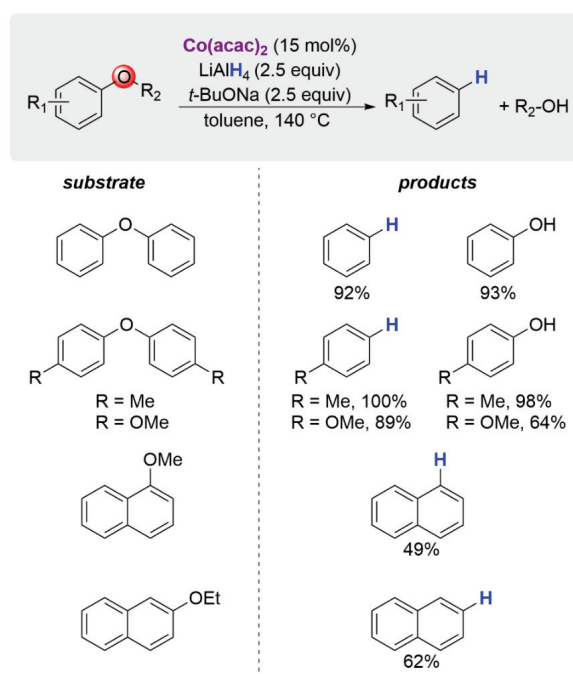
Scheme 29. Co-catalyzed reductive cleavage of various aromatic C–O bonds.

6. REDUCTIVE DESULFURIZATION

In 2018, Yorimitsu and colleagues developed a method for the reduction of aryl sulfones to produce the corresponding arenes using cobalt–NHC as a cataylst, and primary alkylmagnesium reagent as a hydride source.[52] Additionally, they demonstrated versatility by extending their methodology to a variety of organosulphur compounds, including alkenyl and benzyl sulfones, *N*-tosylindole, as well as aryl sulphide and sulphoxide derivatives (Scheme 30).

The proposed reaction mechanism for the reduction of aryl methyl sulphones is presented in Scheme 32. In the presence of alkylmagnesium reagent, a low-val-

ent Co–NHC complex **A** is formed. The oxidative addition of aryl methyl sulfone **I** leads to the formation of arylcobalt methanesulfinate **B**. Intermediate **B** then undergoes the transmetalation with an alkylmagnesium reagent to produce the alkylarylcobalt **C**, followed by subsequent β-hydride elimination and reductive elimination to yield arene **II**. The methanesulphinate anion generated as the leaving group might undergo reduction under the present highly reductive conditions, hence requiring an excess amount of alkylmagnesium reagent (Scheme 31).
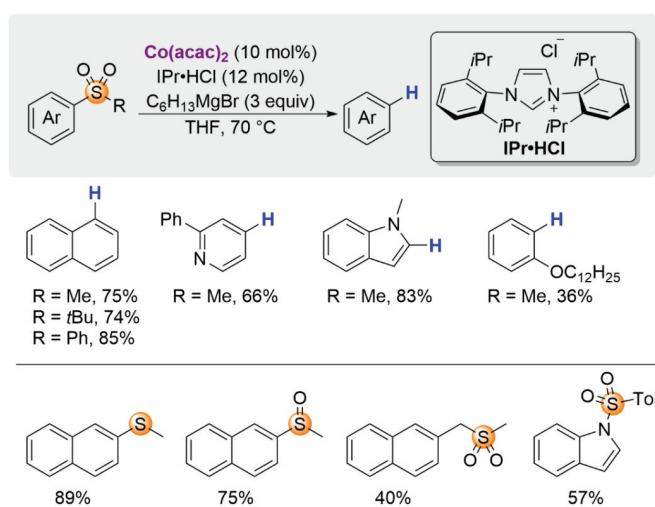
Scheme 30. Cobalt-calatyzed reduction of aryl sulfones and other sulfonyl compounds.
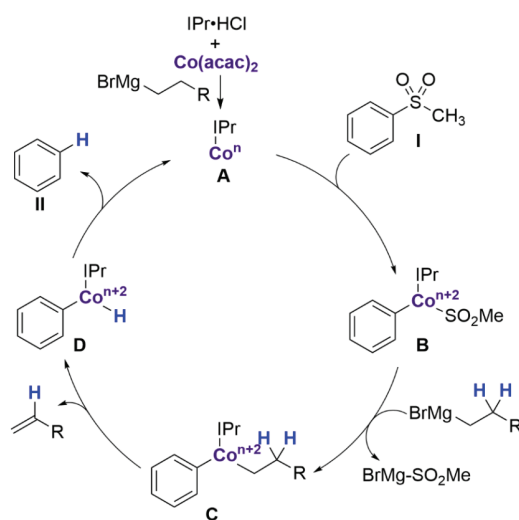
Scheme 31. Plausible reaction mechanism.

7. CONCLUSION

Cobalt-catalysed defunctionalization has emerged as a powerful tool in the field of organic synthesis, offering chemists efficiency and selectivity in the modification of complex molecules. Emerging the defunctionalization strategies are poised to become integral to various energy production methods, such as the conversion of biomass into biofuels. Additionally, the defunctionalization holds great importance in drug synthesis, converting environmentally hazardous molecules (such as pesticides) into less harmful forms and obtaining precursors for the polymer industry.

И З В О Д

РЕАКЦИЈЕ ДЕФУНКЦИОНАЛИЗАЦИЈЕ КАТАЛИЗОВАНЕ КОБАЛТОМ

ЉИЉАНА К. КОРАЧАК и ВЛАДИМИР Д. АЈДАЧИЋ

Иновациони центар Хемијског факултета у Београду, д.о.о. Студентски трг 12–16, Београд

Реакције дефункционализације од великог су значаја у модерној органској хемији. Често, функционална група може бити привремено присутна у молекулу као блокирајућа или заштитна група која се селективно може уклонити из једињења. У овом прегледном чланку хронолошки су описане методе за дефункционализацију органских молекула катализоване кобалтом и његовим комплексним једињењима. Такође, детаљно су приказани реакциони механизми наведених трансформација, као и примена у органској синтези.

(Примљено 18. марта, ревидирано 8. априла, прихваћено 9. априла 2024)

REFERENCES

1. A. Modak, D. Maiti, *Org. Biomol. Chem.* **14** (2016) 21 (https://doi.org/10.1039/C5OB01949D)
2. Ž. Selaković, A. M. Nikolić, V. Ajdačić, I. M. Opsenica, *Eur. J. Org. Chem.* (2022) e202101265 (https://doi.org/10.1002/ejoc.202101265)
3. J. Zakzeski, P. C. A. Bruijnincx, A. L. Jongerius, B. M. Weckhuysen, *Chem. Rev.* **110** (2010) 3552 (https://doi.org/10.1021/cr900354u)
4. J. S. Dickstein, J. M. Curto, O. Gutierrez, C. A. Mulrooney, M. C. Kozlowski, *J. Org. Chem.* **78** (2013) 4744 (https://doi.org/10.1021/jo400222c)
5. O. Navarro, H. Kaur, P. Mahjoor, S. P. Nolan, *J. Org. Chem.* **69** (2004) 3173 (https://doi.org/10.1021/jo035834p)
6. J. F. Hooper, R. D. Young, A. S. Weller, M. C. Willis, *Chem. Eur. J.* **19** (2013) 3125 (https://doi.org/10.1002/chem.201204056)
7. M. Tobisu, R. Nakamura, Y. Kita, N. Chatani, *J. Am. Chem. Soc.* **131** (2009) 3174 (https://doi.org/10.1021/ja810142v)
8. N. Chatani, H. Tatamidani, Y. Ie, F. Kakiuchi, S. Murai, *J. Am. Chem. Soc.* **123** (2001) 4849 (https://doi.org/10.1021/ja0103501)

9. G. Domazetis, B. Tarpey, D. Dolphin, B. R. James, *J. Chem. Soc., Chem. Commun*. (1980) 939 (https://doi.org/10.1039/C39800000939)

10. B. Kokić, B. Vulović, M. Jović, A. Andrijević, V. Ajdačić, I. M. Opsenica, *Eur. J. Org. Chem*. **26** (2023) e202300997 (https://doi.org/10.1002/ejoc.202300997)

11. B. Kokić, Ž. Selaković, A. M. Nikolić, A. Andrijević, B. Anđelković, V. Ajdačić, I. M. Opsenica, *Eur.J. Org.Chem*. (2022) e202201112 (https://doi.org/10.1002/ejoc.202201112)

12. G. R. Lappin, J. D. Sauer, *Alpha Olefns Applications Handbook*, Marcel Dekker, New York, 1989 (ISBN:9780824778958)

13. I. T. Horváth, *Chem. Rev*. **118** (2018) 369 (https://doi.org/10.1021/acs.chemrev.7b00721)

14. R. A. Sheldon, J. K. Kochi, *Org. React*. **19** (2011) 279 (https://doi.org/10.1002/0471264180.or019.04)

15. T.Takeda, *Modern Carbonyl Olefination: Methods and Applications*; John Wiley & Sons, Hoboken, NJ, 2006 (ISBN:978-3-527-60538-5)

16. L. J. Gooßen, N. A. Rodríguez, *Chem. Commun*. (2004) 724 (https://doi.org/10.1039/B316613A)

17. A. John, M. O. Miranda, K. Ding, B. Dereli, M. A. Ortuño, A. M. LaPointe, G. W. Coates, C. J. Cramer, W. B. Tolman, *Organometallics* **35** (2016) 2391 (https://doi.org/10.1021/acs.organomet.6b00415)

18. A. John, M. A. Hillmyer, W. B. Tolman, *Organometallics* **36** (2017) 506 (https://doi.org/10.1021/acs.organomet.6b00940)

19. S. Maetani, T. Fukuyama, N. Suzuki, D. Ishihara, I. Ryu, *Organometallics* **30** (2011) 1389 (https://doi.org/10.1021/om1009268)

20. K. C. Cartwright, J. A. Tunge, *ACS Catal*. **8** (2018) 11801 (https://doi.org/10.1021/acscatal.8b03282)

21. K. C. Cartwright, E. Joseph, C. G. Comadoll, J. A. Tunge, *Chem. Eur. J*. **26** (2020) 12454 (https://doi.org/10.1002/chem.202001952)

22. X. Sun, J. Chen, T. Ritter, *Nature Chem.* **10** (2018) 1229 (https://doi.org/10.1038/s41557-018-0142-4)

23. V. T. Nguyen, V. D. Nguyen, G. C. Haug, H. T. Dang, S. Jin, Z. Li, C. Flores-Hansen, B. S. Benavides, H. D. Arman, O. V. Larionov, *ACS Catal.* **9** (2019) 9485 (https://doi.org/10.1021/acscatal.9b02951)

24. E. N. G. Marsh, M. W. Waugh, *ACS Catal*. **3** (2013) 2515 (https://doi.org/10.1021/cs400637t)

25. N. Terzić Jovanović, V. Ajdačić, *J. Serb. Chem. Soc*. **87** (2022) 669 (https://doi.org/10.2298/JSC220128024T)

26. H. Lu, T. Y. Yu, P. F. Xu, H. Wei, *Chem. Rev*. **121** (2021) 365 (https://doi.org/10.1021/acs.chemrev.0c00153)

27. S. Yuan, H. Sun, S. Zhang, X. Li, *Inorg. Chim. Acta* **439** (2016) 100 (https://doi.org/10.1016/j.ica.2015.10.006)

28. D. J. Abrams, J. G. West, E. J. Sorensen, *Chem. Sci.* **8** (2017) 1954 (https://doi.org/10.1039/C6SC04607J)

29. H. Alawisi, K. F. Al-Afyouni, H. D. Arman, Z. J. Tonzetich, *Organometallics* **37** (2018) 4128 (https://doi.org/10.1021/acs.organomet.8b00668)

30. 30. D. Kolb, M. Morgenstern, B. König, *Chem. Commun*. **59** (2023) 8592 (https://doi.org/10.1039/D3CC02170J)

31. D. Kolb, A. A. Almasalma, M. Morgenstern, L. Ganser, I. Weidacher, B. König, *ChemPhotoChem* **7** (2023) e202300167 (https://doi.org/10.1002/cptc.202300167)
32. A. Dobbs, *J. Org. Chem.* **66** (2001) 638 (https://doi.org/10.1021/jo0057396)
33. A. Ramanathan, L. S. Jimenez, *Synthesis* (2010) 217 (https://doi.org/10.1055/s-0029-1217112)
34. S. Agarwal, S. R. Al-Abed, D. D. Dionysiou, *Environ. Sci. Technol.* **41** (2007) 3722 (https://doi.org/10.1021/es062886y)
35. A. Kokanović, V. Ajdačić, N. Terzić Jovanović, S. Stankic, I. M. Opsenica, *ACS Appl. Nano Mater.* **6** (2023) 15820 (https://doi.org/10.1021/acsanm.3c02743)
36. J. Li, T. Zheng, H. Suna, X. Li, *Dalton Trans.* **42** (2013) 13048 (https://doi.org/10.1039/C3DT50409C)
37. K. S. Chan, C. R. Liu, K. L. Wong, *Tetrahedron Lett.* **56** (2015) 2728 (https://doi.org/10.1016/j.tetlet.2015.04.014)
38. C. Chen, H. Zuo, K. S. Chan, *Tetrahedron* **75** (2019) 510 (https://doi.org/10.1016/j.tet.2018.12.010)
39. R. Z. Liao, S. L. Chen, P. E. M. Siegbahn, *ACS Catal.* **5** (2015) 7350 (https://doi.org/10.1021/acscatal.5b01502)
40. B. Sahoo, A. E. Surkus, M. M. Pohl, J. Radnik, M. Schneider, S. Bachmann, M. Scalone, K. Junge, M. Beller, *Angew. Chem. Int. Ed.* **56** (2017) 11242 (https://doi.org/10.1002/anie.201702478)
41. B. R. P. Reddy, A. Auffrant, C. Gosmini, *Asian J. Org. Chem.* **10** (2021) 3275 (https://doi.org/10.1002/ajoc.202100616)
42. K. M. McCauley, D. A. Pratt, S. R. Wilson, J. Shey, T. J. Burkey, W. A. van der Donk, *J. Am. Chem. Soc.* **127** (2005) 1126 (https://doi.org/10.1021/ja048573p)
43. 43. H. Shimakoshi, M. Tokunaga, T. Babaa, Y. Hisaeda, *Chem. Commun.* (2004) 1806 (https://doi.org/10.1039/B406400C)
44. H. Shimakoshi, Y. Hisaeda, *Chem. Rec.* **21** (2021) 2080 (https://doi.org/10.1002/tcr.202100077)
45. H. Shimakoshi, Y. Hisaeda, *ChemPlusChem* **82** (2017) 18 (https://doi.org/10.1002/cplu.201600303)
46. J. M. Herrmann, B. König, *Eur. J. Org. Chem.* (2013) 7017 (https://doi.org/10.1002/ejoc.201300657)
47. M. Tobisu, K. Yamakawa, T. Shimasakia, N. Chatani, *Chem. Commun.* **47** (2011) 2946 (https://doi.org/10.1039/C0CC05169A)
48. T. Funabiki, Y. Yamazaki, K. Tarama, *J. Chem. Soc., Chem. Commun.* (1978) 63 (https://doi.org/10.1039/C39780000063)
49. J. T. Lee, H. Alper, *Tetrahedron Lett.* **31** (1990) 4101 (https://doi.org/10.1016/S0040-4039(00)97553-1)
50. B. H. Gross, R. C. Mebane, D. L. Armstrong, *Appl. Catal., A* **219** (2001) 281 (https://doi.org/10.1016/S0926-860X(01)00700-1)
51. Y. L. Ren, M. Tian, X. Z. Tian, Q. Wang, H. Shang, J. Wang, Z. C. Zhang, *Catal. Commun.* **52** (2014) 36 (https://doi.org/10.1016/j.catcom.2014.03.036)
52. J. Fukuda, K. Nogi, H. Yorimitsu, *Asian J. Org. Chem.* **7** (2018) 2049 (https://doi.org/10.1002/ajoc.201800473).

Omicron BA.2.86 Pirola nightmare: Empirical formulas and thermodynamic properties (enthalpy, entropy and Gibbs energy change) of nucleocapsid, virus particle and biosynthesis of BA.2.86 Pirola variant of SARS-CoV-2

MARKO E. POPOVIĆ[1]*, MARTA POPOVIĆ[2], GAVRILO ŠEKULARAC[1,3]
and MARIJANA PANTOVIĆ PAVLOVIĆ[1,3#]

[1]*University of Belgrade, Institute of Chemistry, Technology and Metallurgy, Njegoševa 12, 11000 Belgrade, Serbia,* [2]*University of Belgrade, Faculty of Biology, Studentski trg 16, 11000 Belgrade, Serbia, and* [3]*University of Belgrade, Centre of Excellence in Chemistry and Environmental Engineering – ICTM, Belgrade, Serbia*

Abstract: Similarly to a phoenix, SARS-CoV-2 has appeared periodically in waves. The new variants that appeared through mutations have suppressed earlier variants, causing new waves of the pandemic. The Omicron BA.2.86 Pirola variant is the latest in the sequence. An increased infectivity was noticed, which results in rapid spreading, as well as decreased pathogenicity, which results in a lower number of severe cases. However, in the public there is a fear of further development of the epidemic. This analysis was made with the goal to assess the risks in the period of early 2024. Mutations that were developed by the BA.2.86 variant have led to a change in empirical formula and thermodynamic properties. The empirical formula of the BA.2.86 virus particle is $CH_{1.639023}O_{0.284130}N_{0.230031}P_{0.006440}S_{0.003765}$. It is different than those of other variants of SARS-CoV-2, other virus species and cellular organisms. The driving force for the virus multiplication, Gibbs energy change of biosynthesis of the BA.2.86 variant is –221.75 kJ C-mol^{-1}. It is more negative than that of its host tissue. According to the biosynthesis phenomenological equation, the more negative Gibbs energy change of biosynthesis allows the virus to achieve a greater biosynthesis rate and hijack the host cell metabolism. However, the Gibbs energy change of biosynthesis of the BA.2.86 variant is similar to those of the CH.1.1 and XBB.1.16 variants. This means that these variants should have similar multiplication rates and thus similar pathogenicity. Therefore, it seems that there is no ground for fear of an extensive spreading of severe forms, but there are reasons for caution and monitoring of the spreading of the epidemic and potential appearance of new mutations. Moreover, unlike the earlier pandemic waves, during the newest pandemic wave, the infections

---

* Corresponding author. E-mail: marko.popovic@ihtm.bg.ac.rs

807

with influenza, RSV and BA.2.86 variant simultaneously appeared, which deserves an analysis.

INTRODUCTION

Phoenix is an immortal bird that cyclically regenerates. Like a Phoenix, SARS-CoV-2 has cyclically regenerated several dozen times through mutations from Hu-1 to the newest Omicron BA.2.86 Pirola variant. With every new mutation and new variant, SARS-CoV-2 has obtained a new life appearing slightly different from its predecessor. Some of the variants have caused pandemic waves of high amplitude.[1] Differently from the mythological phoenix, the SARS-CoV-2 phoenix has disappeared and reborn in front of our eyes during the three years of the pandemic. Thus, SARS-CoV-2 has appeared in late-2019 in Wuhan and was labeled as the Hu-1 wild type.[2] The mutations of the virus have occurred mostly in the part of the genome that encodes the spike glycoprotein.[3] However, the mutations have occurred in other viral proteins as well.[4] The evolution of viruses and the formation of new variants has been described in the literature.[5–9]

BA.2.86 Pirola is the latest variant of SARS-CoV-2, which is characterized by many mutations.[10] The number of mutations in BA.2.86 variant, compared to the XBB.1.5 variant is similar to the difference between the first Omicron variant and its predecessor Delta variant.[10] This might give the BA.2.86 variant the ability to infect people who have previously had COVID-19 or who have received COVID-19 vaccines, which has raised public concerns.[10] During the late 2023 and early 2024, the BA.2.86 variant has become widely spread.[11] Even though there has been a decrease in number of daily infections worldwide since late 2022, with the appearance of the new Omicron BA.2.86 variant, the number of COVID-19 cases has increased since the mid-2023. Due to this situation, it would be good to perform a physicochemical analysis of the BA.2.86 variant to compare its ability to infect host cells with that of the previous variants of SARS-CoV-2.[12]

SARS-CoV-2 belongs to the *Coronaviridae* family.[13] It is an enveloped virus, with a single stranded positive sense RNA genome.[13] SARS-CoV-2 virus particles contain four kinds of structural proteins: nucleocapsid (N), membrane (M), envelope (E) and spike (S). The nucleocapsid protein binds to the viral RNA and forms the nucleocapsid.[14] The nucleocapsid is enclosed in a lipid bilayer envelope that contains membrane and envelope proteins.[15] The spike proteins point out from the surface of the virus particle. They represent the virus antigens that bind to host cell receptors.[16–20] Moreover, the SARS-CoV-2 genome encodes the viral proteins needed for multiplication, which have been identified as targets for the antiviral medicines.[51,52]

SARS-CoV-2 belongs to RNA viruses.[21] RNA viruses exhibit a great tendency to mutate.[22,23] Mutations lead to change in information content of the viral genome, chemical changes in elemental composition, as well as thermodynamic properties (enthalpy, entropy and Gibbs energy changes of formation and biosynthesis).[24–26] Mutation as a biological phenomenon, except through sequencing, can be detected through the atom counting method, which allows detection of changes in elemental composition that appear as a consequence of mutations.[27] Furthermore, changes in elemental composition lead to changes in thermodynamic properties.[28–31]

Since 2019, in the literature, elemental composition and thermodynamic properties have been reported for several virus species: Ebola,[32] Mpox,[33] SARS-CoV-2,[8,9,16,20,24,25,34] HIV,[35] arboviruses,[35] bacteriophages,[36] *etc*. Biothermodynamic mechanisms that influence infectivity and pathogenicity of different variants and the consequences on epidemiology and mechanisms of spreading of SARS-CoV-2 are available in the literature.[37–42]

The aim of this paper is to explore the changes in empirical formula, molar mass, biosynthesis reactions and thermodynamic properties (enthalpy, entropy, Gibbs energy changes) of formation and biosynthesis of the Omicron BA.2.86 Pirola variant. Based on the obtained results, the goal is to perform an assessment of the risk of spreading of an epidemic/pandemic of the BA.2.86 variant in early 2024. Moreover, the pathogenicity of the BA.2.86 variant will be compared to those of the earlier variants of SARS-CoV-2.

METHODS

Data sources

The genetic sequence of the Omicron BA.2.86 Pirola variant of SARS-CoV-2 was taken from GISAID, the global data science initiative.[43] It can be found under the accession number EPI_ISL_18138566 and is labelled hCoV-19/USA/OH-ODH-SC3032044/2023. Thus, the findings of this study are based on the metadata associated with one sequence available on GISAID up to September 24, 2023, and accessible at https://doi.org/10.55876/gis8.230924yd (please see the Supplementary material to this paper).

The sequence of the nucleocapsid phosphoprotein of SARS-CoV-2 was obtained from the NCBI database,[44] under the accession number QIK50455.1. The sequence of the membrane protein of SARS-CoV-2 was obtained from the NCBI database,[44] under the accession number QHR63293.1. The sequence of the spike glycoprotein of SARS-CoV-2 was obtained from the NCBI database,[44] under the accession number QHR63290.2. The number of protein copies in the virus particle was taken from literature.[45] In a SARS-CoV-2 particle, there are 2368 copies of the nucleocapsid phosphoprotein, 1184 copies of the membrane protein and 222 copies of the spike glycoprotein.[45]

The standard Gibbs energy changes of biosynthesis of the wild type Hu-1, Delta B.1.617.2, Zeta P.2, Eta B.1.525, Theta P.3, Iota B.1.526, Lambda C.37, Mu B.1.621, Kappa B.1.617.1, Omicron B.1.1.529, Omicron BA.2, Omicron BA.2.75, Omicron BQ.1, Omicron BQ.1.1, Omicron XBB, Omicron XBB.1, Omicron BA.5.2, Omicron BF.7, Omicron XBB.1.5,

Omicron BN.1, Omicron CH.1.1, Omicron XBC, Omicron XBB.1.9.1, Omicron XBF and Omicron XBB.1.16 variants of SARS-CoV-2 were taken from the literature.[6-9,18,19,24-26]

Empirical formulas

The empirical formulas and molar masses of the virus particle and nucleocapsid of the Omicron BA.2.86 Pirola variant of SARS-CoV-2 were determined through the atom counting method as described in references.[27,46] The atom counting method is implemented with a computer program, based on genetic sequences, protein sequences and morphological data.[27]

Thermodynamic properties of live matter

Thermodynamic properties of virus particle and nucleocapsid of the Omicron BA.2.86 variant were determined with the Patel–Erickson model[29] and Battley model.[28] To find enthalpy of live matter (*i.e.*, virus particle or nucleocapsid) with the Patel–Erickson model, the empirical formula is used to find the number of electrons transferred to oxygen during complete oxidation, E, with the equation:[29]

$$E = 4n_C + n_H - 2n_O - 0\ n_N + 5n_P + 6n_S \tag{1}$$

E is then used to find standard enthalpy change of combustion of live matter, $\Delta_C H^0$, with the equation:

$$\Delta_C H^0(\text{bio}) = -111.14 \frac{\text{kJ}}{\text{C-mol}} \times E \tag{2}$$

$\Delta_C H^0$ is then used to calculate standard enthalpy change of formation of live matter, $\Delta_f H^0$, with the equation:[29]

$$\Delta_f H^0(\text{bio}) = n_C \Delta_f H^0(\text{CO}_2) + \frac{n_H}{2}\Delta_f H^0(\text{H}_2\text{O}) + \frac{n_P}{4}\Delta_f H^0(\text{P}_4\text{O}_{10}) +$$
$$+ n_S \Delta_f H^0(\text{SO}_3) - \Delta_C H^0 \tag{3}$$

Entropy of live matter is calculated with the Battley model, based on its elemental composition. Standard molar entropy of live matter, S^o_m, is given by the equation:

$$S_m^0(\text{bio}) = 0.187 \sum_J \frac{S_m^0(J)}{a_J} n_J \tag{4}$$

where $S_m^0(J)$ is standard molar entropy of element J, a_J number of atoms of element J in its standard state elemental form, and n_J the number of atoms of element J in the empirical formula of live matter.[28] The summation is over all elements J of which the live matter consists.[28] The Battley model can also be used to find standard entropy change of formation of live matter, $\Delta_f S^0$,[28] if the constant 0.187 is changed to –0.813:

$$\Delta_f S^0(\text{bio}) = -0.813 \sum_J \frac{S_m^0(J)}{a_J} n_J \tag{5}$$

Finally, $\Delta_f S^0$ and $\Delta_f H^0$ are combined to find standard Gibbs energy change of formation, $\Delta_f G^0$, of live matter

$$\Delta_f G^0(\text{bio}) = \Delta_f H^0(\text{bio}) - T\Delta_f S^0(\text{bio}) \tag{6}$$

where T is temperature.[47]

Biosynthesis reactions

Biosynthesis reactions of the virus particle and nucleocapsid of the Omicron BA.2.86 variant were formulated based on their empirical formulas. Biosynthesis reactions are macrochemical equations of conversion of nutrients into new live matter in metabolism.[47] The general biosynthesis reaction for viruses has the form:

$$(\text{Amino acid}) + O_2 + HPO_4^{2-} + HCO_3^- \rightarrow (\text{Bio}) + SO_4^{2-} + H_2O + H_2CO_3 \qquad (7)$$
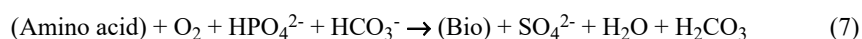
where (Amino acid) represents a mixture of amino acids, which has the empirical formula $CH_{1.798}O_{0.4831}N_{0.2247}S_{0.022472}$.[6,8,9,17,23] Newly synthetized live matter, (Bio), is represented with its empirical formula.[6,8,9,17,23] The source of energy, carbon, nitrogen and sulfur for biosynthesis are the amino acids.[6,8,9,17,23] The electron acceptor is O_2.[6,8,9,17,23] The source of phosphorus is HPO_4^{2-}.[6,8,9,17,23] Excess H^+ generated during biosynthesis are absorbed by the HCO_3^-, which is a part of the bicarbonate buffer.[6,8,9,17,23] Excess sulfur atoms are released in the form of SO_4^{2-}, which is an additional metabolic product.[6,8,9,17,23] The oxidized carbon atoms are released in the form of H_2CO_3, which is also a part of the bicarbonate buffer.[6,8,9,17,23]

Thermodynamic properties of biosynthesis

Thermodynamic properties of biosynthesis of the virus particle and nucleocapsid of the Omicron BA.2.86 variant of SARS-CoV-2 were calculated with the Hess's law. They were found based on the biosynthesis reactions and thermodynamic properties of live matter. Thermodynamic properties of biosynthesis include standard enthalpy change of biosynthesis, $\Delta_{bs}H^0$, standard entropy change of biosynthesis, $\Delta_{bs}S^0$, and standard Gibbs energy change of biosynthesis, $\Delta_{bs}G^0$.[47] They can be found by application of the Hess's law to the biosynthesis reactions:

$$\Delta_{bs}H^0 = \sum\nolimits_{\text{products}} \nu \Delta_f H^0 - \sum\nolimits_{\text{reactants}} \nu \Delta_f H^0 \qquad (8)$$

$$\Delta_{bs}S^0 = \sum\nolimits_{\text{products}} \nu S_m^0 - \sum\nolimits_{\text{reactants}} \nu S_m^0 \qquad (9)$$

$$\Delta_{bs}G^0 = \sum\nolimits_{\text{products}} \nu \Delta_f G^0 - \sum\nolimits_{\text{reactants}} \nu \Delta_f G^0 \qquad (10)$$

where ν represents a stoichiometric coefficient.[6,8,9,17,23,29,47]

RESULTS AND DISCUSSION

Empirical formula and thermodynamic properties of live matter

The empirical formula of the virus particle of the Omicron BA.2.86 variant of SARS-CoV-2 is reported for the first time:
$CH_{1.639023}O_{0.284130}N_{0.230031}P_{0.006440}S_{0.003765}$ (Table I).
Empirical formulas have been reported in the literature for other SARS-CoV-2 variants. The empirical formula of the virus particle of the Hu-1 wild type of SARS-CoV-2 is $CH_{1.6390}O_{0.2851}N_{0.2301}P_{0.0065}S_{0.0038}$.[25] The empirical formula of the virus particle of the Delta variant of SARS-CoV-2 is:
$CH_{1.6383}O_{0.2844}N_{0.2294}P_{0.0064}S_{0.0042}$.[25]
The virus particle of the Omicron BA.1 variant of SARS-CoV-2 is characterized by the empirical formula $CH_{1.6404}O_{0.2842}N_{0.2299}P_{0.0064}S_{0.0038}$.[25] The empirical formula of the virus particle of the Omicron BA.2 variant of SARS-CoV-2 is

$CH_{1.6403}O_{0.2838}N_{0.2298}P_{0.0064}S_{0.0038}$.[26] Moreover, empirical formulas of other virus species have been reported in the literature. The empirical formula of a *Poxviridae* virus particle is $CH_{1.5876}O_{0.3008}N_{0.2538}P_{0.00223}S_{0.00554}$.[33] A *Vaccinia* virus particle is characterized by the empirical formula $CH_{1.5877}O_{0.3232}N_{0.2531}P_{0.00371}S_{0.00540}$.[33] Therefore, every virus species and variant is characterized by a different empirical formula. Based on the empirical formula, it is possible to identify the virus. This provides a rapid method for virus identification through single particle inductively coupled plasma mass spectroscopy, as described by Degueldre.[34]

TABLE I. Empirical formulas and molar masses of the Omicron BA.2.86 Pirola variant of SARS-CoV-2. Empirical formulas have the general form $CH_{n_H}O_{n_O}N_{n_N}P_{n_P}S_{n_S}$, where n_H, n_O, n_N, n_P and n_S are numbers of H, O, N, P and S atoms in the empirical formula, respectively. Molar masses were reported in two forms: molar mass of the empirical formula, *Mr*, and total molar mass of the macromolecular assembly (entire virus particle or entire nucleocapsid), *Mr*(tot)

Parameter	Virus particle	Nucleocapsid
n_H	1.639023	1.570946
n_O	0.284130	0.343118
n_N	0.230031	0.312432
n_P	0.006440	0.006007
n_S	0.003765	0.003349
Mr / g C-mol^{-1}	21.75	23.75
Mr(tot) / MDa	219.7	117.6

Empirical formulas have been reported in the literature for various species of cellular organisms. The empirical formula of *Escherichia coli* (bacteria) is:
$CH_{1.918}O_{0.528}N_{0.257}P_{1.76\times10^{-2}}S_{5.54\times10^{-3}}K_{5.87\times10^{-3}}Mg_{2.07\times10^{-3}}Ca_{8.36\times10^{-4}}$
$Mn_{9.89\times10^{-6}}Fe_{7.82\times10^{-5}}Cu_{1.62\times10^{-6}}Zn_{2.41\times10^{-5}}$.[31] The empirical formula of *Penicillium chrysogenum* (mold fungi) is:
$CH_{2.026}O_{0.511}N_{0.185}P_{9.15\times10^{-3}}S_{4.17\times10^{-3}}K_{3.45\times10^{-3}}Mg_{1.47\times10^{-3}}Ca_{3.69\times10^{-4}}Mn_{1.08\times10^{-5}}Fe_{9.51\times10^{-5}}Cu_{1.24\times10^{-6}}Zn_{2.15\times10^{-5}}$.[31] *Saccharomyces cerevisiae* (yeast fungi) is characterized by an empirical formula:
$CH_{1.613}O_{0.557}N_{0.158}P_{0.012}S_{0.003}K_{0.022}Mg_{0.003}Ca_{0.001}$.[28] The empirical formula of the human organism is:
$CH_{1.7296}O_{0.2591}N_{0.1112}P_{0.0134}S_{0.003}Na_{0.0027}K_{0.0031}Ca_{0.0173}Cl_{0.0018}$.[48]
The empirical formula of the virus particle of the Omicron BA.2.86 variant of SARS-CoV-2 is $CH_{1.639023}O_{0.284130}N_{0.230031}P_{0.006440}S_{0.003765}$ (Table I). Therefore, every class of organisms is characterized by a unique empirical formula different than those of other organisms.

Except for its empirical formula, the Omicron BA.2.86 variant of SARS--CoV-2 has its characteristic thermodynamic properties of live matter (enthalpy, entropy and Gibbs energy change), which were determined in this research

(Table II). The Gibbs energy change of the formation of the Omicron BA.2.86 virus particle is –24.64 kJ C-mol^{-1}, while that of the BA.2.86 nucleocapsid is –33.32 kJ C-mol^{-1} (Table II). Therefore, the virus particle has a greater (less negative) Gibbs energy change than the nucleocapsid. This means that the virus particle has a greater usable energy content. The reason for this are the lipids in the viral envelope. The SARS-CoV-2 virus particle contains a lipid envelope.[13] The lipids in the envelope have a high energy content.[49] Therefore, the usable energy content of the virus particle is greater than that of the nucleocapsid.

TABLE II. Thermodynamic properties of live matter of the Omicron BA.2.86 variant of SARS-CoV-2: standard enthalpy change of formation, $\Delta_f H^0$, standard molar entropy, S_m^0, and standard Gibbs energy change of formation, $\Delta_f G^0$

Name	$\Delta_f H^0$ / kJ C-mol^{-1}	S_m^0 / J C-mol^{-1} K^{-1}	$\Delta_f G^0$ /kJ C-mol^{-1}
Virus particle	–64.43	30.70	–24.64
Nucleocapsid	–75.41	32.47	–33.32

The Gibbs energy changes of formation have been reported in the literature for other virus species and variants. The virus particle of the Hu-1 wild type of SARS-CoV-2 is characterized by a Gibbs energy change of formation –24.8 kJ C-mol^{-1}.[25] Gibbs energy change of formation of the virus particle of the Omicron BA.2.86 variant of SARS-CoV-2 is –24.64 kJ C-mol^{-1} (Table II). Thus, Gibbs energy change of formation of the BA.2.86 variant is different than that of the Hu-1 wild type. Moreover, Gibbs energy change of a *Poxviridae* virus particle is –25.3 kJ C-mol^{-1},[33] while that of a *Vaccinia* virus particle is –30.0 kJ C--mol^{-1}.[33] Thus, the virus particle of the Omicron BA.2.86 variant of SARS-CoV-2 has a different Gibbs energy change of formation than those of the *Vaccinia* and *Poxviridae* virus particles. Therefore, every virus species and variant has a characteristic Gibbs energy change of formation.

Gibbs energy changes of formation of cellular microorganisms can also be found in the literature. Gibbs energy change of formation of some cellular microorganisms are: –66.98 kJ C-mol^{-1} for *Escherichia coli* bacteria, –87.07 kJ C--mol^{-1} for *Saccharomyces cerevisiae* yeast fungi and –18.99 kJ C-mol^{-1} for *Penicillium chrysogenum* mold fungi.[30] Thus, the Gibbs energy changes of these cellular microorganisms are different than that of the Omicron BA.2.86 variant of SARS-CoV-2 (–24.64 kJ C-mol^{-1}). Furthermore, the Gibbs energy change of formation of the human organism is –37.54 kJ C-mol^{-1},[48] which is different than that of the Omicron BA.2.86 variant of SARS-CoV-2. This means that every class of organisms should have a characteristic Gibbs energy change of formation, summarizing the usable energy content in its life matter.

Biosynthesis reaction and thermodynamic properties of biosynthesis

Based on the empirical formulas of the virus particle and nucleocapsid of the Omicron BA.2.86 Pirola variant of SARS-CoV-2, biosynthesis reactions were formulated (Table III). The biosynthesis reaction of the virus particle of the Omicron BA.2.86 variant is:

$$1.023637CH_{1.798}O_{0.4831}N_{0.2247}S_{0.022472} + 0.010469CH_2O + 0.006440HPO_4^{2-} +$$
$$+ 0.025596HCO_3^- \rightarrow CH_{1.639023}O_{0.284130}N_{0.230031}P_{0.006440}S_{0.003765} +$$
$$+ 0.019238SO_2^{2-} + 0.067397H_2O + 0.059701H_2CO_3 \qquad (11)$$
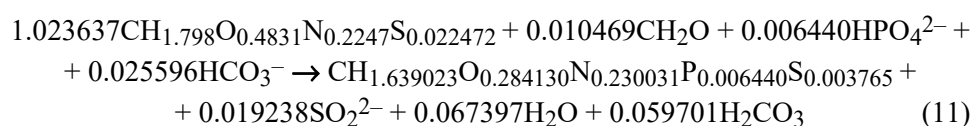
where $CH_{1.798}O_{0.4831}N_{0.2247}S_{0.022472}$ is the empirical formula of amino acids and $CH_{1.639023}O_{0.284130}N_{0.230031}P_{0.006440}S_{0.003765}$ is the empirical formula of the BA.2.86 virus particle (Table I). The biosynthesis reaction of the nucleocapsid of the Omicron BA.2.86 variant is:

$$1.390323CH_{1.798}O_{0.4831}N_{0.2247}S_{0.022472} + 0.492478O_2 + 0.006007HPO_4^{2-} +$$
$$+ 0.043774HCO_3^- \rightarrow CH_{1.570946}O_{0.343118}N_{0.312432}P_{0.006007}S_{0.003349} +$$
$$+ 0.027894 SO_2^{2-} + 0.055049H_2O + 0.434097H_2CO_3 \qquad (12)$$
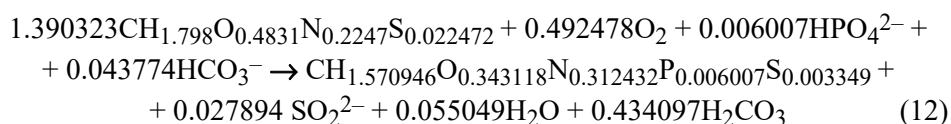
where $CH_{1.570946}O_{0.343118}N_{0.312432}P_{0.006007}S_{0.003349}$ is the empirical formula of the BA.2.86 nucleocapsid (Table I). The biosynthesis reaction of the BA.2.86 virus particle contains both amino acids and carbohydrates as an energy source, while that of the BA.2.86 nucleocapsid contains only amino acids. This means that the biosynthesis of the BA.2.86 virus particle takes more energy than the biosynthesis of the nucleocapsid alone. The reason for this is the higher energy content in the virus particle, due to the lipids in the viral envelope, as discussed above. The lipids in the viral envelope have a high energy content.[49] This means that the virus particle that contains the lipid envelope takes more energy for biosynthesis than the nucleocapsid which doesn't contain lipids. This energy comes

TABLE III. Biosynthesis stoichiometry for the Omicron BA.2.86 variant of SARS-CoV-2. The general biosynthesis reaction has the form (Amino acid) + CH_2O + O_2 + HPO_4^{2-} + HCO_3^- $\rightarrow$ (Bio) + SO_2^{2-} + H_2O + H_2CO_3. "Amino acid" represents a mixture of amino acids with the formula $CH_{1.798}O_{0.4831}N_{0.2247}S_{0.022472}$. "Bio" represents the empirical formula of live matter from Table I

Role	Name	Virus particle	Nucleocapsid
Reactants	Amino acid	1.023637	1.390323
	CH_2O	0.010469	0.000000
	O_2	0.000000	0.492478
	HPO_4^{2-}	0.006440	0.006007
	HCO_3^-	0.025596	0.043774
Products	Bio	1.000000	1.000000
	SO_4^{2-}	0.019238	0.027894
	H_2O	0.067397	0.055049
	H_2CO_3	0.059701	0.434097

from the carbohydrates in the biosynthesis reaction. The biosynthesis reaction of the BA.2.86 virus particle requires more hydrogen phosphate ion than that of the nucleocapsid. HPO_4^{2-} is the phosphorus source for biosynthesis. The higher amount of HPO_4^{2-} in the biosynthesis reaction is due to phospholipids in the envelope of the virus particle.

Based on the biosynthesis reactions, the thermodynamic properties of biosynthesis of the BA.2.86 variant were determined for the first time. The enthalpy change of biosynthesis of the BA.2.86 variant nucleocapsid is –232.88 kJ C-mol^{-1} (Table IV). This means that the enthalpy of biosynthesis contributes favourably to the biosynthesis process. The entropy of biosynthesis of the BA.2.86 nucleocapsid is –37.48 kJ C-mol^{-1} (Table IV). The negative entropy change is unfavourable for the biosynthesis reaction. The Gibbs energy change of biosynthesis of the BA.2.86 variant is –221.75 kJ C-mol^{-1}. The negative Gibbs energy change, which is due to the negative enthalpy change of biosynthesis, means that the biosynthesis process is thermodynamically favourable.

TABLE IV. Thermodynamic properties of biosynthesis for the Omicron BA.2.86 variant of SARS-CoV-2: standard enthalpy change of biosynthesis, $\Delta_{bs}H^0$, standard entropy change of biosynthesis, $\Delta_{bs}S^0$, and standard Gibbs energy change of biosynthesis, $\Delta_{bs}G^0$

Name	$\Delta_{bs}H^0$ / kJ C-mol^{-1}	$\Delta_{bs}S^0$ / J C-mol^{-1} K^{-1}	$\Delta_{bs}G^0$ / kJ C-mol^{-1}
Virus particle	–4.80	6.94	–6.94
Nucleocapsid	–232.88	–37.48	–221.75

Virus–host and virus–virus interactions

Gibbs energy change of biosynthesis represents the driving force for the biosynthesis process.[47] A more negative Gibbs energy change of biosynthesis, $\Delta_{bs}G$, implies a greater biosynthesis rate, r_{bs}, according to the biosynthesis phenomenological equation:

$$r_{bs} = -\frac{L_{bs}}{T}\Delta_{bs}G \qquad (13)$$

where L_{bs} is the biosynthesis phenomenological coefficient and T is temperature.[8,23,25] Gibbs energy change of the biosynthesis of the nucleocapsid of the BA.2.86 Pirola variant of SARS-CoV-2 is –221.75 kJ C-mol^{-1} (Table IV). On the other hand, Gibbs energy change of biosynthesis for the lung tissue is –49.76 kJ C-mol^{-1}.[32] Therefore, the BA.2.86 variant has a much more negative Gibbs energy change of biosynthesis. This means that, according to the biosynthesis phenomenological equation, the biosynthesis rate of the BA.2.86 variant will be much greater than that of its host tissue. Due to this, the infected host cells will produce the virus particles at a much greater rate than their own building blocks. This allows the hijacking of the host cell metabolism by the virus. The virus and its host cell compete for the cellular metabolic machinery and resources. The

competition occurs in the host cell cytoplasm, at the ribosomes. The virus has a much greater driving force of biosynthesis, in the form of negative Gibbs energy. This means that the virus will have a much greater biosynthesis rate, which will allow it to hijack the host cell metabolism.

The Gibbs energy change of biosynthesis is proportional to the biosynthesis rate of a virus, according to the biosynthesis phenomenological equation. In case that several virus species or virus variants are simultaneously in circulation in the population, the virus with the most negative Gibbs energy change of biosynthesis will have a competitive advantage.[18,50] The virus characterized by a more negative Gibbs energy change of biosynthesis will have a greater biosynthesis rate.[18,50] This will allow it to dominate over other viruses circulating in the population.[18,50] Gibbs energy changes of biosynthesis of SARS-CoV-2 variants are shown in Fig. 1. The Gibbs energy change of biosynthesis of the nucleocapsid of the BA.2.86 Pirola variant of SARS-CoV-2 is –221.75 kJ C-mol⁻¹ (Table IV). Gibbs energy changes of biosynthesis of nucleocapsids of other variants under monitoring are –221.21 kJ C-mol⁻¹ for the Omicron CH.1.1 variant[6] and –221.19 kJ C-mol⁻¹ for the Omicron XBB.1.16 variant.[8] Therefore, the Gibbs energy changes of biosynthesis of the BA.2.86, CH.1.1 and XBB.1.16 variants are very similar. This means that in case these SARS-CoV-2 variants appear in a population, they will have very similar biosynthesis rates. This means that no variant will have an advantage in the competition in a short time period. As a result, all three variants should circulate in the population during a pandemic. However, having in mind that even though it is small, the difference in Gibbs energy changes of biosynthesis exists, which is the most negative for the BA.2.86 variant, which means that in a long time period, it will be able to suppress the CH.1.1 and XBB.1.16 variants.
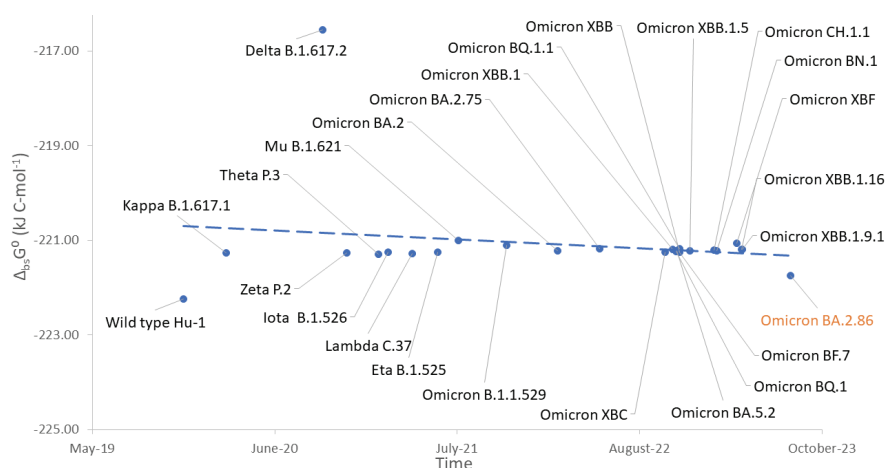
Fig. 1. Gibbs energy changes of biosynthesis of SARS-CoV-2 variants.

The concern expressed in the social media, concerning the greater pathogenicity of the new BA.2.86 variant seems not to be reasonable, since its Gibbs energy change of biosynthesis is only slightly different than that of the other variants. The epidemiological measures that were undertaken in the fight against the other variants that caused the pandemic should result in an adequate response against the spreading of the BA.2.86 variant. However, the data related to kinetics of binding of the new variant to the host cell receptors are still not available. Therefore, in this work, it is not possible to predict with certainty the potential changes in infectivity of the new BA.2.86 variant compared to the other variants of SARS-CoV-2.

The latest wave caused by the Omicron BA.2.86 variant has shown a specific aspect. Unlike the earlier waves caused by earlier SARS-CoV-2 variants, during the latest wave, the epidemics appeared in parallel caused by other viruses. For example, in Serbia, the cases caused by infection with influenza were registered simultaneously. Having in mind that in the same place at the same time, at least 3 different viruses appeared, there was competition between them. The competition between SARS-CoV-2 and other viruses was reported in literature.[6, 50] We must have in mind that the pandemic wave that was reported in literature[50] was of high intensity, with a large number of infected people and a small number with people with natural or artificial immunity. The reported biothermodynamic properties have shown that in that epidemic wave, there was interference. This means that SARS-CoV-2 dominated, while influenza, parainfluenza and RSV were suppressed, because their biothermodynamic properties were not favourable. In the late 2023 and early 2024, the situation is completely different, since the extent of vaccination against COVID-19 was far greater and also the natural immunity of the population was also greater. Thus, the intensity of the pandemic caused by the Omicron BA.2.86 variant is much lower and is about several thousand new cases daily. This has led to a "dilution" of the virus in the population and therefore decreased the ability of spreading. Therefore, despite the still unfavourable thermodynamic properties, there has been a parallel development of epidemics, caused by different viruses. From this we can conclude that even though thermodynamic properties of the antigen–receptor binding and the thermodynamic properties of multiplication of the virus play a biologically important role in the development of the pandemic, an important role is played by epidemiological measures, in the sense of isolation and vaccination. Therefore, vaccination remains the primary method in the fight against the epidemic.

CONCLUSIONS

This research reports for the first time the empirical formula, molar mass, biosynthesis reactions and thermodynamic properties (enthalpy, entropy and Gibbs energy changes) of formation and biosynthesis of the Omicron BA.2.86

Pirola variant of SARS-CoV-2. The empirical formula of the BA.2.86 virus particle is $CH_{1.639023}O_{0.284130}N_{0.230031}P_{0.006440}S_{0.003765}$, which has a molar mass of 21.75 g/C-mol. The empirical formula of the BA.2.86 variant is different than the empirical formulas of other SARS-CoV-2 variants, other virus species and cellular organisms.

The standard Gibbs energy change of formation of the BA.2.86 virus particle is –24.64 kJ C-mol^{-1}, while that of the BA.2.86 nucleocapsid is –33.32 kJ C--mol^{-1}. Gibbs energy change of formation of the virus particle is less negative than that of the nucleocapsid, which implies a greater usable energy content of the virus particle. This is due to the structure of the virus particle. The virus particle is enveloped and contains lipids, which have a high usable energy content and are not present in the nucleocapsid.

The nucleocapsid of the BA.2.86 variant is characterized by a Gibbs energy change of biosynthesis of –221.75 kJ C-mol^{-1}. Gibbs energy change of biosynthesis of the BA.2.86 variant is more negative than that of its host tissue. The more negative Gibbs energy change of biosynthesis means that the virus will have a greater biosynthesis rate than the host tissue, according to the biosynthesis phenomenological equation. The greater biosynthesis rate means that an infected host cell will produce more virus particles than its own building blocks. This allows the virus to hijack the host cell.

Gibbs energy change of biosynthesis of the BA.2.86 variant is very similar to those of the other variants under monitoring: CH.1.1 and XBB.1.16. The Gibbs energy change of biosynthesis represents the driving force for biosynthesis of virus particles and is proportional to their biosynthesis rate. Since the BA.2.86, CH.1.1 and XBB.1.16 variants have similar Gibbs energy change of biosynthesis, they will have similar biosynthesis rates. This means that they will have very similar pathogenicity.

SUPPLEMENTARY MATERIAL

Additional data and information are available electronically at the pages of journal website: https://www.shd-pub.org.rs/index.php/JSCS/article/view/12862, or from the corresponding author on request.

И З В О Д

ОМИКРОН ВА.2.86 ПИРОЛА НОЋНА МОРА: ЕМПИРИЈСКЕ ФОРМУЛЕ И ТЕРМОДИНАМИЧКЕ ОСОБИНЕ (ПРОМЕНЕ ЕНТАЛПИЈЕ, ЕНТРОПИЈЕ И ГИБСОВЕ ЕНЕРГИЈЕ) НУКЛЕОКАПСИДА, ВИРУСНЕ ЧЕСТИЦЕ И БИОСИНТЕЗЕ ВА.2.86 ПИРОЛА ВАРИЈАНТЕ

МАРКО Е. ПОПОВИЋ[1], МАРТА ПОПОВИЋ[2], ГАВРИЛО ШЕКУЛАРАЦ[1,3] и МАРИЈАНА ПАНТОВИЋ ПАВЛОВИЋ[1,3]

[1]*Универзитет у Београду, Институт за хемију, технологију и металургију, Његошева 12, 11000 Београд,* [2]*Универзитет у Београду, Биолошки Факултет, Студентски Трг 16, 11000 Београд и* [3]*Универзитет у Београду, Центар изузетних врдности за хемију и инжењеринг животне средине ИХТМ, Београд*

Слично фениксу, SARS-CoV-2 се периодично појављивао у таласима. Нове варијанте које су се појавиле кроз мутације потиснуле су раније варијанте, што је изазвало нове таласе пандемије. Омикрон ВА.2.86 Пирола варијанта је најновија у низу. Уочена је повећана инфективност, што резултира брзим ширењем, као и смањена патогеност, што резултира мањим бројем тешких случајева. Међутим, у јавности постоји страх од даљег развоја епидемије. Ова анализа је урађена са циљем да се процене ризици у периоду од почетка 2024. године. Мутације које је развила варијанта ВА.2.86 довеле су до промене емпиријске формуле и термодинамичких особина. Емпиријска формула ВА.2.86 вирусне честице је $CH_{1,639023}O_{0,284130}N_{0,230031}P_{0,006440}S_{0,003765}$. Она се разликује се од других варијанти SARS-CoV-2, других врста вируса и ћелијских организама. Погонска сила за умножавање вируса, промена Гибсове енергије биосинтезе варијанте ВА.2.86 је −221,75 kJ C-mol^{-1}. Она је негативнија од промне Гибсове енергије биосинтезе ткива домаћина. Према феноменолошкој једначини биосинтезе, негативнија промена Гибсове енергије биосинтезе омогућава вирусу да постигне већу брзину биосинтезе и преузме метаболизам ћелије домаћина. Међутим, промена Гибсове енергије биосинтезе варијанте ВА.2.86 је слична оној код варијанти CH.1.1 и XBB.1.16. То значи да ове варијанте треба да имају сличне брзине размножавања, а самим тим и сличну патогеност. Дакле, чини се да нема основа за страх од екстензивног ширења тешких облика, али постоје разлози за опрез и праћење ширења епидемије и потенцијалне појаве нових мутација. Штавише, за разлику од ранијих пандемијских таласа, током најновијег пандемијског таласа, истовремено су се појавиле инфекције инфлуенце, RSV и варијанте ВА.2.86, што заслужује анализу.

(Примљено 12. марта, ревидирано 4. априла, прихваћено 8. маја 2024)

REFERENCES

1. G. Campi, A. Perali, A. Marcelli, A. Bianconi, *Sci. Rep.* **12** (2022) 18108 (https://doi.org/10.1038/s41598-022-22816-7)
2. E. C. Holmes, S. A. Goldstein, A. L. Rasmussen, D. L. Robertson, A. Crits-Christoph, J. O. Wertheim, S. J. Anthony, W. S. Barclay, M. F. Boni, P. C. Doherty, J. Farrar, J .L. Geoghegan, X. Jiang, J. L. Leibowitz, S. J. D. Neil, T. Skern, S. R. Weiss, M. Worobey, K. G. Andersen, R. F. Garry, A. Rambaut, *Cell* **184** (2021) 4848 (https://doi.org/10.1016/j.cell.2021.08.017)
3. N. Magazine, T. Zhang, Y. Wu, M. C. McGee, G. Veggiani, W. Huang, *Viruses* **14** (2022) 640 (https://doi.org/10.3390/v14030640)
4. K. Senthilazhagan, S. Sakthimani, D. Kallanja, S. Venkataraman, *Arch. virol.* **168** (2023) 186 (https://doi.org/10.1007/s00705-023-05818-2)
5. A. Aleem, A. B. Akbar Samad, S. Vaqar, in *StatPearls*, StatPearls Publishing, St. Petersburg, FL, 2023

6. M. Popovic, *Microb. Risk Anal.* **24** (2023) 100260
(https://doi.org/10.1016/j.mran.2023.100260)

7. M. Popovic, *Microb. Risk Anal.* **22** (2022) 100232
(https://doi.org/10.1016/j.mran.2022.100232)

8. M. E. Popovic, M. Mihailović, S. Pavlović, *Microb. Risk Anal.* **25** (2023) 100273
(https://doi.org/10.1016/j.mran.2023.100273)

9. M. Popovic, M. Pantović Pavlović, M. Pavlović, *Microb. Risk Anal.* **24** (2023) 100263
https://doi.org/10.1016/j.mran.2023.100263

10. *CDC - Risk Assessment Summary for SARS CoV-2 Sublineage BA.2.86*,
https://www.cdc.gov/respiratory-viruses/whats-new/covid-19-variant.html#:~:text=Huma
n%20cases%3A%20As%20of%20August,CDC's%20Traveler%2Dbased%20Genomic%2
0Surveillance (accessed on August 31, 2023)

11. *Nextstrain - Genomic epidemiology of SARS-CoV-2 with subsampling focused globally
over the past 6 months*, https://nextstrain.org/ncov/gisaid/global/6m?dmin=2023-06-19
(accessed on January 31, 2024)

12. M. E. Popović, G. Šekularac, M. Popović, *Microb. Risk Anal.* **26** (2024) 100290
(https://doi.org/10.1016/j.mran.2024.100290)

13. M. Bartas, A. Volná, C. A. Beaudoin, E. T. Poulsen, J. Červeň, V. Brázda, V. Špunda, T.
L. Blundell, P. Pečinka, *Brief. Bioinf.* **23** (2022) bbac045
(https://doi.org/10.1093/bib/bbac045)

14. W. Wu, Y. Cheng, H. Zhou, C. Sun, S. Zhang, *Virol. J.* **20** (2023) 6
(https://doi.org/10.1186/s12985-023-01968-6)

15. S. Kumar, S. K. Saxena, *Methods* **195** (2021) 23
(https://doi.org/10.1016/j.ymeth.2021.03.007)

16. P. Gale, *Microb. Risk Anal.* **21** (2022) 100198
(https://doi.org/10.1016/j.mran.2021.100198)

17. M. E. Popovic, *Microbiol. Res.* **270** (2023) 127337
(https://doi.org/10.1016/j.micres.2023.127337)

18. M. Popovic, *Microb. Risk Anal.* **23** (2023) 100250
(https://doi.org/10.1016/j.mran.2023.100250)

19. M. Popovic, *Microb. Risk Anal.* **23** (2023) 100249
(https://doi.org/10.1016/j.mran.2023.100249)

20. M. Popovic, M. Popovic, *Microb. Risk Anal.* **21** (2022) 100202
(https://doi.org/10.1016/j.mran.2022.100202)

21. P. V'kovski, A. Kratzel, S. Steiner, H. Stalder, V. Thiel, *Nat. Rev. Microbiol.* **19** (2021)
155 (https://doi.org/10.1038/s41579-020-00468-6)

22. S. Duffy, *PLoS Biol.* **16** (2018) e3000003 (https://doi.org/10.1371/journal.pbio.3000003)

23. M. Popovic, *Vaccines* **10** (2022) 2112 (http://dx.doi.org/10.3390/vaccines10122112)

24. M. Popovic, *Microbiol. Res.* **13** (2022) 937
(http://dx.doi.org/10.3390/microbiolres13040066)

25. M. Popovic, *Microb. Risk Anal.* **22** (2022) 100217
(https://doi.org/10.1016/j.mran.2022.100217)

26. M. Popovic, *Virology* **575** (2022) 36 (https://doi.org/10.1016/j.virol.2022.08.009)

27. M. Popovic, *Comp. Biol. Chem.* **96** (2022) 107621
(https://doi.org/10.1016/j.compbiolchem.2022.107621)

28. E. H. Battley, *Thermochim. Acta* **326** (1999) 7 (https://doi.org/10.1016/S0040-
6031(98)00584-X)

29. E. H. Battley, *Thermochim. Acta* **309** (1998) 17 (https://doi.org/10.1016/S0040-6031(97)00357-2)
30. M. Popovic, *Heliyon* **5** (2019) e01950 (https://doi.org/10.1016/j.heliyon.2019.e01950)
31. M. Popovic, G. B. G. Stenning, A. Göttlein, M. Minceva, *J. Biotechnol.* **331** (2021) 99 (https://doi.org/10.1016/j.jbiotec.2021.03.006)
32. M. Popovic, *Microb. Risk Anal.* **22** (2022) 100236 (https://doi.org/10.1016/j.mran.2022.100236)
33. M. Popovic, *Thermal Sci.* **26** (2022) 4855 (https://doi.org/10.2298/TSCI220524142P)
34. C. Degueldre, *Talanta* **228** (2021) 122211 (https://doi.org/10.1016/j.talanta.2021.122211)
35. P. Gale, *Microb. Risk Anal.* **15** (2020) 100104 (https://doi.org/10.1016/j.mran.2020.100104)
36. T. Maskow, B. Kiesel, T. Schubert, Z. Yong, H. Harms, J. Yao, *J. Virol. Met* **168** (2010) 126 (https://doi.org/10.1016/j.jviromet.2010.05.002)
37. U. Lucia, G. Grisolia, T. S. Deisboeck, *Atti Accad. Peloritana Pericolanti-Classe Sci. Fis. Mat. Natur.* **99** (2021) A3 (https://doi.org/10.1478/AAPP.992A3)
38. U. Lucia, G. Grisolia, T. S. Deisboeck, *Atti Accad. Peloritana Pericolanti-Classe Sci. Fis. Mat. Natur.* **98** (2020) 6 (https://doi.org/10.1478/AAPP.982A6)
39. U. Lucia, T.S. Deisboeck, G. Grisolia, *Front. Phys.* **8** (2020) 274 (https://doi.org/10.3389/fphy.2020.00274)
40. R. J. Head, E. R. Lumbers, B. Jarrott, F. Tretter, G. Smith, K. G. Pringle, S. Islam, J. H. Martin, *Pharm. Res. Persp.* **10** (2022) e00922 (https://doi.org/10.1002/prp2.922)
41. M. Özilgen, B. Yilmaz, *Int. J. Ener. Res.* **45** (2021) 1157 (https://doi.org/10.1002/er.5883)
42. B. Yilmaz, S. Ercan, S. Akduman, M. Özilgen, *Int. J. Exer.* **32** (2020) 314 (http://dx.doi.org/10.1504/IJEX.2020.10030515)
43. S. Khare, C. Gurry, L. Freitas, M .B. Schultz, G. Bach, A. Diallo, N. Akite, J. Ho, R. T. C. Lee, W. Yeo, GISAID Core Curation Team, S.Maurer-Stroh, *China CDC Weekly* **3** (2021) 1049 (https://doi.org/10.46234/ccdcw2021.255)
44. E. W. Sayers, E. E. Bolton, J. R. Brister, K. Canese, J. Chan, D. C. Comeau, R. Connor, K. Funk, C. Kelly, S. Kim, T. Madej, A. Marchler-Bauer, C. Lanczycki, S. Lathrop, Z. Lu, F. Thibaud-Nissen, T. Murphy, L. Phan, Y. Skripchenko, T. Tse, J. Wang, R. Williams, B. W. Trawick, K. D. Pruitt, S. T. Sherry, *Nuc. Ac. Res.* **50** (2022) D20 (https://doi.org/10.1093/nar/gkab1112)
45. B. W. Neuman, M. J. Buchmeier, *Adv. Vir. Res.* **96** (2016) 1 (https://doi.org/10.1016/bs.aivir.2016.08.005)
46. M. Popovic, V. Tadić, M. Mihailović, *J. Biomol. Struct. Dyn.* (2023) 1 (https://doi.org/10.1080/07391102.2023.2256880)
47. U. Von Stockar, in *Biothermodynamics: the role of thermodynamics in Biochemical Engineering*, U. von Stockar, Ed., EPFL Press, Lausanne, 2013, pp. 475–534
48. M. E. Popovic, M. Minceva, *Thermal Sci.* **24** (2020) 4115 (https://doi.org/10.2298/TSCI200109151P)
49. R. T. Balmer, *Modern Engineering Thermodynamics*, Academic Press, Cambridge, MA, USA, 2010. (https://doi.org/10.1016/C2009-0-20199-1)
50. M. Popovic, M. Minceva, *Microorganisms* **9** (2021) 2060 (https://doi.org/10.3390/microorganisms9102060)
51. D. A. Milenković, D. S. Dimić, E. H. Avdović, Z. S. Marković, *RSC Adv.* **10** (2020) 35099 (https://doi.org/10.1039/d0ra07062a)

52. Ž. B. Milanović, M. R. Antonijević, A. D. Amić, E. H. Avdović, D. S. Dimić, D. A. Milenković, Z. S. Marković, *RSC Adv.* **11** (2021), 2838 (https://doi.org/10.1039/d0ra09632f).

SUPPLEMENTARY MATERIAL TO

Omicron BA.2.86 Pirola nightmare: Empirical formulas and thermodynamic properties (enthalpy, entropy and Gibbs energy change) of nucleocapsid, virus particle and biosynthesis of BA.2.86 Pirola variant of SARS-CoV-2

MARKO E. POPOVIĆ[1]*, MARTA POPOVIĆ[2], GAVRILO ŠEKULARAC[1,3]
and MARIJANA PANTOVIĆ PAVLOVIĆ[1,3#]

[1]*University of Belgrade, Institute of Chemistry, Technology and Metallurgy, Njegoševa 12, 11000 Belgrade, Serbia,* [2]*University of Belgrade, Faculty of Biology, Studentski trg 16, 11000 Belgrade, Serbia, and* [3]*University of Belgrade, Centre of Excellence in Chemistry and Environmental Engineering - ICTM, Belgrade, Serbia*

DATA AVAILABILITY

GISAID Identifier:	EPI_SET_230924yd
doi:	10.55876/gis8.230924yd

All genome sequences and associated metadata in this dataset are published in GISAID's EpiCoV database. To view the contributors of each individual sequence with details such as accession number, Virus name, Collection date, Originating Lab and Submitting Lab and the list of Authors, visit 10.55876/gis8.230924yd

Data Snapshot

- EPI_SET_230924yd is composed of 1 individual genome sequences.
- The collection dates range from 2023-07-29 to 2023-07-29;
- Data were collected in 1 countries and territories;

All sequences in this dataset are compared relative to hCoV-19/Wuhan/WIV04/2019 (WIV04), the official reference sequence employed by GISAID (EPI_ISL_402124). Learn more at https://gisaid.org/WIV04.

* Corresponding author. E-mail: marko.popovic@ihtm.bg.ac.rs

Available online at: http://www.shd.org.rs/JSCS

Thermochemistry of pyrolyzed rutin and its esters prepared from facile biocatalytic route

NURUL NADIAH ABD RAZAK[1,2] and MOHAMAD SUFFIAN MOHAMAD ANNUAR[3*]

[1]*Centre for Foundation Studies in Science, Universiti Malaya, 50603 Kuala Lumpur, Malaysia,* [2]*School of Bioscience, Faculty of Pharmacy and Biomedical Sciences, MAHSA University, Bandar Saujana Putra, Jenjarom, Selangor, Malaysia and* [3]*Institute of Biological Sciences, Faculty of Science, Universiti Malaya, 50603 Kuala Lumpur, Malaysia*

Abstract: Pyrolysis of quercetin-3-*O*-rutinoside or rutin and its esters were investigated. Purified ester samples were prepared from lipase-catalyzed esterification of the parent flavonoid, *i.e.*, rutin using acyl donors with different carbon chain length. X-ray diffraction revealed the presence of crystalline peaks in the rutin esters. The degradation activation energies (E_a) as a function of conversion degree α were determined using Kissinger–Akahira–Sunose and Flynn–Wall–Ozawa methods, with corroborative results. Disparity in E_a implies distinct thermal degradation routes. For all studied compounds, degradation is a non-spontaneous process. The presence of acyl moieties and their corresponding carbon chain length in relation to thermodegradation profiles, E_a, entropy (ΔS) and enthalpy (ΔH) changes of the pyrolysis are discussed.

Keywords: activation energy; ester; flavonoid; pyrolysis; thermogravimetry.

INTRODUCTION

Quercetin-3-*O*-rutinoside, or known simply as rutin is a flavonoid with 3--hydroxyflavone backbone comprising of quercetin and disaccharide rutinose (glucose and rhamnose). Rutin is well known for its powerful antioxidant properties[1,2] alongside multiple pharmacological activities that include anti-inflammatory,[3,4] anti-diabetic[5] and anti-leukemia.[6] It has been shown that rutin preparation as a highly purified nanocrystal significantly improved its physicochemical properties, particularly its oral bioavailability.[7]

The potential of flavonoids in theranostic application is limited by their low stability and solubility in the fatty- and aqueous milieu, respectively. To circumvent a number of disadvantages in the traditional chemical synthesis, employing lipase-catalyzed acylation of flavonoid with fatty acid is highly precise for intro-

---

* Corresponding author. E-mail: suffian_annuar@um.edu.my

ducing non-polar group to the former. Enzymatic acylation of flavonoids has been reviewed by the previous literature.[8–10] The reaction is affected by crucial variables such as acyl donor, acyl acceptor, ratios of reactants, and nature of solvent, temperature, reaction time and water content.

Among the flavonoids, there is a strong interest in the synthesis of rutin esters as they possess wide biological activities and pharmacological effects. Rutin esters exhibit higher antioxidant properties in the various experimental conditions studied,[11–13] protect LDL cholesterol from oxidation *in vitro*,[14] inhibit sarco/endoplasmic reticulum Ca^{2+}-ATPase activity,[15] induce the significantly higher levels of micronuclei[16] and decrease the production of vascular endothelial growth factor in human K562 lymphoblastoma cells.[17] Recently, Cardona *et al.* demonstrated that rutin fatty ester formulation with 10 % poly [dimethylsiloxane-*co*-(3-(2-(2-hydroxyethoxy)ethoxy)propyl]methylsiloxane] (PDMSHEPMS) showed significant increase in mucus permeation compared to the formulation without when tested in self-emulsifying delivery system (SEDDS) for oral administration.[18] Researches have shown that rutin esters can be potentially applied in the pharmaceutical, food and cosmetic industries.[8–10]

In this study, rutin esters were synthesized *via* optimized lipase-mediated esterification of rutin, followed by their subsequent isolation to obtain analytical quantity of purified compounds for thermogravimetric studies. X-ray diffraction (XRD) was employed to study the crystallinity properties of purified rutin esters *viz.* rutin laurate, rutin myristate, rutin palmitate relative to the parent molecule, *i.e.*, rutin, along with their thermal degradation attributes; addressing an important gap in the literature on the pyrolysis of high value flavonoids and their fatty acid esters. Kissinger–Akahira–Sunose (KAS) and Flynn–Wall–Ozawa (FWO) methods were adopted to calculate the activation energies associated with calorimetric investigation of rutin and its esters. The findings provide insights on thermal degradation behavior of these valuable compounds; aiding product development alongside potential processing routes for the flavonoid esters.

EXPERIMENTAL

Materials

Lipase from *Candida antarctica* immobilized on acrylic resin (CAL-B), molecular sieve 4 Å, and the acyl acceptor, rutin were purchased from Sigma–Aldrich. Acyl donors *viz.* lauric acid (dodecanoic acid), myristic acid (tetradecanoic acid) and palmitic (hexadecanoic acid), acetone, ammonium formate, methanol and acetic acid were supplied by Merck. Analytical grade solvents and reagents were used as received.

Enzymatic synthesis of rutin ester

The reaction conditions are adopted from the earlier work.[19] Three different carbon chain lengths of acyl donor are selected, *i.e.*, lauric acid (C-12), myristic acid (C-14) and palmitic acid (C-16) for esterification. Filtered rutin (5×10^{-3} M) and fatty acid (0.25 M) were solubilized in 5 mL acetone previously dried with 4 Å molecular sieves. Direct esterification was

started by the addition of 50 mg of immobilized lipase. The reaction was carried out in screw-capped glass tubes shaken horizontally at 200 rpm, 55 °C. After 96 h, 0.2 mL aliquot from the reaction mixture was sampled. Each sample was dried at 70 °C, and re-suspended in 1 mL of methanol and filtered through a 0.22 μm PTFE filter for subsequent analysis by HPLC. Three independent replicates were made for every measurement. Control experiments (without catalyst) were also conducted in parallel.

In order to study the effects of selected reaction parameters, experimental design using full factorial design (FFD) was devised in MINITAB® 15 software. The effects of three key variables *viz.* acyl donor concentration (M, represented by lauric acid), temperature (°C) and enzyme loading (g) were initially screened using full factorial design (FFD). Lipase-catalyzed synthesis of rutin ester was performed in random triplicates with lowest, middle and highest factor levels (Supplementary material to this paper, Table S-I). The effects of studied variables were evaluated in terms of rutin ester yield as the response output.

With three variables, each studied at three levels (minimum, middle and maximum point values), there were 27 experimental runs including triplicates generated by MINITAB® 15 software. The design was completely randomized along with the sampling.

High performance liquid chromatography (HPLC)

Quantitative analysis of rutin and its esters were performed in a HPLC (Jasco, Japan) system equipped with degasser (DG 980 50), binary pump (PU 980), auto sampler (AS 950), column oven (CO 965) and ultraviolet (UV) detector (UV 975). The detector was operated in ultraviolet wavelength detection at 280 nm. A Chromolith® HR RP-18^e column (4.6 mm×10 mm, 2 μm, Merck, Darmstadt, Germany) fitted with analytical guard column (4.6 mm×10 mm×2 μm) was used for separation. The temperature of the column was maintained at 35 °C with a flow-rate of 1 mL min^{-1}. The injection volume was set at 20 μL. The separation of different components of the reaction mixture was performed using a gradient of methanol (A) and water with 0.1 % acetic acid (B) (A/B volume fraction): 0.1 (30/70), 5.0 (100/0), 10.0 (100/0), 11.0 (30/70) and 15.0 min (30/70). The conversion of reactants to acylated flavonoid (rutin ester) was calculated as the percentage difference between initial and residual molar concentration of rutin parent molecule:

$$\text{Conversion (\%)} = 100 \frac{F_{\text{initial}} - F_{\text{residual}}}{[F]_{\text{initial}}} \tag{1}$$

where $[F]_{\text{initial}}$ is the initial rutin concentration and $[F]_{\text{residual}}$ is the residual rutin concentration in the mixture at the end of the reaction. Calibration plot for rutin was constructed using its standard compound dissolved at different molar concentrations in methanol.

The pure rutin esters (rutin laurate, rutin myristate and rutin palmitate) were separated in Agilent HPLC, LC 1200 (Agilent Technologies, USA) system equipped with automatic fraction collector. The operating details for the separation of the mixtures are similar with earlier mentioned method.

Liquid chromatography/tandem mass spectrometry (LC/MS/MS)

Molecular weight analyses for rutin and its esters were performed using a liquid chromatograph (LC, Shimadzu, LC 20 AD, binary pump) interfaced to AB Sciex 3200QTrap LC/MS//MS with Perkin Elmer FX 15 uHPLC system used for integration, calibration, plotting of LC–MS spectra and data processing, for both qualitative and quantitative analyses. A Phenomenex Aqua C18 reversed phase column (50 mm×20 mm, 5 μm particle size) was installed as the stationary phase. Reaction components separation were achieved using different gradients

of 0.1 % formic acid and 5 mM ammonium formate in water (C) and acetonitrile with 0.1 % formic acid and 5 mM ammonium formate (D) as follows (C/D volume fraction): 0.01 (90/10), 8.00 (10/90), 11.00 (10/90), 11.10 (90/10) and 15.00 min (90/10) at a constant flow rate of 0.25 mL min^{-1}. The column oven temperature was operated at 40 °C with the injection volume of 20 μL over the total running time of 15 min. The mass spectrometer was operated in the negative turbo ion spray (ESI) mode, and the electrospray source parameters were fixed as follows: electrospray capillary voltage 3.5 kV, source temperature 500 °C. Nitrogen was used in the electrospray ionization source. The de-solvation gas and source gas flows were at 40 psi. The de-clustering potential and entrance potential were at 40 and 10 V, respectively.

Thermogravimetric analysis (TGA)

Thermal properties of standard rutin and acylated rutin *viz.* rutin laurate, rutin myristate, rutin palmitate were determined using thermogravimetric analysis (TGA) performed using Perkin Elmer TGA 4000 machine (Perkin Elmer, USA). Approximately 8 to 10 mg of the sample was loaded onto the ceramic crucible pan. Each sample was heated from 30 to 800 °C at multiple heating rates of 5, 10, 15 and 20 °C min^{-1} under a nitrogen flow rate of 20 mL min^{-1}.

Thermodynamic and kinetic analyses of thermal degradation of rutin and its esters

The activation energy (E_a) values for thermal degradation of rutin and its esters were calculated using iso-conversional method on the basis that the reaction rate depends on temperature and conversion degree. Compared to model-fitting method, the kinetic approach is preferable as it is sufficiently flexible to allow for any changes in the mechanism during the reaction course, and mass transfer limitation is minimized by the use of multiple heating rates. Two kinetic methods namely Kissinger–Akahira–Sunose (KAS) and Flynn–Wall–Ozawa (FWO) were applied for the analysis of samples thermograms. Mathematical basis and derivation for the analysis are provided in the Supplementary material.

X-ray diffraction (XRD) analysis

Powder X-ray diffraction (XRD) analysis was performed on the prepared sample powder for phase identification and determination of crystallite size using a PANalytical EMPYREAN machine (Analytical, Almelo, Netherlands). The operation voltage and current were at 40 kV and 40 mA, respectively, with a diffraction angle from 10 to 70° applying a resolution of 2θ.

The average crystallite size is determined using Debye–Scherrer equation:

$$D = \frac{\kappa\lambda}{\beta\cos\theta} \tag{2}$$

where D is mean crystallite size, κ is coefficient equal to 0.94, λ is the wavelength of the X--ray radiation used (0.15406 nm), β is full width half maximum intensity measured in radian and θ is the angle from the corrected position.

RESULTS AND DISCUSSION

Liquid chromatography/tandem mass spectrometry (LC/MS/MS)

LC/MS/MS spectra show that a single ester product is formed by the esterification of each aliphatic fatty acids (Supplementary material, Fig. S-1a–d). From the representative spectrum, a distinct signal at *m/z* 791.4 (t_R = 9.64 min) establishes that only a single lauric acid is acylated to each molecule of rutin to yield rutin laurate (Fig. S-1b). It is also observed that longer carbon chain length

of the acyl donor used in the reaction results in longer retention time for the acylated flavonoid, and correspondingly larger m/z value. Individual peak for rutin myristate appears at m/z of 819.5 (t_R = 10.85 min, Fig. S-1c); rutin palmitate presents its major ion peak at m/z 848.8 (t_R = 12.27 min, Fig. S-1d). For each synthesized rutin ester, consistent fragmentation pattern is evident at m/z 463.2 and 591.4 authenticating successful esterification of acyl donor molecule to the rutin parent molecule. The exact position of the esterification in rutin molecule has been authenticated from our previous study, *i.e.*, acylation by the lipase enzyme takes place specifically on the secondary 4'''-OH group of the rhamnose moiety.[19]

Effects of acyl donor carbon chain length on conversion yield

The effects of carbon-chain length of acyl donors on the lipase-mediated esterification of rutin were investigated using aliphatic fatty acids with carbon number ranging from 12 to 16. The progress of esterification reaction was monitored for 120 h, which also included the equilibrium state. The amount of synthesized rutin esters increased with reaction time. However, after 96 h, negligible changes in the rutin ester concentration was observed attributed to the significant amount of water product present in the reaction mixture (data not shown). At equilibrium, comparable conversion and reaction rate were achieved for the three types of rutin esters synthesized (Supplementary material, Fig. S-2). Similar findings are reported in the literature that showed the fatty acid chain length had a slight effect or no significant effect on conversion yield when fatty acids, of medium and high chain length, are used in acetone media.[17,20] However, Viskupicova *et al.*[11] and Ardhaoui *et al.*[21] reported that increasing the carbon number of the aliphatic fatty acids (from C12 up to C18) resulted in gradual decrease in conversion yield of esters with steric hindrance and was suggested as the primary reason. Therefore, the effect of the chain length of the fatty acid (the acyl donor) on esterification yield is difficult to generalize and remains a matter of discussion.[9]

Statistical experimental design of lipase-mediated esterification

From the three acyl donors tested (C12–C16), the esterification of rutin with lauric acid was selected as a model reaction. The effects of selected variables namely lauric acid concentration (M, factor A), enzyme loading (g, factor B) and temperature (°C, factor C) were initially screened using a full factorial design (FFD). A total of 27 experimental runs were generated, and the equilibrium concentration of rutin laurate was assayed at 96 h. Responses for variables screening experiments are shown in Table S-II (Supplementary material). The highest rutin laurate molar concentration was observed when the concentration of lauric acid, enzyme loading and temperature were specified at 0.25 M, 0.05 g and 55 °C, res-

pectively. Conversely, the lowest rutin laurate molar concentration was obtained at the lowest level of each variables when in combination. Detailed analysis of the statistical experimental design results and optimization are provided in the Supplementary material.

X-ray diffraction (XRD)

X-ray diffraction patterns of rutin and its esters are shown in Fig. S-3 (Supplementary material). The diffraction pattern provides important information on material crystallinity including its relative difference to amorphous structure. The average crystallite size of rutin and its corresponding esters are shown in Table I.

TABLE I. Determination of crystallite size using Debye–Scherrer equation; *FWHM*: full-width-at-half maximum; *D*: diameter

Sample	2θ / °	FWHM / °	D / nm
Rutin	15.01	0.3070	27.26
	16.84	0.2558	32.79
	22.24	0.3070	27.54
	26.29	0.2558	33.31
Rutin laurate (R-12)	5.76	0.2047	40.59
	6.79	0.2047	40.61
	9.23	0.3070	27.12
	23.03	0.2558	33.10
Rutin myristate (R-14)	5.74	0.2047	40.59
	6.74	0.2047	40.60
	9.14	0.2558	32.54
	23.03	0.2047	41.37
Rutin palmitate (R-16)	5.64	0.2047	40.58
	6.65	0.3070	27.07
	9.00	0.4093	20.35
	22.63	0.2047	41.37

Rutin exhibits intense and sharp diffraction peaks at 2θ 15.01, 16.83, 22.3 and 26.2° with crystallite size of 27.27, 32.79, 27.54 and 33.31 nm respectively. These results are comparable and consistent with Şamlı *et al.* demonstrating the crystalline behavior of rutin.[22] On the other hand, X-ray diffraction of rutin esters shift towards lower angles and exhibit similar pattern at 5.76, 6.79, 9.23 and 23.03° for rutin laurate, 5.74, 6.74, 9.14 and 23.03° for rutin myristate and 5.64, 6.65, 9.00 and 22.63° for rutin palmitate. At 2θ 5.64 to 5.76°, for all studied esters, equal crystallite size is determined. Sharp peaks in diffractograms of pure rutin and its corresponding esters specify crystalline behavior of the compounds.

The peak top position of rutin 2θ 26.2° shifts to lower angle (2θ 26.2 to 23°) for the corresponding esters with the same peak intensity values. Interestingly, at this angle, comparable crystallite size (33.31 nm) is observed for rutin and rutin

laurate. However, the crystallite size increases from 33.31 (for rutin) to 41.37 nm (for rutin myristate and rutin palmitate). While minor differences are observed in the diffractograms, it categorically excludes possible dramatic alteration in the crystallinity of the samples. It can be concluded that the presence of fatty acid moiety in the rutin ester results in similar crystalline behavior as in pure rutin, and the average size of crystallite is proportional to acyl donor chain length. The esterification of fatty acids with higher chain lengths, such as myristic acid and palmitic acid, disrupts intermolecular hydrogen bonds, leading to the formation of an ordered and compact molecular arrangement and consequently altering the crystalline size of rutin. Similar pattern is observed in the modification of maize starch by esterification with fatty acid moieties.[23] This is further supported by the entropy change values of rutin ester showing increase in orderliness with the increase of fatty acid length (ΔS, Table IV). In general, crystalline substances are physically more stable relative to amorphous ones since their molecules are arranged in a highly ordered, regular pattern.

Thermogravimetric analysis (TGA)

In this study, TGA was used to investigate the thermal behavior of rutin and its corresponding esters. While most thermal degradation studies of rutin and other flavonoids are associated with the thermal treatment of samples,[24–26] there is a noticeable gap in the literature concerning the use of TGA. Weight loss curve provides the information to analyze the changes in sample composition and its thermal stability. First derivative of the curve for a particular sample in relation to changes in temperature is used to show the point at which weight loss is most evident. TG and DTG curves for thermal degradation of rutin and its esters are shown in Fig. 1, and the corresponding data are summarized in Table II.

TG and DTG curves show the degradation of rutin and its corresponding esters occurring in four stages, indicating a complex process with multiple stages (Fig. 1). Although the curves are not radically dissimilar, observable differences for thermograms of rutin and its esters are apparent.

The weight of rutin parent molecule decreases gradually within the range of 30–200 °C, with a mass loss of about 6 %. Using pure rutin compound as a reference, the first degradation stage of rutin esters shifts towards lower temperature. TG curves of rutin esters exhibit initial weight loss of 6–8 % in the temperature range of 30–90 °C (Fig. 1a). The mass loss below 90 °C of rutin laurate is lower than rutin myristate and palmitate (Fig. 1b). For all samples, a small region of weight loss around 100 °C can be seen from their corresponding DTG curves attributed to the evaporation of moisture (Fig. 1b). According to da Costa *et al.* the loss of water molecules (dehydration) of rutin occurs in the first two stages involving molecular rearrangement of rutin polymorphic structure.[27]

With increasing temperature, small molecule and weak chemical bonds gradually decompose and TG curves fall away. It is observed that the first and sec-
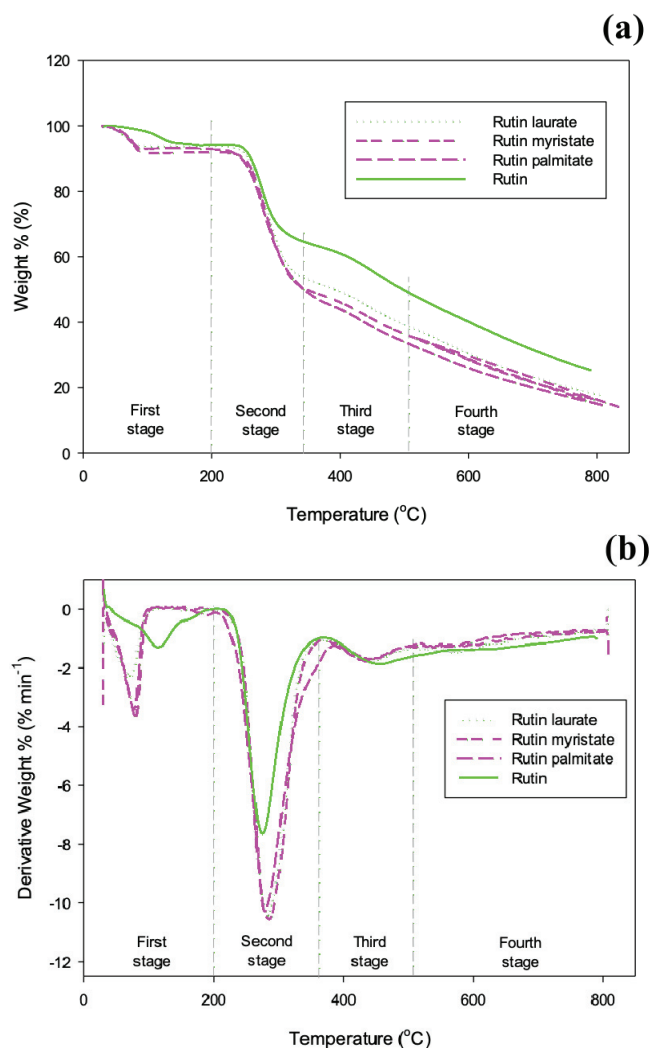
Fig. 1. Thermal decomposition analyses of rutin and its corresponding esters at heating rate of 15 °C min^{-1}: a) TG; b) DTG.

TABLE II. Stages and percentages of mass conversion in thermal degradation of rutin and its esters

Sample	T_i	T_{max}	Degradation stage				
	°C		First	Second	Third	Fourth	Total
Rutin	240.07	272.72	6.06	33.60	12.40	18.43	70.49
Rutin laurate (R-12)	220.19	282.05	5.89	41.74	13.70	20.50	81.87
Rutin myristate (R-14)	219.49	285.13	8.01	43.60	13.62	18.56	83.74
Rutin palmitate (R-16)	217.28	278.86	6.84	47.79	11.15	18.90	84.68

ond degradation stages from the DTG curves of rutin esters are much higher and sharper than for the rutin parent molecule (Fig.1b). The maximum temperature peak (T_{max}) is recorded in the second stage as drastic degradation of rutin and its esters occur. It was also reported that for temperatures above 100 °C, a sharp degradation of rutin was observed.[24] The onset of degradation temperature ($T_{initial}$) is used to indicate resistance to thermal degradation. Rutin is thermally stable up to 240 °C but its ester compounds exhibit lower $T_{initial}$ *viz.* 220, 219 and 217 °C for rutin laurate, rutin myristate and rutin palmitate, respectively (Table II). Thermal stability of rutin esters is lower than that of rutin parent molecule by 20 °C. Rutin is a type of flavonol glycosides consisting of quercetin and disaccharide rutinose (rhamnose and glucose). Based on isothermal profile, da Costa *et al.* reported that the presence of glycoside moieties in rutin alters its thermal degradation rate through lowering of degradation temperature compared to quercetin alone.[27] Relatively high temperature helps to promote the degradation of disaccharide substitution. Introduction of acyl donor to the glycone part of rutin culminates in a comparatively earlier onset of esters degradation. On the other hand, it can be seen that T_{max} for the studied rutin esters are higher than that of parent molecule, which corresponds to the decomposition of acyl donor group present in the esters (Table II).

The second degradation peaks of rutin esters are similar to pure rutin (200 to 390 °C). Major degradation of rutin is characterized by significant mass loss, *i.e.*, ~34 %. With the acyl substituents, mass loss of rutin esters in the second stage increases to 42, 44 and 48 %, respectively, due to longer carbon chain length. Longer chain fatty acid represents higher molecular weight of acyl donor group hence higher percentage of mass loss. Further mass loss occurs in the range of 333 to 498 °C when the evaporation of rutin and its esters come about (~18–20 %). This outcome implies that the degradation of rutin is influenced by temperature.[24] Finally, the compounds gradually decompose into final products at temperature above 498 °C. With longer acyl donor chain length, its decomposition leads to higher percentage of total degradation (Table II).

TG and DTG curves of rutin and its corresponding esters at heating rates of 5, 10, 15, 20 °C min⁻¹ are shown in Figs. 2 and 3, respectively. For all samples, temperatures of recorded degradation stages increase progressively with higher heating rate. Maximum points of TG (Fig. 2) and minimum points of DTG curves (Fig. 3) shift towards higher temperatures. The observation is attributed to faster dissipation rate of heat at higher heating rate, consequently degradation occurs at comparatively higher temperature, thus the shift of TG curves to the right.

From the TG plot of rutin and its esters (Fig. 2), degradation starts at about 30 °C and proceed rapidly with increasing temperature until 270–280 °C. Then, weight loss decreases slowly until final temperature. The temperatures where 50

% weight loss ($T_{50\%}$) of rutin esters occur are lower than that of rutin parent molecule. At heating rates from 5 to 20 °C min^{-1}, $T_{50\%}$ for rutin shifts from 481.93 to 485.5 °C. For rutin laurate, it is about 106 °C lower than that for rutin (376.18 to 381.30 °C), while $T_{50\%}$ for rutin myristate (345.15 to 346.31 °C) and rutin palmitate (332.24 to 346.65 °C) are approximately 137 and 144 °C lower, respectively. In the temperature range of 795–808 °C, degradation of studied esters yields carbon residue approximately 20 % and below ($T_{80\%}$). In contrast, the final carbon residue from pure rutin sample is more than 20 %, corresponding to total weight loss of 22.97, 25.62, 28.99 and 29.46 % at the heating rates of 5, 10, 15 and 20 °C min^{-1}, respectively.
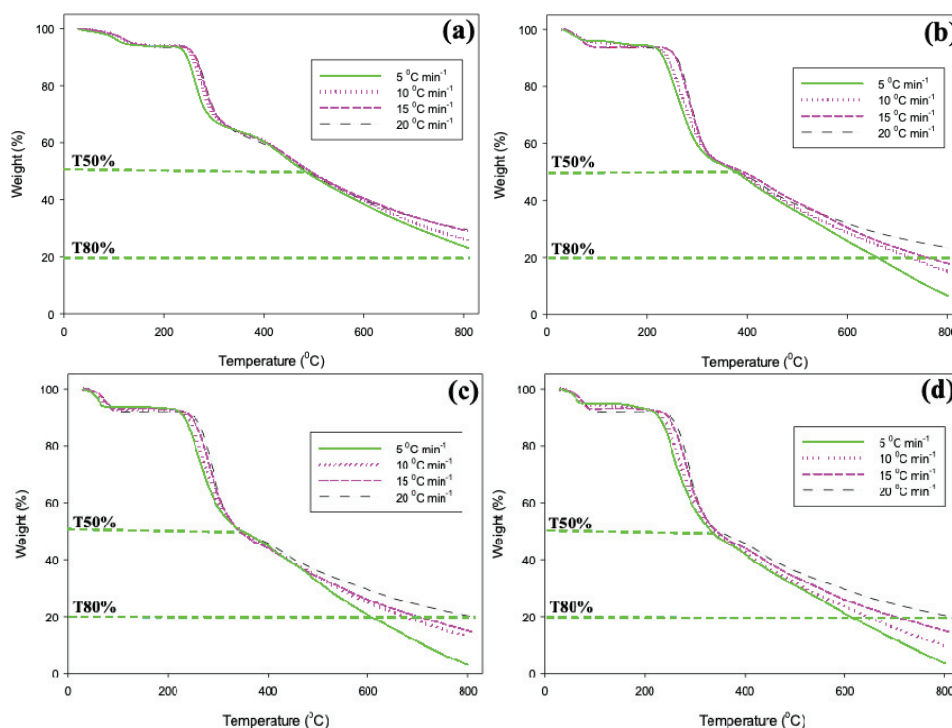
Fig. 2. TG curves of rutin and its corresponding esters at heating rates of 5, 10, 15 and 20 °C min^{-1} :a) rutin, b) rutin laurate, c) rutin myristate and d) rutin palmitate.

In the temperature range of 30–200 °C, DTG peaks of pure rutin are broader than its esters (Fig. 3a). The tailing of the rutin peaks become prevalent as the heating rate increases (indicated by an arrow). In the case of rutin esters (Fig. 3b––d), sharper peaks are observed at the early stage of degradation as heating rate increases. Temperature at the lowest point of the DTG curve indicates the temperature at the highest degradation rate. From Fig. 3, for heating rates of 5 to 20 °C min^{-1}, maximum mass loss rate increases rapidly, *viz.* –3.156 to –12.664 %

min^{-1} (259.88 to 274.57 °C), –2.579 to –14.62 % min^{-1} (270.65 to 283.98 °C), –2.705 to –14.88 % min^{-1} (270.04 to 288.33 °C) and –2.96 to –13.79 % min^{-1} (253.99 to 280.04 °C) for rutin, rutin laurate, rutin mysristate and rutin palmitate respectively.
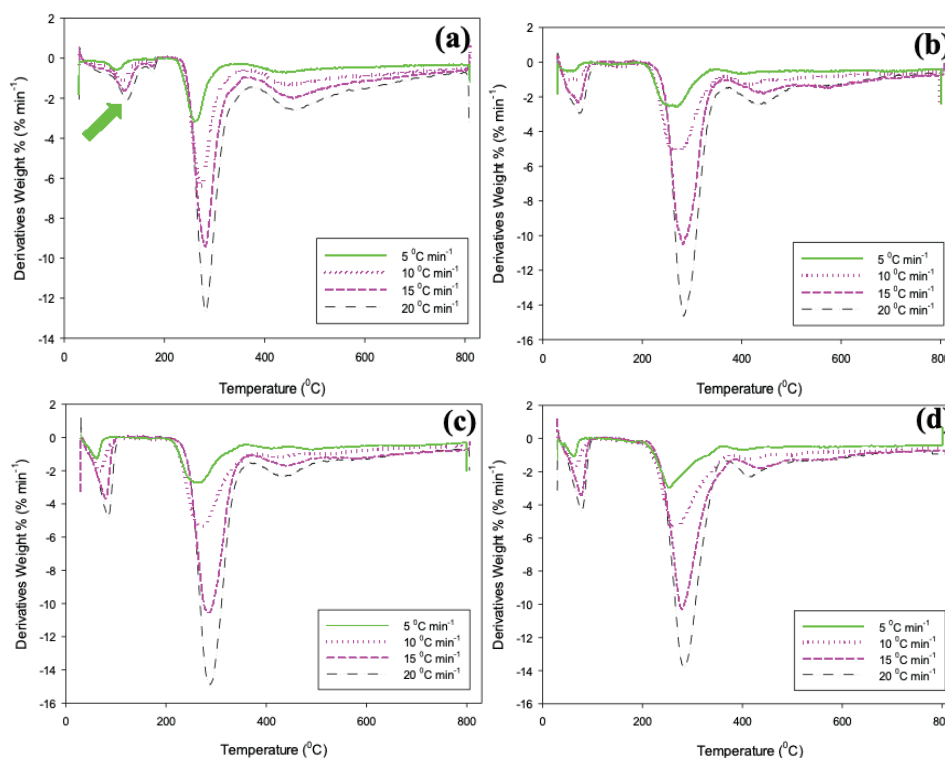
Fig. 3. DTG curves of rutin and its corresponding esters at heating rates of 5, 10, 15and 20 °C min^{-1}: a) rutin, b) rutin laurate, c) rutin myristate and d) rutin palmitate.

Activation energy in thermal degradation of rutin and its corresponding esters

Since the degradation of rutin and its corresponding esters involve multiple stages, the iso-conversional methods (model-free approach), namely KAS and FWO are preferred to calculate the kinetic parameters in order to better understand the process. The two methods allow for estimation of activation energy (E_a) as a function of conversion degree without the need to provide pre-assumption on the reaction function and reaction order. It allows for analysis of multi-step kinetics as a dependence of activation energy on conversion degree, subsequently making deductions with respect to the complexity of the process.

The regression lines based on KAS and FWO methods are presented in Figs. S-7 and S-8 of the Supplementary material, respectively. The regression lines of ln (β/T^2) *versus* $1/T$ for KAS method, and ln β *versus* $1/T$ for FWO method,

based on the same degree of conversion at different heating rates, allow for activation energy calculation from the slope. Excellent linear fitting of all data sets were achieved with coefficient of correlation, $R^2 > 0.98$. E_a values for thermal degradation of rutin and its corresponding esters were determined for mass conversion range of $0.05 < \alpha < 0.90$. The range spans the four separate degradation stages observed (Table II), for the temperature range 30 to 800 °C.

The activation energy (E_a) for thermal degradation of both rutin and its esters, when calculated using KAS and FWO methods, varies with conversion degree throughout the degradation process. Hence, it is obvious that thermal degradation of rutin and its esters proceed through a non-simple process. Nevertheless, for equal α studied, both methods yield E_a values with the high degree of agreement (Table III).

TABLE III. Activation energies calculated using KAS and FWO methods for thermal degradation of rutin and its esters

α	Sample	Kissinger−Akahira−Sunose (KAS) method		Flynn−Wall−Ozawa (FWO) method	
		E_a / kJ mol^{-1}	A	E_a / kJ mol^{-1}	A
0.05	Rutin	77	1.48×10^{10}	80	3.82×10^{10}
	Rutin laurate	81	2.25×10^{12}	82	4.13×10^{12}
	Rutin myristate	76	3.12×10^{11}	78	6.51×10^{11}
	Rutin palmitate	73	7.92×10^{10}	74	1.83×10^{11}
0.30	Rutin	205	5.23×10^{19}	203	3.88×10^{19}
	Rutin laurate	246	2.32×10^{23}	243	3.05×10^{16}
	Rutin myristate	176	2.93×10^{16}	176	4.51×10^{10}
	Rutin palmitate	110	1.82×10^{10}	113	1.37×10^{13}
0.60	Rutin	218	3.49×10^{15}	218	3.40×10^{15}
	Rutin laurate	178	1.34×10^{13}	180	2.11×10^{13}
	Rutin myristate	153	1.60×10^{11}	156	3.22×10^{11}
	Rutin palmitate	101	1.12×10^{7}	107	5.24×10^{7}
0.90	Rutin	224	1.38×10^{12}	228	2.45×10^{12}
	Rutin laurate	65	144307	77	78787
	Rutin myristate	66	62909	77	16028
	Rutin palmitate	67	52652	78	19297

From Table III, for each α, E_a calculated from both methods exhibit very similar trend with respect to the increase in the length of carbon chain of acyl donor with relative error less than 5 %, a considerably low hence tolerable error range.

At the first stage of degradation ($\alpha = 0.05$), rutin and its esters show comparable activation energies, *viz.* 73–81 kJ mol^{-1} for KAS method and 74–82 kJ mol^{-1} for FWO method (Table III). These values are in accord with the weight losses shown in Table II, attributable to loss of water molecules and evaporation of volatile compounds. For pure rutin, the E_a values calculated by both KAS and

FWO methods grew larger in magnitude throughout the progressive α, *i.e.*, 0.05 to 0.90, and increasing degradation temperature (*i.e.*, E_a 77 to 224 kJ mol^{-1} for KAS method; 80 to 228 kJ mol^{-1} for FWO method, Table III). The observed trend is in stark contrast to its corresponding esters where they exhibit a maximum in E_a when $\alpha = 0.30$, before it decreases, and corroborated by both KAS and FWO methods. The observations implicitly identify distinct thermal degradation routes undergone by rutin and its corresponding esters, as most likely non--elementary. For α range from 0.60 to 0.90, E_a values for thermal degradation of pure rutin are consistently highest compared to its corresponding esters. E_a values for the latter increase from $\alpha = 0.05$ to $\alpha = 0.30$, and decrease steeply afterwards (Table III).

For all three rutin esters, highest E_a is at $\alpha = 0.30$ as determined and agreed by both KAS and FWO methods (Table III). It is hypothesized that at $\alpha = 0.30$, and coincided with the second DTG peak, the calculated E_a is minimal activation requirement for breaking of ester bond between acyl donor chain and rutin parent molecule. The E_a for decomposition of rutin ester to rutin and acyl donor fraction is suggested to depend upon the length of acyl donor carbon chain where E_a decreases with the increase in the carbon length of acyl moiety attached to rutin parent molecule, and it is clearly inferable from Table III with respect to α 0.30 to 0.60 as agreed by both KAS and FWO methods. It is proposed that the stable C–C distribution within rutin parent molecule is reduced as the carbon length of attached acyl moiety increases. The mean bond enthalpies in the aromatic rings of quercetin and its sugar moiety are much higher than that of rutin parent molecule bonded to aliphatic carbons. These results agreed with the roasting studies by Rohn *et al.*[28] They reported that thermal degradation behavior of several quercetin glycosides are subjected to the types and position of their sugar moieties. The main product is the aglycone quercetin which remains stable as thermal degradation progresses at 180 °C for 60 min. The E_a data obtained in this study, specifically in the α range of 0.30–0.60, also implied that the rutin esters studied may follow distinct mechanisms in their thermal degradation.

At $\alpha = 0.90$, corresponding to the final degradation stage, the highest E_a value for rutin parent molecule is revealed by both KAS and FWO methods (224 and 228 kJ mol^{-1}, respectively). For the three rutin esters, the E_a values are in range of 65 to 67 kJ mol^{-1} obtained using KAS method, and comparably similar at 77 to 78 kJ mol^{-1} by FWO method. The E_a value of rutin is almost three times higher than those for its esters at $\alpha = 0.90$, corresponding to the degradation of sugar moiety of the rutin. In contrast, significantly lower E_a values are determined for the three rutin esters, *i.e.*, the energy barrier to overcome in the internal chain breaking of separated acyl moiety during the final stage of degradation. These results corroborate with the almost equal observed mass loss 18–20 %

(Table II) for the three rutin esters studied. The findings made in this study agree with da Costa *et al.*[25]

Thermodynamic parameters of rutin and rutin esters

Thermodynamic parameters, while essential in providing insight into the nature of thermal degradation, are often overlooked for phytochemicals that include flavonoid compounds.[29] The thermodynamic parameters in the thermal degradation of rutin and its esters are summarized in Table IV.

TABLE IV. Thermodynamic parameters in thermal degradation of rutin and its esters at different conversion levels at the heating rate of 20 °C min^{-1}

α	Sample	Kissinger−Akahira−Sunose (KAS) Method			Flynn−Wall−Ozawa (FWO) method		
		ΔH kJ mol^{-1}	ΔG kJ mol^{-1}	ΔS J K^{-1} mol^{-1}	ΔH kJ mol^{-1}	ΔG kJ mol^{-1}	ΔS J K^{-1} mol^{-1}
0.05	Rutin	75	98	−60	76	97	−52
	Rutin laurate	78	84	−17	79	84	−12
	Rutin myristate	73	85	−34	75	85	−28
	Rutin palmitate	70	86	−45	72	85	−38
0.30	Rutin	200	135	119	199	135	117
	Rutin laurate	242	138	188	238	137	184
	Rutin myristate	171	140	57	171	139	57
	Rutin palmitate	105	140	−61	108	138	−54
0.60	Rutin	212	185	37	213	185	38
	Rutin laurate	172	178	−9	174	178	−5
	Rutin myristate	148	180	−46	151	179	−40
	Rutin palmitate	96	183	−125	102	180	−113
0.90	Rutin	217	245	−30	220	244	−26
	Rutin laurate	57	211	−163	68	258	−188
	Rutin myristate	58	208	−170	69	239	−182
	Rutin palmitate	60	211	−171	70	238	−180

The values of ΔH, ΔG and ΔS calculated at different conversion levels and the highest rate of the degradation occurrence. Positive ΔH indicates thermal degradation of rutin and its esters is endothermic (Table IV). These results corroborate the DSC results obtained by the other findings that show rutin samples exhibit endothermic events.[30,31] A comparable ΔH value for rutin is observed at α = 0.30 to 0.90 which maybe happen due to greater thermal resistance of the pure rutin molecule. It is suggested pyrolytic decomposition is mainly regulated by the stable C–C distribution. Hydrogen bonds and aromatic, π electron interactions develop between the rings A and C may influence the stabilization efficiency of the rutin. Lower value of ΔH for rutin esters corresponds to lower energy constraint for their thermal degradation relative to pure rutin. Lower values of ΔH are observed with longer acyl chain length. One plausible explan-

ation might be that during the pyrolysis process, after the weak bonds degraded (α = 0.05) and then aromatic, π electron interactions develop between the rings started to degrade accounted for the further increase in ΔH and activation energies. The whole pyrolysis is mainly controlled by 15-carbon flavone skeleton of flavonoid rutin and its intermediate products during pyrolysis. It is hypothesized that above 260 °C, degradation involves the saccharide moiety and it interferes with the stabilization reactions.[1] Disaccharides are temperature-sensitive, particularly during high-temperature processing. In this case, the degradation of the acylated saccharides become more profound with longer acyl chain length reflected by lower value of ΔH (α = 0.30 to 0.60). The long hydrocarbon chain allows less interactions to take place inside the aromatic rings, demanding less energy to break these bonds. At the highest degradation (α = 0.30), the variances in positive ΔH values of rutin esters are calculated at 67–71, 63–66 and 130–137 kJ mol⁻¹ corresponding to differences between rutin laurate and rutin myristate, rutin myristate and rutin palmitate, rutin laurate and rutin palmitate respectively. The range shown is provided from calculation based on KAS and FWO methods (Table IV).

The Gibbs energy change (ΔG) values calculated for thermal degradation of rutin and its esters are positive, corresponding to a non-spontaneous and thermodynamically non-favorable process. At any specific α, negligible variation of ΔG between rutin and its esters are observed. For all studied compounds, the ΔG values increase with temperature. At the time of this report, the ΔG values for pyrolysis of crystalline, different single-type flavonoid esters are yet to be reported. Possibly related are ΔG values estimated for thermal degradation of total flavonoid compound (TFC) in sweet cherries extract ranging 86–105 kJ mol⁻¹.[32]

In terms of entropy change (ΔS, Table IV), rutin parent compound shows positive ΔS indicative of its tendency towards energy and matter dispersal. Conversely, acylated rutins show transition from positive to negative values of ΔS, which reflect less tendency towards energy and matter dispersal for them. It is inferred that the acylation of rutin results in ester compounds that are not likely to be progressing towards a state of disorder. Reduced energy is needed as the compounds adopt more ordered structures.

CONCLUSION

Analyses of activation energy as a function of conversion degree, alongside thermodynamic parameters in the pyrolysis of rutin and its fatty acid esters filled an important void in the literature, and yield useful insights to potential product processing and development routes. Significant variations in activation energies were seen with conversion levels for rutin and its esters ranging from 65 to 246 kJ mol⁻¹. The ΔH (60 to 242 kJ mol⁻¹) and ΔG (84 to 245 kJ mol⁻¹) values for all compounds were positive, indicating endothermic and non-spontaneous nature

of pyrolysis. ΔS shows significant variation with conversion levels ranging from –188 to 180 J K^{-1} mol^{-1}. This clearly represents complex chemistry of thermal conversion with reactions of widely varying kinetic character occurring at different stages of conversion.

SUPPLEMENTARY MATERIAL

Additional data and information are available electronically at the pages of journal website: https://www.shd-pub.org.rs/index.php/JSCS/article/view/12453, or from the corresponding author on request.

И З В О Д

ТЕРМОХЕМИЈА ПИРОЛИЗОВАНОГ РУТИНА И ЊЕГОВИХ ЕСТАРА ПРИПРЕМЉЕНИХ ЈЕДНОСТАВНИМ БИОКАТАЛИТИЧКИМ ПУТЕМ

NURUL NADIAH ABD RAZAK[1,2] и MOHAMAD SUFFIAN MOHAMAD ANNUAR[3]

¹Centre for Foundation Studies in Science, Universiti Malaya, 50603 Kuala Lumpur, Malaysia, ²School of Bioscience, Faculty of Pharmacy and Biomedical Sciences, MAHSA University, Bandar Saujana Putra, Jenjarom, Selangor, Malaysia and ³Institute of Biological Sciences, Faculty of Science, Universiti Malaya, 50603 Kuala Lumpur, Malaysia

Истраживана је пиролиза кверцетин-3-*O*-рутинозида или рутина, и његових естара. Пречишћени узорци естара су припремљени липазом-катализованом естерификацијом полазног флавоноида, тј. рутина, користећи ацил доноре са различитом дужином угљеничног ланца. Дифракција X-зрака је открила присуство кристалиничних пикова код естара рутина. Активационе енергије деградације (E_a) као функције степена конверзије одређене су методама Kissinger–Akahira–Sunose и Flynn–Wall–Ozawa, са узајамно подржавајућим резултатима. Неподударање у E_a имплицира различите путеве термалне деградације. За сва испитивана једињења, деградација није спонтан процес. Присуство ацил структурних елемената и дужина њихових ланаца угљеника дискутовано је у односу на термодеградационе профиле, E_a и промена ентропије (ΔS) и енталпије (ΔH) при пиролизи.

REFERENCES

1. B. Kirschweng, D. M. Tilinger, B. Hégely, G. Samu, D. Tátraaljai, E. Földes, B. Pukánszky, *Eur. Polym. J.* **103** (2018) 228 (https://doi.org/10.1016/j.eurpolymj.2018.04.016)
2. A. M. Mahmoud, *Exp. Toxicol. Pathol.* **64** (2012) 783 (https://doi.org/10.1016/j.etp.2011.01.016)
3. W. Lee, S. K. Ku, J. S. Bae, *Food Chem. Toxicol.* **50** (2012) 3048 (https://doi.org/10.1016/j.fct.2012.06.013)
4. D. S Kim, S. B Lim, *Prev. Nutr. Food Sci.* **22** (2017) 131 (https://doi.org/10.3746/pnf.2017.22.2.131)
5. A. Hunyadi, A. Martins, T. J. Hsieh, A. Seres, I. Zupkó, *PLoS ONE* (2012) (https://doi.org/10.1371/journal.pone.0050619)

6. J. P. Lin, J. S. Yang, J. J. Lin, K. C. Lai, H. F. Lu, C. Y. Ma, R. S. C. Wu, K. C. Wu, F. S. Chueh, W. G. Wood, J. G. Chung, *Environ. Toxicol.* **27** (2012) 480 (https://doi.org/10.1002/tox.20662)

7. R. Mauludin, R. H. Müller, C. M. Keck, *Int. J. Pharm.* **370** (2009) 202 (https://doi.org/10.1016/j.ijpharm.2008.11.029)

8. L. Chebil, C. Humeau, A. Falcimaigne, J. M. Engasser, M. Ghoul, *Process Biochem.* **41** (2006) 2237 (https://doi.org/10.1016/j.procbio.2006.05.027)

9. J. Viskupicova, M. Ondrejovic, T. Maliar, in *Biochemistry*, D. Ekinci, Ed., InTech Europe, Rijeka, 2021, p. 263 (https://doi.org/10.5772/34174)

10. M. E. M. de Araújo, Y. E. Franco, M. C. Messias, G. B. Longato, J. A. Pamphile, P. D. O. Carvalho, *Planta Med.* **83** (2017) 7 (https://doi.org/10.1055/s-0042-118883)

11. J. Viskupicova, M . Danihelova, M. Ondrejovic, T. Liptaj, E. Sturdik, *Food Chem.* **123** (2010) 45 (https://doi.org/10.1016/j.foodchem.2010.03.125)

12. B. Mbatia, S. S. Kaki, B. Mattiasson, F. Mulaa, P. Adlercreutz, *J. Agric. Food Chem.* **59** (2011) 7021 (https://doi.org/10.1021/jf200867r)

13. A. D. M. Sørensen, L. K. Petersen, S. de Diego, N. S. Nielsen, B. M. Lue, Z. Yang, X. Xu, C. Jacobsen, *Eur. J. Lipid Sci. Tech.* **114** (2012) 434 (https://doi.org/10.1002/ejlt.201100354)

14. B. M. Lue, N. S. Nielsen, C. Jacobsen, L. Hellgren, Z. Guo, X. Xu, *Food Chem.* **123** (2010) 221 (https://doi.org/10.1016/j.foodchem.2010.04.009)

15. J. Viskupicova, M. Majekova, L. Horakova, *J. Muscle Res. Cell. M.* **36** (2015) 183 (https://doi.org/10.1007/s10974-014-9402-0)

16. G. Kodelia, K. Athanasiou, F. N. Kolisis, *Appl. Biochem. Biotech.* **44** (1994) 205 (https://doi.org/10.1007/BF02779657)

17. F. Mellou, H. Loutrari, H. Stamatis, C. Roussos, F. N. Kolisis, *Process Biochem.* **41** (2006) 2029 (https://doi.org/10.1016/j.procbio.2006.05.002)

18. M. I. Cardona, N. M. N. Le, S. Zaichik, D. M. Aragón, A. Bernkop-Schnürch, *Int. J. Pharm.* **562** (2019) 180 (https://doi.org/10.1016/j.ijpharm.2019.03.036)

19. N. N. A. Razak, M. S. M. Annuar, *Ind. Eng. Chem. Res.* **54** (2015) 5604 (https://doi.org/10.1021/acs.iecr.5b00996)

20. A. Kontogianni, V. Skouridou, V. Sereti, H. Stamatis, F. N. Kolisis, *Eur. J. Lipid Sci. Technol.* **103** (2010) 655 (https://doi.org/10.1002/1438-9312(200110)103:10<655::AID-EJLT655>3.0.CO;2-X)

21. M. Ardhaoui, A Falcimaigne, S. Ognier, J. M. Engasser, P. Moussou, G. Pauly, M. Ghoul, *J. Biotechnol.* **110** (2004) 265 (https://doi.org/10.1016/j.jbiotec.2004.03.003)

22. M. Şamlı, O. Bayraktar, F. Korel, *J. Incl. Phenom. Macromol.* **80** (2014) 37 (https://doi.org/10.1007/s10847-014-0396-4)

23. S. Sun, Y. Jin, Y. Hong, Z. Gu, L. Cheng, L. Zhaofeng, L. Caiming. *Food Hydrocoll.* **110** (2021) 106224 (https://doi.org/10.1016/j.foodhyd.2020.106224)

24. H. Chaaban, I. Ioannou, L. Chebil, M. Slimane, C. Gérardin, C. Paris, C. Charbonnel, L. Chekir, M. Ghoul, *J. Food Process. Preserv.* **41** (2017) e13203 (https://doi.org/10.1111/jfpp.13203)

25. Ç. Kadakal, T. Duman, R. Ekinci. *Food Sci. Technol.* **38** (2017) 667-673 (https://doi.org/10.1590/1678-457X.11417)

26. Ç. Kadakal, T. Duman, *Pamukkale Üniversitesi Mühendislik Bilimleri Dergisi* **24** (2018) 1370-1375 (https://doi.org/10.5505/pajes.2017.03779)

27. E. M. da Costa, J. M. Barbosa Filho, T. G. do Nascimento, R. O. Macêdo, *Thermochim. Acta* **392** (2002) 79 (https://doi.org/10.1016/S0040-6031(02)00087-4)

28. S. Rohn, N. Buchner, G. Driemel, M. Rauser, L.W. Kroh, *J. Agric. Food Chem.* **55** (2007) 1568 (https://doi.org/10.1021/jf063221i)
29. N. Stănciuc, G. Râpeanu, in *Non-Alcoholic Beverages*, A. Grumezescu, A.M. Holban, Eds., Woodhead Publishing, Sawston, 2019, p. 407 (ISBN 9780128152706)
30. D. C. de Medeiros, S. S. Mizokami, N. Sfeir, S. R. Georgetti, A. Urbano, R. Casagrande, W. A. Verri, M. M. Baracat, *ACS Omega* **4** (2019) 1221-1227 (https://doi.org/10.1021/acsomega.8b02868)
31. M. K. Remanan, F. Zhu, *Food Chem.* **353** (2021) 128534 (https://doi.org/10.1016/j.foodchem.2020.128534)
32. M. Turturică, N. Stănciuc, G. Bahrim, G. Râpeanu, *Food Bioprocess Tech.* **9** (2016) 1706 (https://doi.org/10.1007/s11947-016-1753-7).

Thermochemistry of pyrolyzed rutin and its esters prepared from facile biocatalytic route

NURUL NADIAH ABD RAZAK[1,2] and MOHAMAD SUFFIAN MOHAMAD ANNUAR[3]*

[1]Centre for Foundation Studies in Science, Universiti Malaya, 50603 Kuala Lumpur, Malaysia, [2]School of Bioscience, Faculty of Pharmacy and Biomedical Sciences, MAHSA University, Bandar Saujana Putra, Jenjarom, Selangor, Malaysia and [3]Institute of Biological Sciences, Faculty of Science, Universiti Malaya, 50603 Kuala Lumpur, Malaysia

Table S-I. Factor and level set up for FFD screening experiment

Factor	Level		
	Lowest	Middle	Highest
Lauric acid (M)	0.05	0.15	0.25
Temperature (ºC)	35	45	55
Enzyme loading (g)	0.03	0.04	0.05

Mathematical basis and derivation for thermochemical analysis

Thermal degradation rate under a linear heating rate is expressed by equation (*S1*):

$$\beta \left(\frac{d\alpha}{dt} \right) = k(T)f(\alpha) \qquad (S1)$$

where β is heating rate (°C min^{-1}), k is the rate constant (min^{-1}), T is temperature (Kelvin), t is time (s) and $f(\alpha)$ is a function describing dependence of reaction rate on the extent of reaction, α. α is degree of conversion expressed by equation (*S2*):

$$\alpha = \frac{M_0 - M_t}{M_0 - M_f} \qquad (S2)$$

where M_0 refers to the initial weight, M_t refers to the sample weight at time t and M_f refers to the final weight.

The temperature (*T*) dependence of the rate constant is described by the Arrhenius equation. Thus, the rate of heterogenous solid state reaction can be described by:

---

* Corresponding author. E-mail: suffian_annuar@um.edu.my

S192

$$\frac{d\alpha}{dt} = Ae^{-\frac{E_a}{RT}}f(\alpha)$$

(S3)

where A pre-exponential Arrhenius factor, E_a activation energy, and R universal gas constant. Comparing eqs. (*S1*) and (*S3*) gives:

$$\frac{\delta\alpha}{\delta t} = \frac{A}{\beta}e^{-\frac{E_a}{RT}}f(\alpha)$$

(S4)

Integration of Eq. (*S4*) yields

$$\int_0^\alpha \frac{d\alpha}{f(\alpha)} = g(\alpha) = \frac{A}{\beta}\int_{T_0}^T e^{-\frac{E_a}{RT}}\,dT$$

(S5)

For the KAS method, the Coats−Redfern approximation of $p(x) \approx e^{-x}/x^2$ is applied for the temperature integration to obtain Eq. (*S6*):

$$g(\alpha) = \frac{A}{\beta} \cdot \frac{RT^2}{E_a} \cdot e^{-\frac{E_a}{RT}}$$

(S6)

By taking natural logarithm, Eq. (*S6*) is expressed as Eq. (*S7*):

$$\ln\left(\frac{\beta}{T^2}\right) = \ln\left(\frac{AR}{E_a g(\alpha)}\right) - \frac{E_a}{RT}$$

(S7)

The activation energy is obtained from a plot of ln *(β /T²)* versus *1/T* for a given value of conversion, *α*, where the slope is equal $-E_a/R$.

For the FWO method, Doyle's approximation, which is given as *log* (*p(x)*) = −2.315−0.4567*x* is applied for temperature integration as shown in Eq. (*S8*):

$$g(\alpha) = \frac{A}{\beta}0.00484 e^{-\left(1.052\frac{E_a}{RT}\right)}$$

(S8)

By taking natural logarithm, Eq. (*S8*) is expressed as Eq. (*S9*):

$$\ln(\beta) = \ln\left(\frac{AE_a}{Rg(\alpha)}\right) - 5.331 - 1.052\frac{E_a}{RT}$$

(S9)

where a plot of ln (*β*) versus *1/T* is fitted for E_a calculation from the slope.
The enthalpy, ΔH is calculated using Eq. (*S10*):

$$\Delta H = E_a - RT$$

(S10)

The pre-exponential factor (*A*), the Gibbs free energy (ΔG), and the entropy (ΔS) are calculated using Eqs. (*S11*), (*S12*) and (*S13*), respectively:

$$A = \beta \cdot E_a \cdot e^{\left(\frac{E_a}{RT}\right)}$$

(S11)

$$A = \beta \cdot E_a \cdot e^{\left(\frac{E_a}{RT}\right)}$$

(S12)

$$\Delta S = \left(\frac{\Delta H - \Delta G}{T}\right)$$

(S13)

where K_B is Boltzmann constant and *h* is Planck constant.
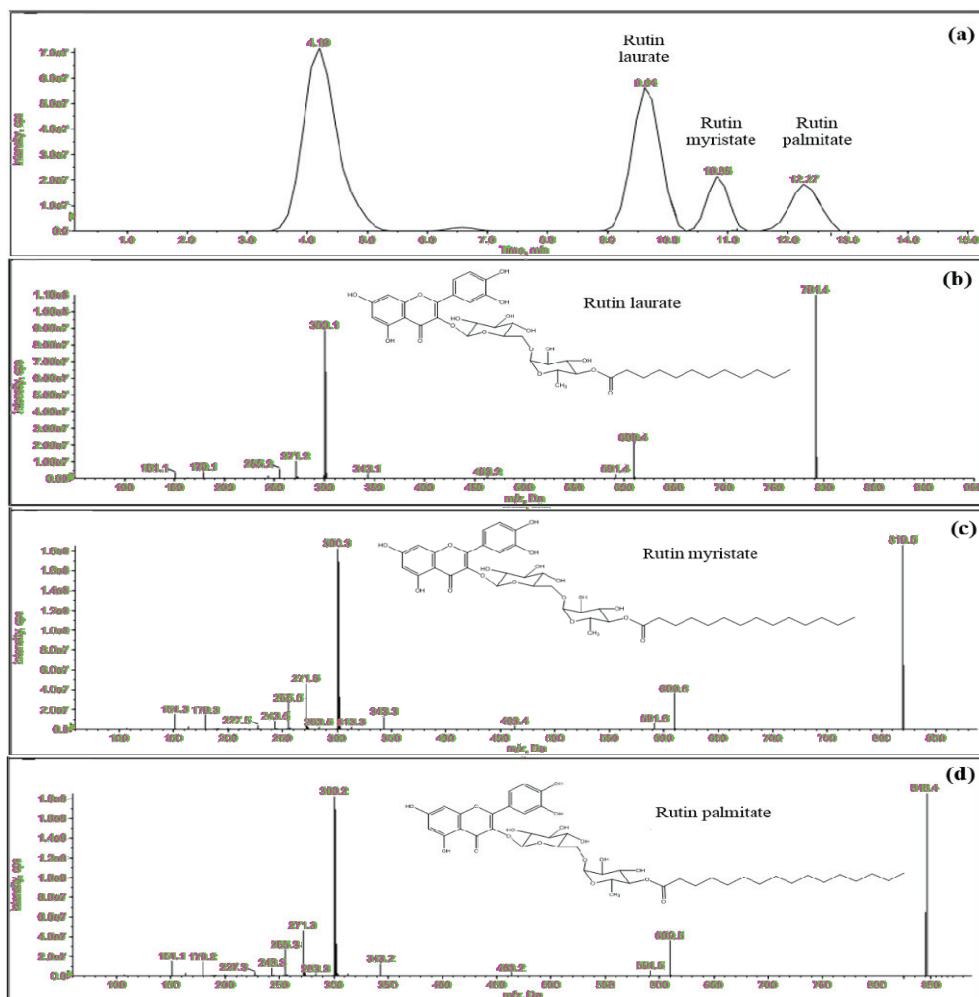
Figure S-1 LC/MS/MS chromatograms for rutin esters: (a) rutin and their ester peaks (b) fragmentation pattern of acylated rutin with lauric acid (c) fragmentation pattern of acylated rutin with myristic acid (d) fragmentation pattern of acylated rutin with palmitic acid.
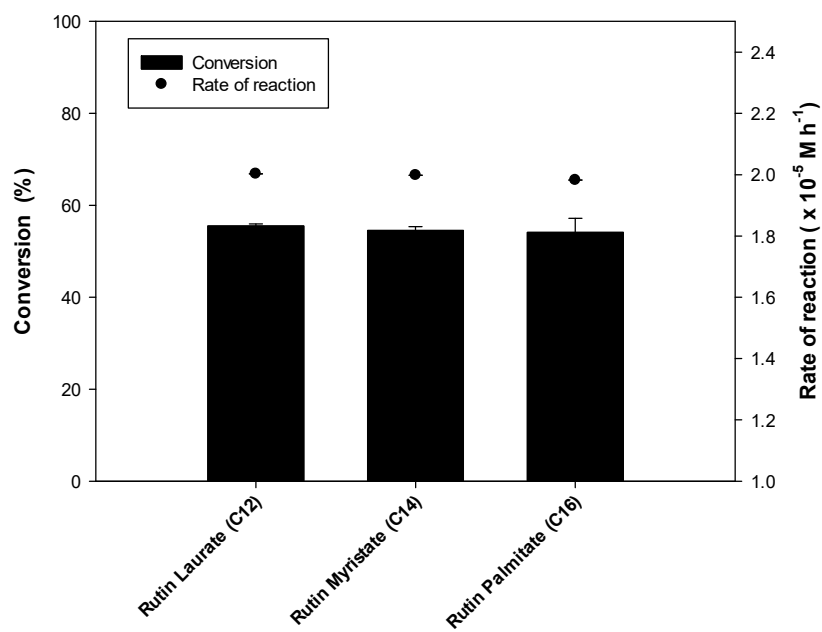
Figure *S-2*. Conversion percentage and reaction rate of esterification of rutin with lauric acid, myristic acid and palmitic acid.
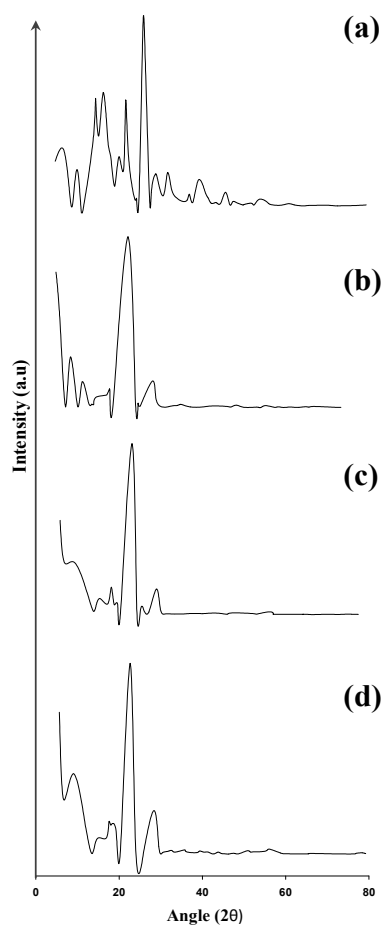
Figure *S3* X-Ray diffractograms of rutin and its corresponding esters (a) rutin (b) rutin laurate (c) rutin myristate (d) rutin palmitate

Table S-II. Responses of FFD experimental runs as a function of different combinations of variables and their levels

Run	Lauric acid (M)	Enzyme loading (g)	Temperature (ºC)	Rutin laurate ($\times 10^{-6}$ M)
1	0.05	0.03	35	2.11
2	0.05	0.03	35	2.08
3	0.05	0.03	35	2.19
4	0.05	0.03	55	4.97
5	0.05	0.03	55	4.83
6	0.05	0.03	55	4.66
7	0.05	0.05	35	5.61
8	0.05	0.05	35	5.41
9	0.05	0.05	35	5.63
10	0.05	0.05	55	7.02
11	0.05	0.05	55	7.11
12	0.05	0.05	55	6.73
13	0.15	0.04	45	11.62
14	0.15	0.04	45	11.35
15	0.15	0.04	45	11.3
16	0.25	0.03	35	3.16
17	0.25	0.03	35	3.01
18	0.25	0.03	35	3.13
19	0.25	0.03	55	10.12
20	0.25	0.03	55	9.61
21	0.25	0.03	55	9.89
22	0.25	0.05	35	7.56
23	0.25	0.05	35	7.8
24	0.25	0.05	35	7.61
25	0.25	0.05	55	12.06
26	0.25	0.05	55	12.16
27	0.25	0.05	55	12.12

Analysis of Statistical Experimental Design Results

Analysis of variance (ANOVA) on full order model terms (main-, 2-way and 3-way effects) using Minitab® 15 software reveals good correlation with R^2- and R^2- *adjusted* value of 0.9986 and 0.9980 respectively (Table SIII). The effects of lauric acid molar concentration, enzyme and temperature, and their interaction effects (AB, AC, and BC) are found significant in all cases ($p < 0.05$). The single effect of full interaction (ABC) is also significant owing to all main effects are significant. The *F*-value for the studied factors shows temperature ($F = 3884.52$) variable exerts the strongest influence on the response followed by lauric acid molar concentration ($F = 2929.40$) and enzyme loading ($F = 2523.37$).

RAZAK and ANNUAR

Table S-III. ANOVA for the effects of lauric acid molar concentration, temperature and enzyme loading on rutin laurate production

Factor	DoF	Adj SS (× 10⁻⁷)	Adj MS (× 10⁻⁷)	F	p
Main factor	3	21.2	7.1	3112.43	0.000
Lauric acid (A)		6.6	6.6	2929.40	0.000
Enzyme (B)		5.7	5.7	2523.37	0.000
Temperature (C)		8.8	8.8	3884.53	0.000
2-way interactions	3	2.5	0.8	360.75	0.000
Lauric acid*Enzyme (AB)		0.1	0.1	25.56	0.000
Lauric acid*Temperature (AC)		1.9	1.9	841.36	0.000
Enzyme*Temperature (BC)		0.5	0.5	215.33	0.000
3-way interactions	1	0.000	0.000	17.41	0.001
Lauric acid*Enzyme*Temperature (ABC)		0.000	0.000	17.41	0.001
Residual Error	18	0.000	0.000		
Total	26	6.6	6.6		

DoF: Degrees of freedom; *Adj SS*: Adjusted sum of squares; *Adj MS*: Adjusted mean of squares; *F*: *F*-statistic; *p*: *p*-statistic

The main effect plots were constructed based on the mean of rutin laurate molar concentration for each factor level. Slope of the plot determines the magnitude of response change with respect to variable change (Figure *S4*). The mean increases from low to high level when the effect of a factor is positive, and *vice versa* when the effect is negative. The effects of all factors are positive as shown by the increase in experimental means when each factor changes from low- to high level. Steeper line indicates a stronger effect of the variable on the experimental response. However, the differences in the relative steepness of the response slopes for lauric acid molar concentration, temperature and enzyme loading variables are not comparable *vis-à-vis* the variable change.
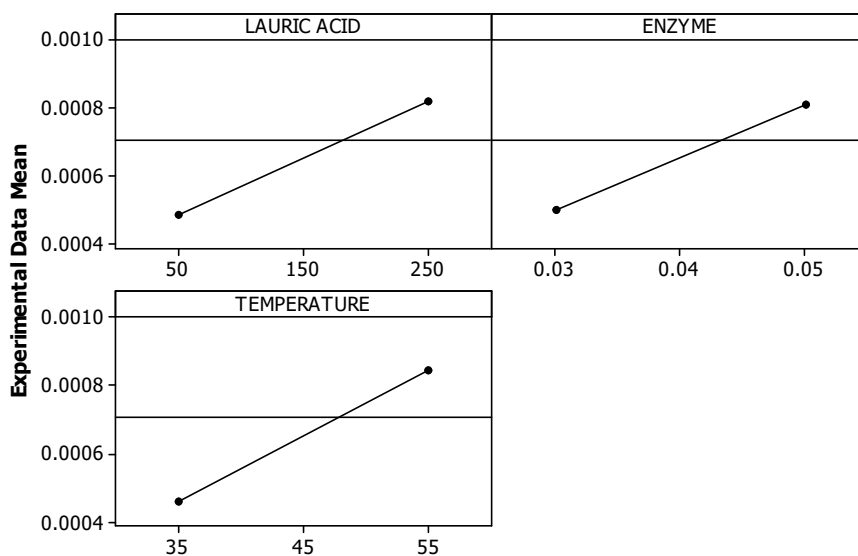
Figure *S-4*. Main effect plots representing the effects of lauric acid molar concentration, temperature and enzyme loading on rutin laurate production

Normal probability plot is used to identify substantive departures from normality. One point on the plot is assigned to each effect. The points which are close to a line fitted to the middle group of points represent those estimated factors that do not demonstrate any significant effect on the response variables. The points far away from the line represent the real factor effects. The normal probability plot is shown in Figure *S5*. The effects of main factors (A, B, and C) and their interactions (AC) are considered to be real considering their significant distance away from the vertical line. Point ABC, BC and AB are attributed to random occurrences. Temperature shows the strongest effect since its point lie furthest from the line, also in agreement with the *F*-value in Table SIII. The factor effects decrease in the following order *viz*. C > A > B > AC > BC > AB > ABC.

Normal Plot of the Standardized Effects
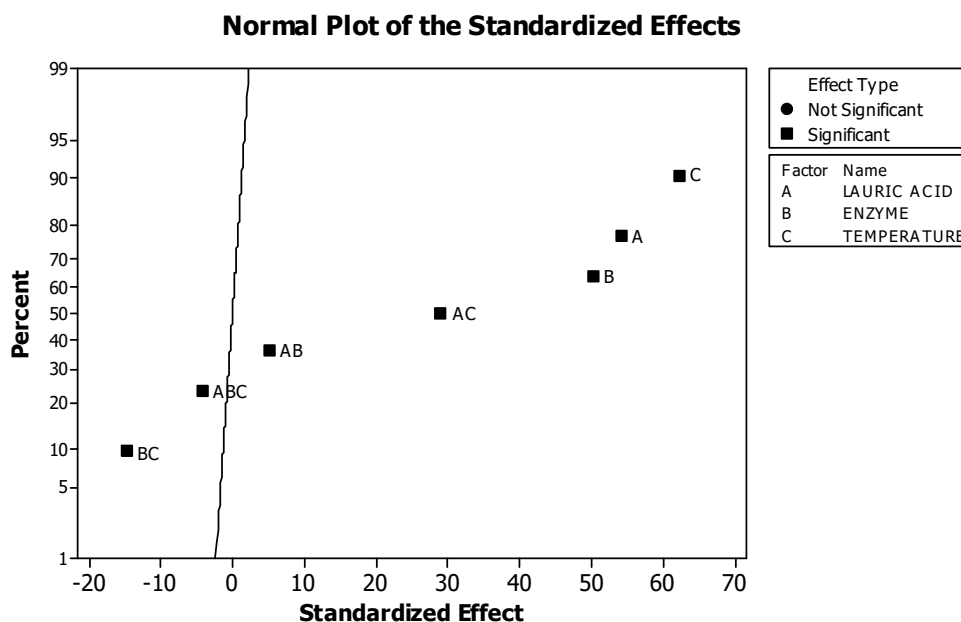
Figure *S-5*. Normal plot of the standardized effects of lauric acid molar concentration, temperature and enzyme loading on rutin laurate production

To evaluate the fitted model, residual analysis was performed with standardized residuals (Figure *S6*). Residual values are derived from experimental values deducted by the model fitted values (Residuals = Experimental values – Model fitted values). The normal probability plot of residuals (Figure *S6a*) shows that the residuals are normally distributed as all standardized residual points exhibit approximately a linear pattern. By observing the residuals against fitted (predicted) values (Figure *S6b*), a random pattern of residuals on both sides of standardized zero line indicates low probability of systematic errors in the experiment (± 2). The normal probability assumption is also corroborated by the general bell-shape curve of the histogram constructed for standardized residuals (Figure *S6c*). It also indicates that the error associated with the experimental data are largely due to random occurrences. In addition, experimental order shows negligible effect on the data collected from the absence of clear pattern in standardized residuals versus observation order plot (Figure *S6d*). Generally, experimental points are reasonably scattered without obvious trend; hence supporting a valid assumption of normal distribution for the collected data.
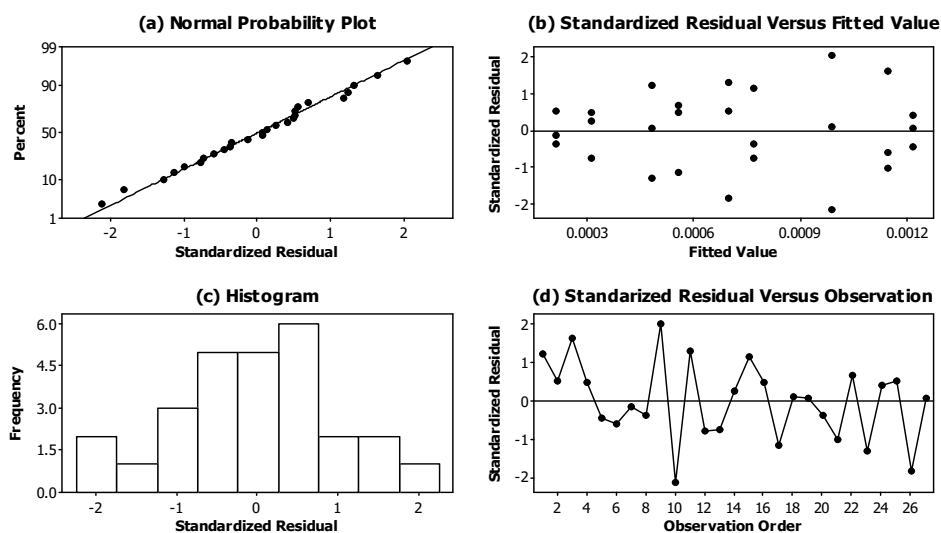
Figure *S-6* Residual plots

Based on Anderson-Darling (*AD*) analysis for possible violation of normality assumption, the *AD* value (= 0.552) is found to be insignificant ($p = 0.141$). Using calculated data from the model, the normal probability plot of residuals shows that the observed values follow closely the theoretical distribution (not shown). It can be concluded that the pattern of residuals follows, in general, a normal distribution; thus, implying the collected data are less likely subjected to non-random errors.
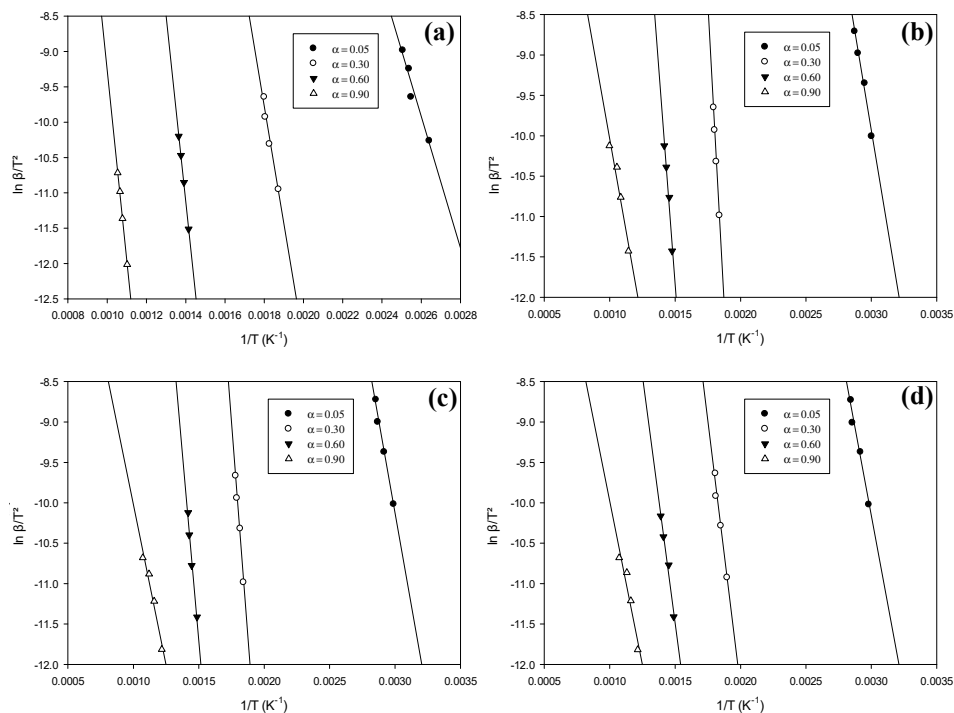
Figure *S-7* Regression lines of rutin and its esters based on KAS method at heating rates of 5, 10, 15, 20 °C min^{-1} (a) rutin (b) rutin laurate (c) rutin myristate (d) rutin palmitate *(Standard deviation of the duplicate measurements was <7 %).*
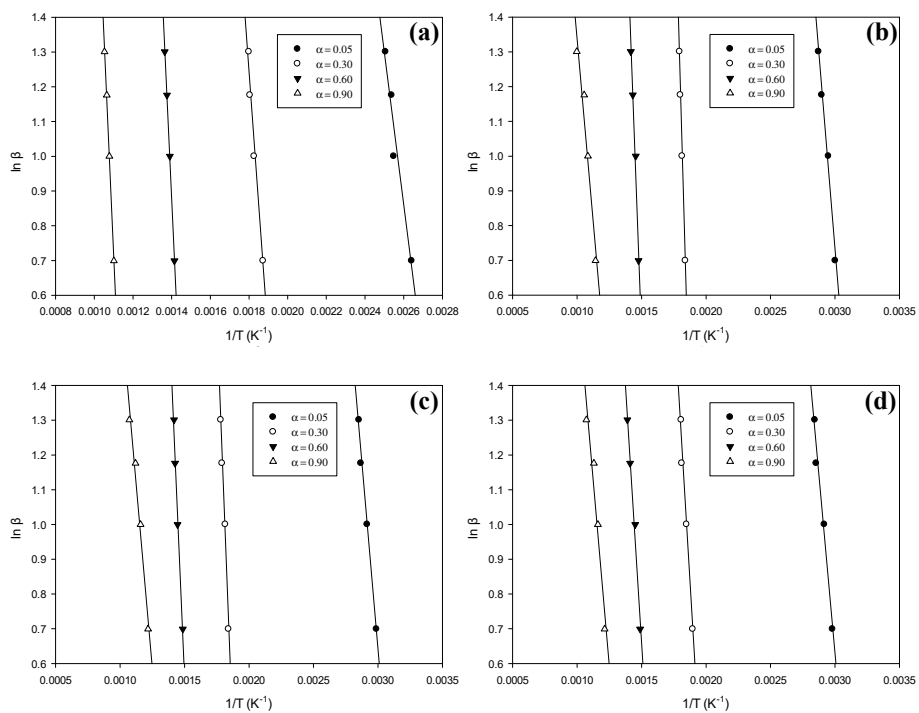
Figure *S8* Regression lines of rutin and its esters based on FWO method at heating rates of 5, 10, 15, 20 °C min^{-1} (a) rutin (b) rutin laurate (c) rutin myristate (d) rutin palmitate (*Standard deviation of the duplicate measurements was <7 %*)

Ph,
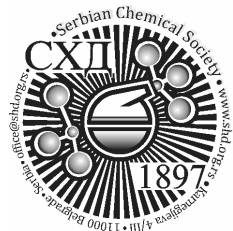
Investigation of adsorption properties of SF$_6$ decomposed gases (SO$_2$ and SO$_2$F$_2$) on pristine and Ti-decorated SWCNT surfaces: A DFT study

ELHAM GHOLAMREZAI KOHAN[1], HOSSEIN MOHAMMADI-MANESH[1]*
and FOROUGH KALANTARI FOTOOH[2]

[1]*Department of Chemistry, Faculty of Science, Yazd University, Yazd, Iran and* [2]*Department of Chemistry, Yazd Branch, Islamic Azad University, Yazd, Iran*

Abstract: DFT calculations were employed to investigate the adsorption of gases produced from SF$_6$ decomposition (SO$_2$ and SO$_2$F$_2$) on pristine and Ti--decorated single-walled carbon nanotubes (Ti-(8,0) SWCNT). All structures were relaxed and their structural and electronic properties were investigated before and after gas adsorption on the surface of the nanotubes. (Ti-(8,0) SWCNT) was found to have high chemisorption sensitivity to Ti, SO$_2$F$_2$ and SO$_2$ adsorptions on its surface. The electronic properties of (8,0) SWCNT were altered from semiconductor to metallic upon decoration with Ti, as demonstrated by the calculated band structures and the density of states (DOS). SO$_2$F$_2$ and SO$_2$ adsorption on the surface of (Ti-(8,0) SWCNT) from different sides transformed the conductor (Ti-(8,0) SWCNT) into a semiconductor nanotube. To more carefully study the nature of adsorption, partial density of states (PDOS) calculations were also made. Additionally, Ti decoration induced a magnetization of approximately 2.61 μ_B in (8,0) SWCNT, which disappeared after gas adsorption.

Keywords: gas adsorption; carbon nanotube; modified nanotube; electronic properties; charge transfer.

INTRODUCTION

Sulphur hexafluoride (SF$_6$) has been widely used in gas-insulated equipment, but it can decompose into SO$_2$F$_2$, SO$_2$ and other compounds[1] under partial discharge over time. Various methods, such as gas chromatography and detector tubes,[2] have been used to identify SF$_6$ decomposition products. Since the carbon nanotube discovery in 1991,[3] it has been widely used in nanotechnology, energy storage materials, gas adsorption properties[4] and hydrogen storage.[5] In addition

---

* Corresponding author. E-mail: mohammadimanesh@yazd.ac.ir

to their essential applications, numerous studies have focused on preparing CNTs for gas detection due to their excellent properties, including higher sensitivity, faster response, and the ability to detect a wider variety of gases. To improve the detection properties of CNTs, various methods have been suggested, including decorating or doping them with metal atoms to enhance their functionality in identifying a wide range of gases.[6] Kong *et al.* have reported the gas sensing properties of single-walled CNTs, laying the groundwork for the application of one-dimensional nanomaterials in gas detection.[7] Zhao *et al.* have studied the adsorption of N_2 gas and various gas molecules on (5,5) SWCNTs and bundles using DFT. They observed weak interactions between SWCNTs and gas molecules, which did not significantly influence the electronic structures of carbon nanotubes.[8] In another study, Zhou *et al.* have investigated the adsorption of SO_2, CH_3OH and CH_4 on Pd-decorated (5,5) CNTs. The strong binding energies and significant electron charge transfers indicated the promising potential of Pd--CNTs for the detection of these gas molecules.[9] Ozekmekci *et al*. investigated the adsorption of hydrogen sulphide onto gallium, germanium and boron doped (4,0) single-walled carbon nanotubes (SWCNTs) using DFT. Their results showed that all doped SWCNT structures have negative Gibbs energy change and adsorption energy values, indicating their potential for H_2S removal *via* adsorption.[10] Patrignani *et al*. studied the adsorption of NO and CO on pristine and metal-decorated (8,0) SWCNT using DFT. Both gases caused a slight deformation of the nanotube curvature in the direction of the adsorbed molecule. Their research demonstrated that decorating SWCNTs with transition metals (Sc, Cr, Fe and Ni) enhances both molecule adsorption and sensing performance.[11] The selection of the (8,0) zigzag SWCNT is driven by its semiconducting properties and heightened sensitivity to conductivity changes, making it a preferred choice for gas detection.[12] Furthermore, an increase in the tube diameter results in a smaller broken symmetry factor (larger *n*), thereby enhancing the adsorption capability of the SWCNT.[13] Recently, experimental and theoretical simulations have indicated the potential for uniform coating of carbon nanotubes with Ti atoms. The nearly empty d orbitals of Ti facilitate interactions with ligands such as gases. Consequently, the charge transfer occurs from the ligands highest occupied orbital to the empty orbital in Ti. This is followed by a reverse charge donation from the d orbital back to the ligand's lowest unoccupied orbital. This intricate charge transfer process, along with the covalent bonding with Ti, leads to the formation of a stable Ti–C bond.[14] It's noteworthy that there is a lack of reports concerning the application of Ti-decorated carbon nanotubes for detecting SF_6 decomposition products in gas insulation equipment. Thus, this study holds significant importance as it offers fresh insights into the development of gas sensors through the use of Ti-decorated SWCNTs for this specific purpose. In this study, we investigated the gas sensing properties of (8,0) SWCNT and Ti-décor-

ated (8,0) SWCNT for SF_6 decomposed gases (SO_2F_2 and SO_2), using DFT calculations. We analysed the structural parameters, adsorption energies, density of states (DOS), band structures and partial density of states (PDOS) in order to describe the interaction between the gases and SWCNTs.

COMPUTATIONAL METHOD

The adsorption of SO_2 and SO_2F_2 molecules to the surfaces of both pristine and Ti-decorated (8,0) SWCNTs was calculated using the Quantum-Espresso software package.[15] The GGA-PBE functional was used to account for exchange-correlation effects.[16] A typical (8,0) SWCNT was created in a supercell with lattice constants $a = 26.46$ Å and $c = 4.26$ Å. The Monkhorst-Pack scheme with a 1×1×10 k-point grid was used to sample the Brillouin-zone.[17] An energy cut-off of 60 Ry was set for the wave function in all structures. The VdW-Grimme--D2 approach was used to correct van der Waals interactions in the calculations. The Xcrysden software was used to display the geometries obtained from DFT calculations. In this study, SO_2 and SO_2F_2 molecules were adsorbed on different sides of the (8,0) SWCNT and Ti-decorated (8,0) SWCNT. The structural and electronic properties, such as band structures, density of states (DOS) and partial density of states (PDOS), were calculated. Furthermore, the magnetization was assessed through spin-polarized calculations. To investigate the stability of (Ti-(8,0) SWCNT) structure, the formation energy for Ti adsorbed on the surface of (8,0) SWCNT is defined as:

$$E_f = E_{Ti/swcnt} - E_{swcnt} - E_{Ti} \tag{1}$$

where $E_{Ti/swcnt}$, E_{swcnt} and E_{Ti} are total energies of the Ti-SWCNT, isolated SWCNT and isolated Ti atom, respectively. The adsorption energy is computed to describe the gas-surface interaction:[18]

$$E_{ads} = E_{surface/gas} - E_{surface} - E_{gas} \tag{2}$$

where the parameter $E_{surface/gas}$ represents the total energy of adsorbed structures, $E_{surface}$ and E_{gas} are the energies of optimized pristine or Ti decorated (8,0) SWCNT and the isolated gas molecules, respectively. Based on Eq. (2), the negative values with greater absolute values of adsorption energy indicate favourable adsorptions. We utilized Bader charge analysis[19,20] for a comprehensive understanding of the gas adsorption mechanism. Charge transfer between Ti and SWCNT is determined by the equation:

$$Q_t = Q_{Ti/swcnt} - Q_{Ti} \tag{3}$$

where $Q_{Ti/swcnt}$ and Q_{Ti} represent the charge transfer for the Ti decorated on SWCNT and isolated Ti, respectively. The charge transfer for each gas adsorption process is calculated as:

$$Q_a = Q_{gas/surface} - Q_{gas} \tag{4}$$

Here, $Q_{gas/surface}$ and Q_{gas} denote the charge transfer amount after adsorption by the gas and isolated gas, respectively. A negative value of charge transfer indicates the acceptance of electrons by the gas molecules.

RESULTS AND DISCUSSION

Adsorption of SO$_2$ to pristine (8,0) SWCNT

The optimized structure of the pristine (8,0) SWCNT with the number of carbon atoms is depicted in Fig. 1. As shown in Fig. 1, after optimization, the C1–C2 and C1–C3 bond lengths of the (8,0) SWCNT are approximately 1.43 and 1.42 Å, respectively, which are consistent with previous findings.[21]
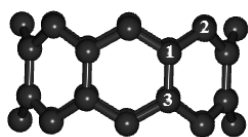
Fig. 1. The optimized structure of pristine (8, 0) SWCNT.

The SO$_2$ molecule was added in front of the C1 atom of the nanotube from both S and O sides. To distinguish between them, SO$_2$–S–CNT is used when SO$_2$ is adsorbed from the S side, and SO$_2$–O–CNT is applied when SO$_2$ is adsorbed from the O side. Fig. 2 shows the optimized configurations of SO$_2$–S–CNT and SO$_2$–O–CNT.
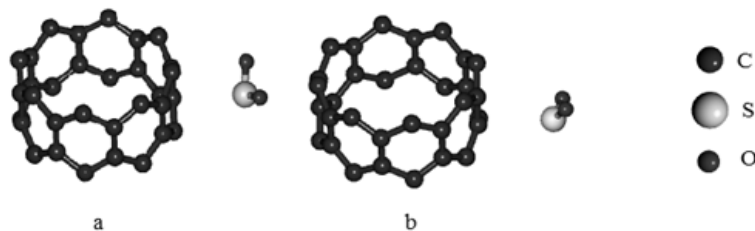
Fig. 2. The optimized configurations of SO$_2$–S–CNT (a) and SO$_2$–O–CNT (b).

From Fig. 2, it is apparent that the SO$_2$ molecule is situated at a considerable distance from the (8,0) SWCNT in SO$_2$–S–CNT and SO$_2$–O–CNT configurations, with distances of 3.04 and 3.28 Å, respectively. The adsorption energies of SO$_2$ in SO$_2$–S–CNT and SO$_2$–O–CNT configurations are –0.24 and –0.23 eV, respectively. Table I presents the nearest bonding distances (*D*) and adsorption energies of all structures. Low adsorption energy values and long distances suggest weak adsorption of SO$_2$ to the (8,0) SWCNT in both configurations. Band structures and DOSs of each structure are illustrated later on. The results confirm that (8,0) SWCNT is a semiconductor with a band gap of 0.59 eV, consistent with previous studies.[22] Upon the SO$_2$ adsorption, a new band emerges above the Fermi level in the conduction band of both configurations which can be attributed to p orbitals of S and O atoms of the SO$_2$ molecule. However, the band gaps do not change significantly after adsorption, as seen in Table I. All structures exhibit overlapping of spin up and spin down bands, indicating no induced magnetiz-

ation after SO_2 adsorption from both sides. To gain further insight into the nature of adsorption, the partial densities of states (PDOSs) are presented later on. It was observed that p orbitals of S and O atoms in SO_2 have high density at about –7 eV and are hybridized with p orbitals of the carbon atom in (8,0) SWCNT. However, this hybridization is far from the Fermi level and does not result in bond formation in either configuration. Therefore, the adsorption of SO_2 does not significantly alter the magnetic or electronic properties of (8,0) SWCNT, which is in consistent with previous findings.[22] For visualizing electronic distribution, the Bader charge analyses calculated the charge difference before and after gas adsorption on nanotube surfaces. The charge transfer for all configurations was computed using Eq. (4) and is presented in Tables I and II. As indicated in Table I, no significant electron transfers were observed between SO_2 gas and (8,0) SWCNT in SO_2–S–CNT and SO_2–O–CNTconfigurations.

TABLE I. Nearest atoms and their distances (D), adsorption energies (E_{ads}), band gaps (E_g) and magnetization (μ) of (8,0) SWCNT before and after gas adsorption and Bader charge analysis for all configurations (Q_g)

Configuration	To	D	E_{ads} / eV	E_g / eV	μ	Q_g
SWCNT	–	–	–	0.59	0	–
SO_2–S–CNT	C–S	3.04	–0.24	0.56	0	–0.05
SO_2–O–CNT	C–S	3.28	–0.23	0.57	0	–0.07
SO_2F_2–F–CNT	C–F	3.22	–0.79	0.58	0	–0.01
SO_2F_2–O–CNT	C–O	3.19	–0.78	0.58	0	–0.01

TABLE II. Formation energies (E_f), nearest atoms and their distances (D), adsorption energies (E_{ads}), band gaps (E_g) and magnetization (μ) of (Ti-(8,0) SWCNT) before and after gas adsorption and Bader charge analysis for all configurations (Q_g)

Configuration	E_f / eV	to	D	E_{ads} / eV	E_g / eV	μ	Q_g
Ti–SWCNT	–1.65	Ti–C	2.19			2.61	
SO_2–S–Ti–CNT		Ti–O	1.90	–4.77	0.43	0	–1.02
SO_2–O–Ti–CNT		Ti–O	1.93	–3.58	0.52	0	–0.95
SO_2F_2–F–Ti–CNT		Ti–F	1.77	–6.74	0.30	0	–1.29
SO_2F_2–O–Ti–CNT		Ti–O	1.68	–5.39	0.50	0	–1.18

Adsorption of SO_2F_2 to (8,0) SWCNT

The optimized configurations of SO_2F_2–F–CNT and SO_2F_2–O–CNT, which represent the adsorption of the SO_2F_2 molecule to the SWCNT from F and O sides, respectively, are shown in Figs. 3 and 4.

The results show that, after optimization, the SO_2F_2 molecule is located at a distance of 3.22 and 3.19 Å from the CNT in SO_2F_2–F–CNT and SO_2F_2–O––CNT configurations, respectively. Table I displays the adsorption energies and the nearest distance (D) between SO_2F_2 and the C atom of (8,0) SWCNT. The results reveal that the adsorption energy of SO_2F_2 is more negative than that of SO_2,
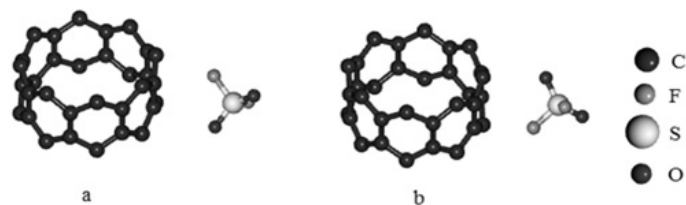
Fig. 3. The optimized configurations of (8,0) SWCNT after SO_2F_2 adsorption: a) from F side $(SO_2F_2$–F–CNT) and b) from O side $(SO_2F_2$–O–CNT).
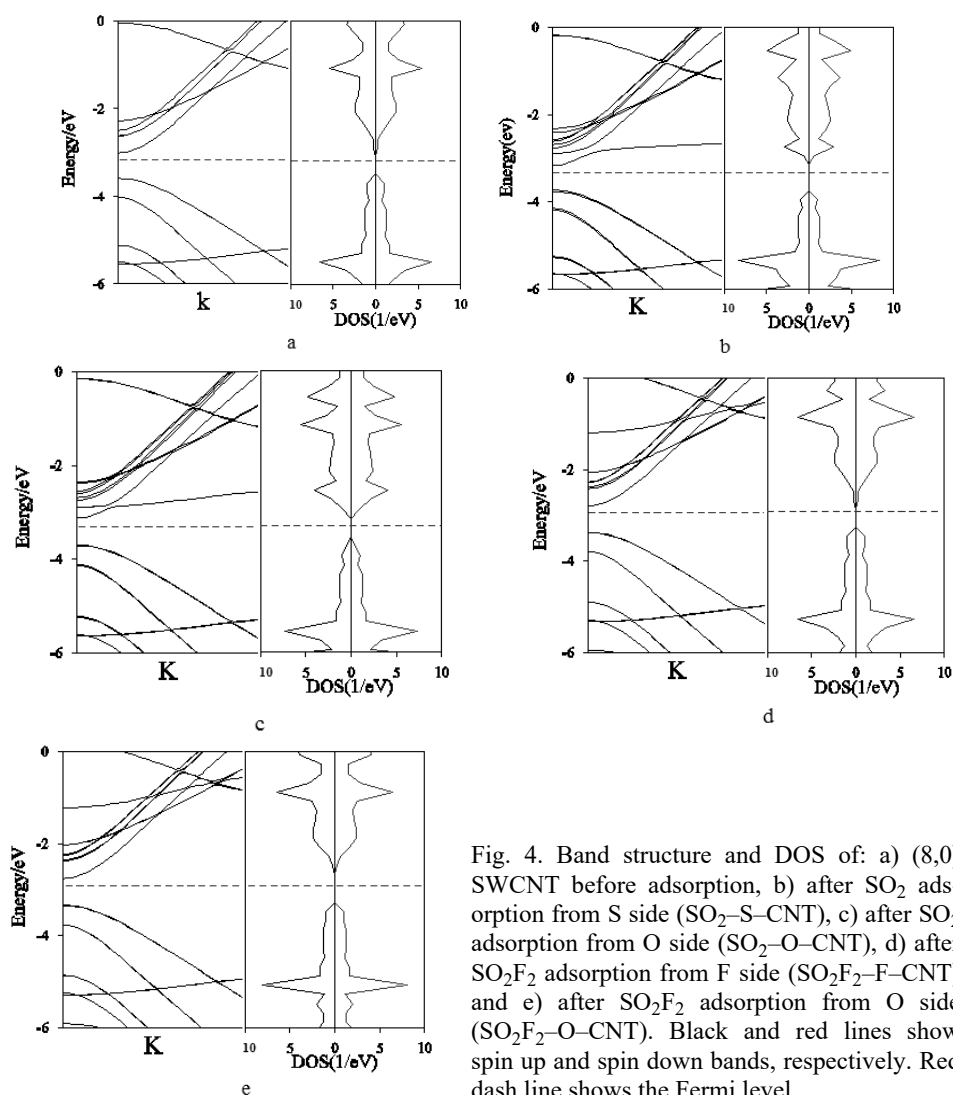
Fig. 4. Band structure and DOS of: a) (8,0) SWCNT before adsorption, b) after SO_2 adsorption from S side $(SO_2$–S–CNT), c) after SO_2 adsorption from O side $(SO_2$–O–CNT), d) after SO_2F_2 adsorption from F side $(SO_2F_2$–F–CNT) and e) after SO_2F_2 adsorption from O side $(SO_2F_2$–O–CNT). Black and red lines show spin up and spin down bands, respectively. Red dash line shows the Fermi level.

favouring SO_2F_2 adsorption over SO_2 onto SWCNT. Nevertheless, the conjunction of extended distances and low adsorption energies suggests a weak adsorption. Fig. 4 shows the band structure and DOS results of SO_2F_2 adsorption on SWCNT. The conduction band of the system displays new energy levels that are far from the Fermi level and do not significantly affect the band gap. The PDOS of these structures are also illustrated in Fig. 5. Spin up and spin down peaks for both configurations are symmetric, which can be attributed to non-magnetic nature of these structures. Our PDOS findings demonstrate that p orbitals of O and F atoms of SO_2F_2 in both configurations are located far from the Fermi level, and cannot hybridize with p orbital of carbon atom in the (8,0) SWCNT, located near the Fermi level. This reinforces the conclusion that SO_2F_2 adsorption is weak, as suggested by our electronic calculations. the Charge analyses given in Table I reveal minimal charge transfer from SO_2F_2 gas to the surface of (8,0) SWCNT in both SO_2F_2–F–CNT and SO_2F_2–O–CNT configurations. Thus, the electronic calculations substantiate the notion that SO_2F_2 adsorption onto (8,0) SWCNT is weak.

Fig. 5. PDOS of: a) (8,0) SWCNT before adsorption, b) after SO_2 adsorption from S side (SO_2–S–CNT), c) after SO_2 adsorption from O side (SO_2–O–CNT), d) after SO_2F_2 adsorption from F side (SO_2F_2–F–CNT) and e) after SO_2F_2 adsorption from O side (SO_2F_2–O–CNT). Left and right side of each graph show the spin up and spin down bands, respectively. Red dash line shows the Fermi level.

Adsorption of SO₂ to Ti-(8,0) SWCNT

The Fig. 6a shows the optimized structure of a Ti-decorated (8,0) SWCNT. Initially, the Ti atom was located in front of the C1 atom of the nanotube at the equilibrium C–Ti distance. As seen in Fig. 6a, the Ti atom moves to the hollow part of the CNT after optimization, in agreement with prior studies.[23] The nearest distance between C atom of the nanotube and Ti atom after optimization is approximately 2.19 Å. The formation energy, calculated using Eq. (1), is about –1.65 eV, confirming the stability of this modified nanotube. The SO_2 molecule was then adsorbed to this modified nanotube from the S and O sides, resulting in SO_2–S–Ti–CNT and SO_2–O–Ti–CNT configurations, respectively.
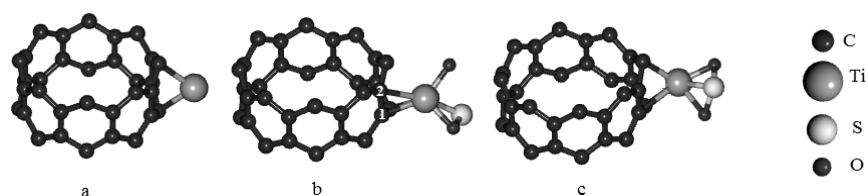
Fig. 6. The optimized configurations of: a) Ti–CNT before adsorption, b) after SO_2 adsorption from S side (SO_2–S–Ti–CNT) and c) after SO_2 adsorption from O side (SO_2–O–Ti–CNT).

Adsorption of SO₂F₂ to Ti-(8,0) SWCNT

SO_2F_2 molecule was adsorbed to Ti-modified nanotube from F and O sides, referred to as SO_2F_2–F–Ti–CNT and SO_2F_2–O–Ti–CNT, respectively. The optimized configurations of the (Ti-(8,0) SWCNT) after the adsorption of SO_2F_2 from both sides are depicted in Fig. 7.
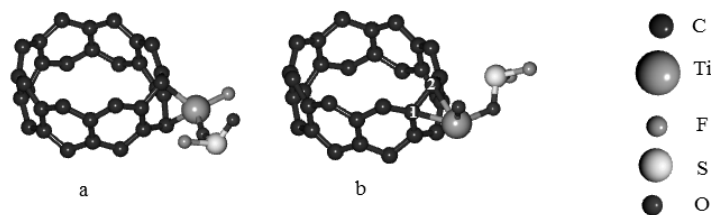
Fig. 7. The optimized configurations of Ti-decorated (8,0) SWCNT after SO_2F_2 adsorption: a) from F side (SO_2F_2–F–Ti–CNT) and b) from O side (SO_2F_2–O–Ti–CNT).

The band structures and DOSs of the (Ti-(8,0) SWCNT) structure are presented in Fig. 8a. The results indicate that the decoration of titanium on the surface of (8,0) SWCNT results in the appearance of new bands near the Fermi level, leading to a transition from a semiconductor to a metallic carbon nanotube. The density of states increase near the Fermi level, consistent with earlier findings.[24] The splitting of spin up and spin down bands near the Fermi level induces a
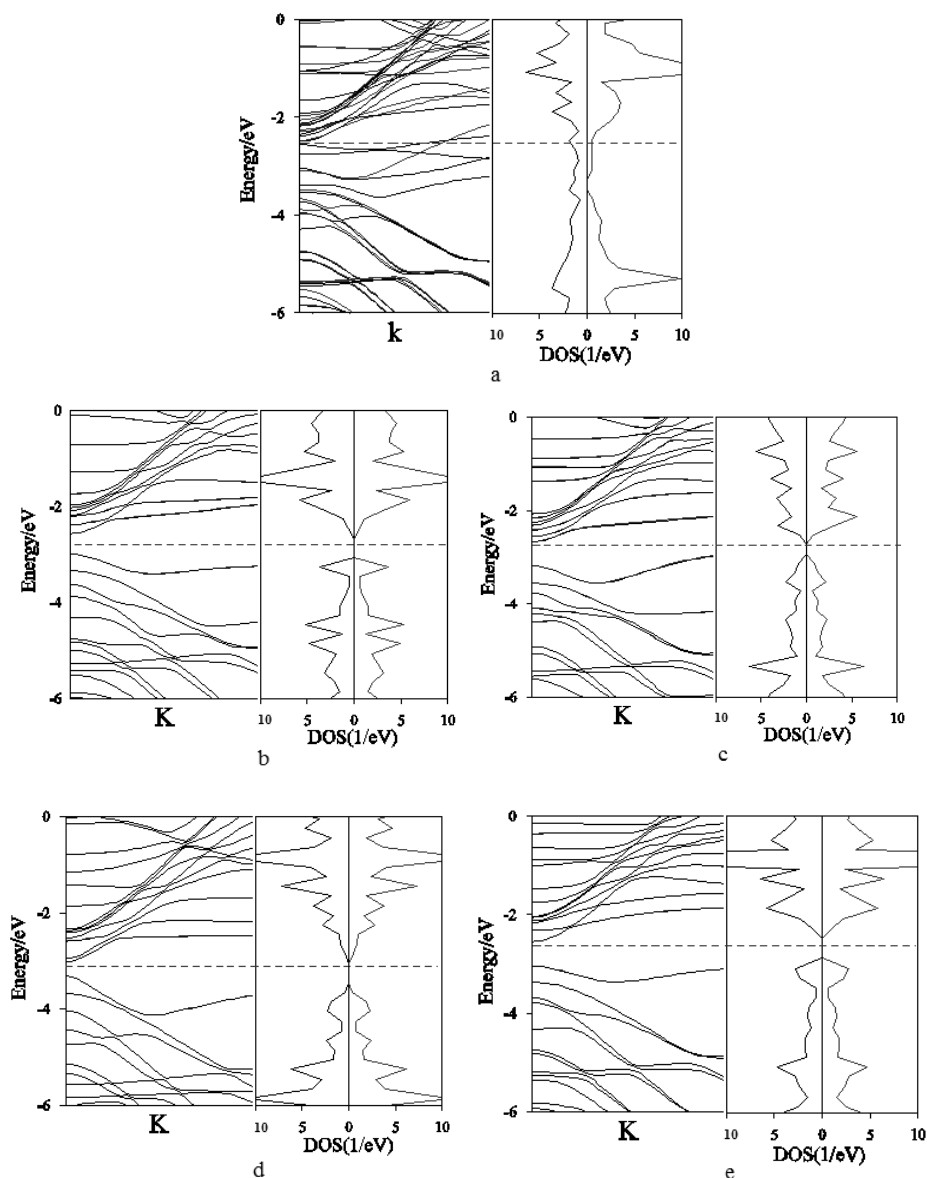
Fig. 8. Band structure and DOS of: a) Ti–SWCNT before adsorption, b) after SO_2 adsorption from S side (SO_2–Ti–S–CNT), c) after SO_2 adsorption from O side (SO_2–O–Ti–CNT), d) after SO_2F_2 adsorption from F side (SO_2F_2–F–Ti–CNT) and e) after SO_2F_2 adsorption from O side (SO_2F_2–O–Ti–CNT). Black and red lines show spin up and spin down bands, respectively. Red dash line shows the Fermi level.

magnetization of about 2.61 μ_B in (Ti-(8,0) SWCNT). By calculating both the magnetization and conductivity of this structure, it is possible to identify the

adsorption of Ti on the surface of (8,0) SWCNT. Fig. 9a displays the PDOS of (Ti-(8,0) SWCNT), showing that the s and d orbitals of the Ti atom are unsymmetrical and lead to the magnetization of the Ti-decorated (8,0) SWCNT. These orbitals are hybridized with p orbitals of C atom of (8,0) SWCNT at the Fermi level, resulting in the formation of a Ti-C bond. Since the carbon atom is more electronegative than titanium, the electrons move towards the carbon atom, leading to a partially filled molecular orbital, as reported previously.[23] Bader charge analysis, for Ti and SWCNT charge transfer (calculated using Eq. (3)), reveals a significant positive excess charge of +0.86e on the bonded Ti atom. These findings support the concept of charge transfer from the bonded Ti atom to the SWCNT, consistent with earlier investigations.[23,24] Therefore, Ti atom creates active sites that promote surface chemical reactions and support faster sensing. All molecules are bonded to the surface through the Ti atom of (Ti-(8,0) SWCNT), which is a more suitable site than other atoms for gas adsorption. The optimized structures of (Ti-(8,0) SWCNT) after the adsorption of SO_2 from both sides are shown in Fig. 6, and the corresponding parameters and adsorption energies are illustrated in Table II. As depicted in Fig. 6b, after SO_2 adsorption from S side in SO_2–S–Ti–CNT configuration, Ti atom moves to the centre of the C1–C2 bond, and the C1–C2 bond length increases from 1.46 Å in Ti-(8,0) SWCNT to 1.54 Å. The results reveal that after adsorption, one O atom dissociates from the adsorbed molecule. The distance between the Ti and separated O atom of SO_2 is approximately 1.93 Å, while the Ti atom is bonded to both O and S of OS at distances of 1.90 and 2.35 Å, respectively. In SO_2–O–Ti–CNT configuration, the Ti atom remains above the hollow site of (8,0) SWCNT. The results show that in this configuration, the Ti atom is bonded to all three atoms of the SO_2 molecule. The nearest distance between the Ti atom of (Ti-(8,0) SWCNT) and the O atom of SO_2 is 1.93 Å. In both configurations, the O atoms are close to the Ti atom, which can be attributed to the strong electronegativity of the oxygen atom, in agreement with previous reports.[25] Due to the strong interaction between the Ti atom and the dissociated O atom of SO_2 in SO_2–S–Ti––CNT configuration, it can be concluded that more electrons transfer from (Ti--(8,0) SWCNT) to the SO_2 molecule in this configuration than in SO_2–O–Ti––CNT configuration, which is consistent with previous works.[26] Table II displays the adsorption energies of SO_2 in SO_2–S–Ti–CNT and SO_2–O–Ti–CNT configurations as –4.77 and –3.58 eV, respectively. The results suggest that SO_2 adsorption from S side is energetically more favoured in SO_2–S–Ti–CNT configuration compared to SO_2–O–Ti–CNT configuration. These adsorption energies are more negative than those in pristine SWCNT. The band structures and DOSs of SO_2 adsorption to (Ti-(8,0) SWCNT) are illustrated in Fig. 8. After SO_2 adsorption, it appears that the half-occupied levels of (Ti-(8, 0) SWCNT) shift up to the conduction band due to electron transfers from the Ti atom to the SO_2 mole-
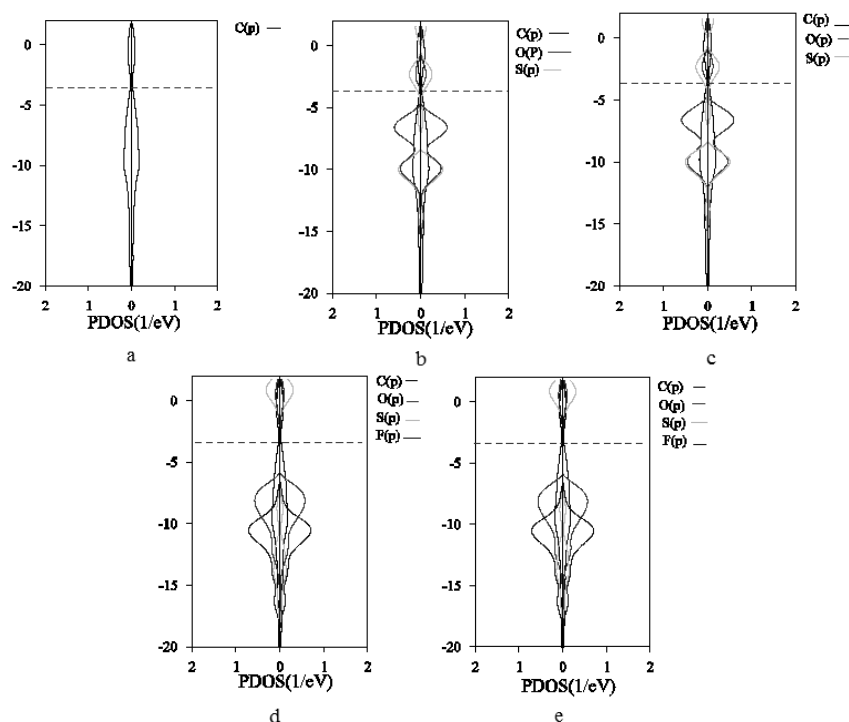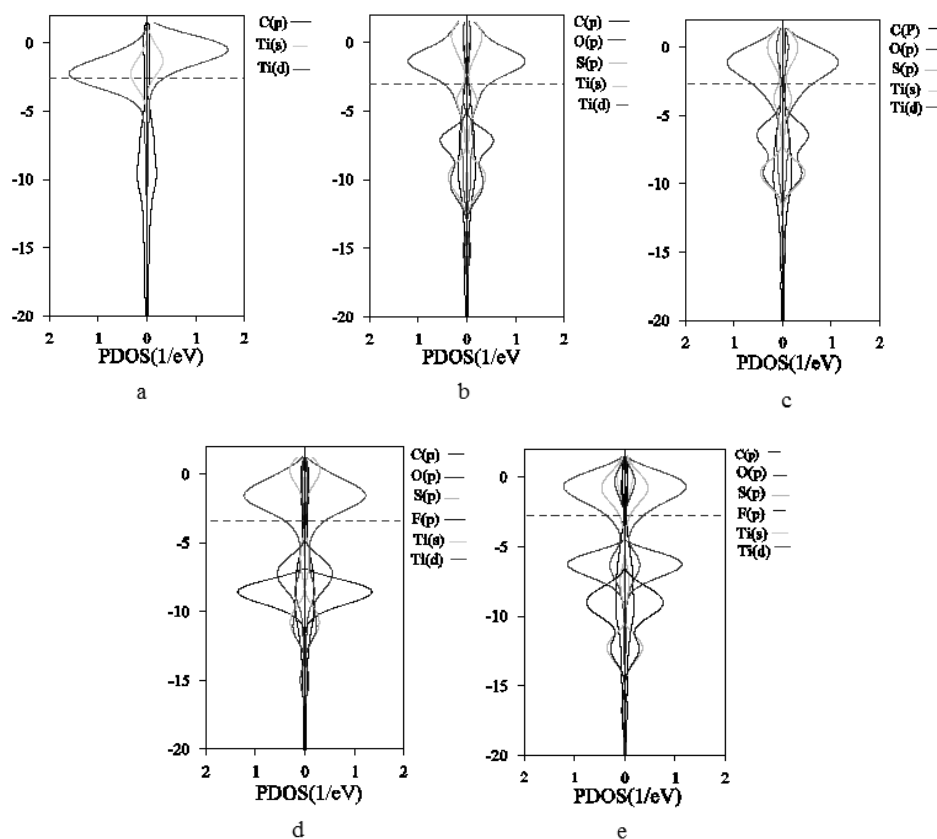
Fig. 9. PDOS of: a) Ti–SWCNT before adsorption, b) after SO_2 adsorption from S side (SO_2–S–Ti–CNT), c) after SO_2 adsorption from O side (SO_2–O–Ti–CNT), d) after SO_2F_2 adsorption from F side (SO_2F_2–F–Ti–CNT) and e) after SO_2F_2 adsorption from O side (SO_2F_2–O–Ti–CNT). Left and right side of each graph show the spin up and spin down bands, respectively. Red dash line shows the Fermi level.

cule. The band gap of (Ti-(8,0) SWCNT) is increased to 0.43 and 0.52 eV in SO_2–S–Ti–CNT and SO_2–O–Ti–CNT configurations, respectively. The spin up and spin down levels overlap, indicating no magnetic character in these configurations. For further comparison, the PDOSs of SO_2 adsorption in SO_2–S–Ti––CNT and SO_2–O–Ti–CNT configurations are presented in Fig. 9b and c, respectively. In SO_2–S–Ti–CNT configuration, the d orbitals of the dissociated O atom of the SO_2 molecule have a high density at the Fermi level, confirming more electron transfer in SO_2–S–Ti–CNT configuration than in SO_2–O–Ti–CNT configuration. After the SO_2 adsorption, the d orbitals of the Ti atom are presented at the Fermi level and are hybridized with p orbitals of O and S atoms of the SO_2 molecule, which leads to the chemical adsorption in both configurations.

The comparison of Fig. 9b and c with Fig. 9a shows that the polarization of Ti orbitals is removed, confirming the electron transfer from Ti atom to the SO_2 molecule. Therefore, SO_2 adsorption alters both the electronic properties and magnetism of (Ti-(8,0) SWCNT). The Bader charge analysis results are presented in Table II. The analysis reveals more substantial electron transfer in the SO_2–S–Ti–CNT configuration compared to the SO_2–O–Ti–CNT configuration. The negative value of Q_g for SO_2 adsorption in both configurations signifies the electron transfer from the (Ti-(8,0) SWCNT) to SO_2 molecule.

In SO_2F_2–F–Ti–CNT configuration, the Ti atom remains above the hollow site of the (Ti-(8,0) SWCNT), as shown in Fig. 7a. The C–Ti bond length decreases from 2.19 Å in the (Ti-(8,0) SWCNT) to 2.09 Å. The results indicate that after the adsorption, one F atom dissociates from the adsorbed molecule. This dissociative adsorption is similar to the adsorption of SO_2F_2 to the PtN_3––CNT surface.[27] The distance between the Ti atom and the separated F atom of SO_2F_2 is approximately 1.77 Å. The Ti atom forms a bond with O atom of SO_2F at a distance of 1.85 Å. In SO_2F_2–O–Ti–CNT configuration, after adsorption of SO_2F_2 from O side, Ti atom moves to the centre of the C1–C2 bond, as depicted in Fig.7b. This causes an increase in the C1–C2 bond length from 1.46 Å in (Ti--(8,0) SWCNT) to 1.52 Å, thereby increasing the orbital overlap after adsorption. The results indicate that after adsorption, one O atom dissociates from the adsorbed molecule. Therefore, a strong bond is formed. The distance between the Ti atom and separated O atom of SO_2F_2 is approximately 1.68 Å. The Ti atom forms a bond with the O atom of SO_2F at a distance of 2.08 Å. The adsorption energies in both configurations and the nearest distance between SO_2F_2 and the Ti atom of (Ti-(8,0) SWCNT) (D) are presented in Table II. The high adsorption energies and the dissociation of SO_2F_2 post-adsorption in both configurations imply robust adsorption, aligning with prior reports.[24] The results demonstrate that the SO_2F_2 adsorption energy in SO_2F_2–F–Ti–CNT configuration is more negative than in SO_2F_2–O–Ti–CNT configuration, which can be attributed to the dissociated F atom and its higher electronegativity in SO_2F_2–F–Ti–CNT configuration. Fig. 8 shows the DOS and band structures of SO_2F_2 adsorption on (Ti--(8,0) SWCNT). As depicted in Fig. 8d, when SO_2F_2 is adsorbed to (Ti-(8,0) SWCNT) from F side in SO_2F_2–F–Ti–CNT configuration, the Fermi level shifts down, and two bands near the Fermi level shift up to the conduction band, which can be attributed to the d orbitals of the Ti atom. The conductor Ti-decorated nanotube changes to a semiconductor nanotube with a band gap of 0.30 eV and no magnetic property after adsorption. On the other hand, when SO_2F_2 is adsorbed to (Ti-(8,0) SWCNT) from O side in SO_2F_2–O–Ti–CNT configuration, the DOS at the Fermi level approaches zero, and the band gap increases to 0.50 eV (refer to Fig. 8e for band structure and DOS). The PDOSs of SO_2F_2 adsorption in SO_2F_2–F–Ti–CNT and SO_2F_2–O–Ti–CNT configurations are illustrated in Fig.

9d and e, respectively. Comparison of Fig. 9d and e reveals that the p orbitals of the dissociated F atom in SO_2F_2–F–Ti–CNT configuration have high density at the Fermi level, whereas the valence orbitals of the dissociated O atom in SO_2F_2–O–Ti–CNT configuration have low density at the Fermi level. This confirms the stronger interaction between (Ti-(8,0) SWCNT) and SO_2F_2 gas in SO_2F_2–F–Ti–CNT configuration. The spin up and spin down electronic states overlap in both configurations of SO_2F_2, and no magnetization can be observed in these configurations. The valence orbitals of all atoms of the SO_2F_2 molecule also appear at the Fermi level and are hybridized with the high–intensity peaks of the Ti atom, which leads to chemical bond formation in these configurations. The bader charge analysis reveals greater charge transfer in the SO_2F_2–F–Ti–CNT configuration compared to SO_2F_2–O–Ti–CNT, as shown in Table II. The negative charge transfer value for SO_2F_2 adsorption in both configurations indicates electron donation from the (Ti-(8,0) SWCNT) to the gas molecule.

CONCLUSION

In this study, we examined the adsorption of gases resulting from the decomposition of SF_6 (SO_2 and SO_2F_2) on the surface of pristine and Ti-decorated (8,0) SWCNTs from different sides using DFT calculations. The formation energy revealed that Ti-decorated (8,0) SWCNT is thermodynamically stable. To investigate the interaction between gases and SWCNTs, we calculated the adsorption energy, the band structures, the density of states, the partial density of states, the magnetic behaviour, the charge transfer and the conductivity. The principal conclusions are as follows:

1. SO_2 and SO_2F_2 weakly adsorb on (8,0) SWCNT, without altering its electronic properties.

2. Decorating (8,0) SWCNT with titanium shifts electronic properties from semiconducting to metallic, acting as an active site for SF_6 decomposed gas adsorption.

3. The strong adsorption of SO_2 and SO_2F_2 on Ti-(8,0) SWCNT changes the system conductivity from metallic to semiconductor.

4. The conductivity order after SO_2 and SO_2F_2 adsorption on (Ti-(8,0) SWCNT) from different sides is as follows: SO_2F_2–F–Ti–CNT < SO_2–S–Ti––CNT < SO_2F_2–O–Ti–CNT < SO_2–O–Ti–CNT.

5. The negative charge transfer values for SO_2F_2 and SO_2 adsorptions indicates the electron donation from the (Ti-(8,0) SWCNT) to gas molecules.

Based on the sensing mechanism, (Ti-(8,0) SWCNT) can be used to prepare a gas chemiresistor sensor for the detection of SF_6 decomposed products (SO_2 and SO_2F_2) in SF_6 insulated equipment.

И З В О Д

ИСПИТИВАЊЕ ОСОБИНА АДСОРПЦИЈЕ ГАСОВА НАСТАЛИХ РАЗГРАДЊОМ SF_6
(SO_2 И SO_2F_2) НА НЕДИРНУТИМ И Ti-УКРАШЕНИМ SWCNT ПОВРШИНАМА:
DFT СТУДИЈА

ELHAM GHOLAMREZAI KOHAN[1], HOSSEIN MOHAMMADI-MANESH[1] и FOROUGH KALANTARI FOTOOH[2]

[1]Department of Chemistry, Faculty of Science, Yazd University, Yazd, Iran и [2]Department of Chemistry, Yazd Branch, Islamic Azad University, Yazd, Iran

DFT израчунавања су искоришћена за истраживање адсорпцију гасова прозве-
дених разградњом SF_6 (SO_2 и SO_2F_2) на недирнутим и Ti-украшеним једнозидним
угљеничним наноцевима (Ti-(8,0) SWCNT). Све структуре су релаксиране и њихове
структурне и електронске особине истражене пре и после адсорпције гаса на повр-
шини наноцеви. За (Ti-(8,0) SWCNT) је нађено да има високу хемисорпцијску
осетљивост на Ti, SO_2F_2 и SO_2 адсорпције на својој површини. Електронске особине
(8,0) SWCNT су се промениле од полупроводничких на металне додавањем Ti, како
је показано израчунатим структурама трака и густинама стања (DOS). SO_2F_2 и SO_2
адсорпција на површини (Ti-(8,0) SWCNT) са различитих страна преводи проводну
(Ti-(80) SWCNT) у полопроводну наноцев. Да би пажљиво испитали природу ад-
сорпције, урађена су и израчунавања парцијалних густина стања (PDOS). Додатно,
додавање Ti индукује магнетизацију од приближно 2.61 μ_B у (8,0) SWCNT, која
нестаје након адсорпције гаса.

(Примљено 2. фебруара, ревидирано 1. марта, прихваћено 17. априла 2024)

REFERENCES

1. I. Sauers, H. W. Ellis, L. G. Christophorou, *IEEE Trans. Elect. Insul.* **2** (1986) 111
   (https://doi.org/10.1109/TEI.1986.348932)
2. X. Zhang, B. Yang, W. Liu, J. Zhang, *Proc. Eng*. **29** (2012) 4107
   (https://doi.org/10.1016/j.proeng.2012.01.628)
3. S. Iijima, *Nature* **354** (1991) 56 (https://doi.org/10.1038/354056a0)
4. D. R. Kauffman, A. Star, *Angew. Chem. Int. Ed.* **47** (2008) 6550
   (https://doi.org/10.1002/anie.200704488)
5. R. Ströbel, J. Garche, P. T. Moseley, L. Jörissen, G. Wolf, *J. Power Sources* **159** (2006)
   781 (https://doi.org/10.1016/j.jpowsour.2006.03.047)
6. S. Demir, M. F. Fellah, *Surf. Sci.* **701** (2020) 121689
   (https://doi.org/10.1016/j.susc.2020.121689)
7. J. Kong, N. R. Franklin, C. Zhou, M. G. Chapline, S. Peng, K. Cho, H. Dai, *Science* **287**
   (2000) 622 (https://doi.org/10.1126/science.287.5453.622)
8. J. Zhao, A. Buldum, J. Han, J. P. Lu, *J. Nanotech.* **13** (2002) 195
   (https://doi.org/10.1088/0957-4484/13/2/312)
9. X. Zhou, W. Q. Tian, X. L. Wang, *Sens. Actuators, B* **151** (2010) 56
   (https://doi.org/10.1016/j.snb.2010.09.054)
10. G. Gecim, & M. Ozekmekci, *Surf. Sci.* **711** (2021) 121876
    (https://doi.org/10.1016/j.susc.2021.121876)
11. M. Patrignani, J. Juan, O. Nagel, W. Reimers, R. Luna, P. V. Jasen, *Powr Tech*. (2024)
    119691 (https://doi.org/10.1016/j.powtec.2024.119691)
12. P. O. Krasnov, T. V. Basova, A. Hassan, *Appl. Surf. Sci*. **457** (2018) 235
    (https://doi.org/10.1016/j.apsusc.2018.06.282)

13. W. Li, J. J. Ma, P. Liu, Z. L. Pan, Q. Y. He, *Appl. Surf. Sci.* **335** (2015) 17 (https://doi.org/10.1016/j.apsusc.2015.01.181)
14. L. L. Yu, S. Zhang, Q. Dong, X. Z. Meng, W. Q. Tian, *J. Comput. Theor. Nanosci.* **8** (2011) 1811 (https://doi.org/10.1166/jctn.2011.1887)
15. P. Giannozzi, S. Baroni, N. Bonini, M. Calandra, R. Car, C. Cavazzoni, D. Ceresoli, G. Chiarotti, M. Cococcioni, I. Dabo, A. DalCorso, S. deGironcoli, S. Fabris, G. Fratesi, R. Gebauer, U. Gerstmann, C. Gougoussis, A. Kokalj, M. Lazzeri, L. Martin-Samos, N. Marzari, F. Mauri, R. Mazzarello, S. Paolini, A. Pasquarello, L. Paulatto, C. Sbraccia, S. Scandolo, G. Sclauzero, A. Seitsonen, A. Smogunov, P. Umari, R. M. Wentzcovitch, *J. Phys: Cond. Matter*. **21** (2009) 395502 (https://doi.org/10.1088/0953-8984/21/39/395502)
16. J. P. Perdew, K. Burke, M. Ernzerhof, *J. Phys. Rev. Lett.* **77** (1996) 3865 (https://doi.org/10.1103/PhysRevLett.77.3865)
17. H. J. Monkhorst, J. D. Pack, *J. Phys. Rev., B* **13** (1976) 5188 (https://doi.org/10.1103/PhysRevB.13.5188)
18. S. F. Boys, F. G. M. P. Bernardi, *J. Mol. Phys.* **19** (1970) 553 (https://doi.org/10.1080/00268977000101561)
19. E. Sanville, S. D. Kenny, R. Smith, G. Henkelman, *J. Comp. Chem.* **28** (2007) 899 (http://doi.org/10.1002/jcc.20575)
20. W. Tang, E. Sanville, G. Henkelman, *J. Phys.: Cond. Matter* **21** (2009) 084204 (https://doi.org/10.1088/0953-8984/21/8/084204)
21. X. Zhang, Y. Gui, Z. Dai, *Appl. Surf. Sci.* **315** (2014) 196 (https://doi.org/10.1016/j.apsusc.2014.07.056)
22. X. Zhang, J. Zhang, J. Tang, B. Yang, *J. Comp. Theor. Nanosci.* **9** (2012) 1096 (https://doi.org/10.1166/jctn.2012.2149)
23. F. Mei, X. Ma, Y. Bie, G. Xu, *J. Theor. Comp. Chem.* **16** (2017) 1750065 (https://doi.org/10.1142/S0219633617500651)
24. K. W. Kayang, E. Nyankson, J. K. Efavi, V. K. Apalangya, B. I. Adetunji, G. Gebreyesus, A. Yaya, *Res. Phys*. **12** (2019) 2100 (https://doi.org/10.1016/j.rinp.2019.02.062)
25. X. Zhang, Y. Gui, H. Xiao, Y. Zhang, *App. Surf. Sci.* **379** (2016) 47 (https://doi.org/10.1016/j.apsusc.2016.04.048)
26. H. Huang, Y. Yu, M. Zhang, *App. Surf. Sci.* **505** (2020) 144622 (https://doi.org/10.1016/j.apsusc.2019.144622)
27. H. Cui, X. Zhang, D. Chen, J. Tang, *App. Surf. Sci.* **447** (2018) 594 (https://doi.org/10.1016/j.apsusc.2018.03.232).

Exploring the efficacy of natural compounds against SARS-CoV-2: A synergistic approach integrating molecular docking and dynamic simulation

NABILA AOUMEUR[1], MEBARKA OUASSAF[2], SALAH BELAIDI[2]*, NOUREDDINE TCHOUAR[1], LOFTI BOURAGAA[2], IMANE YAMARI[3], SAMIR CHTITA[3]** and LEENA SINHA[4]

[1]*University of Sciences and Technologies of Oran (USTO), Laboratory of Process Engineering and Environment, BP 1503 Oran 31000, Algeria, [2]Biskra University, LMCE Laboratory, Department of Matter Sciences, Biskra, Algeria, [3]Hassan II University of Casablanca, Laboratory of Analytical and Molecular Chemistry, Casablanca, Morocco and [4]University of Lucknow, Department of Physics, 226007 Lucknow, India*

Abstract: The primary aim of the current investigation is to contribute to SARS-CoV-2 research by identifying potential lead compounds for clinical applications, with a specific focus on inhibitors targeting the main protease (M^{pro}). In this research, molecular docking analysis was conducted using the software molecular operating environmental (MOE) to evaluate the potency of bioactive compounds sourced from medicinal plants as inhibitors of SARS-CoV-2 M^{pro}. Among 118 natural compounds with anti-HIV characteristics, the top seven candidates (h3, h84, h85, h87, h90, h108 and h110), were identified based on their superior binding energies with comparison to the reference ligand N3. These selected compounds exhibited binding affinities of –33.996, –35.336, –32.615, –32.154, –33.452, –31.903 and –40.360 kJ mol^{-1}, respectively. To further refine our shortlist of potential candidates for human application, we examined the drug-likeness, and the pharmaceutical attributes of these compounds using the SwissADME web server. Among them, only two compounds, namely h85 and h87, demonstrated favorable pharmacological properties suitable for human administration. These two compounds were subsequently shortlisted for further investigation. To explore the conformational stability of ligands within the M^{pro} active site, we performed molecular dynamics (MD) simulations. These simulations showed reliable and steady trajectories, supported by analyses of root-mean-square-fluctuation (*RMSF*) and root-mean-square deviation (*RMSD*). These findings and favorable molecular properties as well as interaction profiles suggest that these two lead compounds

---

* Corresponding authors. E-mail: (*)s.belaidi@univ-biskra.dz; (**) samir.chtita@univh2c.ma

857

may be promising SARS-CoV-2 therapeutic candidates. They present exciting starting points for further drug design.

Keywords: SARS-CoV-2; natural compounds; molecular docking; ADMET properties; dynamic simulation.

INTRODUCTION

With human-to-human transmission, the corona-virus 2 (SARS-CoV-2), which originated in China, quickly spread over the world and impacted a greater population.[1] This novel corona-virus disease 2019 (COVID-19), is called severe respiratory syndrome corona-virus 2 (SARS-CoV-2), and was first identified in December 2019 in the city of Wuhan, Hubei Province of China. Its high reproductive capacity played a pivotal role in the ensuing pandemic, leading to a significant loss of human lives, as documented by Huang *et al.*[2–4]

The World Health Organization (WHO) declared this disease a global health problem on January 30, 2020 with absolute urgency, involving international bodies, due to its continued progression. COVID-19 has spread to 200 nations worldwide,[5] with the United States, India, Brazil, Colombia, Russia, Spain, the United Kingdom and France being the most affected countries.[6] The most recent update states that the corona-virus family is a wide group of viruses that may cause disease in both humans as well as animals. Humans can get respiratory infections from many corona-virus strains, which can range from common colds to more serious diseases.[7]

As a zoonotic virus, SARS-CoV-2 has the potential to spread from animals to humans in the future, serving as a warning and indicator for sensible COVID--19 control and prevention efforts.[8] From its spread, SARS-CoV-2 generated rapid genomic changes, stimulating viral type selection. The WHO defines a variation of concern (VOC) as a viral variety that has evolved to outcompete other variations and affect public health.[9,10]

The COVID-19 pandemic has accelerated antiviral treatment research and use to unprecedented levels. Many chronic viral illnesses including HIV and hepatitis C have been successfully treated with antivirals. However, their use to treat acute viral infections like COVID-19 is limited. Computational tools have enabled the rapid analysis and sharing of viral genomes in recent years and allow near--real-time monitoring of viral alterations.[11]

These computational tools can predict the virus's replicative fitness and adaptation to the human host.[9]

The chymotrypsin-like protease (3CL^{pro}), commonly referred to as the main proteases (M^{pro}) and one or more known papain-like proteases with its abbreviation (PL^{pro}) are the two primary viral proteases found in coronaviruses.

The main proteases, recognized as M[pro] or 3CLpro, play a vital role in the viral replication process. Their function involves cleaving polyproteins at various sites, leading to the production of different functional proteins.[12]

These 3CLpro enzymes are indispensable for coronavirus (CoV) replication, especially in the case of the severe pandemic caused by SARS-CoV and SARS-CoV-2 in the 21st century. Consequently, these have been tested as targets that have promising power for the design and development of broad-spectrum technologies of anti-CoV19 medications.[13]Most efforts to produce novel SARS-CoV-2 3CLpro inhibitors are based on previously published SARSCoV 3CL[pro] inhibitors due to the significant association between the 14 various kinds of 3CL[pros] generated from coronaviruses, as shown by their phylogenetic links. Because it is a potential target for managing different CoVs by limiting viral multiplication and pathogenesis, 3CL[pro] has attracted a lot of attention from both the academic and business realms. The development of new anti-CoV drugs continues to rely heavily on the separation of active molecules from natural products. The use of naturally occurring substances that have been extracted from plants to treat a wide range of illnesses has received attention.[14] Many molecules of diverse chemical structures, from medicinal plants, have been proven to contain antiviral activity. Indicating that plants constitute a vast and unexplored potential supply of antiviral medicines. There is an outstanding review study on antiviral drugs extracted from plants.[15] There have been findings from molecular docking simulation studies using natural products and well-known antiviral medications to find possible therapeutic agents against the non-structural proteins of SARS-CoV-2.[16,17]

Biothermodynamic studies have provided intriguing insights into the complex dynamics of SARS-CoV-2 interactions by revealing the dynamic interactions between viral components and host receptors in epidemiology and pathophysiology research.[18–20]

Key findings from biothermodynamic studies on the interaction between SARS and CoV-2 are as follows. First, compared to Bat-CoV spikes, the spike glycoprotein (S-glycoprotein) of SARS-CoV-2 has a stronger affinity for the human ACE-2 receptor.[19] Second, the gut microbial ecology can be disrupted by even moderate instances of SARS-CoV-2 infection, which can result in a less stable gut microbiota.[20]

Third, although the pathogenicity of more recent SARS-CoV-2 variants, such as BF.7 and BA.5.2, has not changed, they are more contagious.[21,22] Fourth, fevers between 311 and 312 K can increase neutralizing antibodies binding affinities to the spike protein, which may reduce SARS-CoV-2's ability to infect others. Finally, Omicron sublineage spike glycoproteins bind to the ACE2 receptor more strongly at colder temperatures, which raises the possibility of increased viral transmission in the fall and winter.[19,23]

Previously, a prototype thermodynamic equilibrium model was developed for determining the dose–response potential of a respiratory virus such as SARS-CoV-2.[19]

Our study focused on 118 naturally occurring substances that have antiviral characteristics and particularly target HIV-1 (anti-HIV1). We selected these chemicals based on their potential, which has been previously identified, and the pathophysiological symptoms of COVID-19 and HIV-1 were shown to be identical. We additionally identified antiviral drug databases to be a useful source of motivation,[24] as agents against the SARS-CoV-2 (M^pro) with significant roles in viral replication/transcription and host cell recognition. This is achieved through the application of MD simulations, complemented by the computational assessment of drug-like and ADMET (absorption, distribution, metabolism, excretion and toxicity) properties for the highest-ranking compounds.[25–30]

We anticipate that this investigation will offer a comprehensive understanding of the binding and interaction between antiviral agents and the SARS-CoV-2 main protease (M^pro).

MATERIAL AND METHODS

Ligand identification

This study assembled a dataset comprising 118 natural chemical inhibitors specific to HIV-1, drawing upon previous research findings as documented in the literature.[16,30] Detailed information is available in Supplementary material to this paper (Fig. S-1 and Table S-I).

Table S-II of the Supplementary material outlines the binding energies of the 118 different chemicals to the protein identified by the PDB ID 6LU7. Fig. S-1 visually represents the optimized 2D molecular structures. These structures were generated using HyperChem 8.03 software[31] after an initial of sketch Marvin software.[32] The optimization of antiviral natural product geometries commenced with molecular mechanics[33] utilizing the MM+ force field with *RMS* = 0.0041 kJ/Å.[34] In addition, the PM3 semi-empirical approach was applied for subsequent geometric re-optimization.

Molecular docking simulations

The 3D structure of M^pro protein bound with N3 inhibitor was taken from the PDB website: Protein Data Bank (http://www.rcsb.org) with the PDB (ID: 6LU7).[35] In addition, MOE software (MOE, version 2007.09)[36,37] is applied for re-docking of co-ligands with the target and also for docking the studied molecules with M^pro SARS-CoV-2 protein.

The initial step involves the preparation of two proteins. By removing water molecules, the N3 inhibitor and adding polar hydrogen atoms into the structural conformation, as outlined by (Chtita *et al.*, 2022).[16] Subsequently, ligands designated for docking undergo structural optimization, and hydrogen atoms are added. According to Chtita *et al.*,[16] the site of action is defined as the volume occupied by the co-crystallized ligands in the pocket of each target following a well-determined orientation.

At pH 7.0, the PDB incoherence was adjusted, and the protonation state was assigned using the structure preparation mode of the MOE software. Alignment of key residues involved in ligand binding, such as: His41, Cys145, Met49, Thr45, Asp187, Asp187, Phe140, Arg188, Asn142, Gln189, Met165, Glu166 and His172, is remarkably high (*RMSD* = 0.99 Å)

in the ligand/binding pockets of the main protease of the SARS-CoV-2 virus, as shown in Fig. 1. It is thought that they facilitate the substrate's grid opening to the active state.[38]
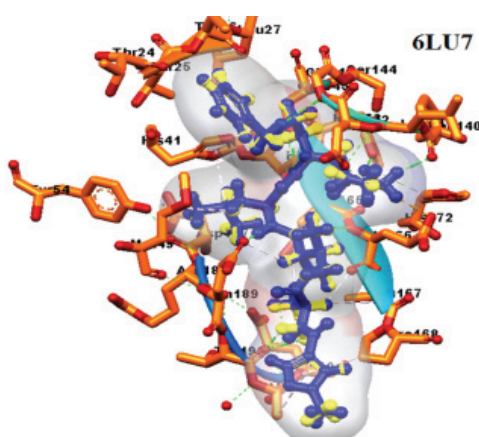
Fig 1. Binding -pocket with important residues of SARS-CoV-2virus M^{pro}(6LU7).

This study investigates molecular docking, examining the interactions between docked molecules and the key active sites. To determine which molecule exhibited the most effective interaction with the target, the results were based on the binding energy.[12,16]

In silico *pharmacokinetics analysis*

The development of novel drugs relies significantly on understanding their pharmacodynamic and pharmacokinetic properties. That interplays ADME and toxicology of chemicals within body, providing crucial insights into how a drug is processed and eliminated. Several methods, including Lipinski's Rule of Five (Ro5), were used to consider factors like Log *P* ligand molecular weight, and hydrogen bond donor and acceptor that serves as pivotal tools in predicting a compound's bioavailability.[39] Additionally, our investigation integrated Swiss ADME (http://www.swissadme.ch/) as a comprehensive platform to evaluate ADMET characteristics.[40]

Dynamics simulations

Molecular dynamics simulations of the two top-ranked ligand–protein complexes was made by using the Desmond module in Schrödinger software version 2021-3,[41] with the force fields: OPLS[42] to analyze and interpret the stability of the different interactions involved between the top-docked ligands and the protein in terms of binding affinity.

As a requirement for the limits, the system under study was delimited by an orthorhombic simulation box with 10 Å in three dimensions. The SPC is the solvation model water used in this simulation. The system was neutralized by adding 10 Na$^+$ and 6 Cl$^-$, and then 0.1 M NaCl was added as salt to modeling the physiology of the human body. The simulated system was optimized and reduced *via* the steepest descent minimization to eliminate steric collisions. The MDS was then run for 1ns at NVT equilibrium at 300 K, followed by NPT equilibrium by setting the experimental condition at 1.01325 bar and 300 K for the full simulation time (100 ns), to stabilize the system at the required conditions.

In the simulation, the first system, 6LU7-h85, comprised 43,652 atoms with 12,961 water molecules and had a net charge distribution of +10 from sodium ions and –6 from chloride ions. Conversely, the second system, 6LU7-h87, contained 43,643 atoms and 12,958

water molecules, and maintained the same charge distribution of +10 from sodium ions and –6 from chloride ions. Finally, many parameters were determined at the end of the simulation: we determine the mean square fluctuation/*RMSF* and the mean square deviation/*RMSD*, and all the protein–substrate interactions, with qualitative and quantitative aspects. The Desmond Structure program Schrödinger,[41] was used to create the graphics.

RESULTS AND DISCUSSION

Molecular docking investigation

This study focused on the protease Mpro, specifically targeting the (PDB ID 6LU7), as a prospective protein for inhibition of COVID-19. In the pursuit of proposing new inhibitors for 6LU7, it was important to investigate the inhibition mechanism employed by the most promising compound identified through comprehensive screening. Upon comparing the docked energies of all examined molecules, it becomes apparent that a significant proportion of ligands exhibit superior energy scores. This indicates that these compounds assume a more favorable docking pose compared to the reference ligand N3 ($C_{35}H_{48}N_6O_8$), whose interaction energy is listed in Table S-II as (–32.615 kJ/mol). To visualize the interactions of the reference ligand N3 within the active site of 6LU7 the MOE software was utilized. The analysis revealed that the reference ligand N3 when bound to the main protease then protease refers to an enzyme capable of degrading the peptide bonds connecting two amino acids present in proteins, so demonstrates inhibitory activity by making conventional hydrogen bonds with the amino acid Ser46 and one with Pro168 amino acid; π-alkyl interactions with Met49, His 163, His 41; and carbon-hydrogen bond with Gln189 of the enzyme (Fig. 2a).

Table I presents the results of molecular docking. Notably, the more negative binding energy values indicate that the complex has a good stability (Fig. 2a).The active site of the receptor enzyme comprises residues such as Met 49, Phe140, His41, Met165, Lue141, Glu166, His164, Gln192, His172, Leu27, Val42, Gln192, Thr190, Phe181, Asp187, Ala191, Cys145, Phe140, Arg188, Leu27 and Leu141.

The seven compounds h3, h84, h85, h87, h90, h108 and h110, which have the best binding score with the 6lu7 protein, are presented in (Fig. 2b).

Docked conformation of the compounds demonstrated that they are engaged in desirable interactions with the binding-pocket residues of the target protein, such as hydrophobic interactions, polar interactions, and hydrogen bonding. Hydrogen bonding or hydrogen bridge is an intermolecular or intramolecular force involving a hydrogen atom and an electronegative atom such as oxygen, nitrogen and fluorine. The intensity of a hydrogen bond is intermediate between that of a covalent bond and that of van der Waals forces.

The hydrogen bond binds with key residues inside the pocket are considered to be a determining factor in the average binding of the ligand with the active site of the receptor. The increased number of hydrogen bonds in the complex between

the ligand and protein may account for the higher binding affinity. The work of Imberty *et al*. indicates that interactions with distances between (2.5 and 3.1 Å), are considered strong interactions.[43] The hydrogen bond distances between the active site residues and the seven most favorable compounds range from 2.01 to 3.05 Å (Table I).

N3

(a)

Ligand	Ligand-receptor interactions	Affinity, kJ/mol
h3		−33.996

(b)
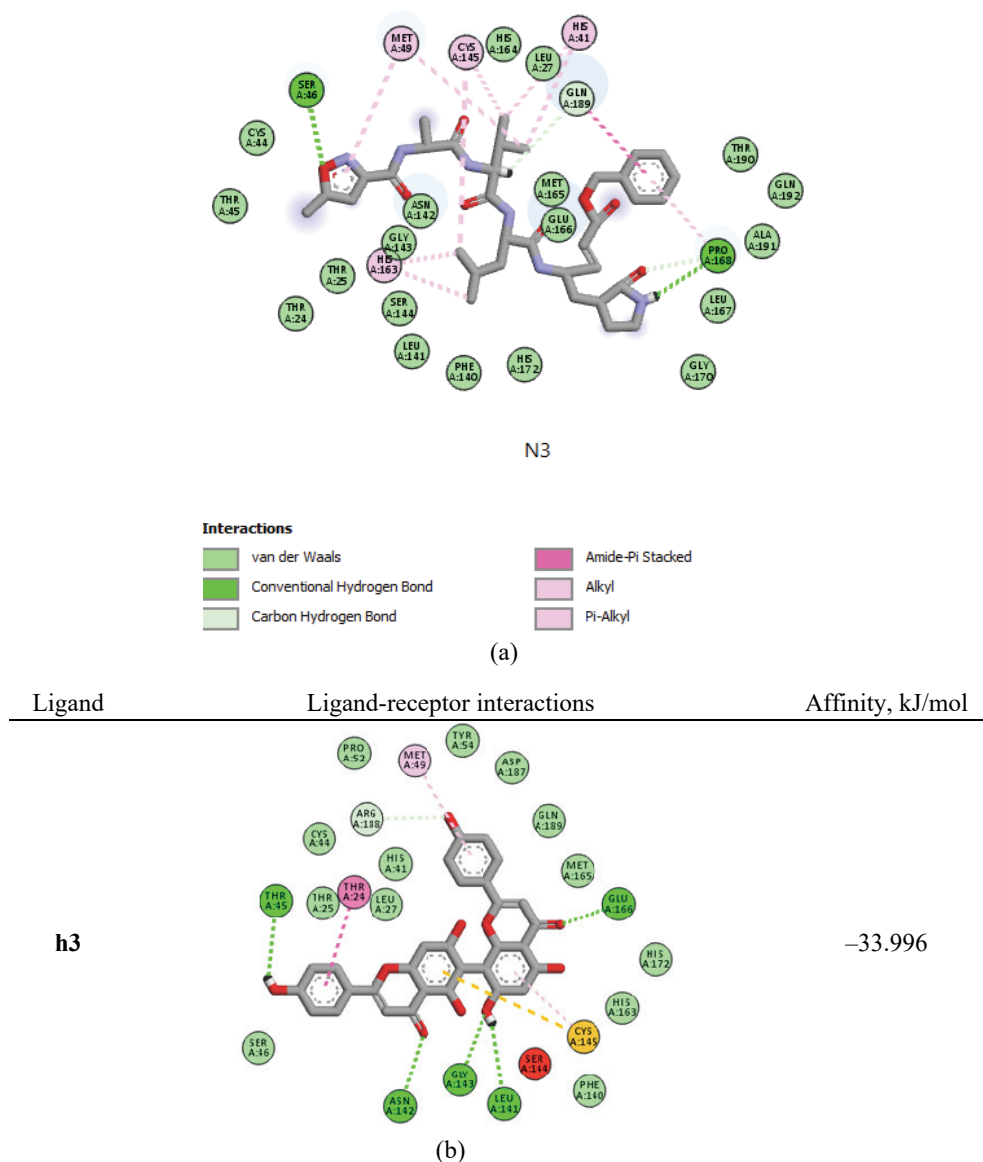
Fig. 2. a) Diverse binding interactions of 6LU7 with N3 inhibitor; b) summary of docking interactions for M^pro SARS-CoV-2 protein.

h84   −35.336

h85   −32.615

h87   −32.154

Fig. 2. Continued.

h90   −33.452

h108   −31.903

h110   −40.360

Fig. 2. Continued.

Several antiviral medication studies have shown that inhibiting protease activity may cure several diseases caused by viruses. Hence, proteases emerge as potential targets for novel antiviral interventions. This inclination is grounded in the fundamental role that proteases assume during viral replication processes.[44]

TABLE I. Types of residue interactions and bond distances of the compounds examined with the residues of target protein 6LU7; strong interaction: 2.5 Å < *D* < 3.10 Å, and average interaction: 3.1 Å< *D* < 3.55 Å[43]

Compd.	Interaction type	Interaction residues of 6lu7	Distance, Å	Type of HB interaction
h3	H-Bond	Asn142, Glu166, Leu141, Gly143	3.05, 2.21, 2.24, 2.01, 2.36	Strong
	Pi-Anion	Cys 145	4.82	–
h84	H-Bond	Thr26, Glu166, Cys145	2.82, 2.98, 2.92	Strong
	Pi-Anion	Met 49	4.94	–
h85	H-Bond	Thr26, Ser144, Glu166, Cys 145	2.71, 2.38, 2.19, 2.62	Strong
	Pi-Anion	Cys 145	5.40	–
h87	H-Bond	Glu166	2.81	Strong
	Pi-Anion	Cys145	5.39	–
h90	H-Bond	Thr26, Glu166, Cys 145	2.37, 2.58, 2.19	Strong
	Pi-Anion	Cys 145	5.46	–
h108	H-Bond	Thr26, Glu166	2.11,2.30	Strong
h110	H-Bond	Thr26, Thr190, Thr25, Met165, His 164	2.90, 1.80, 2.85, 2.63, 2.72, 2.34	Strong
	Pi-Anion	Glu166	3.83	Average

To highlight potential drug candidates, an ADMET scan was done to examine the pharmacokinetics of the top-ranked ligands (h3, h84, h85, h87, h90, h108 and h110). An *in-silico* investigation allows for the exploration of pharmacokinetic parameters (ADMET). In medicinal chemistry, a key focus is the significance of high oral bioavailability in optimizing bioactive molecules for therapeutic purposes.

Drug-likeness and pharmacokinetic properties

Drug like-likeness or drug-like mainly evaluates the possibility for a molecule to become a drug in the future, orally based on its bioavailability. ADME predictions were conducted utilizing the freely accessible using the web-based software SwissADME,[40] on the following link: http://www.swissadme.ch. For drug-likeness studies, several rules were applied such as Lipinski's rule,[39] Veber's rule,[45] Ghose's rule,[46] Muegge's rule[47] and Egan's rule ,[48] these filters were recently tested in recent works.[49,50] The prediction, drug-likeness and ADME calculation results are shown in Tables II and III. According Table II, only the compounds h85, h87 and h90 exhibit a single violation according to Lipinski's rule. Meanwhile, three compounds (h3, h84 and h108 display more than one violation; however, they remain in the category of bioavailable ligands, but are less selective.[38]

The compound h110 displayed 4 violations (*HBD* > 5, *HBA* > 10, *MWt* > 500 Da, *TPSA* > 140 Å), therefore this ligand could have an oral bioavailability problem.

TABLE II. Results of applying Lipinski's Rule

Property	Bioactive compound						
	h3	h84	h85	h87	h90	h108	h110
MW (<500 Da)	538.46	583.63	539.59	525.57	532.58	512.51	1009.01
Log *P* (< 5)	0.25	1.70	2.59	2.40	1.37	1.32	1.02
H-bond donor (< 5)	6	2	1	1	1	5	11
H-bond acceptor (< 10)	10	11	9	9	9	8	15
Violations	3	3	1	1	1	2	4

TABLE III. Drug-likeness properties and ADME prediction of bioactive ligands

Drug-likeness property	Bioactive compound						
	h3	h84	h85	h87	h90	h108	h110
Lipinski	No	No	Yes	Yes	Yes	No	No
Veber (≤ 10 Rot, ≤ 140 *TPSA*)	No	Yes	Yes	Yes	Yes	No	No
TPSA / Å^2	181.80	134.34	95.65	95.66	119.44	144.52	275.13
Log (*S* / mol L^{-1})	–6.75	–5.55	–6.20	–5.84	–5.64	–6.19	–12.12
Bioavailability score	0.17	0.17	0.55	0.55	0.55	0.55	0.17
PAINS alert	0	0	0	0	0	0	0
GI	Low	Low	High	High	High	Low	Low
BBB permeability	No	No	No	No	No	No	No
Log *Kp*	–6.01	–7.15	–6.08	–6.30	–6.62	–5.93	–5.23
-Cyp1A2 inhibitor	No	No	Yes	Yes	Yes	Yes	No
-Cyp2C19 inhibitor	No	No	No	No	No	No	No
-Cyp2C9 inhibitor	No	No	No	No	No	Yes	No
-Cyp2D6 inhibitor	No	Yes	Yes	Yes	Yes	Yes	No
-Cyp3A4 inhibitor	No	No	No	No	No	No	No

The Veber filter stipulates that the *PSA*: polar surface area less than 140 Å^2 and the number of rotatable bonds (*nRotb* < 10 Å) for a ligand. On the contrary, compounds h3, h108 and h110 have *PSA* exceeding 140 Å^2, indicating a propensity for suboptimal bioavailability.

All of the compounds are well-suited for attaching to their targets because they contain less than 10 rotatable bonds, which helps them get away from the entropic penalty.

Three candidates showed less rule violations: Lipinski, Veber and Veber rules, those are the compounds h85, h87 and h90.Hence, based on Lipinski's "rule of five", Veber's rule and ADME characteristics, compounds h85, h87 and h90 may be the most suitable drug candidates amongst the originally chosen compounds.

Nevertheless, the RO5 test does not prove that the molecule has drug-like properties. The oral bioavailability of a drug, denoted *%F*, is the proportion of the administered dose which can reach the site of action. A score of 55 % is considered satisfactory, meaning it passes the five-fold test. With a score of 55 %, the substances h85, h87 and h90 demonstrated acceptable bioavailability. [38]

According to the results presented in Table III, we can say that the molecules h84, h8 and h90 have moderate solubility in aqueous solution, except h3, h85, h108 and h110, which have low solubility in the aqueous phase. According to the ADME properties, the absorption of the molecule in the intestine is described by the gastrointestinal (*GI*) factor, which is observed to be high; this explains that the compounds h85, h87 and h90 are strongly absorbed in the gastrointestinal system.

Certain parameters that can be exploited in computational calculation with a more or less reasonable degree of accuracy include penetration across the CNS: central nervous system or the BBB: the blood-brain barrier. It's noteworthy that all the compounds do not present any permeability through the BBB barrier.

Two molecules were found capable of passing ADME profiling for the study of toxicity among the seven molecules. using the Pro-Tox web server with reference to the Globally Harmonized System.[51]

The significant enzyme in the family of CYP: CYP3A4, is responsible for metabolism of half of all medications. Another enzyme in the family, CYP2C9, metabolizes several pharmaceuticals that are used in clinical settings, including the drug diclofenac and celecoxib.[52] The Table IV shows that the bioactive ligand h87 is a substrate for CYP2C9.

TABLE IV. Toxicity of bioactive compounds

Compound	Hepatotoxicity	Carcinogenicity	Mutagenicity	Cytotoxicity	LD_{50} / mg kg^{-1}
h3	No	No	No	No	2430
h84	No	No	No	No	3000
h85	No	No	No	Yes	500
h87	No	No	No	Yes	500
h90	No	No	Yes	No	500
h108	No	No	No	No	1500
h110	No	No	No	No	2000

Compounds h84, h85, h87, h90, and h108 in our study act as inhibitors for the CYP2D6 enzyme, which is crucial in metabolizing about 25 % of known pharmaceuticals, contributing to potential clinical issues. However, two compounds, h3 and h110, identified in Table IV, are non-inhibitors of CYP2D6.

The Boiled-Egg Plot, a feature available through SwissADME, is used to assess BBB barrier permeability and passive gastrointestinal absorption of the compounds under investigation. This graph juxtaposes the lipophilicity of a compound with its *TPSA* surface area.[40,53] Compounds located in the inner yellow region result in gastrointestinal absorption in the white region, are predicted to possess permeability across the blood-brain barrier. Conversely, compounds beyond the gray zone may have physicochemical properties less conductive to passive gastrointestinal absorption and blood–brain barrier penetration.

An influential participant in the natural elimination of various medications with diverse molecular structures, the permeability glycoprotein (*P-gp*) serves as a crucial protein transporter.[50] The chemicals that are expected to be pumped up from the brain or the gastrointestinal lumen as substrates of the P-glycoprotein (PGP+) are shown by the points colored by blue (h84, h85, h87 and h90). Points in red, such as molecules h3 and h108, are associated with P-glycoprotein non--substrates (PGP-).

Compounds h85, h87 and h90, positioned in the white region of the SwissADME Boiled-Egg Plot (Fig. 3), are expected to behave like small ligands, which have a high likelihood of gastrointestinal absorption. Conversely, compounds h3, h84 and h108, located in the grey region, are expected to have less--than-ideal brain permeability across the membrane CNS.[52]
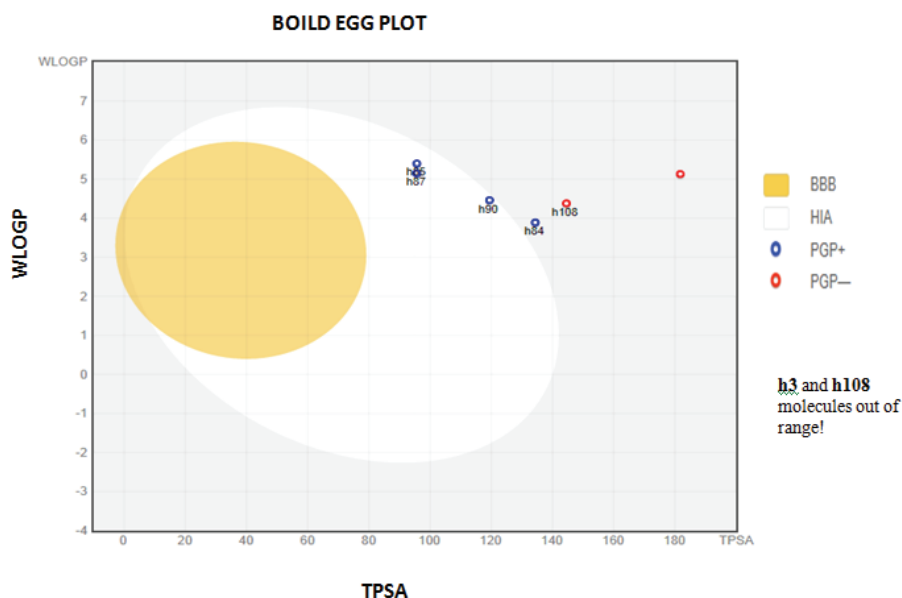
Fig 3. Boiled-Egg Plot.

The Pro-Tox online server provides predictions for four toxicity endpoints, which include hepatotoxicity, cytotoxicity, carcinogenicity, and mutagenicity. Additionally, it calculates an LD_{50} value for acute toxicity in rats (Table IV). Except for h85 and h87, which had positive predictions for cytotoxicity and carcinogenicity, the results demonstrated that all other compounds proved to be non--toxic. The results of LD_{50} of all compounds are presented in Table IV, and the value of h3, h84, h108 and h110is high, 1500–3000 mg/kg, which recommended that these compounds only have a lethal effect at high doses. Comparing that, the

three bioactive ligands h85, h87 and h90 with lower doses are more lethal than the compounds with higher LD_{50}.

Compounds h85 and h87 adhered to the rules with no more than one violation, displaying favorable ADMET proprieties. This suggests their potential as orally active lead molecules. Consequently, h85 and h87 were selected as models for MD investigation, specifically focusing on their stability within the Mpro binding site.[49]

Conformational dynamics and stability

We investigated the conformational stability, structural dynamics, and protein–ligand interactions of the h85 andh87 compounds and the 6LU7 receptor using 100 ns (MD simulation). The *RMSD* values for the two complexes started with a constant rise and are progressively equilibrating with just a slight variation, as expected. The *RMSD* for h85-6LU7 slightly deviates between 40 and 70 ns, then stays balanced and averages about 2.4 Å until the completion of the run (Fig. 4c). For the second complex h87-6LU7, the *RMSD* values of protein and
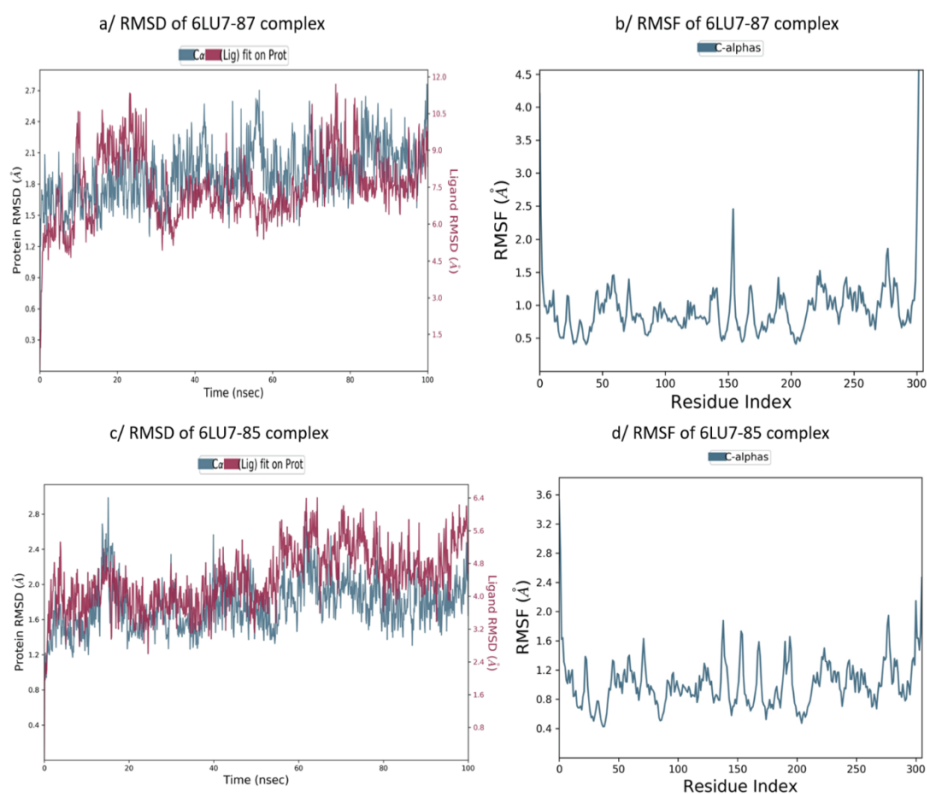

Fig 4. a) *RMSD* plot of 6LU7-h87 complex. b) *RMSF* plot of C-alpha atoms for 6LU7-h87. c) *RMSD* plot of 6LU7-h85 complex. d) *RMSF* plot of C-alpha atoms for 6LU7-h85.

ligand remain constant at around 2.4 Å (Fig. 4a). Both *RMSD*s exhibit minimal change after achieving equilibrium and both systems have C-alpha *RMSD*s less than 2.8 Å, suggesting that they are stable.

The study of the stability of complexes under consideration was further assessed by studying the evolution of their *RMSF*, as illustrated in Fig. 4b and d. The *RMSF* was used to measure each residue's flexibility capability and to investigate inhibitor binding to the target.[54] *RMSF* was performed on the protein backbone in this study, and it demonstrates a similar trend in both systems. The average *RMSF* values for h85-6LU7 and h87-6LU7 were 2.5 and 2, respectively. Furthermore, the residues 150 and 300 in h85-6LLU7 are very flexible, and the h87––6LU7 fluctuation arises at residues 140, 150–200 and 280–300. Moreover, the residues in the helix and loop (150–300) closest to the ligand show some fluctuation and flexibility. There is an h85-6LU7 flexible loop with a fluctuation greater than 4.5. Overall, the *RMSF* figure demonstrates that the binding of h85 and h87 to 6LU7 does not influence residual fluctuations, indicating that these complexes are adequately stable.

By observing the interaction histogram throughout the simulation duration (Fig. 5), there are at least three residues (GLU166, GLN189 and THR190) that
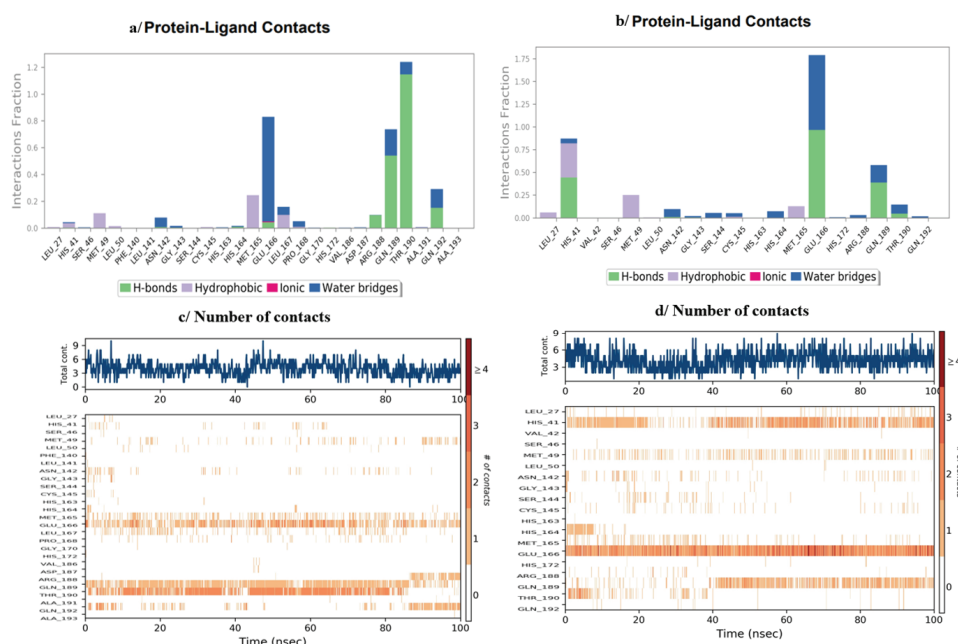

Fig. 5. MD simulations results of h85 and h87. a) The histogram of 6LU7-h85 interactions throughout the trajectory. b) The histogram of 6LU7-h87 interactions throughout the trajectory. c) Bar charts of 6LU7-h85 number of contacts. d) Bar charts of 6LU7-h85 number of contacts.

interact between ligand h85 and COVID-19 main protease for 100 ns either through hydrogen bonds, hydrophobic interactions or water bridges (Fig. 5a), which have the greatest number of contacts between 2 and 3 (Fig. 5c). While ligand h87 formed three important interactions with the main protease (HIS41, GLU166 and GLN189), including hydrogen bonds, water bridges and hydrophobic bridges (Fig. 5b), the number of contacts went from 2 to 3 (Fig. 5d).

CONCLUSION

The coronavirus pandemic, which has affected many countries and changed the rhythm of life during the years 2020–2022, is now a one of the main concern for the whole globe. In this study, we prepared 118 natural compounds and used advanced molecular docking and dynamic simulation to characterize and screen potential bioactive compounds against the coronavirus. Only 7 compounds demonstrated good binding affinity in comparison to the reference bioactive compound N3. The overall binding energies of the seven ligands except h110 ranged between –31.903 and –35.336 kJ/mol, which is similar to the energy value of the reference ligand N3 (–32.615 kJ/mol).

Based on the ADME analysis and molecular docking investigations, two specific ligands, h85 and h87, have shown potential as inhibitors of the coronavirus. This study serves as a preliminary selection to allow further experimental studies; by *in vitro* and *in vivo* methods to explore the pharmacokinetic aspects and adverse effects of these two compounds, for the design of possible future potential drugs against SARS-CoV-2.

SUPPLEMENTARY MATERIAL

Additional data and information are available electronically at the pages of journal website: https://www.shd-pub.org.rs/index.php/JSCS/article/view/12757, or from the corresponding author on request.

ИЗВОД

ИСТРАЖИВАЊЕ ЕФИКАСНОСТИ ПРИРОДНИХ ПРОИЗВОДА ПРЕМА SARS-COV-2: СИНЕРГИСТИЧКИ ПРИСТУП КОЈИ УКЉУЧУЈЕ СИМУЛАЦИЈЕ МОЛЕКУЛСКИМ ДОКИНГОМ И МОЛЕКУЛСКОМ ДИНАМИКОМ

NABILA AOUMEUR[1], MEBARKA OUASSAF[2], SALAH BELAIDI[2], NOUREDDINE TCHOUAR[1], LOFTI BOURAGAA[2], IMANE YAMARI[3], SAMIR CHTITA[3] и LEENA SINHA[4]

¹University of Sciences and Technologies of Oran (USTO), Laboratory of Process Engineering and Environment, BP 1503 Oran 31000, Algeria, ²Biskra University, LMCE Laboratory, Department of Matter Sciences, Biskra, Algeria, ³Hassan II University of Casablanca, Laboratory of Analytical and Molecular Chemistry, Casablanca, Morocco и ⁴University of Lucknow, Department of Physics, 226007 Lucknow, India

Главни циљ овог истраживања је да допринесе истраживању SARS-CoV-2 идентификацијом потенцијалних водећих једињења за клиничке примене, са посебним фокусом на инхибиторе који циљају главну протеазу (M^pro). У овом истраживању урађена је докинг анализа користећи софтвер *molecular operating environmental* (MOE) за процену потенцијала биоактивних једињења, добијених из лековитих биљака, као инхибитора

SARS-CoV-2 M^{pro}. Међу 118 природних производа са *anti*-HIV карактеристикама, седам најбољих кандидата (h3, h84, h85, h87, h90, h108 и h110), је идентификовано на основу бољих енергија везивања у поређењу са референтним лигандом N3. Ова одабрана једињења показују везивне афинитете од -33,996, −35,336, −32,615, −32,154, −33,452, −31,903, односно −40,360 kJ mol^{-1}. Да би даље сузили листу потенцијалних кандидата за примену код људи, испитали смо сличност са лековима, и фармацеутске атрибуте ових једињења користећи SwissADME мрежни сервер. Међу њима, само два једињења, наиме h85 и h87, су показала пожељне фармаколошке особине погодне за примену код људи. Ова два једињења су потом издвојена за даље испитивање. Да би истражили конформациону стабилност лиганада у M^{pro} активном месту, извели смо симулације молекулском динамиком (MD). Ове симулације су показале поуздане и постојане трајекторије, подржане анализом средњих квадратних флуктуација (*RMSF*) и средњих квадратних девијација (*RMSD*). Ови налази и пожељне молекулске особине и интеракциони профили сугеришу да ова два водећа једињења могу бити обећавајући SARS-CoV-2 терапијски кандидати. Она су узбудљиве полазне тачке за даљи дизајн лекова.

REFERENCES

1. W. Guan, Z. Ni, Y. Hu, W. Liang, C. Ou, J. He, L. Liu, H. Shan, C. Lei, D. Hui, B. Du, L. Li, G. Zeng, K. Yuen, R. Chen, C. Tang, T. Wang, P. Chen, J. Xiang, S. Li, J. L. Wang, Z. Liang, Y. Peng, L. Wei, Y. Liu, Y. H. Hu, P. Peng, J. M. Wang, J. Liu, Z. Chen, G. Li, Z .Zheng, S. Qiu, J. Luo, C. Ye , S. Zhu, N. Zhong, *N. Eng. J. Med.* **382** (2020) 17085 (https://doi.org/10.1056/NEJMoa2002032)
2. C. Huang, Y. Wang, X. Li, L. Ren, J. Zhao, Y. Hu, L. Zhang, G. Fan, J. Xu, X. Gu, Z. Cheng, T. Yu, J. Xia, Y. Wei, W. Wu, X. Xie, W. Yin, H. Li, M. Liu, B. Cao, *Lancet* **395** (2020) 497 (https://doi.org/10.1016/S0140-6736(20)30183-5)
3. Y. C. Wu, C. S. Chen,Y. J. Chan. *J. Chinese Med. Assoc.* **83** (2020) 217 (https://doi.org/10.1097/JCMA.0000000000000270)
4. Z.Y.Zu, M. D. Jiang, P. P. Xu, W. Chen, Q. Q. Ni, G. M. Lu, L. J. Zhang, *Radiology* **296** (2020) E15 (https://doi.org/10.1148/radiol.2020200490)
5. A. A. T. Naqvi, K. Fatima, T. Mohammad, U. Fatima, I. K. Singh, A. Singh, S. M . Atif, G. Hariprasad, G. M. Hasan, M. I. Hassan, *Mol. Basis Dis*. **1866** (2020) 165878 (https://doi.org/10.1016/j.bbadis.2020.165878)
6. S.Mahmud, S.Biswas, G. Kumar Paul, A. M. Mita, S. Afrose, M. Robiul Hasan, M. Sharmin Sultana Shimu, M. A. R. Uddin, M. Salah Uddin, S. Zaman, K. M. Kaderi Kibria, M. Arif Khan, T. Bin Emran, M. Abu Saleh, *Arab. J. Chem.* **14** (2021) 103315 (https://doi.org/10.1016/j.arabjc.2021.103315)
7. N. Zhu, D. Zhang, W. Wang, X. Li, B. Yang, J. Song, X. Zhao, B. Huang, W. Shi, R. Lu, P. Niu, F. Zhan, X. Ma, D. Wang, W. Xu, G. Wu, G. F Gao, W.A. Tan, *N. Eng. J. Med.* **382** (2020) 727 (https://doi.org/10.1056/NEJMoa2001017)
8. X. Cui, Y. Wang, J. Zhai, M. Xue, C. Zheng, L. Yu, *Virus Research* **328** (2023) 199075 (https://doi.org/10.1016/j.virusres.2023.199075)
9. R. Gili, R. Burioni, *J. Transl. Med.* **21** (2023) 251(https://doi.org/10.1186/s12967-023-04095-6)
10. WHO world Health Organization [WHO], *Tracking SARS-CoV-2 variants*, 2023, https://www. who.int/activities/tracking-SARS-CoV-2-variants
11. W. T. Harvey, A. M. Carabelli, B. Jackson, R. K. Gupta, E. C. Thomson, E. M. Harrison, C. A. Ludden, R. Reeve, A. Rambaut, COVID-19 Genomics UK (COG-UK) Consortium,

S. J. Peacock, D. L. Robertson, *Nat. Rev. Microbiol.* **19** (2021) 409 (https://doi.org/10.1038/s41579-021-00573-0)

12. S. O. Aftab, M. Z. Ghouri, M. U. Masood, Z. Haider, Z. Khan, A. Ahmad, N. Munawar, *Transl. Med.* **18** (2020) 275(https://doi.org/10.1186/s12967-020-02439-0)

13. R. Yu, L. Chen, R. Lan, R. Shen, P. Li, *Int. J. Antimicrob. Agents* **56** (2020) 106012 (https://doi.org/10.1016/j.ijantimicag.2020.106012)

14. M. Lounasmaa, P. Hanhunen, M. Westersund, N. Halonen, *Alkaloids: Chem. Biol.* **52** (1999) 103(https://doi.org/10.1016/S0099-9598(08)60026-7)

15. R. M. Perez, *Pharm. Biol.* **41** (2003) 107 (https://doi.org/10.1076/phbi.41.2.107.14240)

16. S. Chtita, R. T. Fouedjou, S. Belaidi, L. A. Djoumbissie, M. Ouassaf, F. A. Qais, M Bakhouch, M. Efendi, T. T. Tok, M. Bouachrine, T. Lakhlifi, *Struct Chem*. **33** (2022) 1799 (https://doi.org/10.1007/s11224-022-01939-7)

17. J. G. Africa, H. C. Arturo, L. J. Bernardo, J. K. Ching, O. C. de la Cruz, J. B. Hernandez, R. J. Magsipoc, C. T. Sales, J. C. Agbay, G. L. Neri, M. T. Quimque, A. P. Macabeo, *Philipp. J. Sci*. **151** (2021) 35 (https://doi.org/10.56899/151.01.04)

18. P. Gale, *Micro. Risk. Anal*. **21** (2022)100198 (https://doi.org/10.1016/j.mran.2021.100198)

19. P. Gale, *Micro. Risk. Anal*. **16** (2020) 100140 (https://doi.org/10.1016/j.mran.2020.100140)

20. M. Popovic, *Micro. Risk. Anal*. **23** (2023) 100250 (https://doi.org/10.1016/j.mran.2023.100250)

21. M. Popovic and M. Popovic, *Micro. Risk. Anal*. **21** (2022)100202 (https://doi.org/10.1016/j.mran.2022.100202)

22. M. Popovic, *Micro.Risk.Anal.***24** (2023) 100260 (https://doi.org/10.1016/j.mran.2023.100260)

23. M. E. Popovic, M. P. Pavlovic, M. Papovic, *Micro. Risk. Anal*. **25** (2023) 100280

24. (https://doi.org/10.1016/j.mran.2023.100280)

25. B. Hemmateenejad, K. Javidnia, M. Nematollahi, M. Elyasi, *J. Iran. Chem. Soc.* **6** (2009) 420 (https://doi.org/10.1007/BF03245853)

26. A. Aouidate, A. Ghaleb, S. Chtita, M. Aarjane, A. Ousaa, H. Maghat, A. Sbai, M. Choukrad, M. Bouachrine, T. Lakhlifi, *J. Biomol. Struct. Dyn*. **39** (2021)4522 (https://doi.org/10.1080/07391102.2020.1779130)

27. R. Banerjee, L. Perera, L. M. V. Tillekeratne, *Drug .Discov. Today* **26** (2021) 804 (https://doi.org/10.1016/j.drudis.2020.12.005)

28. P. K. Doharey, V. Singh, M. R. Gedda, A. K. Sahoo, P. K. Varadwaj, B. Sharma, *J. Biomol. Struct. Dyn*. **40** (2022) 5588 (https://doi.org/10.1080/07391102.2021.1871956)

29. M. T. J. Quimque, K. I. R. Notarte, R. A. T. Fernandez, M. A. O. Mendoza, R. A. D. Liman, J. A. K. Lim, L. A. E. Pilapil, J. K. H. Ong, A. M. Pastrana, A. Khan, D. Q. Wei, A. P. G. Macabeo, *J. Biomol. Struct. Dyn.* **39** (2021) 4316 (https://doi.org/10.1080/07391102.2020.1776639)

30. V. N. O. de Leon, J. A. H. Manzano, D. Y. H. Pilapil, R. A. T. Fernandez, J. K. A. R. Ching, M. T. J. Quimque, J.C.M. Agbay, K. I. R. Notarte, A. P. G. Macabeo, *J. Genet. Eng. Biotechnol*. **19** (2021) 104 (https://doi.org/10.1186/s43141-021-00206-2)

31. D. Li, J. Luan, L. Zhang, *Biochem. Biophys. Res. Commun.* **538** (2021) 72 (https://doi.org/10.1016/j.bbrc.2020.11.083)

32. HYPERCHEM Molecular Modeling System, Hypercube. Inc., Gainesville, FL, 2007

33. MARVINSKETCH 17.1.2, ChemAxon 2017 (http://www.chemaxon.com)

34. S. Belaidi, R. Mazri, H. Belaidi, T. Lanez, D. Bouzidi, *Asian J. Chem.* **25** (2013) 9241 (https://doi.org/10.14233/ajchem.2013.15199)
35. A. Kerassa, S. Belaidi, D. Harkati, T. Lanez, O. Prasad, L. Sinha, *Rev. Theor. Sci.* **4** (2016) 85 (https://doi.org/10.1166/rits.2016.1050)
36. S. Chtita, A.Belhassan, A. Aouidate, S. Belaidi, M. Bouachrine, T. Lakhlifi, *Comb. Chem. High Throughput Screen*. **24** (2021) 441 (https://doi.org/10.2174/1386207323999200730205447)
37. Molecular Operating Environment (MOE), Version 2007.09, Chemical Computing Group, Inc., Montreal, Quebec, 2005 (http://www.Chemcomp.com)
38. P. S. Das, A. Kokardekar, C. M. Breneman, *J. Chem. Inf. Model*. **49** (2009) 2863 (https://doi.org/10.1021/ci900317x)
39. M. Ouassaf, S. Belaidi, S. Khamouli, H. Belaid, S. Chtita, *Acta Chim. Slov.* **68** (2021) 289 (https://doi.org/10.17344/acsi.2020.5985)
40. C. A. Lipinski, F. Lombardo, B. W. Dominy, P. J. Feeney, *Adv. Drug. Deliv. Rev.* **46** (2001) 3 (https://doi.org/10.1016/s0169-409x(00)00129-0)
41. A. Daina, O. Michielin, V. Zoete, *Sci. Rep.* **7** (2017) 42717 (https://doi.org/10.1038/srep42717)
42. Schrödinger Release 2021-3: Maestro-Desmond Interoperability Tools, Schrödinger, LLC, New York
43. K. Roos, C. Wu, W. Damm, M. RebouL, J. M. Stevenson, C. Lu, M. K. Dahlgren, S. Mondal, W. Chen, L. Wang, R. Abel, R. A. Friesner, E. D. Harder, *J. Chem. Theory Comput.* **15** (2019) 1863(https://doi.org/10.1021/acs.jctc.8b01026)
44. A. Imberty, C. Gautier, J. Lescar, S. Pérez, L. Wyns, R. Loris, *J. Biol. Chem.* **275** (2000) 17541 (https://doi.org/10.1074/jbc.M000560200)
45. K. O. Chang, Y. Kim, S. Lovell, A. D. Rathnayake, W. C. Groutas, *Viruses* **11** (2019) 197 (https://doi.org/10.3390/v11020197)
46. D. F. Veber, S. R. Johnson, H. Y. Cheng, B. R. Smith, K. W. Ward, K. D. Kopple, *J. Med. Chem.* **45** (2002) 2615 (https://doi.org/10.1021/jm020017n)
47. A. K. Ghose, V. N. Viswanadhan, J. J. Wendoloski, *J. Comb. Chem.* **1** (1999) 55 (https://doi.org/10.1021/cc9800071)
48. I. Muegge, S. L. Heald, D. Brittelli, *J. Med. Chem.* **44** (2001) 1841 (https://doi.org/10.1021/jm015507e)
49. W. J. Egan, K. M. Merz, J. J. Baldwin, *J. Med. Chem*. **43** (2000) 3867 (https://doi.org/10.1021/jm000292e)
50. A. Zerroug , S. Belaidi, I. BenBrahim, L. Sinha, S. Chtita, *J. King Saud Univ. Sci*. **31** (2019) 595-560 (https://doi.org/10.1016/j.jksus.2018.03.024)
51. N. Aoumeur, S. Belaidi, N. Tchouar, M. Ouassaf, T. Lanez, S. Chtita, *Mor. J. Chem.* **9** (2021) 274 (https://doi.org/10.48317/IMIST.PRSM/morjchem-v9i2.19884)
52. H. Nour, O. Daoui, O. Abchir, S. ElKhattabi, S. Belaidi, S. Chtita, *Heliyon* **8** (2022) e11991 (https://doi.org/10.1016/j.heliyon.2022.e11991)
53. A. Daina, V. Zoete, *J. Med. Chem.* **6** (2016) 1117 (https://doi.org/10.1002/cmdc.201600182)
54. V. Zoete, A. Daina, C. Bovigny, O. Michielin, *J. Chem. Info. Model.* **56** (2016) 1399 (https://doi.org/10.1021/acs.jcim.6b00174)
55. S. Ghahremanian, M. M. Rashidi, K. Raeisi, D. Toghraie. *J. Mol. Liq*. **354** (2022) 118901 (https://doi.org/10.1016/j.molliq.2022.118901).

Exploring the efficacy of natural compounds against SARS-CoV-2: A synergistic approach integrating molecular docking and dynamic simulation

NABILA AOUMEUR[1], MEBARKA OUASSAF[2], SALAH BELAIDI[2]*, NOUREDDINE TCHOUAR[1], LOFTI BOURAGAA[2], IMANE YAMARI[3], SAMIR CHTITA[3]**
and LEENA SINHA[4]

[1]*University of Sciences and Technologies of Oran (USTO), Laboratory of Process Engineering and Environment, BP 1503 Oran 31000, Algeria,* [2]*Biskra University, LMCE Laboratory, Department of Matter Sciences, Biskra, Algeria,* [3]*Hassan II University of Casablanca, Laboratory of Analytical and Molecular Chemistry, Casablanca, Morocco* and [4]*University of Lucknow, Department of Physics, 226007 Lucknow, India*

Figure S-1: Antiviral natural products h1–h118 with significant binding affinities against SARS-CoV-2
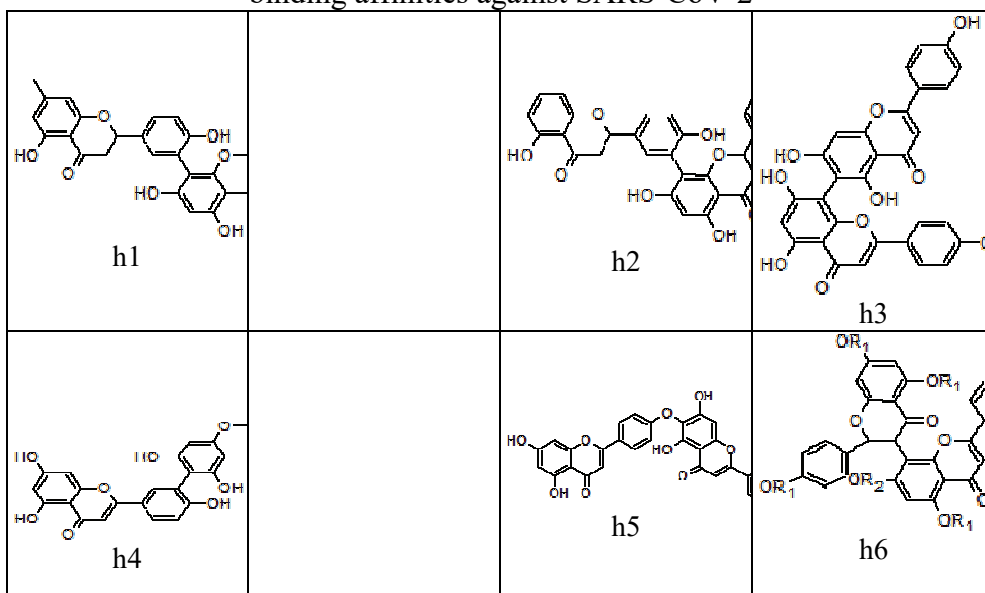
* Corresponding authors. E-mail: (*)s.belaidi@univ-biskra.dz; (**) samir.chtita@univh2c.ma

h7		h8	h9
h10		h11	h12
h13		h14	h15
h16		h17	h18
h19		h20	h21
h22		h23	h24

h25		**h26**	**h27**
h28		**h29-32**	**h33-36**
h37-h40		**h41-h47**	**h48-h50**
h51-h53		**h54-h55**	**h56-h62**
h63-h65		**h66-h70**	**h71-h77**
h78-h80		**h81-h87**	**h88-h94**

h95-h103	h104-h107	h108
h109	h110	h111
h112	h113	h114
h115	h116	h 117
	h118	
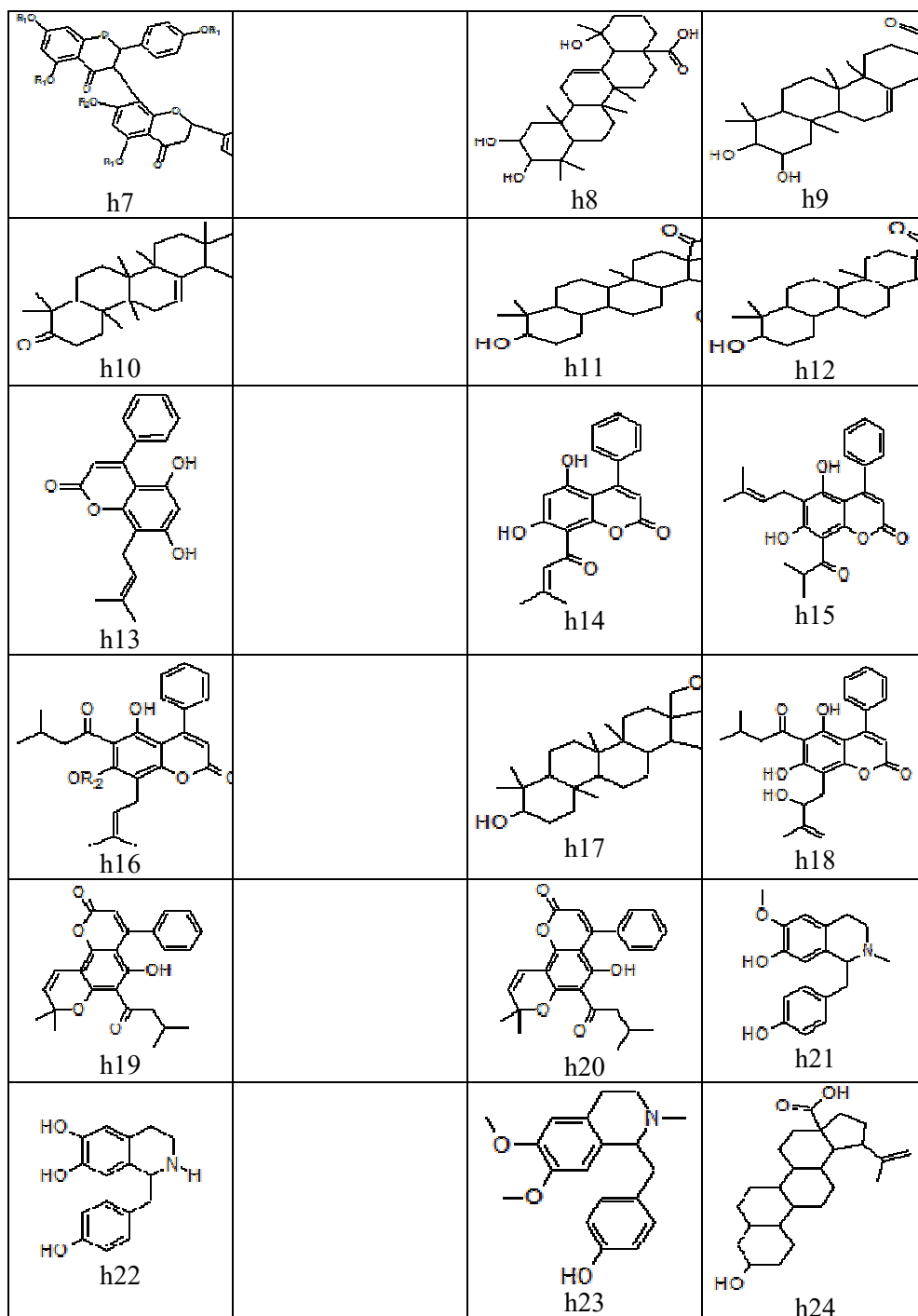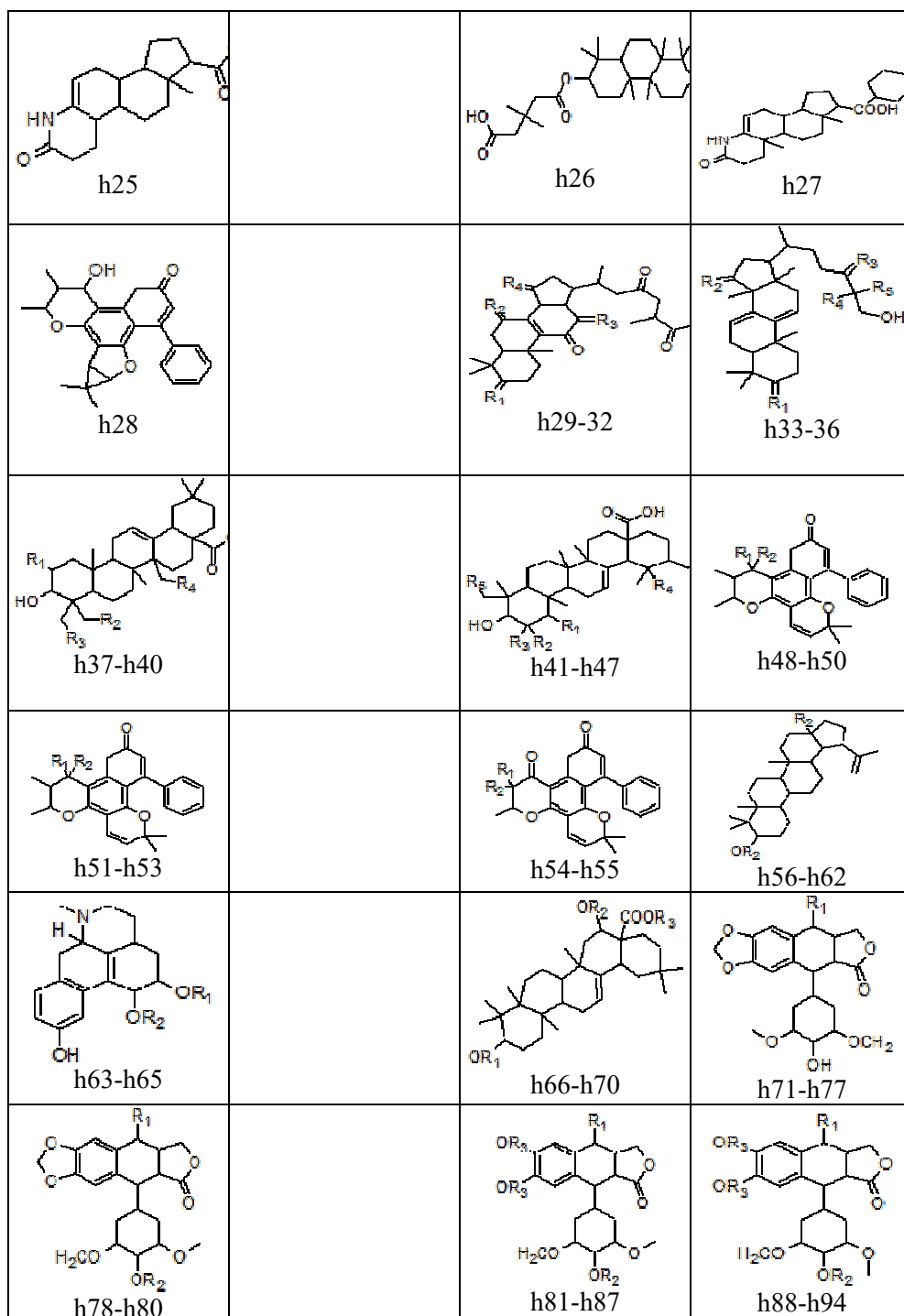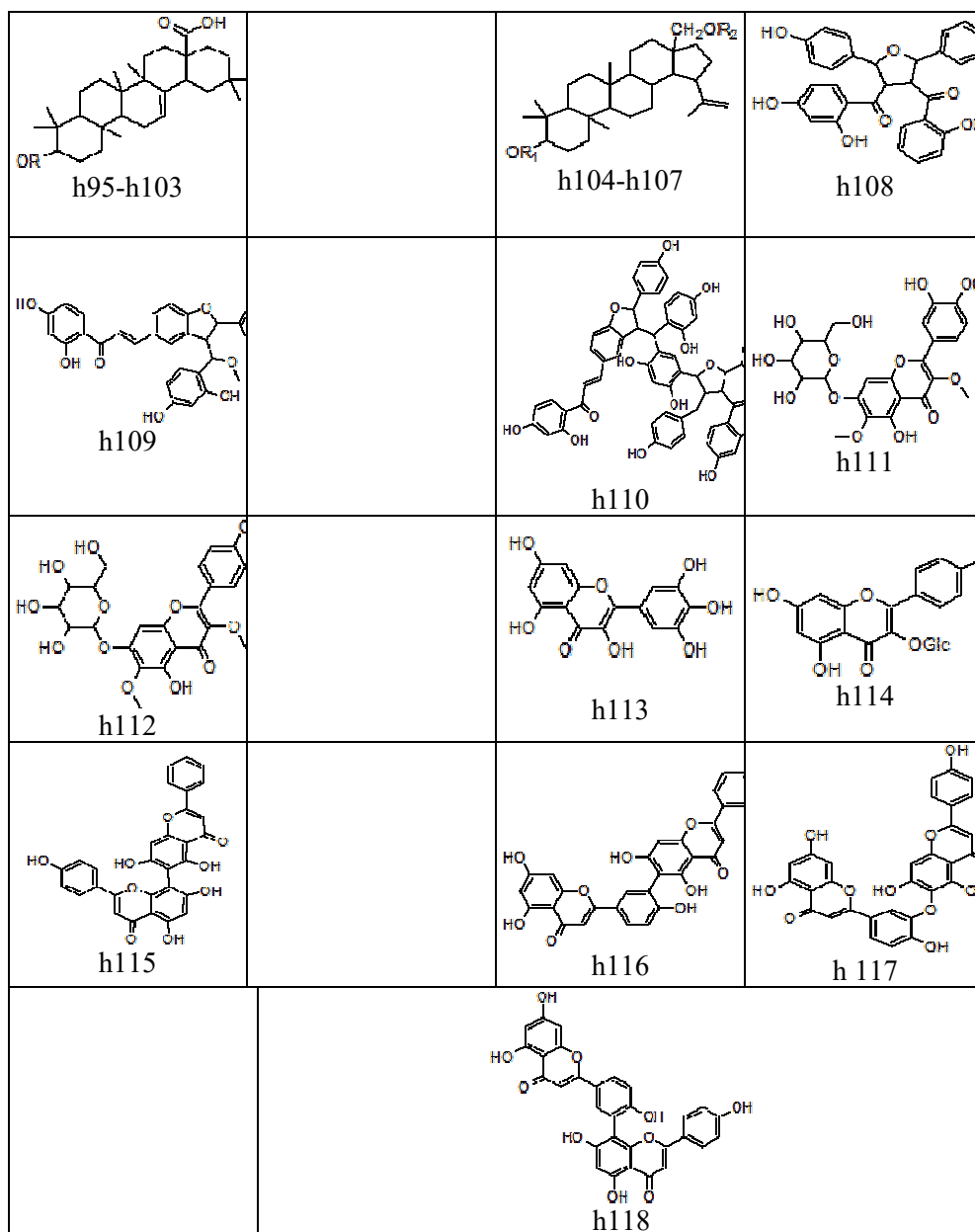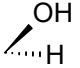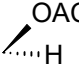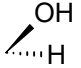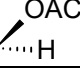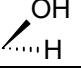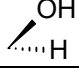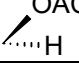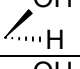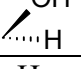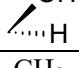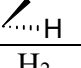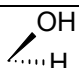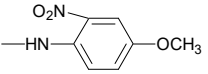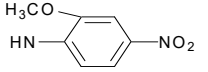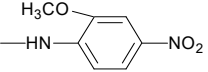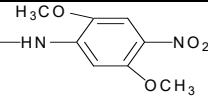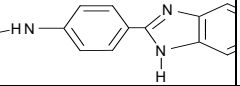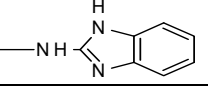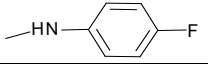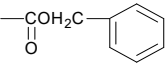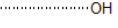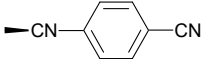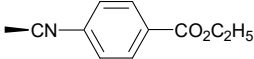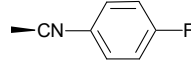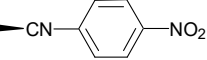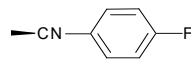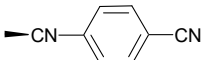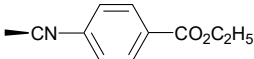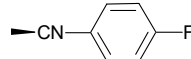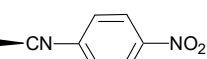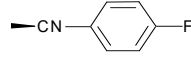
Table S-I: Functional group

	R1	R2	R3	R4	R5
h29	OH / ⸜H	O	OAC / ⸜H	OH / ⸜H	-
h30	OAC / ⸜H	OH / ⸜H	OH / ⸜H	O	-
h31	O	O	OAC / ⸜H	O	-
h32	OH / ⸜H	OH / ⸜H	O	O	-
h33	OH (wedge)	H_2	OH / ⸜H	OH	CH_3
h34	O	OH / ⸜H	CH_3	CH_3	CH_2OH
h35	O	H_2	CH_3	CH_3	CH_2OH
h36	O	H_2	OH / ⸜H	OH	CH_3
h37	H	H	H	H	-
h38	OH	H	OH	H	-
h39	OH	OH	H	H	-
h40	H	H	H	OH	-
h41	H	H	H	OH	H
h42	H	H	H	H	H
h43	H	OH	H	H	H
h44	H	OH	H	H	OH
h45	H	OH	OH	OH	H
h46	H	OH	OH	OH	H
h47	OH	OH	OH	OH	H
h48,h51	H	OH	-	-	-
h49,h52	OH	H	-	-	-
h50,h53	H	OAc	-	-	-
h54	Me	H	-	-	-
h55	H	Me	-	-	-
h56	H	COOH	-	-	-
h57	H	CH_2OH	-	-	-
h58	H	$COOCH_2COOC$	-	-	-

		H$_3$			
h59	Ac	COOH	-	-	-
h60	COC$_6$H$_5$	COOH	-	-	-
h61	COCH=CHCH$_3$	COOH	-	-	-
h62	COCH$_2$CH$_2$COOH	COOH	-	-	-
h63	Me	OH	-	-	-
h64	Me	Me	-	-	-
h65	H	Me	-	-	-
h66	H	H	H	-	-
h67	H	H	Me	-	-
h68	Ac	H	Me	-	-
h69	Ac	Ac	H	-	-
h70	Butyryl	H	Me	-	-
h71		-	-	-	-
h72		-	-	-	-
h73		-	-	-	-
h74		-	-	-	-
h75		-	-	-	-
h76		-		-	-
h77		-	-	-	-
h78		-	-	-	-
h79			-	-	-
h80			-	-	-
h81		Me	H	-	-

h82	⋯⋯⋯⋯⋯OH	Me	Me	-	-
h83	CN—⟨⟩—CN	H	Me	-	-
h84	CN—⟨⟩—$CO_2C_2H_5$	H	Me	-	-
h85	CN—⟨⟩—F	Me	Me	-	-
h86	CN—⟨⟩—NO_2	H	Me	-	-
h87	CN—⟨⟩—F	H	Me	-	-
h88	⋯⋯⋯⋯⋯OH	Me	H	-	-
h89	⋯⋯⋯⋯⋯OH	Me	Me	-	-
h90	CN—⟨⟩—CN	H	Me	-	-
h91	CN—⟨⟩—$CO_2C_2H_5$	H	Me	-	-
h92	CN—⟨⟩—F	Me	Me	-	-
h93	CN—⟨⟩—NO_2	H	Me	-	-
h94	CN—⟨⟩—F	H	Me	-	-

R

Table S-II: Results 6LU7 enzyme SCORE with studied ligands.

N°.Comp.	S-Score (kJ/mol)	N°.Comp.	S-Score (kJ/mol)	N°.Comp.	S-Score (kJ/mol)
h1	-30.270	h47	-26.376	h91	-32.782
h2	-32.405	h48	-18.045	h92	-30.940
h3	-33.996	h49	-27.214	h93	-32.489
h4	-29.433	h50	-27.214	h94	-32.405
h5	-30.144	h51	-28.051	h95	-23.906
h6	-32.112	h52	-8.206	h96	-24.409
h7	-34.708	h53	-26.879	h97	-25.665
h8	-22.315	h54	-28.595	h98	-25.623
h9	-23.655	h55	-28.553	h99	-10.718
h10	-22.064	h56	-22.608	h100	-25.790
h11	-14.528	h57	-23.362	h101	-24.785
h12	-23.822	h58	-26.000	h102	-25.790
h13	-27.130	h59	-25.958	h103	-8.499
h14	-25.539	h60	-25.330	h104	-26.586
h15	-30.144	h61	-23.362	h105	-25.330
h16	-31.024	h62	-22.776	h106	-27.256
h17	-22.818	h63	-25.455	h107	-26.628
h18	-30.479	h64	-25.413	h108	-31.903
h19	-29.977	h65	-25.120	h109	-33.075
h20	-30.103	h66	-21.101	h110	-40.360
h21	-26.753	h67	-20.682	h111	-30.144
h22	-25.706	h68	-23.404	h112	-28.595
h23	-25.204	h69	-25.790	h113	-23.069

AOUMEUR *et al.*

h24	-22.399	h70	-26.376	h114	-30.103
h25	- 26.041	h71	-31.149	h115	-33.578
h26	-17.291	h72	-29.768	h116	-31.066
h27	-15.742	h73	-32.489	h117	-32.238
h28	-28.888	h74	-31.610	h118	-30.479
h29	-26.000	h75	-31.526	Réf (N3)	-32.615
h30	-25.916	h76	-30.061		
h31	-29.140	h77	-29.851		
h32	-6.070	h78	-30.144		
h33	-26.669	h79	-30.270		
h34	-24.618	h80	-30.270		
h35	-24.367	h81	-26.376		
h36	-26.795	h82	-27.758		
h37	-26.795	h83	-27.758		
h38	-24.450	h84	-35.336		
h39	-23.822	h85	-32.615		
h40	-22.776	h86	-31.735		
h41	-24.576	h87	-32.154		
h42	-23.278	h88	-25.874		
h43	-25.037	h89	-28.679		
h44	-25.413	h90	-33.452		
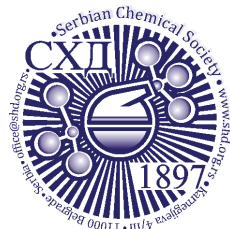
Investigation of structural, dynamic and dielectric properties of an aqueous potassium fluoride system at various concentrations by molecular dynamics simulations

AYOUB LAHMIDI, SANAA RABII, ABDELKBIR ERROUGUI*, SAMIR CHTITA,
MHAMMED EL KOUALI and MOHAMMED TALBI

*Laboratory of Analytical and Molecular Chemistry, Faculty of Sciences Ben M'Sick,
Hassan II University of Casablanca, Morocco*

Abstract: Potassium-ion-based batteries have emerged as promising alternatives to traditional lithium-ion batteries for energy storage systems due to their affordability, wide accessibility and comparable chemical characteristics to lithium. This study employs molecular dynamics simulations to explore the physical phenomena of potassium fluoride in aqueous solutions. The interatomic interactions were defined using the OPLS-AA force field, while the SPC/E water model and ions were represented as charged Lennard–Jones particles. The simulations were conducted across concentrations ranging from 0.1 to 1.0 mol kg^{-1}. The insights derived from this investigation provide valuable understanding into the behaviour of KF electrolytes and their potential utility in energy storage systems. A comprehensive comprehension of the impact of KF electrolyte concentration on structural, dynamic and dielectric properties is pivotal for the design and optimization of potassium-ion batteries, as well as other electrochemical devices leveraging KF-based electrolytes. This research significantly contributes to the ongoing endeavours aimed at developing efficient and economically viable energy storage solutions that transcend the confines of traditional lithium-ion batteries.

Keywords: molecular dynamics; potassium fluoride; hydration phenomenon; self-diffusion coefficient; dielectric constant; energy storage system.

INTRODUCTION

In recent years, a surge of interest has emerged in the pursuit of new battery technologies aimed at addressing the limitations of standard lithium-ion batteries.[1,2] One such promising development involves batteries centred around potassium ions, which hold potential as alternatives for energy storage systems.[3,4] These potassium-ion batteries offer several advantages over their lithium-ion

---

877

counterparts, including reduced costs, abundant availability and comparable chemical properties.[5–7]

Lithium-ion batteries have become the preferred choice across various applications, ranging from portable devices to electric automobiles.[8,9] However, their production costs remain relatively high due to limited global lithium reserves and intricate extraction processes.[10,11] Furthermore, lithium-ion batteries heavily rely on cobalt, a rare and costly material entangled with ethical and environmental concerns in its mining.[12,13] These factors have prompted researchers and scientists to explore alternative battery chemistries that can offer similar or enhanced performance while being more economically feasible and sustainable.

Significantly, potassium is an abundant element present in the Earth's crust and readily available, rendering it a cost-effective substitute for lithium.[14,15] Its widespread availability ensures a steady and sustainable supply chain, reducing the concerns related to resource scarcity.[7] Additionally, the potassium ions exhibit comparable chemical properties to lithium ions, enabling them to demonstrate akin electrochemical behaviour and energy storage capabilities.[16–18] Recent studies have exhibited promising results in the development of potassium-ion batteries.[19,20] Researchers have made substantial progress in augmenting battery performance, energy density, and cycle life, rendering these batteries more viable for practical applications.[21,22] These advancements primarily revolve around the design of suitable electrode materials, electrolyte formulations and battery architectures, all geared towards optimizing the performance and stability of the potassium-ion batteries.[23–25] Within various applications, particular attention has been directed towards the electrolytic system involving a fluoride anion and potassium cation due to its significance.[26–29] Nonetheless, a comprehensive examination of the existing literature uncovers a scarcity of molecular equilibrium simulation studies targeting $KF_{(aq)}$ systems within the specified concentration range.

The organization of this paper is as follows: Section 2 include the details for the MD simulations. Section 3 elucidates and presents the theoretical equations employed in this investigation. Section 4 deals with the study's findings, including computed structural and dynamical characteristics, alongside the dielectric constant at different concentrations. Lastly, Section 5 summarizes the conclusions and concluding remarks.

COMPUTATIONAL DETAILS

In this research, we conducted molecular dynamics (MD) simulations at a temperature of 298.15 K to investigate the behaviour of potassium fluoride (KF) within aqueous solutions of varying concentrations. To describe the interatomic potentials between ions and water components,[30] we employed the optimized potentials for liquid simulations-all atom (OPLS-AA) force field. The simulations were carried out using GROMACS-2020-6[31,32] under the NPT ensemble, wherein both particle number (*N*) and pressure were held constant at 1 bar using

Parrinello–Rahman pressure coupling.[33] To maintain the temperature at 298.15 K, a Nosé––Hoover thermostat was used.[34,35]

The simulations were carried out for a total of 10^8 steps, with each time step set to 0.1 fs, resulting in a simulation time of 100 ns. This extended simulation time allowed for a comprehensive exploration of the system's dynamics and behaviour. For representing water molecules, we employed the widely used SPC/E model,[36] known for its accuracy in reproducing numerous solution properties.

The interaction between ions and water molecules was depicted through Coulombic interactions and a short-range Lennard–Jones (LJ) potential,[37] with the ions interacting selectively with oxygen or hydrogen atoms within the water molecules, Table I. The main aim of this study is to gain insights into the behaviour and properties of potassium fluoride within an aqueous solution. Through our simulations we computed the radial distribution functions (RDFs) for different ion pairs, uncovering the microstructural characteristics of the solutions. Furthermore, we determined the hydration numbers by integrating the RDFs. Additionally, we evaluated the dynamic and dielectric properties of different components by modelling the self-diffusion coefficient and relative permittivity (ε). These simulations provided a comprehensive understanding of the interatomic interactions and dynamics within the system, shedding light on the structural, dynamical and dielectric properties of the potassium fluoride solution.

TABLE I. Lennard–Jones interactions and electrostatic forces parameters within the force fields of water and ions[38,39]

Element	q / e	σ_{LJ} / Å	ε_{LJ} / kcal* mol^{-1}
K$^+$	1.00000	4.93463	0.00033
F$^-$	−1.00000	2.73295	0.72000
O$_w$	−0.84760	3.16560	0.65017
H$_w$	0.42380	3.16549	0.15532

Theoretical formalism

In this system, both the interactions between ions {ion–ion} and ions with dipoles {ion––dipole} are modelled using a combination of Coulombic and Lennard–Jones potentials. The general representation of the potential is :[40]

$$U_{ij}(r) = \frac{q_i q_j}{r_{ij}} + 4\varepsilon_{ij}[(\frac{\sigma_{ij}}{r_{ij}})^{12} - (\frac{\sigma_{ij}}{r_{ij}})^6] \tag{1}$$

The equation incorporates the charge of the the atom (or ion), denoted as q_i, and is essential in describing the Coulombic potential. Additionally, the Lennard–Jones parameters σ_{ij} and ε_{ij} are determined using the combination rules from Eqs. (2) and (3), respectively:

$$\sigma_{ij} = \frac{\sigma_i + \sigma_j}{2} \tag{2}$$

$$\varepsilon_{ij} = \sqrt{\varepsilon_i \varepsilon_j} \tag{3}$$

These combination rules play a pivotal role in the computation of the Lennard–Jones potential, responsible for describing the attractive and repulsive forces operating among particles. By employing this generalized potential equation, we attain invaluable insights into the intri-

---

* 1 kcal = 4184 J

cate interplay of forces within the system, thus contributing to a comprehensive grasp of its structural and dynamic behaviours.

For the analysis of structural properties within aqueous solutions, a crucial methodology involves the calculation of the radial distribution function (RDF), denoted as $g_{ij}(r)$, pertaining to various pairs of ions. Eq. (4) presented below encapsulates the mathematical representation of $g_{ij}(r)$ function, which characterizes the spatial distribution of ion pairs i and j. This equation quantifies the possibility of locating an ion i at a distance r_{ij} from ion j within the solution:[26,41]

$$g_{ij}(r) = 4\pi r^2 \rho \mathrm{d}r \tag{4}$$

To determine the coordination numbers, $n_{ij}(r)$, associated with different ions, we integrated the radial distribution function by:[41,42]

$$n_{ij}(r) = 4\rho_i \int_0^{r_{\min}} g_{ij}(r)\mathrm{d}r \tag{5}$$

This integration provides an estimation of the number of water molecules surrounding M^+ within the distance range from 0 to $r_{\min}$. Here, $g_{ij}(r)$ represents the RDFs for the i–j pair, while ρ_i denotes the number density of particles corresponding to the minimum of the first peak in the RDF. This analysis allowed us to gain insights into and quantify the extent of ion––water molecule interactions within the specific environment surrounding M^+ in the solution.

To characterize dynamic properties, our focus lies in computing the self-diffusion coefficient (D), a pivotal factor for representing the translational motion of particles within the aqueous system. This coefficient is determined by analysing the long-time limit of the mean square displacement (MSD) using Einstein's relation:[26]

$$D = \frac{1}{6}\lim_{t\to\infty}\frac{\mathrm{d}}{\mathrm{d}t}\frac{1}{N}\sum_{i=1}^{N}[\,|\,r(t_0+t) - r(t_0)\,|^2] \tag{6}$$

In Eq. (6), $r(t_0 + t)$ denotes the position vector of the molecule's (or ion's) centre of mass at time t. Through the analysis of the temporal evolution of the centre of mass position, we acquire enhanced insights into the diffusive patterns and motion of particles within the aqueous system.

Moreover, in the pursuit of deriving the dielectric constant of non-polarizable fluids, we evaluate the fluctuations in the total dipole moment (M) within the simulation volume. Eq. (7) provides the mathematical representation of this calculation:[26]

$$\varepsilon = \frac{4}{3K_\mathrm{B}T\langle V\rangle}(\langle M^2\rangle - \langle M\rangle^2) \tag{7}$$

Here, M represents the cumulative sum of individual dipole moments (μ_i) contributed by all particles in the system, where N denotes the total number of particles. The examination of these fluctuations furnishes significant insights into the dielectric characteristics of the non--polarizable fluid system, elucidating its electrical properties and interactions.

<div align="center">RESULTS AND DISCUSSION</div>

Structural proprieties

The evolution of concentration within an electrolytic solution is a pivotal aspect for understanding the structural characteristics of complex systems, especially in the presence of an aqueous medium. However, upon analysing the litera-

ture, it has become evident that there exists a dearth of data concerning the influ-ence of concentration on the $KF_{(aq)}$ system. Furthermore, this study leads us to the conclusion that the calculated density of these solutions exhibits a linear decrease as the concentration increases. To provide a comprehensive overview of the studied system, Table II presents our molecular simulation data, including parameters such as density, volume, number of hydrogen bonds, total energy, kinetic energy and structural properties of this system at various concentrations. The initial analysis aims to highlight the strong correlation between concentration and the examined physicochemical properties, thus enhancing our understanding of the dissolution process of potassium fluoride within an aqueous medium.

TABLE II. Simulation values reveals thermodynamic and structural properties of $KF_{(aq)}$ system at different concentrations

Parameter	C / mol kg^{-1}					Exp. data
	0.1	0.3	0.5	0.8	1.0	
ρ / 10^3 kg m^{-3}	1.005	1.011	1.032	1.053	1.067	–
V / nm^3	64.529	63.932	63.419	62.569	62.019	–
E_{tot} / 10^5 kJ mol^{-1}	–0.886	–0.951	–1.009	–1.107	–1.173	–
$E_{kinetic}$ / 10^5 kJ mol^{-1}	0.161	0.160	0.159	0.158	0.158	–
Number of H-bonds per H	1.677	1.702	1.724	1.765	1.793	–
$r_{(K\text{-}Ow)}$ / Å	2.720	2.720	2.720	2.720	2.720	2.80[43]
Hydration number ($_{CNK+}$)	6.602	6.634	6.665	6.708	6.735	6.40[44]
$r_{(F\text{-}Ow)}$ / Å	2.600	2.600	2.600	2.600	2.600	2.64[45]
Hydration number ($_{CNF\text{-}}$)	6.329	6.334	6.341	6.351	6.360	6.10[45]
						6.80[44]

To explore the local structure of the electrolyte system, we performed mole-cular dynamics simulations in a canonical NVT ensemble. This allowed us to calculate hydration data for all constituents, encompassing ions and water mole-cules. In particular, we scrutinized the pair correlations among ions, ion–water, and water–water interactions using radial distribution functions (RDFs). Our investigation centred on aqueous KF electrolytes maintained at a temperature of 298.15 K.

The RDFs, acquired across diverse concentrations spanning from 0.1 to 1.0 (mol kg^{-1}), have been obtained and are graphically depicted in Figs. 1–3. These RDF graphs offer valuable insights into the spatial arrangement and interplay between ions and water molecules within the KF electrolyte system. By analys-ing these RDFs, we gain enhanced comprehension of local structural attributes and their fluctuations with changing concentration levels. This research contri-butes to a more comprehensive understanding of the system's behaviour.

Radial distribution functions have yielded valuable insights into the micro-structural properties of the electrolytic system in KF aqueous solution. Fig 1a illustrates the $g_{K–Ow}(r)$ first peak, which was detected at a distance of 0.272 nm,

indicating a well-defined coordination shell around the potassium cation. The second hydration shell was observed in the range of distance between 0.466 and 5.921 nm, suggesting the presence of additional water molecules in the environment. The $g_{F-Hw}(r)$ in Fig 1b exhibited dual peaks as well, with the initial peak observed at a separation of 0.159 nm, followed by a secondary peak at 0.305 nm. These findings are consistent with both experimental results and computer simulations conducted on the KF aqueous system.[43,45]
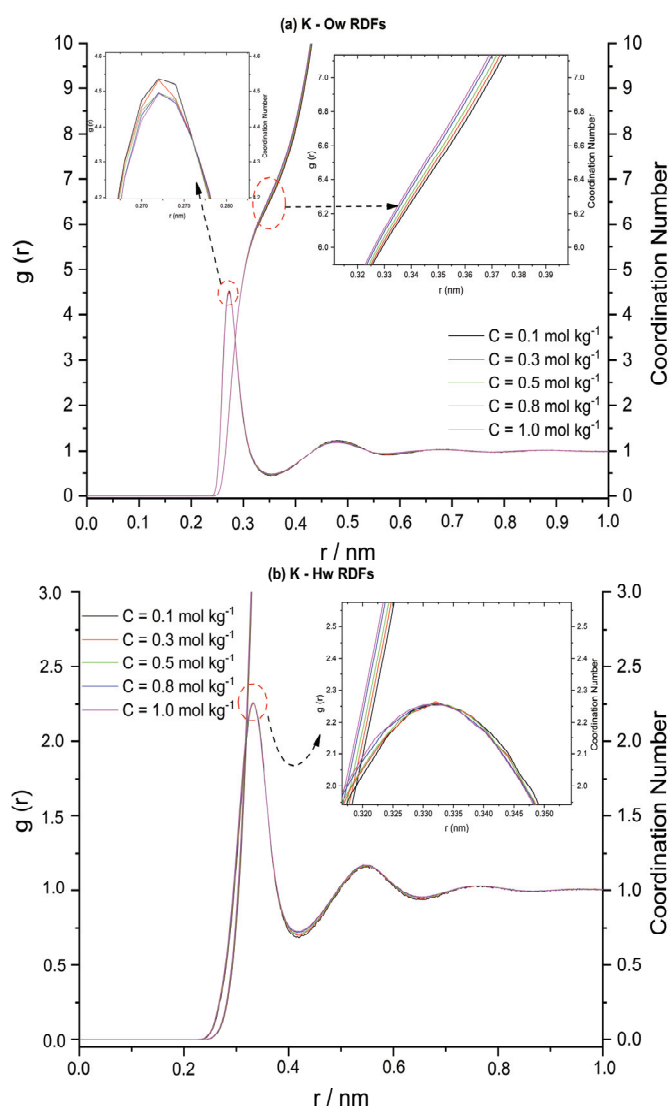
Fig. 1. $g_{K-Ow}(r)$ and $g_{K-Hw}(r)$ for potassium cation at various concentrations.
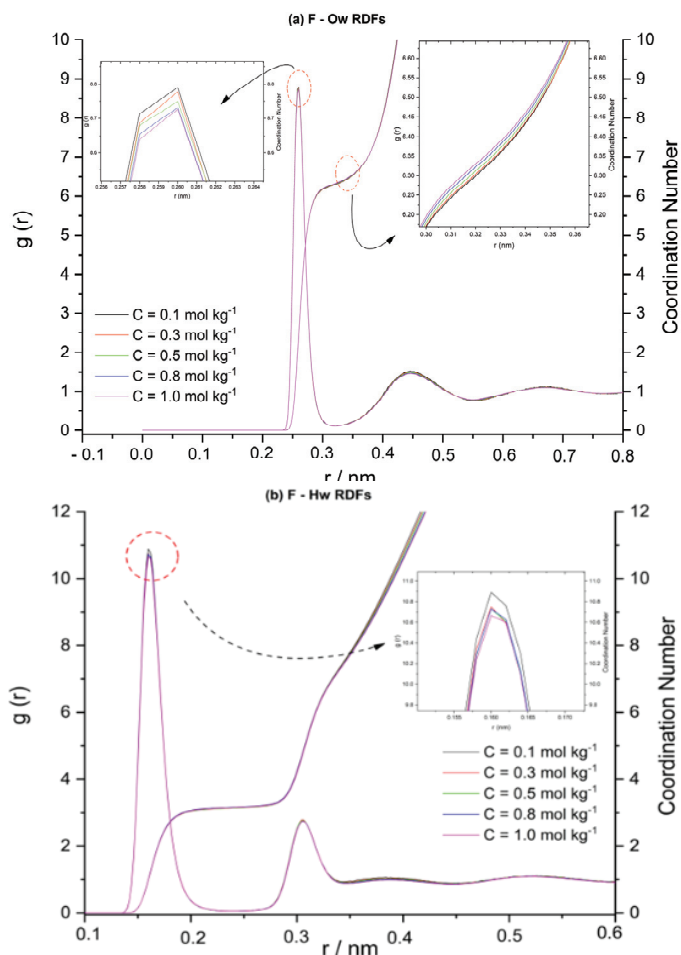
Fig. 2. $g_{F\text{-Ow}}(r)$ and $g_{F\text{-Hw}}(r)$ for fluoride anion at various concentrations.

The analysis of Fig. 2 demonstrates that the $g_{F–Hw}(r)$ function indicates the existence of two distinct peaks at distances of 0.160 and 0.305 nm, respectively. This suggests a double-layer hydration of the fluoride anion. Similarly, the $g_{F–Ow}(r)$ curve also exhibits two peaks. The first peak is observed at a distance of 0.260 nm, followed by the second one between 0.328 and 0.344 nm.

Moreover, the coordination numbers of potassium and fluoride ions increase in an almost linear with increasing concentrations. This suggests a disruption in ion-dipole interactions and an augmentation in ion–ion interactions. These coordination numbers range from 6.602 to 6.735 for K^+ and from 6.329 to 6.360 for F^-. This can be attributed to the significant difference in electronegativity between the ions, which amounts to $\Delta\eta = 3.16$ for this specific system. This difference will enable strong hydrogen bonding with H_2O molecules. Consequently,

the combined effects of $M^+ \cdots H_2O$ and $M \cdots H_2O$ interactions contribute to the dissociation of KF into its fundamental ions, which leads to increased levels of hydration for F^- and K^+, especially as concentrations rise.
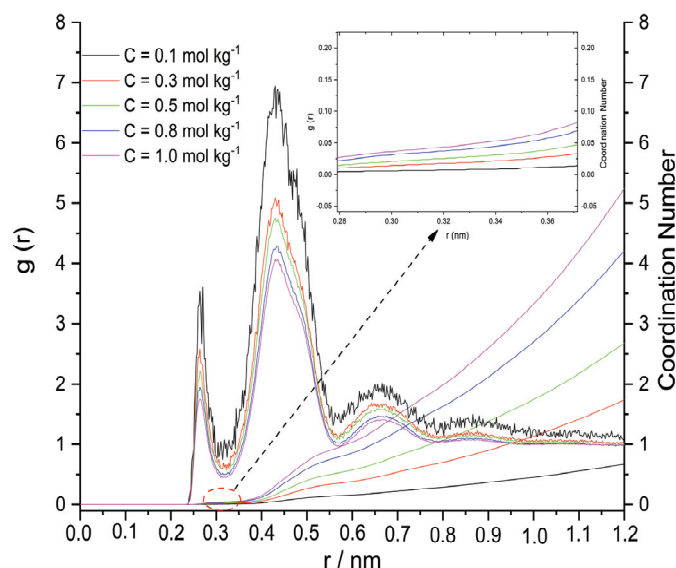
Fig. 3. Radial distribution functions $\{g_{K\text{-}F}(r)\}$ at various concentrations.

The analysis of Fig. 3 highlights the presence of four distinct groups of ion pairs. The first peak, observed at a distance of 0.264 nm, depicts ion pairs in contact (CIP). The existence of solvent-separated ion pairs (SIP) is confirmed by the second peak located at 0.428 nm. The double solvent-separated ion pairs (2SIP) are clearly identified by the third peak at a distance of 0.664 nm. Finally, free ions are represented by the last peak, which is less intense and covers a broader range of positions between 0.788 and 0.959 nm.

Moreover, the analysis of RDF variations reveals that as concentration increases, the presence of CIPs weakens, leading to a slight decrease in the coordination numbers (*CN*) of the K^+ and F^-. The strong intensity of CIPs underscores the significant binding energy between the two ions, owing to the high value of the electronegativity difference attributed to the fluoride ion.

In Fig. 4a, the increase in concentration brings forth noticeable microstructural effects in the aqueous $KF_{(aq)}$ system. The variation in the $g_{Ow-Ow}(r)$ functions demonstrates a decline in the peak intensities' maximum values. The analysis of this phenomenon signifies a considerable distortion in the structure due to intensified Ow–Ow interactions as the concentration rises. Consequently, there is a growing concentration of ions in the system, responsible for arranging water molecules regularly, thereby leading to modifications in the local structure.
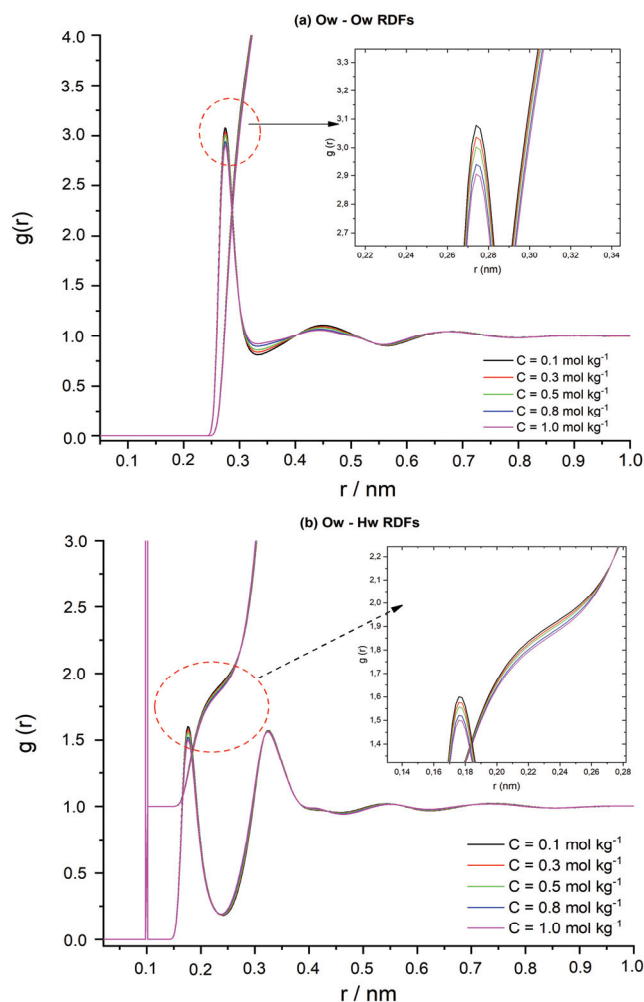
Fig. 4. $g_{Ow\text{-}Ow}(r)$ and $g_{Ow\text{-}Hw}(r)$ functions at various concentrations.

Moreover, Fig 4b illustrates the impact of concentration on the distribution of the hydrogen bond network. This is proved by the diminishing peak intensities as the concentration increases, indicating a reduction in the count of hydrogen bonds between Ow and Hw. This shift can be attributed to the strong competition between the highly electronegative fluoride anion and the oxygen atom. This competition leads to the breaking of the hydrogen bonds created by the solvent molecules (H_2O).

Dynamical and dielectric properties

Table III presents newly calculated data for the dielectric constant and self--diffusion coefficient specific to aqueous $KF_{(aq)}$ systems at various concentrat-

ions, using the molecular dynamics approach at T = 298.15 K. The analysis of Fig. 5 reveals a gradual reduction in self-diffusion coefficients as the concentration increases. Notably, this decrease is more pronounced for water molecules compared to ions, a phenomenon attributed to the stronger influence of Coulomb forces on ions.

TABLE III. Molecular dynamics results for the dielectric and dynamic properties of water molecules, ions and KF electrolyte at various concentrations

C / mol kg^{-1}	D_{KF}	D_{H_2O}	D_{K+}	D_{F-}	Dielectric constant (ε)	Exp. data
0.1	2.5048 ±0.0252	2.5100 ±0.0239	1.8857 ±0.1246	1.1589 ±0.5037	70.2847 ± 0.4007	–
0.3	2.3891 ±0.0317	2.4040 ±0.0253	1.7974 ±0.2715	0.8693 ±0.0112	68.3135 ± 0.3450	–
0.5	2.2808 ± 0.0199	2.3093 ±0.0265	1.5111 ±0.3044	0.8416 ±0.0072	65.3158 ±0.4313	D_{H_2O} = 2.30[46]
0.8	2.1763 ±0.0700	2.2236 ±0.0638	1.4416 ±0.3613	0.7639 ±0.0338	62.1923 ± 0.1745	–
1.0	2.0115 ±0.0130	2,0507 ±0.0399	1.2499 ±0.1183	0.6842 ±0.0466	60.0358 ±0.4034	D_{H_2O} = 2.14[46] ε = 60.8[47]
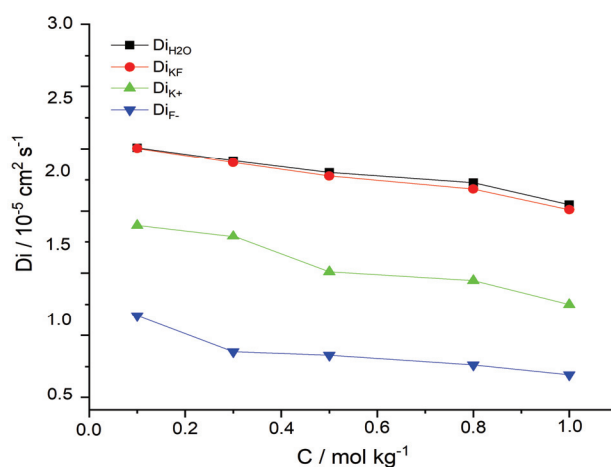
Fig. 5. Self-diffusion coefficients of both water molecules and ions within the aqueous KF system at different concentrations.

Fig. 6 illustrates that the dielectric constant values also display a decline with increasing concentration. This decrease is primarily attributed to the strength of the electric field created by the two ions (K$^+$ and F$^-$) within the aqueous solution, which weakens the polarization of the KF$_{(aq)}$ electrolytic system. Furthermore,

our results concerning the dielectric constant are in good agreement with other values from experimental data.[46,47]
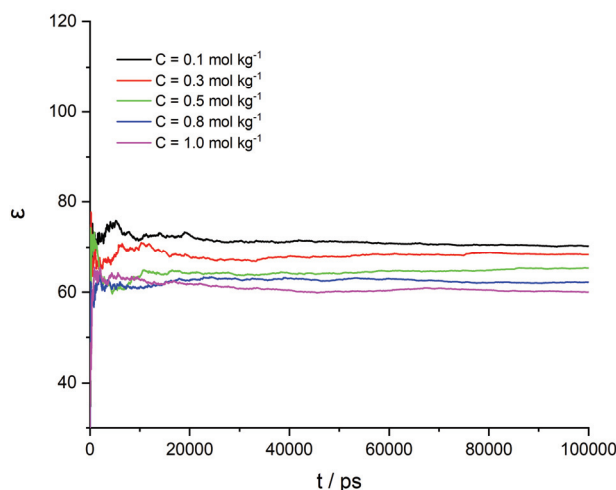
Fig. 6. Variations of the dielectric constant (ε) for the aqueous KF system as a function of simulation time at different concentrations.

CONCLUSION

In this study, we applied a molecular dynamics approach to investigate the structural, dynamical, and dielectric properties of the $KF_{(aq)}$ binary electrolyte system. The chosen method has proven highly effective for the examination of such materials in aqueous solutions. Through our molecular simulations, we gained valuable insights into the interactions between water molecules and ions (K^+, F^-), shedding light on the formation and stability of ion pairs and the intricate network of hydrogen bonds within the present aqueous electrolytic system.

Moreover, our investigation led to the determination of new simulation data regarding the self-diffusion coefficients and the dielectric constants across a broad range of concentrations, from infinite dilution to saturation, using the molecular dynamics approach. These results offer a comprehensive overview of the concentration-dependent effects on the mobility and the dielectric behaviour in potassium fluoride aqueous solutions. This knowledge significantly contributes to the understanding of the various mechanisms at play in this complex system.

Overall, this work represents a significant advancement in optimizing the use of KF electrolytes in numerous sectors, particularly within the realm of potassium-based rechargeable battery technology. The findings from our study gives the potential to enhance the efficiency and the performance of such electrolytes in industrial applications.

И З В О Д

ИСПИТИВАЊЕ СТРУКТУРНИХ, ДИНАМИЧКИХ И ДИЕЛЕКТРИЧНИХ СВОЈСТАВА ВОДЕНИХ РАСТВОРА КАЛИЈУМ-ФЛУОРИДА РАЗЛИЧИТИХ КОНЦЕНТРАЦИЈА ПОМОЋУ МОЛЕКУЛСКЕ ДИНАМИКЕ

AYOUB LAHMIDI, SANAA RABII, ABDELKBIR ERROUGUI, SAMIR CHTITA, MHAMMED EL KOUALI
и MOHAMMED TALBI

Laboratory of Analytical and Molecular Chemistry, Faculty of Sciences Ben M'Sick, Hassan II University of Casablanca, Morocco

Батерије које се заснивају на калијуму су обећавајућа алтернатива традицоналним литијум-јонским батеријама за системе за складиштење енергије услед њихове приступачности, широке доступности и хемијских карактеристика сличних литијуму. У овом раду примењене су симулације молекулске динамике да би се испитали физички феномени калијум флуорида у воденим растворима. Међуатомске интеракције су дефинисане применом OPLS-AA поља сила, док су SPC/E модел воде и јони представљени као наелектрисане Ленард–Џонсове честице. Симулације су урађене за опсег концентрација од 0,1 до 1,0 mol kg^{-1}. Резултати добијени у овом истраживању доприносе разумевању потенцијалне примене KF електролита у системима за складиштење енергије. Свеобухватно размевање утицаја концентрације KF електролита на структурне, динамичке и диелектричне особине је кључно за дизајн и оптимизацију калијум-јонских батерија, као и других електрохемијских уређаја који користе електролите засноване на KF. Ово истраживање доприноси текућим напорима усмереним ка развоју ефикасних и економски одрживих решења за складиштење енергије који превазилазе ограничења традиционалних литијум-јонских батерија.

(Примљено 6. новембра, ревидирано 23. децембра 2023, прихваћено 19. јануара 2024)

REFERENCES

1. A. Tomaszewska, Z. Chu, X. Feng, S. O'Kane, X. Liu, J. Chen, C. Ji, E. Endler, R. Li, L. Liu, Y. Li, S. Zheng, S. Vetterlein, M. Gao, J. Du, M. Parkes, M. Ouyang, M. Marinescu, G. Offer, B. Wu, *eTransportation* **1** (2019) 100011 (https://doi.org/10.1016/j.etran.2019.100011)
2. Y. Kim, W. M. Seong, A. Manthiram, *Energy Storage Mater.* **34** (2021) 250 (https://doi.org/10.1016/j.ensm.2020.09.020)
3. K. Beltrop, S. Beuker, A. Heckmann, M. Winter, T. Placke, *Energy Environ. Sci.* **10** (2017) 2090 (https://doi.org/10.1039/C7EE01535F)
4. X. Lin, J. Huang, H. Tan, J. Huang, B. Zhang, *Energy Storage Mater.* **16** (2019) 97 (https://doi.org/10.1016/j.ensm.2018.04.026)
5. H. Xu, H. Chen, C. Gao, *ACS Mater. Lett.* **3** (2021) 1221 (https://doi.org/10.1021/acsmaterialslett.1c00280)
6. R. Rajagopalan, Y. Tang, X. Ji, C. Jia, H. Wang, *Adv. Funct. Mater.* **30** (2020) 1909486 (https://doi.org/10.1002/adfm.201909486)
7. J.-Y. Hwang, S.-T. Myung, Y.-K. Sun, *Adv. Funct. Mater.* **28** (2018) 1802938 (https://doi.org/10.1002/adfm.201802938)
8. Y. Mekonnen, A. Sundararajan, A. I. Sarwat, in *Proceedings of SoutheastCon 2016*, 2016, pp. 1–6 (https://doi.org/10.1109/SECON.2016.7506639)

9. X. Zeng, M. Li, D. Abd El-Hady, W. Alshitari, A. S. Al-Bogami, J. Lu, K. Amine, *Adv. Energy Mater.* **9** (2019) 1900161 (https://doi.org/10.1002/aenm.201900161)
10. H. Vikström, S. Davidsson, M. Höök, *Appl. Energy* **110** (2013) 252 (https://doi.org/10.1016/j.apenergy.2013.04.005)
11. S. Ziemann, D. B. Müller, L. Schebek, M. Weil, *Resour. Conserv. Recycl.* **133** (2018) 76 (https://doi.org/10.1016/j.resconrec.2018.01.031)
12. R. T. Nguyen, R. G. Eggert, M. H. Severson, C. G. Anderson, *Resour. Conserv. Recycl.* **167** (2021) 105198 (https://doi.org/10.1016/j.resconrec.2020.105198)
13. G. Zubi, R. Dufo-López, M. Carvalho, G. Pasaoglu, *Renew. Sustain. Energy Rev.* **89** (2018) 292 (https://doi.org/10.1016/j.rser.2018.03.002)
14. J. Zhao, X. Zou, Y. Zhu, Y. Xu, C. Wang, *Adv. Funct. Mater.* **26** (2016) 8103 (https://doi.org/10.1002/adfm.201602248)
15. Y. Xu, C. Zhang, M. Zhou, Q. Fu, C. Zhao, M. Wu, Y. Lei, *Nat. Commun.* **9** (2018) 1720 (https://doi.org/10.1038/s41467-018-04190-z)
16. S. Zhang, Y. Liu, Q. Fan, C. Zhang, T. Zhou, K. Kalantar-Zadeh, Z. Guo, *Energy Environ. Sci.* **14** (2021) 4177 (https://doi.org/10.1039/D1EE00531F)
17. L. Jiang, Y. Lu, C. Zhao, L. Liu, J. Zhang, Q. Zhang, X. Shen, J. Zhao, X. Yu, H. Li, X. Huang, L. Chen, Y.-S. Hu, *Nat. Energy* **4** (2019) 495 (https://doi.org/10.1038/s41560-019-0388-0)
18. K. Kubota, M. Dahbi, T. Hosaka, S. Kumakura, S. Komaba, *Chem. Rec.* **18** (2018) 459 (https://doi.org/10.1002/tcr.201700057)
19. J. C. Pramudita, D. Sehrawat, D. Goonetilleke, N. Sharma, *Adv. Energy Mater.* **7** (2017) 1602911 (https://doi.org/10.1002/aenm.201602911)
20. Z. Jian, Y. Liang, I. A. Rodríguez-Pérez, Y. Yao, X. Ji, *Electrochem. Commun.* **71** (2016) 5 (https://doi.org/10.1016/j.elecom.2016.07.011)
21. M. Sajjad, F. Cheng, W. Lu, *RSC Adv.* **11** (2021) 25450 (https://doi.org/10.1039/D1RA02445K)
22. X. Lu, M. E. Bowden, V. L. Sprenkle, J. Liu, *Adv. Mater.* **27** (2015) 5915 (https://doi.org/10.1002/adma.201502343)
23. S. Liu, L. Kang, J. Henzie, J. Zhang, J. Ha, M. A. Amin, M. S. A. Hossain, S. C. Jun, Y. Yamauchi, *ACS Nano* **15** (2021) 18931 (https://doi.org/10.1021/acsnano.1c08428)
24. Y.-S. Xu, S.-Y. Duan, Y.-G. Sun, D.-S. Bin, X.-S. Tao, D. Zhang, Y. Liu, A.-M. Cao, L.-J. Wan, *J. Mater. Chem., A* **7** (2019) 4334 (https://doi.org/10.1039/C8TA10953B)
25. Y. Wu, Y. Sun, Y. Tong, X. Liu, J. Zheng, D. Han, H. Li, L. Niu, *Energy Storage Mater.* **41** (2021) 108 (https://doi.org/10.1016/j.ensm.2021.05.045)
26. A. Errougui, M. Talbi, M. Kouali, *E3S Web Confer.* **297** (2021) 01009 (https://doi.org/10.1051/e3sconf/202129701009)
27. T. Noël, Y. Cao, G. Laudadio, *Acc. Chem. Res.* **52** (2019) 2858 (https://doi.org/10.1021/acs.accounts.9b00412)
28. A. Errougui, M. Talbi, M. El Kouali, *Egypt. J. Chem.* **65** (2022) 1 (https://doi.org/10.21608/ejchem.2021.67302.3453)
29. A. Errougui, A. Lahmidi, S. Chtita, M. El Kouali, M. Talbi, *J. Solut. Chem.* **52** (2023) 176 (https://doi.org/10.1007/s10953-022-01222-7)
30. G. A. Kaminski, R. A. Friesner, J. Tirado-Rives, W. L. Jorgensen, *J. Phys. Chem., B* **105** (2001) 6474 (https://doi.org/10.1021/jp003919d)

31. M. J. Abraham, T. Murtola, R. Schulz, S. Páll, J. C. Smith, B. Hess, E. Lindahl, *SoftwareX* **1**–**2** (2015) 19 (https://doi.org/10.1016/j.softx.2015.06.001)
32. B. Hess, C. Kutzner, D. Van Der Spoel, E. Lindahl, *J. Chem. Theory Comput.* **4** (2008) 435 (https://doi.org/10.1021/ct700301q)
33. M. Parrinello, A. Rahman, *J. Appl. Phys.* **52** (1981) 7182 (https://doi.org/10.1063/1.328693)
34. S. Nosé, *Mol. Phys.* **52** (1984) 255 (https://doi.org/10.1080/00268978400101201)
35. W. G. Hoover, *Phys. Rev., A* **31** (1985) 1695 (https://doi.org/10.1103/PhysRevA.31.1695)
36. H. J. C. Berendsen, J. R. Grigera, T. P. Straatsma, *J. Phys. Chem.* **91** (1987) 6269 (https://doi.org/10.1021/j100308a038)
37. S. I. Sandler, & J. K. Wheatley, *Chem. Phys. Lett.* **10** (1971) 375 (https://doi.org/10.1016/0009-2614(71)80313-5)
38. C. J. Fennell, A. Bizjak, V. Vlachy, K. A. Dill, *J. Phys. Chem., B* **113** (2009) 6782 (https://doi.org/10.1021/jp809782z)
39. J. Zielkiewicz, *J. Chem. Phys.* **123** (2005) 104501 (https://doi.org/10.1063/1.2018637)
40. S. Reiser, S. Deublein, J. Vrabec, H. Hasse, *J. Chem. Phys.* **140** (2014) 044504 (https://doi.org/10.1063/1.4858392)
41. *Experimental Determination of Partial and Environmental Structure Functions in Non-crystalline Systems — Fundamental Aspects*. in *Anomalous X-Ray Scattering for Material Characterization: Atomic-Scale Structure Determination*, Y. Waseda, Ed., Springer, Berlin, 2002, pp. 9–20 (https://doi.org/10.1007/3-540-46008-X_2)
42. M. Guo, W. Wang, H. Lu, *Fluid Phase Equilib.* **60** (1990) 37 (https://doi.org/10.1016/0378-3812(90)85041-8)
43. X. Zhang, X. Liu, M. He, Y. Zhang, Y. Sun, X. Lu, *Fluid Phase Equilib.* **518** (2020) 112625 (https://doi.org/10.1016/j.fluid.2020.112625)
44. S. Deublein, J. Vrabec, H. Hasse, *J. Chem. Phys.* **136** (2012) 084501 (https://doi.org/10.1063/1.3687238)
45. Y. Laudernet, T. Cartailler, P. Turq, M. Ferrario, *J. Phys. Chem., B* **107** (2003) 2354 (https://doi.org/10.1021/jp0223814)
46. D. W. McCall, D. C. Douglass, *J. Phys. Chem.* **69** (1965) 2001 (https://doi.org/10.1021/j100890a034)
47. F. E. Harris, C. T. O'Konski, *J. Phys. Chem.* **61** (1957) 310 (https://doi.org/10.1021/j150549a009).

Modelling a cyclic staircase voltammetry of two electron transfers coupled by a chemical reaction on a rotating disk electrode[•]

MILIVOJ LOVRIĆ*

Divkovićeva 13, Zagreb 10090, Croatia

Abstract: Two electrode reactions that are coupled by a chemical reaction are called an ECE mechanism. The model of this mechanism which has an unstable intermediate is developed for staircase voltammetry on the rotating disk electrode. It is assumed that both electrode reactions are fast and reversible and that the chemical reaction may appear to be of the second order and reversible. The influence of the concentration of an electro-inactive component of the chemical reaction is investigated, and the conditions under which the reaction turns into the first order one, and becomes totally irreversible, are reported.

Keywords: an ECE mechanism; steady-state response; logarithmic analysis; kinetic currents.

INTRODUCTION

The electrochemical reactions of *p*-nitrosophenol,[1,2] adriamycin,[3] benzene-sulfonyl fluoride,[4,5] hexacyanochromate(III),[6] tocopherol,[7] methylcatechol[8,9] and dopamine[10] consist of two electron transfers that are coupled by a chemical reaction between the product of the first electrode reaction and the reactant of the second one.[11–13] The acronym of this mechanism is ECE and its theory is developed for both polarography[14–19] and voltammetry,[20–27] on either expanding or stationary planar and spherical electrodes. Depending on the difference between standard potentials of two electrode reactions, the response of ECE mechanism may consist of either two waves or a single wave.[28] This mechanism can be considered as a special case of multiple electron transfer reactions, with coupled chemical processes that are described by the extended schemes of squares.[29–32] Under the steady state conditions on the rotating disk electrodes the kinetics of chemical reaction in the ECE mechanism can be measured.[33–37] In this paper the

---

891

theory of ECE is extended to the general case of the unstable intermediate in cyclic staircase voltammetry on the rotating disk electrode.

MODEL

It is assumed that an electrolytic solution contains a dissolved reactant of the first electrode reaction and an electro-inactive substance Y that cannot react with the mentioned reactant. The first electron transfer is a fast and reversible electro-oxidation. Its product cannot participate in the second electron transfer, but it can react with the substance Y to produce a new electroactive compound G that can be oxidized to the final product H. The standard potentials of the first and the second electrode reactions are equal, or the one of the second reaction is lower. Hence, the second reactant G is oxidized at the same potentials as the initial reactant A. Both chemical reaction and the second electrode reaction are reversible in the chemical and electrochemical senses, respectively. The described mechanism can be represented by the following chemical equations:

$$\text{A} \leftrightarrows \text{B} + \text{e}^- \tag{1}$$
$$\text{B} + \text{Y} \leftrightarrows \text{G} \tag{2}$$
$$\text{G} \leftrightarrows \text{H} + \text{e}^- \tag{3}$$

On the rotating disk electrode the mass transfer and currents are defined by the following system of differential equations and the initial and boundary conditions:

$$\frac{\partial c_A}{\partial t} = D\frac{\partial^2 c_A}{\partial x^2} - v\frac{\partial c_A}{\partial x} \tag{4}$$

$$\frac{\partial c_B}{\partial t} = D\frac{\partial^2 c_B}{\partial x^2} - v\frac{\partial c_B}{\partial x} - k_f c_B c_Y + k_b c_G \tag{5}$$

$$\frac{\partial c_Y}{\partial t} = D\frac{\partial^2 c_Y}{\partial x^2} - v\frac{\partial c_Y}{\partial x} - k_f c_B c_Y + k_b c_G \tag{6}$$

$$\frac{\partial c_G}{\partial t} = D\frac{\partial^2 c_G}{\partial x^2} - v\frac{\partial c_G}{\partial x} + k_f c_B c_Y - k_b c_G \tag{7}$$

$$\frac{\partial c_H}{\partial t} = D\frac{\partial^2 c_H}{\partial x^2} - v\frac{\partial c_H}{\partial x} \tag{8}$$

$$t = 0, x \geq 0 : c_A = c_A^*, c_B = 0, c_Y = c_Y^*, c_G = 0, c_H = 0 \tag{9}$$

$$t > 0, x \rightarrow \infty : c_A \rightarrow c_A^*, c_B \rightarrow 0, c_Y \rightarrow c_Y^*, c_G \rightarrow 0, c_H \rightarrow 0 \tag{10}$$

$$x = 0 : c_{B,x=0} = c_{A,x=0}\exp(F(E - E_1^0)/RT) \tag{11}$$

$$c_{H,x=0} = c_{G,x=0}\exp(F(E - E_2^0)/RT) \tag{12}$$

$$D(\frac{\partial c_A}{\partial x})_{x=0} = \frac{I_1}{FS} \tag{13}$$

$$D(\frac{\partial c_B}{\partial x})_{x=0} = -\frac{I_1}{FS} \tag{14}$$

$$D(\frac{\partial c_Y}{\partial x})_{x=0} = 0 \tag{15}$$

$$D(\frac{\partial c_G}{\partial x})_{x=0} = \frac{I_2}{FS} \tag{16}$$

$$D(\frac{\partial c_{\mathrm{H}}}{\partial x})_{x=0} = -\frac{I_2}{FS} \tag{17}$$

$$v = -0.510\omega^{3/2}\nu^{-1/2}x^2 \tag{18}$$

$$K = \frac{k_{\mathrm{f}}}{k_{\mathrm{b}}} \tag{19}$$

The meanings of all symbols are reported in Table I.

TABLE 1. The meanings of symbols

Symbol	Meaning
c_Z	Concentration of species Z
$c_{\mathrm{A}}^*, c_{\mathrm{Y}}^*$	Bulk concentrations of species A and Y
D	Diffusion coefficient
δ	Diffusion layer thickness
ΔE	Potential increment
Δt	Time increment
Δx	Space increment
E	Potential
E_1^0, E_2^0	Standard potentials
F	Faraday constant
I_1, I_2	Currents
ν	Kinematic viscosity
$k_{\mathrm{f}}, k_{\mathrm{b}}$	Rate constants of chemical reaction
K	Equilibrium constant of chemical reaction
ω	Rotation rate
R	Gas constant
S	Electrode surface area
t	Time
T	Temperature
τ	Step duration
v	Flow rate of solution

The Eqs. (4)–(8) were solved by the finite difference method.[38] The current was calculated for the staircase cyclic voltammetry. The dimensionless current is defined by the following equations:

$$\Phi = (I_1 + I_2)\delta_{\mathrm{SS}} / FSc_A^*D \tag{20}$$

$$\delta_{\mathrm{SS}} = 1.61D^{1/3}\nu^{1/6}\omega^{-1/2} \tag{21}$$

The following parameters were not changed: $D = 10^{-5}$ cm²/s, $\nu = 10^{-2}$ cm²/s, $\Delta t = 10^{-5}$ s, $D\Delta t/\Delta x^2 = 0.2$, $\Delta E = 1$ mV and $\tau = 10$ ms.

RESULTS AND DISCUSSION

An ECE mechanism can be recognized by performing the electrochemical experiments in the absence and the presence of the electro-inactive compound Y if it is possible. An imaginary response is presented in Fig. 1 for the reversible and

A)

B)
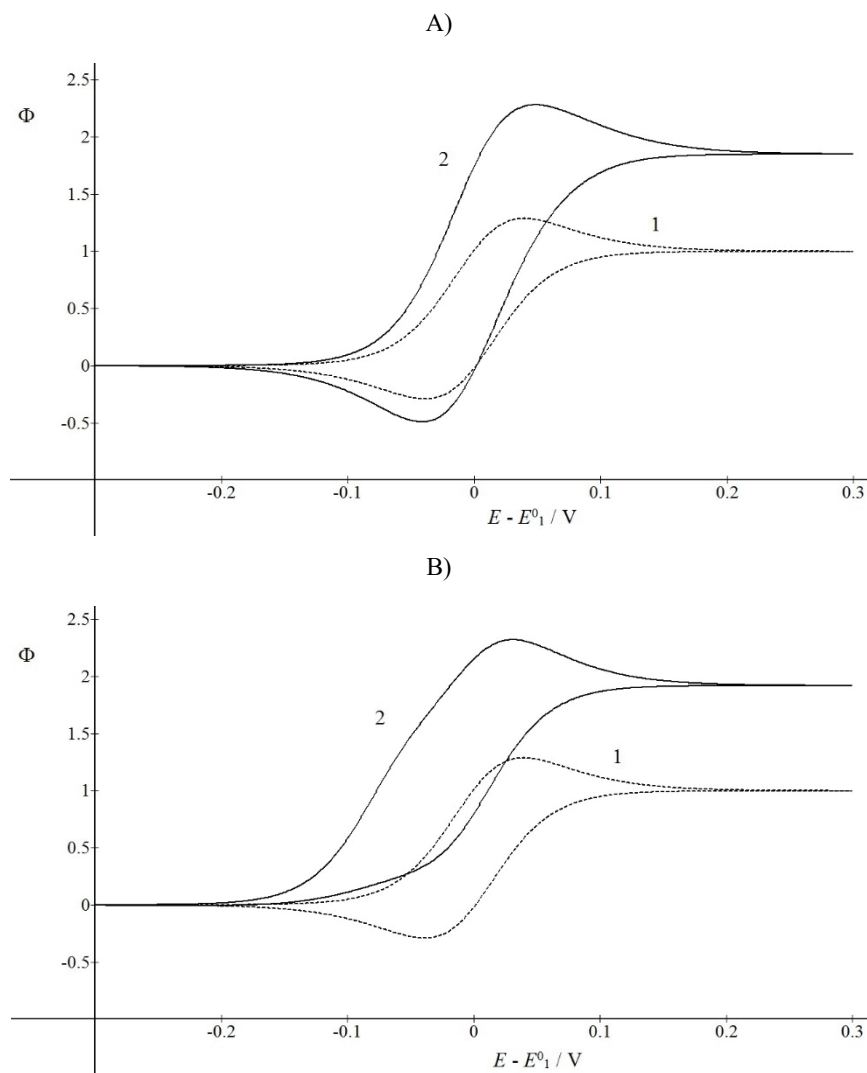
Fig. 1. Dimensionless cyclic staircase voltammograms of the ECE mechanism on the rotating disk electrode. $E_1^0 = E_2^0$, $D = 10^{-5}$ cm²/s, $\nu = 10^{-2}$ cm²/s, $\Delta t = 10^{-5}$ s, $D\Delta t/\Delta x^2 = 0.2$, $\Delta E = 1$ mV and $\tau = 10$ ms, $\omega = 4\pi$ rad/s, $k_f c_A^* = 10^3$ s⁻¹, $Kc_A^* = 1$ (A) and 10^3 (B) and $c_Y^* / c_A^* = 0$ (1) and 1 (2).

irreversible chemical reactions. It is also assumed that the standard potentials of the first and the second electrode reactions are equal and that both reactions are electrochemically reversible, as well as that the rotation rate of the disk electrode is rather low. In the absence of Y the voltammogram is characterised by the limiting current that is determined by the single electron transfer and the concentration of the initial reactant A (see Eq. (20)). Dimensionless peak currents ($\Phi_{p,ox}$

= 1.29 and $\Phi_{p,red}$ = –0.29) appear at 0.039 V and –0.039 V $vs.$ E_1^0, respectively. If the bulk concentrations of A and Y are equal, the dimensionless limiting current increases to 1.74, which can be explained by the increasing number of exchanged electrons, and the peak currents depend on the dimensionless equilibrium constant Kc_A^*. The chemical reaction is reversible if $Kc_A^* = 1$ and irreversible if $Kc_A^* = 10^3$. In the first case, the peak currents of the oxidation and reduction are equal to 2.28 and –0.49, respectively, and the peak potentials are 0.048 V and –0.042 V $vs.$ E_1^0. The rate of chemical reaction depends on the product $k_f c_A^*$ and the value assumed in Fig. 1 corresponds to a rather fast reaction that can transform the second reactant G into the first product B, in the reverse branch of the voltammogram. This is the origin of the reduction peak at –0.042 V. However, if $Kc_A^* = 10^3$ the backward rate constant of the chemical reaction is very small and the second voltammogram in Fig. 1B exhibits the oxidation peak at 0.031 V, but there is no reduction peak in the reverse branch. This form of the response is the indication of an irreversible chemical reaction in the ECE mechanism.

Fig. 2 shows the voltammograms influenced by the decreasing stability of the intermediate G. If $E_2^0 - E_1^0$ = –0.1 V, the second reactant G is oxidized at the electrode surface as soon as it is produced by the chemical reaction, and the response shows some characteristics of the concerted transfer of two electrons. Comparing to the curve 1, the oxidative maximum is higher and the reductive minimum is deeper, while the peak separation decreases from 90 to 67 mV and the median of peak potentials of curve 2 is –0.043 V $vs.$ E_1^0, which is close to $(E_2^0 + E_1^0)/2$ that is predicted for infinitely fast chemical reaction.[39] However
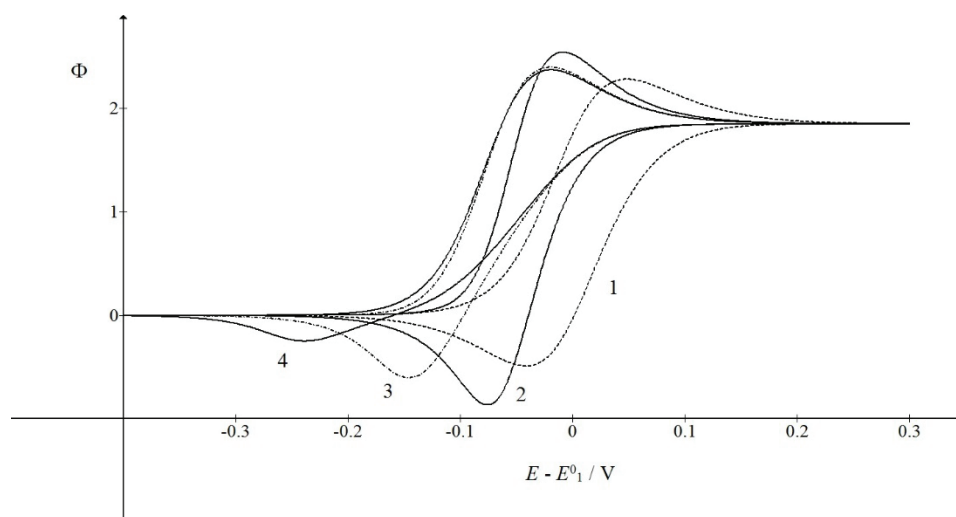
Fig. 2. Dependence of the ECE response on the second standard potential. $Kc_A^* = 1$, $c_Y^* = c_A^*$ and $(E_2^0 - E_1^0)/\text{V} = 0$ (1), –0.1 (2), –0.2 (3) and –0.3 (4). All other parameters are as in Fig. 1.

the further decreasing of the difference $E_2^0 - E_1^0$ causes the diminishing of the reductive peak in the reverse branch of the voltammograms. Although the medians of peak potentials of curves 3 and 4 are –0.083 and –0.130 V, the peak separation increases to 126 and 220 mV, respectively. This is caused by the diffusion of the final product during the reverse scan, as can be seen in Fig. 3. Depending on the second standard potential, the peak potential of reduction of H is lower than –0.042 V, and more time is needed to reach it. During this time the concentration of H near the electrode surface is diminished and lower current is obtained by its reduction. This is another reason why the ECE may appear irreversible.
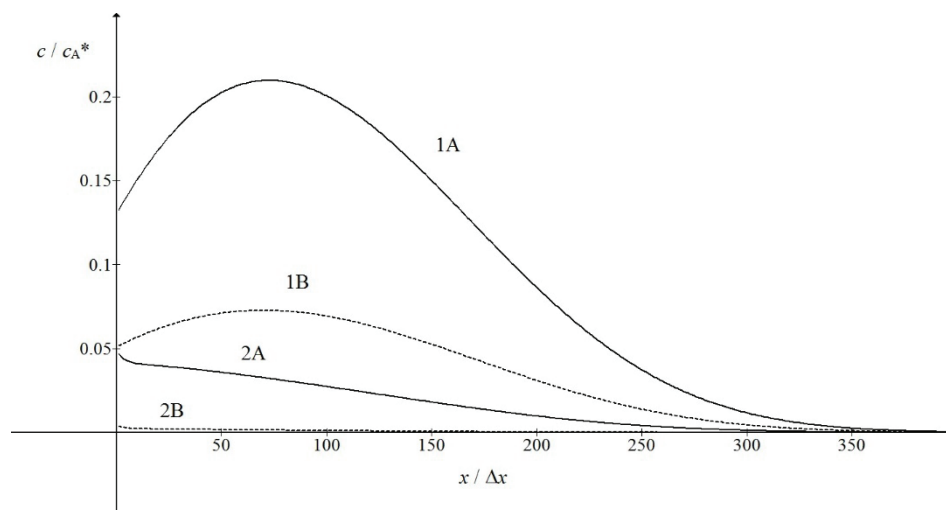
Fig. 3. Dimensionless concentrations of the final product H (1) and the second reactant G (2) during the reverse scan in cyclic voltammetry at –0.076 V (A) and –0.239 V (B). $(E_2^0 - E_1^0)$ / V = –0.1 (A) and –0.3 (B). All other parameters are as in Fig. 2.

Under the influence of the increasing rotation rate, the maximum and minimum of the voltammogram of ECE mechanism gradually vanish and the response acquires the form of polarographic wave. This is shown in Fig. 4. The half--wave potential of the oxidative branch of polarogram is –0.003 V *vs.* E_1^0 and the one of the reductive reverse branch is 0.003 V. This difference appears because the calculated response corresponds to the near steady-state conditions. At lower scan rates the two branches are overlapped and $E_{1/2} - E_1^0 = 0$ V for equal diffusion coefficients. The limiting current of polarogram is lower than the limiting current of voltammogram, because the reactants spend more time near the electrode surface if the rotation rate is lower. Hence, the chemical reaction appears faster at lower rotation rate.

Fig 5 describes the logarithmic analyses of the oxidative branches of steady state voltammograms that correspond to various standard potentials of the second

electrode reaction. If $E_2^0 = E_1^0$ and chemical reaction is reversible this function is a straight line with the slope of the inverse function $\Delta(E - E_1^0)/\Delta\log(\Phi/(\Phi_{\lim} - \Phi)) = 0.062$ V and $E_{1/2} - E_1^0 = -0.003$ V. So, the two parallel single electron transfers appear as a simple one electron wave. If $E_2^0 - E_1^0 = -0.1$ V this analysis is a curve with two parallel asymptotes and a steeper middle part. The inverse slope in the middle is 0.044 V and the one of asymptotes is 0.062 V. This is in the agreement with the theory of a simple EE mechanism with an unstable intermediate.[39] The half-wave potential is –0.041 V, which is close to the medium value of the peak potentials of curve 2 in Fig. 2. The half-wave potentials of the curves 3 and 4 in Fig. 5A are –0.054 and –0.055 V, respectively. This is similar to the potentials of maxima of curves 3 and 4 in Fig. 2, which are –0.020 and –0.019 V, respectively. This shows that the oxidation of the second reactant G can start only after the first reactant A is oxidized, regardless of the standard potential of the second electrode reaction.
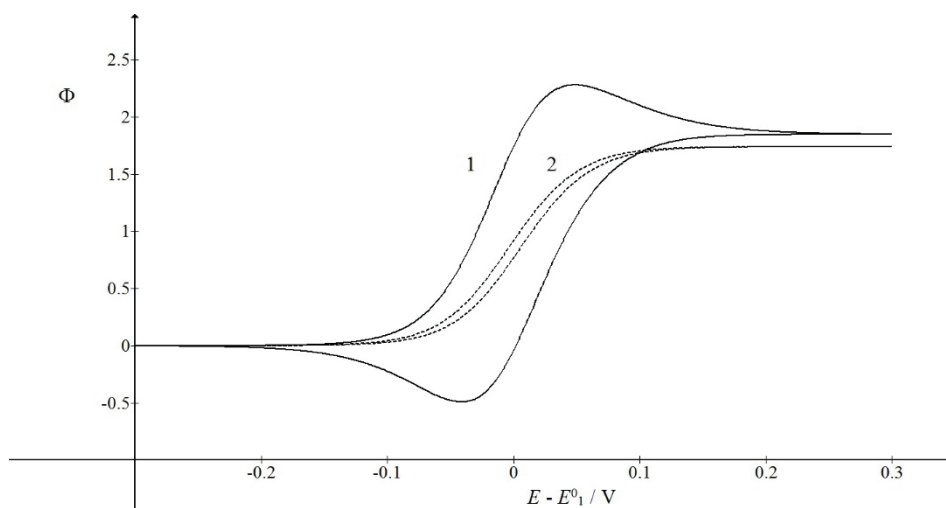
Fig. 4. Influence of the electrode rotation rate on the ECE responses. $E_2^0 = E_1^0$ and $\omega/$ rad s$^{-1} = 4\pi$ (1) and 40π (2). All other parameters are as in Fig. 2.

The logarithmic analyses of the ECE waves that are influenced by the irreversible chemical reaction are shown in Fig. 5B. If both standard potentials are equal, the slope in the middle is lower than the slopes of the asymptotes and the half-wave potential is –0.030 V *vs.* E_1^0. The chemical reaction is consuming the first product B, and the whole ECE response appears at lower potential. Also, a small separation of the two electron transfers can be noted. If $E_2^0 - E_1^0 = -0.1$ V the logarithmic analysis acquires a regular form and the half-wave potential i –0.060 V. This is because the mechanism becomes irreversible.

A)

B)
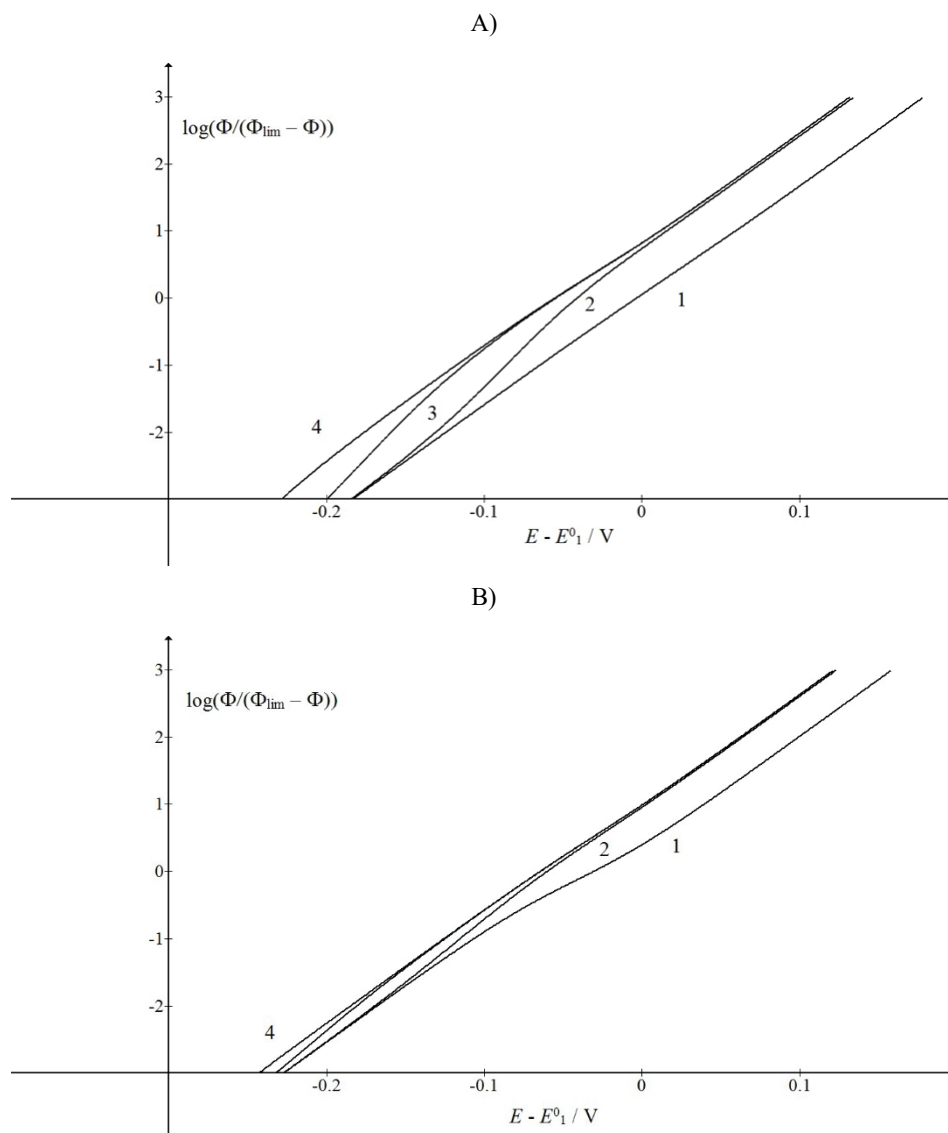
Fig. 5. Influence of the second standard potential on the logarithmic analyses of the ECE responses at high rotation rate. $Kc_A^* = 1$ (A) and 10^3 (B), $\omega = 40\pi$ rad/s and $(E_2^0 - E_1^0)$ / V = 0 (1), –0.1 (2), –0.2 (3) and –0.3 (4). All other parameters are as in Fig. 2.

Fig. 6 shows the dependence of the dimensionless limiting currents of the waves on the logarithm of the product of the forward rate constant and the bulk concentration of the compound Y. This product can be achieved either by the variation of the product $k_f c_A^*$, keeping the ratio $c_Y^* / c_A^* = 1$, or by the variation of the ratio c_Y^* / c_A^*, keeping the product $k_f c_A^* = 1$ s^{-1}. Note that log($k_f c_Y^*$) =
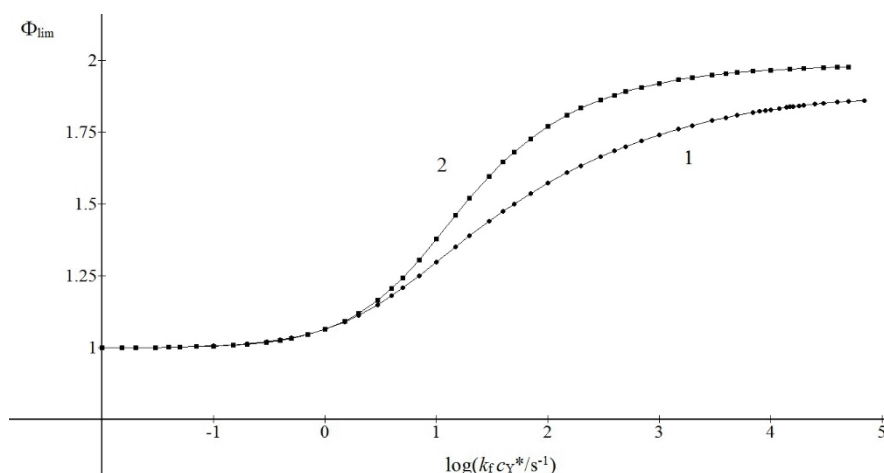
Fig. 6. Relationship between limiting currents of the ECE responses and the logarithm of the product $k_f c_Y^*$. $E_2^0 = E_1^0$, $Kc_A^* = 1$, $\omega = 40\pi$ rad/s and $c_Y^* = c_A^*$ (1) and $k_f c_A^* = 1$ s^{-1} (2). All other parameters are as in Fig. 1.

$\log(k_f c_A^*)$ + $\log(c_Y^* / c_A^*)$. The results of these two procedures are not equal because of the diffusion of Y. Experimentally, these procedures can be performed if the concentrations of A and Y can be changed independently. If the bulk concentration of Y is fixed, then the product $k_f c_Y^*$ is also fixed and the kinetics of the ECE mechanism can be changed only by the variation of the rotation rate of electrode. In this research it is assumed that the concentration of Y can be changed. The basic difference between compounds A and Y is that the currents of both electrode reactions depend on the concentration of the first reactant A, but not on the concentration of compound Y. The latter is determining the forward rate of chemical reaction only. If the ratio c_Y^* / c_A^* is low, the chemical reaction consumes Y, regardless of the bulk concentration of A. The higher is c_A^*, the higher are currents and more Y is consumed. The change of Y concentration can be neglected only if the ratio c_Y^* / c_A^* is very high. Fig. 6 shows that for $c_Y^* = c_A^*$ the variation of reactant A concentration causes the increasing of limiting current to $\Phi_{lim} = 1.50$ if $k_f c_Y^* = 50$ s^{-1} and that this current increases to 1.86 if $k_f c_Y^* = 6\times10^4$ s^{-1}. For $k_f c_A^* = 1$ s^{-1} the variation of Y concentration results in $\Phi_{lim} = 1.52$ if $k_f c_A^* = 20$ s^{-1} and $\Phi_{lim} = 1.98$ if $k_f c_Y^* = 5\times10^4$ s^{-1}. Fig. 7 shows that the ratio of concentrations of Y and A influences the form of the ECE responses. The corresponding half-wave potentials are shown in Fig. 8. If $c_Y^* = c_A^*$ the wave looks like a single electron polarogram and its $E_{1/2}$ changes from –4 to –1 mV. If $c_Y^* / c_A^* = 5\times10^4$ and $k_f c_A^* = 1$ s^{-1}, the response consists of two poorly separated waves and the half-wave potential is –0.054 V *vs.* E_1^0. Within the interval $1 < \log(k_f c_Y^*) < 3$ there is a linear relationship:

$$E_{1/2} - E_1^0 = -0.016\log(k_f c_Y^*) + 0.012 \text{ V} \qquad (22)$$
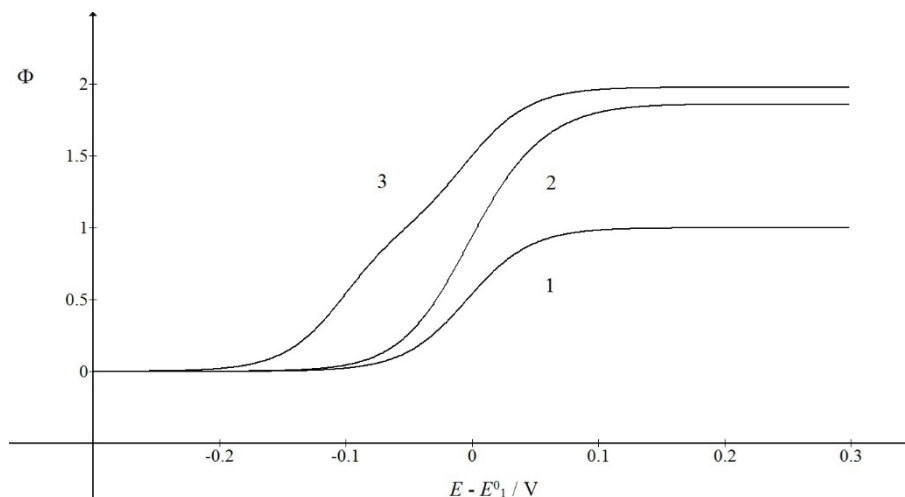
Fig. 7. Polarograms of the ECE mechanism; $k_f c_A^*$ / s^{-1} = 0 (1), 6×10^4 (2) and 1 (3) and c_Y^* / c_A^* = 0 (1), 1 (2) and 5×10^4 (3). All other parameters are as in Fig. 6.
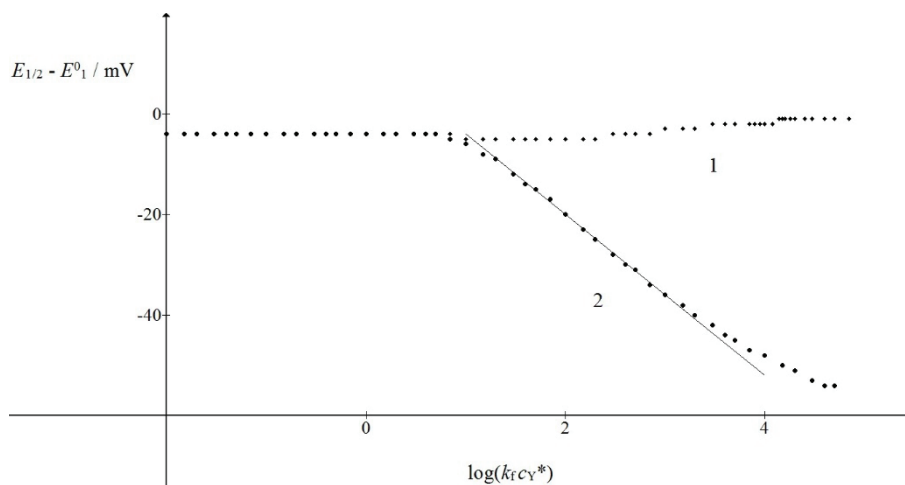
Fig. 8. Half-wave potentials of the ECE mechanism with reversible chemical reaction; $c_Y^* = c_A^*$ (1) and $k_f c_A^* = 1$ s^{-1} (2). The straight line is defined by Eq. (22). All other parameters are as in Fig. 6.

The bulk concentration of Y influences only the forward rate of the chemical reaction, making the latter irreversible. This could mean that the responses corresponding to high values of the dimensionless equilibrium constant do not depend on the concentration of the compound Y. In Fig. 9 it is shown that this hypothesis is not true. The limiting currents are marked by 1 in Fig. 9A and were cal-

A)

B)
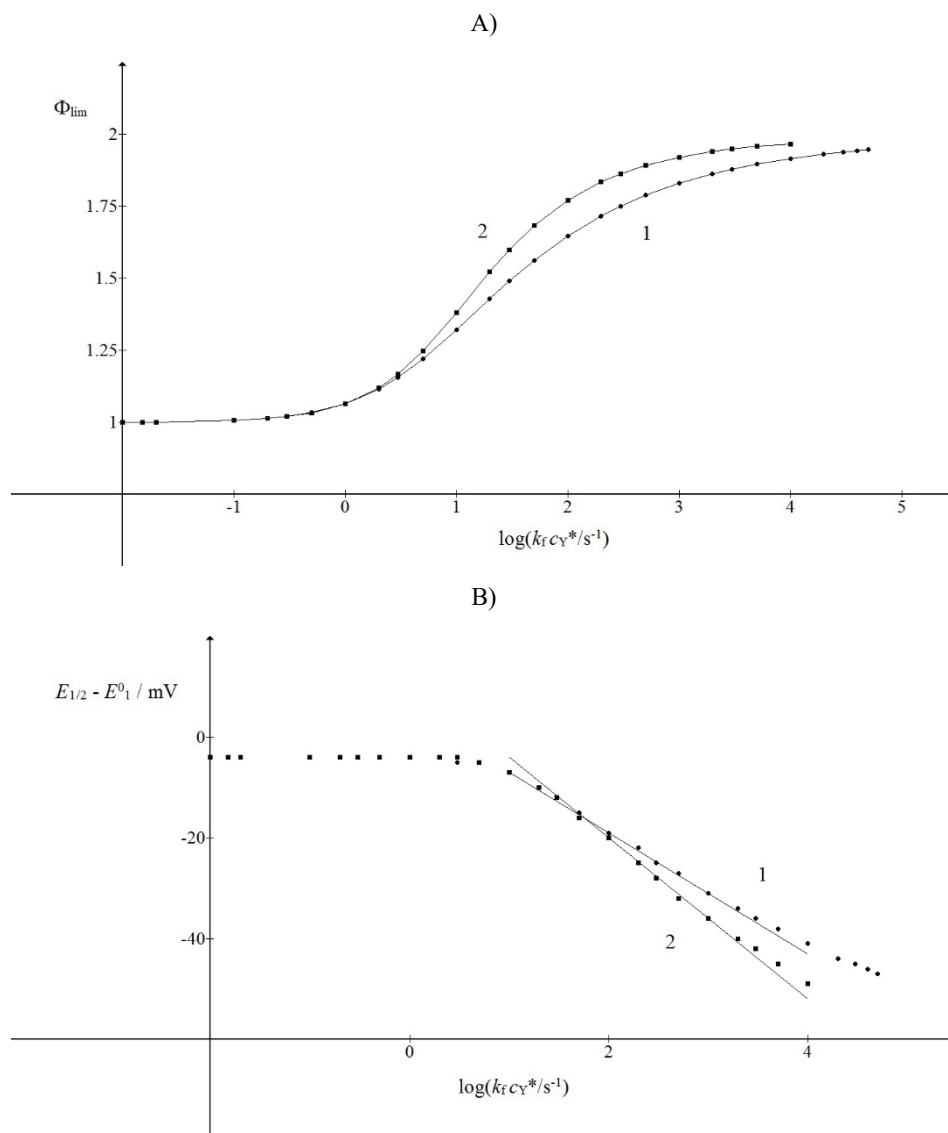
Fig. 9. The dependence of limiting currents (A) and half-wave potentials (B) of the ECE responses on the logarithm of the product $k_f c_Y^*$. $Kc_A^* = 10^3$ and $c_Y^* = c_A^*$ (1) and $k_f c_A^* = 1$ s^{-1} (2). The straight lines 1 and 2 are defined by Eqs. (23) and (22), respectively. All other parameters are as in Fig. 6.

ulated by the variation of the product $k_f c_A^*$, assuming that $Kc_A^* = 10^3$ and $c_Y^* / c_A^* = 1$. The same results were obtained for $Kc_A^* = 10^4$, which means that the responses in Fig. 9 correspond to totally the irreversible chemical reaction. These kinetic currents are characterized by $\Phi_{lim} = 1.56$ if $k_f c_Y^* = 50$ s^{-1} and $\Phi_{lim} = 1.95$

if $k_f c_Y^* = 5 \times 10^4$ s^{-1}. These values are higher than those shown by curve 1 in Fig. 6, but they are lower than the limiting currents calculated by the variation of c_Y^* / c_A^* ratio keeping $k_f c_A^* = 1$ s^{-1} and $K c_A^* = 10^3$. These currents are shown by curve 2 in Fig. 9A. They are marked by $\Phi_{lim} = 1.52$ if $k_f c_Y^* = 20$ s^{-1} and $\Phi_{lim} = 1.97$ if $k_f c_Y^* = 10^4$ s^{-1}. These values are identical to the curve 2 in Fig. 6. So, again, it can be concluded that the effect of chemical reaction is the highest if the diffusion of compound Y can be neglected, and the chemical reaction is totally irreversible. In the simulation these conditions can be fulfilled if $c_Y = c_Y^*$ and $k_b = 0$. The results of such simulation are reported in Table II, and compared with the curve 2 in Fig. 9A. A small difference can be seen within the interval $1 < k_f c_Y^* < 100$. This means that the assumption $c_Y = c_Y^*$ is justified if $c_Y^* / c_A^* > 100$. The half-wave potentials of the irreversible ECE mechanisms are shown in Fig. 9B. They can be approximated by the straight lines in the interval $1 < \log(k_f c_Y^*) < 3$. The line 1 in Fig. 9B is defined by the following equation:

$$E_{1/2} - E_1^0 = -0.012\log(k_f c_Y^*) + 0.005 \text{ V} \qquad (23)$$

The line 2 in this figure is defined by Eq. (22).

TABLE II. Limiting currents of the ECE waves influenced by the first order and the second order chemical reactions

$\log(k_f c_Y^*)$	Φ_{lim} ($c_Y = c_Y^*$)	Φ_{lim} (Fig. 9A)
0	1.068	1.064
0.3	1.126	1.120
0.48	1.175	1.168
0.7	1.255	1.247
1	1.388	1.381
1.3	1.527	1.523
1.48	1.602	1.599
1.7	1.684	1.682
2	1.771	1.771

CONCLUSIONS

The ECE mechanism which consists of the two electrochemically reversible electrode reactions that are linked by a chemical reaction of the primary product B and the compound Y depends on the stability of the intermediate G. If the two waves appear, the limiting current of the second one depends on the kinetics of chemical reaction, and the rate constant can be estimated under certain conditions.[37] In this paper the two electro-oxidations with equal standard potentials were investigated. It is shown that the response is a single wave and that the limiting current depends on the kinetics of chemical reaction and its stability constant. The mechanism appears irreversible if the second standard potential is lower than the first one and also if the stability constant is high and the concen-

tration of the compound Y is much higher than the concentration of the initial reactant. The second order reaction depends on the diffusion of Y, but this can be neglected at very high concentrations and the reaction becomes to be the first order and totally irreversible. Under these conditions the mechanism is independent of the stability constant.

ИЗВОД

МОДЕЛОВАЊЕ ВОЛТАМЕТРИЈЕ СА ПРАВОУГАОНИМ ТАЛАСИМА ЗА ДВОЕЛЕКТРОНСКУ ИЗМЕНУ СПРЕГНУТУ СА ХЕМИЈСКОМ РЕАКЦИЈОМ НА РОТИРАЈУЋОЈ ДИСК ЕЛЕКТРОДИ

MILIVOJ LOVRIĆ

Divkovićeva 13, Zagreb 10090, Croatia

Електрохемијска реакција двоелектронске измене спрегнута са хемијском реакцијом се назива ECE механизам. У овом истраживању је развијен модел волтаметрије са правоугаоним таласима на ротирајућој диск електроди, који укључује нестабилан интермедијар. Претпостављено је да су оба електрохемијска ступња брза и реверзибилна и да је хемијски ступањ реверзибилна реакција другог реда. Испитиван је утицај концентрације електрохемијски неактивне компоненте у хемијском ступњу и одређени су услови под којима тај ступањ постаје иреверзибилан и првог реда.

(Примљено 23. новембра 2023, ревидирано 12. јануара, прихваћено 1. марта 2024)

REFERENCES

1. R. S. Nicholson, I. Shain, *Anal. Chem*. **37** (1965) 190 (https://doi.org/10.1021/ac60221a003)
2. G. S. Alberts, I. Shain, *Anal. Chem*. **35** (1963) 1859 (https://doi.org/10.1021/ac60205a019)
3. Š. Komorsky-Lovrić, M. Lovrić, *Collect. Czech. Chem. Commun*. **72** (2007) 1398 (https://doi.org/10.1135/cccc20071398)
4. P. Sanecki, K. Kaczmarski, *J. Electroanal. Chem*. **471** (1999) 14 (https://doi.org/10.1016/S0022-0728(99)00243-0)
5. P. Sanecki, P. Skital, K. Kaczmarski, *Electroanalysis* **18** (2006) 981 (https://doi.org/10.1002/elan.200603487)
6. S. W. Feldberg, Lj. Jeftić, *J. Phys. Chem*. **76** (1972) 2439 (https://doi.org/10.1021/j100661a017)
7. G. J. Wilson, C. Y. Lin, R. D. Webster, *J. Phys. Chem., B* **110** (2006) 11540 (https://doi.org/10.1021/jp0604802)
8. R. N. Adams, M. D. Hawley, S. W. Feldberg, *J. Phys. Chem*. **71** (1967) 851 (https://doi.org/10.1021/j100863a011)
9. D. Nematollahi, S. M. Golabi, *J. Electroanal. Chem*. **481** (2000) 208 (https://doi.org/10.1016/S0022-0728(99)00500-8)
10. Y. Li, M. Liu, C. Xiang, Q. Xie, S. Yao, *Thin Solid Films* **497** (2006) 270 (https://doi.org/10.1016/j.tsf.2005.10.048)
11. P. T. Sanecki, C. Amatore, P. M. Skital, *J. Electroanal. Chem*. **546** (2003) 109 ()https://doi.org/10.1016/S0022-0728(03)00138-4

12. P. T. Sanecki, P. M. Skital, *Electrochim. Acta* **53** (2008) 7711 (https://doi.org/10.1016/j.electacta.2008.05.023)
13. R. Gulaboski, V. Mirčeski, I. Bogeski, M. Hoth, *J. Solid State Electrochem*. **16** (2012) 2315 (https://doi.org/10.1007/s10008-011-1397-5)
14. S. O. Engblom, J. C. Myland, K. B. Oldham, *Anal. Chem*. **66** (1994) 3182 (https://doi.org/10.1021/ac00091a029)
15. M. D. Hawley, S. W. Feldberg, *J. Phys. Chem*. **70** (1966) 3459 (https://doi.org/10.1021/j100883a015)
16. C. Amatore, J. M. Saveant, *J. Electroanal. Chem*. **86** (1978) 227 (https://doi.org/10.1016/S0022-0728(78)80371-4)
17. J. Galvez, A. Molina, R. Saura, F. Martinez, *J. Electroanal. Chem*. **127** (1981) 17 (https://doi.org/10.1016/S0022-0728(81)80464-0)
18. B. Kastening, *Anal. Chem*. **41** (1969) 1142 (https://doi.org/10.1021/ac60277a016)
19. H. R. Sobel, D. E. Smith, *J. Electroanal. Chem*. **26** (1970) 271 (https://doi.org/10.1016/S0022-0728(70)80310-2)
20. M. Mastragostino, L. Nadjo, J. M. Saveant, *Electrochim. Acta* **13** (1968) 721 (https://doi.org/10.1016/0013-4686(68)85007-8)
21. C. Amatore, J. M. Saveant, *J. Electroanal. Chem*. **85** (1977) 27 (https://doi.org/10.1016/S0022-0728(77)80150-2)
22. R. S. Nicholson, I. Shain, *Anal. Chem*. **37** (1965) 178 (https://doi.org/10.1021/ac60221a002)
23. M. A. Mann, J. C. Helfrick Jr, L. A. Bottomley, *J. Electrochem. Soc*. **163** (2016) H3101 (http://dx.doi.org/10.1149/2.0151604jes)
24. A. B. Miles, R. G. Compton, *J. Electroanal. Chem*. **499** (2001) 1 (https://doi.org/10.1016/S0022-0728(00)00460-5)
25. J. J. O'Dea, K. Wikiel, J. Osteryoung, *J. Phys. Chem*. **94** (1990) 3628 (https://doi.org/10.1021/j100372a049)
26. A. B. Miles, R. G. Compton, *J. Phys. Chem., B* **104** (2000) 5331 (https://doi.org/10.1021/jp0006882)
27. Š. Komorsky-Lovrić, M. Lovrić, *To Chem. J.* **2** (2019) 142 (http://purkh.com/index.php/tochem)
28. R. Gulaboski, V. Markovski, Zh. Jihe, *J. Solid State Electrochem*. **20** (2016) 3229 (https://doi.org/10.1007/s10008-016-3230-7)
29. E. Laborda, J. M. Gomez-Gil, A. Molina, *Phys. Chem. Chem. Phys*. **19** (2017) 16464 (https://doi.org/10.1039/c7cp02135f)
30. C. Batchelor-McAuley, Q. Li, S. M. Dapin, R. G. Compton, *J. Phys. Chem., B* **114** (2010) 4094 (https://doi.org/10.1021/jp1008187)
31. D. Menshykau, C. Batchelor-McAuley, R. G. Compton, *J. Electroanal. Chem*. **651** (2011) 118 (https://doi.org/10.1016/j.jelechem.2010.11.024)
32. G. J. Wilson, C. Y. Lin, R. D. Webster, *J. Phys. Chem., B* **110** (2006) 11540 (https://doi.org/10.1021/jp0604802)
33. H.Balslev, D. Britz, *Acta Chem. Scand*. **46** (1992) 949
34. R. Saravanakumar, P. Pirabaharan, L. Rajendran, *Electrochim. Acta* **313** (2019) 441 (https://doi.org/10.1016/j.electacta.2019.05.033)
35. X. Y. Liu, Y. P. Liu, Z. W. Wu, *Thermal Sci*. **26** (2022) 2459 (https://doi.org/10.2298/TSCI2203459L)

36. R. Umadevi, J. Visuvasam, K. Venugopal, L. Rajendran, *1st Int. Conf. Math. Tech. Appl. AIP Conf. Proc.* **2277** (2020) 130013 (https://doi.org/10.1063/5.0025822)
37. M. Lovrić, *Turk. J. Chem.* **46** (2022) 1226 (https://doi.org/10.55730/1300-0527.3429)
38. J. Strutwolf, W. W. Schoeller, *Electroanalysis* **8** (1996) 1034 (https://doi.org/10.1002/elan.1140081111)
39. M. Lovrić, *J. Serb. Chem. Soc.* **53** (1988) 211.

Biochar from agricultural biomass: Green material as an ecological alternative to solid fossil fuels

EMILIJA VUKIĆEVIĆ[1]*, JELENA ISAILOVIĆ[2], GORDANA GAJICA[3], VESNA ANTIĆ[2] and BRANIMIR JOVANČIĆEVIĆ[1]#

[1]*University of Belgrade, Faculty of Chemistry, Studentski trg 12–16, 11000 Belgrade, Serbia,* [2]*University of Belgrade, Faculty of Agriculture, Nemanjina 6, 11080 Zemun, Belgrade, Serbia and* [3]*University of Belgrade – Institute of Chemistry, Technology and Metallurgy, Njegoševa 12, Belgrade, Serbia*

Abstract: The stalks left after harvesting corn, tomatoes, and tobacco have no further use and are usually burned on agricultural land. In our work samples of this waste were collected and pyrolyzed at 400 °C for 30 min in a nitrogen atmosphere. The solid residue (biochar) obtained by pyrolysis was analyzed, and the results were compared with widely used solid fuels such as wood, coal, coke and charcoal. The heat values of biochar from tomato, tobacco, corn ZP 6263, and corn BC 398 stalks were 24.12, 23.09, 26.24 and 25.78 MJ kg^{-1}, respectively. These values are significantly higher than the heat value of wood, which is about 12.50 MJ kg^{-1}. The ash content of biochar was 12–20 %, which is consistent with the ash content of solid fuels. No heavy metals were found in biochar samples. The results show that biochar obtained from the pyrolysis of agricultural waste, such as tomatoes, tobacco and corn stalks, has good potential for use as a solid fuel.

Keywords: biochar; agricultural waste; solid fuel.

INTRODUCTION

Fossil fuel consumption has increased significantly in the last few decades, leading to environmental problems, including greenhouse gas (GHG) emissions and deterioration of air quality caused by different gaseous pollutants and fine particles. The production of carbon-neutral and low-GHG fuels from renewable sources, such as biomass, is increasingly important in gradually replacing conventional fossil fuels.[1] Although there are other renewable energy sources, such as wind, sun, geothermal and hydrothermal, biomass is still the most abundant and readily available, considering that a large part comes from agriculture, which

907

is one of the most crucial production sectors in the world, responsible for food manufacture.[2] Biomass can be defined as the biodegradable part of products: waste and residues from agriculture, forestry and related industries, as well as the biodegradable part of industrial and municipal waste. Slow pyrolysis, performed at low temperatures and low heating rates, has been practiced for many years to maximize the yield of solid char.[3] Biochar is a solid carbon-rich substance produced during the thermochemical processing of various biomass. Biochar has multiple advantages and potentials as a cheap and environmentally friendly material. It can replace more expensive synthetic carbon materials for many applications in nanocomposites, energy storage, sensors, and biosensors.[4] As a green material, biochar has attracted great interest in promoting carbon sequestration and reducing GHG emissions. It is also an additive to improve soil quality, increase crop production, and control soil and water pollution.[5]

Unfortunately, raw biomass is not an ideal energy source, and its direct use faces significant obstacles arising from its properties, such as poor grindability, high moisture content and low energy density. For example, poor grinding of biomass material caused by its fibrous structure significantly increases energy consumption and is a challenge during fuel preparation. As for the high moisture content, it lowers the maximum combustion temperature and consequently can reduce the thermal efficiency and increase the emission of pollutants. To overcome these disadvantages, a pre-treatment process is necessary to improve the quality of biomass-derived fuel.[6] Compared to traditional fuels such as coal, natural gas and oil, biomass fuel and biochar, is a neutral, sustainable alternative with controlled pollutant emission.[7]

This paper describes the characterization of a solid product – biochar obtained by pyrolysis of tomato, tobacco and corn stalks. Despite the range of feedstocks and techniques available for biochar production, relatively few works report understanding the correlation between physical and thermochemical properties related to its potential use as a solid fuel for energy production.[8] Corn, tobacco and tomatoes are widely grown and used in almost all regions of Serbia and the surrounding countries. Thus, much waste is available after harvesting and fruit picking. Residual stalks are agricultural waste usually broken down by the burning process in the fields. This treatment is known to cause severe environmental pollution and destruction of agricultural land. As is well known, combustion creates problems not only by the emission of pollutants that are harmful to the environment but also those that can enter the food chain through the growth of new plants. Therefore, the goal of this work was to reuse this agricultural waste through the production of biochar in the pyrolysis process, as well as the assessment of the potential exploitation of biochar in the form of biofuel.[5]

EXPERIMENTAL

Biomass samples

The samples used in this research were collected in the fall of 2022 in Serbia and air-dried for 30 days before use. The corn stalks collected near the town of Šabac originated from two corn hybrids: ZP 6263 and BC 398. For this research, stalks with leaves were cut approximately 5–10 cm from the ground. Tobacco stalks were collected in the area of Semberija, near the town of Bijeljina. Virginia-type tobacco stalks were cut a few centimeters above the ground. Tomato stalks, type Optima F1, were taken after picking fruits in the greenhouse near Pirot. The stems were pulled from the roots, and the roots were cut off the stalks. The stalks and leaves were cut with scissors into smaller pieces, with an average length of 10 cm. All samples were sieved so that particles of 2–5 mm size used in the experiments were obtained.

Pyrolysis process

Dry samples of agricultural waste were used for pyrolysis experiments. Pyrolysis was performed at a temperature of 400 °C for 30 min using an MTF 10/15/130 tube furnace from Carbolite, UK. Pyrolysis occurs under a constant flow of nitrogen (99.999 %) at 150 cm^3 min^{-1}. The heating rate was 100 °C per min. The pyrolysis of each sample was repeated about 20 times under the same conditions to obtain enough solid residues for analysis. Bio-oil was collected in acetone HPLC, while biochar was dispersed in acetone HPLC and then filtered, *i.e.*, washed, before further analyses. The biochar was washed to remove the remaining liquid fraction (bio-oil) that may have remained on it.

Characterization of biomass and biochar samples

Characterization of biomass samples included determination of ash content, cellulose, hemicellulose and lignin content, heat value, elemental composition (the content of C, H, N, S) and thermogravimetric analysis (TGA). The physicochemical characterization of obtained biochar samples included similar analyses: determination of ash content, elemental analysis and heat value, ICP-OES analysis, and FTIR analysis. Ash content was determined by burning 1 g of sample in the oven at 750 °C (ASTM D2584, ASTM D5630). The method used to determine cellulose, hemicellulose, and lignin content was based on the properties of these compounds to dissolve in different solvents.[9] Extractive substances: 1 g of biomass (*B*) was mixed with 60 ml of HPLC acetone at 90 °C for 2 h. After that, samples were dried in an oven at 110 °C until constant weight (*E*). The amount of extractive substances was calculated as:

$$(B - E) = \text{Amount of extractives (g)} \tag{1}$$

Hemicellulose content: 150 ml of sodium hydroxide solution (0.5 mol l^{-1}) was added to extractives-free biomass. The temperature (80 °C) was controlled using a hot plate for 3.5 h. Samples were washed with deionized water until they were free from Na$^+$. Samples were dried in an oven at 110 °C until constant weight was obtained (*H*). The amount of hemicellulose was calculated as:

$$(E - H) = \text{Amount of hemicelluloses} \tag{2}$$

Lignin content: 30 ml of 98.99 % sulfuric acid was added to extractives-free biomass (*E*). Samples were left for 24 h at ambient temperature and boiled at 100 °C using a hot plate for 1 h. Samples were filtered, and the solid residue was washed using deionized water until it was free from sulfate ions. After that, samples were dried in an oven at 110 °C until constant weight was obtained (*L*). Value *L* corresponds to the amount of lignin.

Cellulose amount (*C*) was determined as:

$$1\ \text{g} - ((B - E) + (E - H) + L) = \text{Amount of cellulose } (C) \tag{3}$$

The heat value of the sample was determined using the IKA C400 instrument by standard method SRPS CEN/TS 16023:2014. Elemental analysis was performed using a CHNS/O element analyzer (Elementar Analysensysteme GmbH, Langenselbold, Germany). Inductively coupled plasma-optical emission spectroscopy (ICP-OES) was performed using Spectroblue TI ICP-OES instrument and method EPA M 200.7, while for sample preparation, method EPA M 3052/ISO 2598-1 was used. The thermal behavior of biomass was investigated by thermogravimetric analysis (TGA) on TA Instruments TGA Q500, Thermogravimetric analyzer (Delaware, USA). About 10 mg of the biomass was placed into the platinum crucible, loaded into the TG furnace, and heated from 25 to 700 °C at 5 °C min^{-1}. The FTIR spectra of the biochar samples were acquired using an IRAffinity-1 spectrometer (Shimadzu, Japan). Spectra were collected in the 4000–400 cm^{-1} spectral range, with a resolution of 4 cm^{-1}. Before analysis, the solid biochar sample was crushed, mixed with KBr and pressed into pellets.

RESULTS AND DISCUSION

Characterization of different types of biomass

Before pyrolysis, biomass samples were characterized. The aim was to determine important physicochemical characteristics of dried samples and choose relevant conditions for the pyrolysis process. The contents of ash, extractives, hemicellulose, cellulose and lignin are shown in Table I. It is essential to note the high cellulose, hemicellulose and lignin content in all biomass samples. Hemicellulose is the dominant component in each sample, followed by cellulose and lignin. This composition makes biomass suitable for obtaining carbon-rich materials. Regarding literature data, hemicellulose, cellulose, and lignin decompose over different temperature ranges; generally, hemicellulose decomposes at a lower temperature range (220–315 °C), than cellulose (315–400 °C), while lignin decomposes over a broad range of temperatures (150–900 °C). Compared to cellulose and hemicellulose, the breakdown of lignin is a complicated and complex phenomenon.[10] It is known that a higher lignin content leads to a higher biochar yield. In contrast, a higher hemicellulose and cellulose content leads to a higher yield of liquid fraction. Our results showed that tobacco possesses the highest lignin content, while corn BC 398 has the highest hemicellulose and cellulose content. So, the highest biochar yield was expected from tobacco waste. The lowest yield was expected from corn BC 398.

TABLE I. Chemical composition (%) of biomass samples; Ext – extractives; Hem – hemicellulose; Cell – cellulose; Lig – lignin

Sample	Ash	Ext	Hem	Cell	Lig	Hem+Cell
Corn ZP 6263	4.78	6.00	45.72	28.86	19.42	74.58
Corn BC 398	4.25	4.23	48.24	34.28	13.25	82.52
Tobacco	4.66	5.53	40.00	28.90	25.57	68.90
Tomato	7.67	3.33	49.57	29.58	17.52	79.15

Table II shows the results of elemental analysis and heat values. These results are consistent with cellulose, hemicellulose and lignin content. All samples showed the highest content of carbon (40.44–45.68 %), followed by hydrogen, nitrogen and sulfur.

TABLE II. Elemental composition and heat value of biomass samples

Sample	C, %	H, %	N, %	S, %	Heat value / MJ kg^{-1}
Corn ZP 6263	45.68	6.44	0.86	0.38	17.81
Corn BC 398	44.49	6.29	3.21	0.00	18.17
Tobacco	44.41	6.19	1.03	6.60	17.14
Tomato	40.44	6.09	2.01	0.00	18.68

TGA of biomass samples

Thermogravimetric analysis is crucial for characterizing biomass as a raw material for fuel production and understanding the pyrolysis process. Biomass is converted into biochar by pyrolysis in an inert atmosphere at high temperatures. Thermogravimetric analysis of biomass samples was used to determine the optimal decomposition temperature to be used in the pyrolysis process. The TGA and dTGA curves of the biomass samples are shown in Fig. 1, while the characteristic temperatures obtained from the curves can be seen in Table III. The TGA curves for the analyzed samples were very similar, which is not surprising considering that the thermal behavior of the sample depends on its chemical structure.
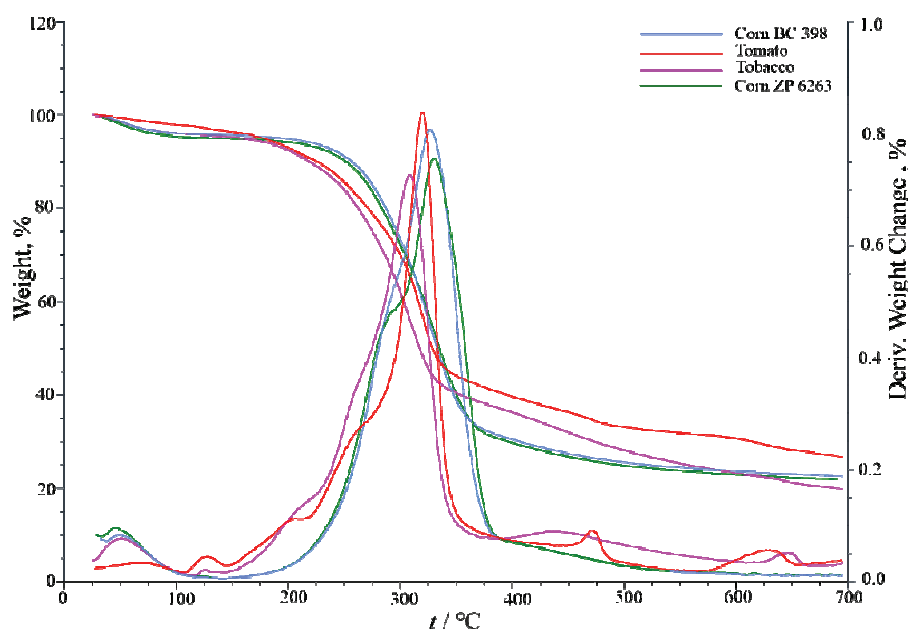
Fig. 1. TGA curves of tobacco, tomato and corn stalks.

According to literature data, lignin decomposes in the temperature range of 311.5–461.3 °C as the most stable component of biomass. Cellulose is less stable and decomposes in the 326.8–369.7 °C temperature range. As the least stable, hemicellulose decomposes in the temperature range of 223.4–332.8 °C.[11]

TABLE III. Data obtained by thermogravimetric analysis of tobacco, tomato and corn stalks

Sample	Loss at 120 °C, %	t_{max} / °C	Residue at 400 °C, %	Residue at 700 °C, %
Corn ZP 6263	4.82	330	31.5	21.81
Corn BC 398	4.18	327	32.5	22.57
Tobacco	4.22	309	37.6	19.80
Tomato	2.55	320	41.5	26.72

Three phases are distinguished on each TG curve from Fig. 1. The first phase refers to the evaporation of the remaining moisture in the biomass samples.[11] It can be noted that the first mass loss occurs at a temperature of about 120 °C and is about 2.5 % for tomatoes and almost 5 % for corn samples. The second phase corresponds to the highest mass loss, with a peak on the dTG curve from 309 °C (tobacco) to 330 °C (corn samples). Peak maxima are marked with t_{max} and given in Table III. The second phase ends at temperatures above 400 °C, while the third phase and complete degradation ends at about 700 °C. The solid residue, *i.e.*, biochar, is formed during the third degradation phase. The residue at 700 °C was from 9.80 % for tobacco to 26.72 % for tomato (Table III).

Yield of pyrolysis products

Pyrolysis is the thermal destruction of biomass in the absence of air/oxygen, which produces valuable liquid oils, gases, and solid products. Different conditions lead to the creation of products in different proportions. Many techniques have been developed to increase yields or improve the quality of said products. Pyrolysis can be slow, fast or flash, depending on the heating rate. Also, if necessary, it can be catalyzed. When biomass is pyrolyzed at low heating rates (5–7 K min⁻¹), a smaller proportion of liquid and gaseous products along with a more significant proportion of biochar are obtained. Fast pyrolysis occurs at a heating rate of about 300 °C min⁻¹, which can be used to get a higher liquid product yield. Flash pyrolysis occurs when the reaction time is only a few seconds or less. The heating rate is very high, and this type is used to increase the yield of liquid and gaseous products.[10]

In this work, pyrolysis was performed at 400 °C for 30 min. The weight of obtained biochar and bio-oil was measured after the pyrolysis process. Yields were calculated in relation to the initial weight of biomass. The yield of the gaseous fraction was calculated by subtracting the yield of biochar and bio-oil from 100 %. The yields of all products obtained by pyrolysis of corn, tobacco, and tomato stalks are given in Table IV.

TABLE IV. Yield of bio-oil, biochar and gaseous products obtained by pyrolysis of corn, tobacco and tomato stalks

Product yield, %	Corn ZP 6263	Corn BC 398	Tobacco	Tomato
Bio-oil	33.5	22.8	28.5	20.5
Biochar	30.6	29.7	34.3	36.5
Gas	35.8	47.6	37.2	43.0

The yield of biochar was around 30 %. Values ranged from 29.7 % for biochar from corn stalks BC 398 to 36.5 % from tomato stalks (Table IV). The obtained yields by pyrolysis (Table IV) were slightly lower than the solid residues obtained by thermogravimetric analysis at 400 °C (Table III). According to TGA results, the residue at 400 °C was 31.5 % for corn ZP 6263, 32.5 % for corn BC 398, 37.6 % for tobacco and 41.5 % for tomato stalks. At 700 °C, the solid residue ranged from 19.80 % for the tobacco sample to 26.82 % for the tomato sample (Table III). The results showed that the pyrolysis temperature was adequately selected and the yield of biochar obtained by the pyrolysis process followed the expected values obtained based on TGA.

Biochar is formed in the last step of thermal degradation of biomass. As can be seen in Fig. 1, complete degradation is achieved at temperatures higher than 400 °C. Lignin, as the most stable compound, does not entirely decompose at 400 °C, so it partially remains as a solid residue. Regarding literature data, with increasing pyrolysis temperature, the yield of the solid residue decreases, and the yield of the liquid fraction increases.[12] Therefore, lower temperatures (such as 400 °C at which we conducted experiments) favor biochar production.

Characterization of biochar samples

Biochar has been characterized, and its properties are compared with solid fuels such as wood, coal, coke and charcoal. Some of the most important features are given in Table V.

TABLE V. Ash content and elemental composition of obtained biochar

Sample	Ash content, %	C, %	H, %	N, %	S, %
Corn ZP 6263	12.84	69.62	4.96	1.64	0.00
Corn BC 398	19.12	65.08	3.51	1.76	0.00
Tobacco	16.54	60.84	4.37	1.49	0.00
Tomato	19.19	52.87	4.21	2.61	0.00

The main characteristic of fuel is its ash content. The literature states that the ash content of different types of coal is 5–50 %.[13] The ash content of biochar samples was 12–20 %, which is in accordance with literature data. The nitrogen content was low (1.49–2.61 %), corresponding to the fuel's characteristics. The content of hydrogen, an element that significantly contributes to the combustible characteristics of the fuel, was from 3.51 % in corn biochar BC 398 to 4.96 % in

corn biochar ZP 6263. The content of sulfur was below the detection limit, which can be explained by the fact that sulfur, during pyrolysis, quickly builds gaseous compounds that do not remain in solid or liquid fractions.

As is well known, solid fuels such as wood, coal, coke and charcoal are widely used. Due to its composition, wood has been used as a solid fuel since the dawn of man. Wood is mainly formed from cellulose. Coal is a light brown to black sedimentary rock of organic origin that can burn. Coals are formed in swamps by the deposition and accumulating dead plant material made of cellulose, lignin, tannin, *etc*. During the deposition of plant material, a series of complex biochemical (diagenetic) changes occur under the influence of microorganisms. In anoxic conditions, lignite and brown coal are formed by changing organic matter under the influence of microorganisms and elevated pressure. Furthermore, due to temperature, elevated pressure, and mineral catalysts, complex geochemical (catagenetic) changes in organic matter lead to coal formation.[13] Therefore, coal is described as a hydrocarbon fuel consisting of various substances containing carbon, hydrogen and oxygen, as well as smaller amounts of sulfur and nitrogen.[14] Coals can differ according to the origin of organic matter, degree of maturity, class, and purpose.[15] The most interesting here are wet coals that contain a large amount of carbonized cellulose, lignin, and hemicellulose residues. Dark coal and hard coal are examples of wet coal.[13] Coal can be converted into various products by processes similar or the same as pyrolysis. Pyrolysis or dry distillation processes convert dark coal into charcoal with a higher heat value. The exact process is used to obtain coke from hard coal.[13] Carbon content is one of the main characteristics that describe the fuel properties of a compound or mixture. The carbon content of biochar from corn, tobacco, and tomato stalks was compared with the carbon content of commonly used solid fuels and presented in Fig. 2.

The carbon content ranges from about 50 % in wood to about 95 % in coke. In the biochar produced in this work, the carbon content was 52.8 % in tomato biochar, 60.84 % in tobacco biochar, 65.08 % in corn BC 398 biochar, and the highest percentage was 69.62 % in biochar from corn ZP 6268. It can be concluded that any biochar is a carbon-rich material. Therefore, its carbon content is similar to solid fuels (wood, coal, coke, and charcoal). The main characteristic, we wanted to monitor and compare, was the heat value of the obtained biochar samples.

There are many different types of coal with different heat values. Here, for comparing heat values, high-grade anthracite of the coal type, which has the highest carbon content and heat value of 34.9 MJ kg^{-1}, was used. The heat value of coke is 32.6 MJ kg^{-1}, and that of charcoal is 25.7 MJ kg^{-1}. Fig. 3 compares the heat values of standard solid fuels[16–18] with the biochar samples' values from this work.
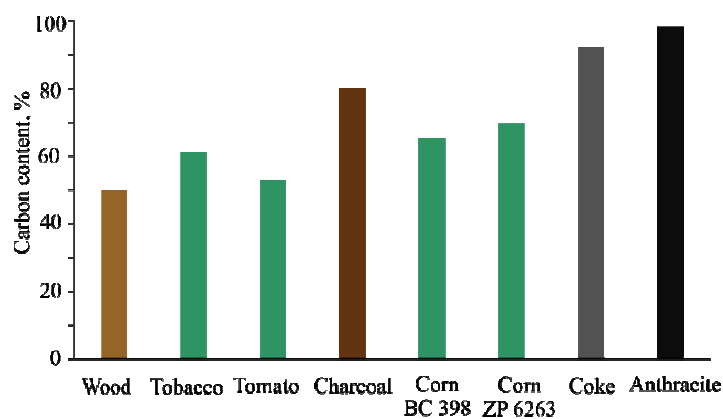
Fig. 2. Carbon content in obtained biochars and widely used solid fuels.
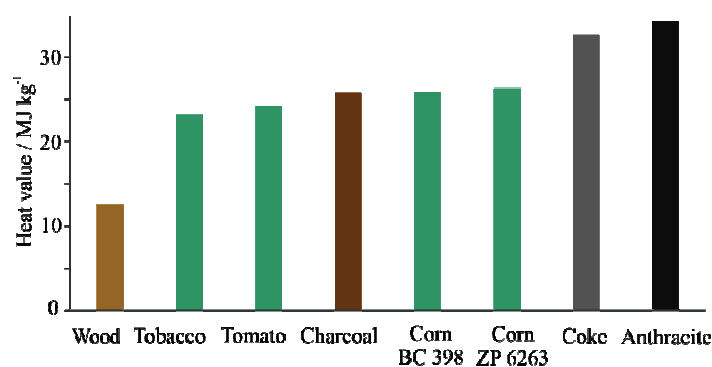
Fig. 3. Heat values of standard solid fuels (wood, charcoal, coke, anhracite) and biochar samples from this work.

Considering the results, it can be concluded that biochar produced from corn, tobacco, and tomato stalks possess a high heat value, which is between the heat value of wood and coke. The heat value of tobacco and tomato biochar is lower than coal, but biochar from both corns has a higher heat value. Therefore, these types of biochar have the potential to be used as another type of solid fuel.

ICP-OES analysis showed that each biochar contains different elements that could be interesting from other perspectives and for other uses of these materials. Table VI presents some major elements (metals, sulfur, and phosphorus) that occur in high concentrations.

All biochar samples contain high Na, K, Ca, Mg and S concentrations. However, biochar produced from tomatoes has the highest concentration of these elements, contributing to its promising potential for the use as a fertilizer. The concentration of Cu is highest in biochar obtained from tobacco, which contributes to the basic properties of biochar. The highest concentration of Al was in biochar obtained from tomatoes. This element comes from the soil. The Si con-

centration is highest in BC 398 maize biochar and very similar to ZP 6263 maize biochar. In contrast, the silicon concentration is much lower in tobacco and tomato biochar. Phosphorus is the most abundant in tobacco biochar, followed by BC 398 and tomato corn biochar, and the least abundant in ZP 6263 corn biochar. Data from the literature show which elements can be found in materials obtained from agricultural biomass. The main components of wood fuel ash are Ca, K, Mg and Si. The amounts of other elements, such as P, S, Na, and Al, are significantly lower. Si, K, and Ca dominate in fuel from agricultural biomass, followed by elements such as Mg, S, P, Na, Al, and Fe, which occur in lower concentrations.[19]

TABLE VI. Most abundant elements obtained by ICP-OES analysis

Element content, mg kg^{-1}	Corn ZP 6263	Corn BC 398	Tobacco	Tomato
Na	<100.00	<100.00	260.93	10285.00
K	18930.00	16654.00	74037.00	42518.00
Mg	4385.00	5440.00	3030.00	11451.00
Ca	9474.00	12949.00	25399.00	49513.00
Cu	17.65	17.48	25.00	16.85
Al	250.80	391.46	234.88	676.01
Si	31705.00	37198.00	5349.00	3350.00
P	2148.00	3250.00	3353.00	3001.00
S	594.42	974.03	3753.00	4336.00

It is important to emphasize that the concentrations of heavy metals were below the detection limit, which is significant for the quality of ash after combustion. The results of ICP-OES analysis showed that biochars have good potential for use as solid fuels. It is known that certain elements appear in agricultural biomass as a result of fertilization or post-harvest processing.[19]

The results obtained by FTIR analysis (Fig. 4) showed the presence of several different functional groups.

The peak obtained in the region between (3000–3700 cm^{-1}) corresponds to the OH stretch of water molecules of hydroxyl groups (OH) and phenols. Peaks in the 2900–3000 cm^{-1} region correspond to aliphatic C–H stretching vibrations. These peaks can be attributed to structures formed by the thermal degradation of cellulose and hemicellulose.[20] At about 1600 cm^{-1}, peaks originating from vibrations of double C=C bonds were determined. Peaks at 1300–1450 cm^{-1} are attributed to the in-plane bending of C–H bonds.[21] In tobacco and both corn biochars, peaks at 1000–1100 cm^{-1} are observed, corresponding to the C–O group, which may be present in various compounds produced in degradation processes. Finally, the peaks in the 400–900 cm^{-1} region belong to aromatic C–H stretch, –Si–O–Si–, Al–O, Al–O–Si or stretching Si–O groups.[21,22] This is consistent with literature data and ICP-OES analysis results, which showed the presence of Al and Si.
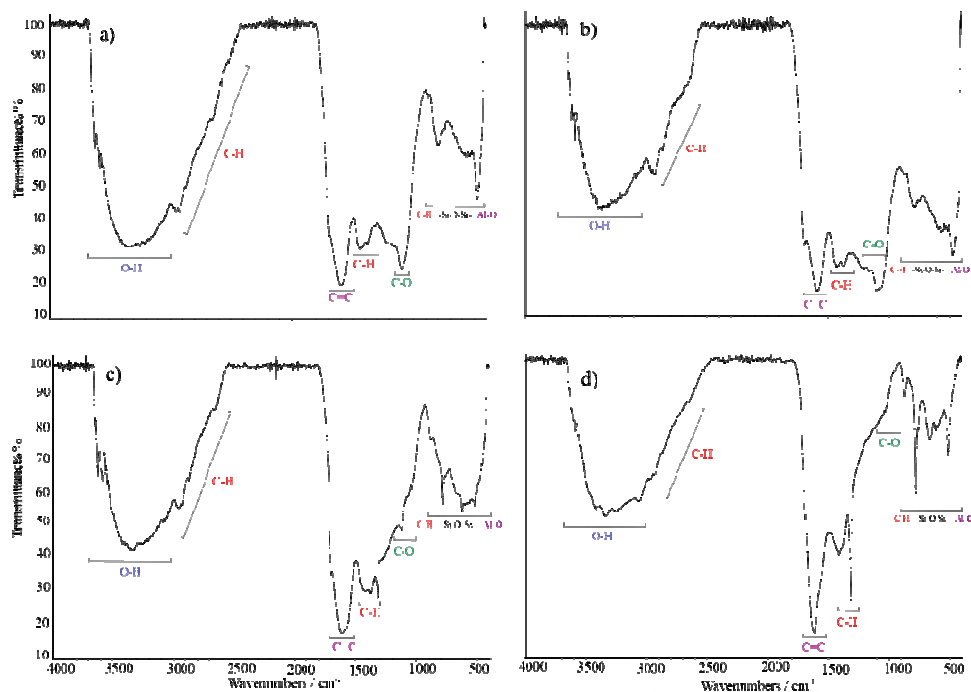
Fig. 4. FTIR spectra of biochar from corn BC 398 (a), corn ZP 6263 (b), tobacco (c) and tomato (d) stalks.

CONCLUSION

In this work, agricultural biomass, *i.e.*, corn, tobacco, and tomato stalks, widely available in many locations in Serbia, were used for the pyrolysis process. Biomass samples were characterized after air drying, and the results showed its promising potential for high-quality pyrolysis products. Pyrolysis was performed at a lower temperature of 400 °C, where the solid residue is the dominant product. The biochar samples' ash content and heat value indicate good fuel characteristics. The heat values of biochar, which are 23.09–26.24 MJ kg^{-1}, correspond to the heat value of charcoal. Still, it is lower than the corresponding values for coke and anthracite and much higher than the heat value of wood. The results also showed that the heat value of biochar produced from corn stalks is slightly higher than the corresponding value for coal. In comparison, the heat value of biochar from tobacco and tomato stalks is lower. The ash content of each analyzed biochar is relatively low, corresponding to good fuel characteristics. ICP--OES analysis showed high concentrations of elements such as Ca, K, Mg, Na, S and P, while toxic elements and heavy metals were below the detection limit. This leads to the conclusion that no heavy metals will remain in the ash after combustion. The general conclusion is that biochar obtained by pyrolysis of corn,

tobacco and tomato stalks can be considered green material with a good potential for use as a solid fuel. Pyrolysis of agricultural biomass to obtain biochar is a convenient, environmentally friendly way to reduce this type of waste and get new valuable products.

И З В О Д

БИОУГАЉ ИЗ ПОЉОПРИВРЕДНЕ БИОМАСЕ: ЗЕЛЕНИ МАТЕРИЈАЛ КАО ЕКОЛОШКА АЛТЕРНАТИВА ЧВРСТИМ ФОСИЛНИМ ГОРИВИМА

ЕМИЛИЈА ВУКИЋЕВИЋ[1], ЈЕЛЕНА ИСАИЛОВИЋ[2], ГОРДАНА ГАЈИЦА[3], ВЕСНА АНТИЋ[2] и БРАНИМИР ЈОВАНЧИЋЕВИЋ[1]

[1]Универзитет у Београду – Хемијски факултет, Студентски трг 12–16, 11000 Београд, [2]Универзитет у Београду – Пољопривредни факултет, Немањина 6, 11080 Земун, и [3]Универзитет у Београду – Институт за хемију, технологију и металургију, Његошева 12 11000 Београд

Стабљике које остају након жетве кукуруза и дувана, као и брања парадајза, немају даљу употребу и обично се спаљују на пољопривредном земљишту. У нашем раду узорци овог отпада су прикупљени и пиролизовани на 400 °C у атмосфери азота током 30 min. Анализиран је чврсти остатак (биоугаљ) добијен пиролизом, а резултати су упоређени са широко коришћеним конвенционалним чврстим горивима као што су дрво, угаљ, кокс и дрвени угаљ. Калоријске вредности биоугља из стабљика парадајза, дувана, кукуруза ZP 6263 и кукуруза BC 398 биле су 24,12, 23,09, 26,24 и 25,78 MJ kg^{-1}. Ове вредности су знатно веће од калоријске вредности дрвета која износи око 12,50 MJ kg^{-1}. Садржај пепела у биоугљу је био 12–20 %, што је у складу са садржајем пепела код чврстих горива. У узорцима биоугља нису пронађени тешки метали. Резултати показују да биоугаљ добијен пиролизом пољопривредног отпада, као што су стабљике парадајза, дувана и кукуруза, има добар потенцијал за употребу као чврсто гориво.

(Примљено 26. јануара, ревидирано 21. фебруара, прихваћено 20. априла 2024)

REFERENCES

1. S. Wang, G. Dai, H. Yang, Z. Luo, *Prog. Energy Comb. Sci.* **62** (2017) 33 (https://doi.org/10.1016/j.pecs.2017.05.004)
2. D. Fetjah, L. Ainlhout, B. Ihssane, A. Houari, Z. Idardare, L. Bouqbis, *J. Ecol. Eng.* **22** (2021) 36 (https://doi.org/10.12911/22998993/133964)
3. S. N. Đurić, S. D. Brankov, T. R. Kosanić, M. B. Ćeranić, B. B. Nakomčić-Smaragdakis, *Therm. Sci.* **18** (2014) 533 (https://doi.org/10.2298/TSCI120711021D)
4. Z. Hu, L. Wei, *J. Compos. Sci.* **7** (2023) 354 (https://doi.org/10.3390/jcs7090354)
5. R. Font, J. Moltó, A. Gálvez, M. D. Rey, *J. Anal. App. Pyrol.* **85** (2009) 268 (https://doi.org/10.1016/j.jaap.2008.11.026)
6. Z. Liu, G. Han, *Fuel* **158** (2015) 159 (https://doi.org/10.1016/j.fuel.2015.05.032)

7. B. Song, P. Hall, *Front. Energy Res.* **8** (2020) (https://doi.org/10.3389/fenrg.2020.00058
8. W. A. Wan Ab Karim Ghani, P. S. Fernandez, M. Q. Halele, S. Sobri, J. Jasni, *MATEC Web Conf.* **62** (2016) 04003 (https://doi.org/10.1051/matecconf/20166204003)
9. M. A. Maisyarah, L. J. Shiun, A. F. Nasir, H. Haslenda, H. W. Shin, *Chem. Eng. Trans.* **72** (2019) 79 (https://doi.org/10.3303/CET1972014)
10. H. B. Goyal, D. Seal, R. C. Saxena, *Ren. Sustain. Energy Rev.* **12** (2008) 504 (https://doi.org/10.1016/j.rser.2006.07.014)
11. D. Chen, K. Cen, X. Zhuang, Z. Gan, J. Zhou, Y. Zhang, H. Zhang, *Comb. Flame* **242** (2022) 112142 (https://doi.org/10.1016/j.combustflame.2022.112142)
12. X. He, Z. Liu, W. Niu, L. Yang, T. Zhou, D. Qin, Z. Niu, Q. Yuan, *Energy* **143** (2018) 746 (https://doi.org/10.1016/j.energy.2017.11.062)
13. I. Kojic, *PhD Thesis*, Faculty of Chmistry,Belgrade, 2022 (in Serbian) (https://phaidrabg.bg.ac.rs/view/o:25866)
14. R. Arisanti, *STI* **3** (2018) 100 (https://doi.org/10.26554/sti.2018.3.2.100-106)
15. P. I. Premović, R. S. Nikolić, M. P. Premović, *Geol. Soc., London, Spec. Public.* **125** (1997) 201 (https://doi.org/10.1144/GSL.SP.1997.125.01.16)
16. P. Grammelis, N. Margaritis, E. Karampinis, *Fuel Flex. Energy Gener.* (2016) 29 (https://doi.org/10.1016/B978-1-78242-378-2.00002-X)
17. I. V. Miroshnichenko, D. V. Miroshnichenko, I. V. Shulga, Y. S. Balaeva, V. V. Pereima, *Coke Chem*. **62** (2019) 143 (https://doi.org/10.3103/S1068364X19040057)
18. A. O. Otieno, P. G. Home, J. M. Raude, S. I. Murunga, A. Gachanja, *Heliyon* **8** (2022) e10272 (https://doi.org/10.1016/j.heliyon.2022.e10272)
19. M. Praspaliauskas, N. Pedišius, D. Čepauskienė, M. Valantinavičius, *Biomass Conv. Bioref.* **10** (2019) 937 (https://doi.org/10.1007/s13399-019-00457-7)
20. C. Hadey, M. Allouch, M. Alami, F. Boukhlifi, I. Loulidi, *Sci. World J.* **2022** (2022) 2554475 (https://doi.org/10.1155/2022/2554475)
21. A. Supriya, R. Samantray, S. C. Mishra, *IOP Conf. Ser.: Mater. Sci. Eng.* **178** (2017) 012022 (https://doi.org/10.1088/1757-899X/178/1/012022)
22. H. Huang, N. G. Reddy, X. Huang, P. Chen, P. Wang, Y. Zhang, Y. Huang, P. Lin, A. Garg, *Sci Rep.* **11** (2021) 7419 (https://doi.org/10.1038/s41598-021-86701-5).

Two-stage thermocatalytic conversion of waste XLPE to diesel-like fuel

UFUK SANCAR VURAL[1]*, ABDULLAH YINANC[2] and HUSEYIN CAHIT SEVINDIR[3]

[1]*Pasabayir Mh. Mehmetcik Cd. 77/18, Bandirma, Balikesir, Turkey,* [2]*Tekirdag Namik Kemal University, Corlu Vocational School of Technical Sciences, Tekirdag, Turkey and* [3]*Suleyman Demirel University, Department of Environmental Engineering, Faculty of Engineering, Isparta, Turkey*

Abstract: Cross-linked polyethylenes (XLPE) are not preferred in industrial pyrolysis applications and mechanical recovery methods due to great thermo-chemical resistance to heat and deformation. The studies on pyrolysis of XLPE up to 600 °C on obtaining fuel have generally yielded high levels of wax and have not been of interest to the energy sector. In this study, two-stage pyrolysis of XLPE was carried out catalytically and also without catalyst (thermal, T--pyr) under 500 °C with heating rates of 5 and 10 °C min^{-1}. In the pyrolysis experiments, three different catalytic studies were performed by adding MCM--41 + HZSM-5 catalyst mixture to the polymer phase only (PPC-pyr), by filling Cu(I)-MAS + HZSM-5 catalyst mixture to the gas outlet column only (GPC--Pyr) and adding catalyst mixtures in both polymer phase and gas phase (MPC--pyr). The highest diesel-like fuel (91.40 wt. %) was obtained in multiphase catalytic pyrolysis experiments at 460 °C with a heating rate of 5 °C min^{-1}. The calorific value, kinematic viscosity, density, flash point and cetane number of the fuel were found as 45.97 MJ kg^{-1}, 2.72 cSt, 832.5 kg m^{-3}, 57 and 59 °C, respectively. The results of the two-stage catalytic cracking and the heating rate profile will be a guide for industrial pyrolysis applications. The simple feasibility for industrial applications showed that it would be a very profitable investment.

Keywords: cross-linked polyethylene; thermal cracking; heterogenous catalysis; zeolite.

INTRODUCTION

Cross-linked polyethylenes are cross-linked thermoset polymers made from low-density (LDPE) or high-density polyethylene (HDPE), commonly known as XPE or XLPE. Cross-linked polyethylenes are synthesized by three different

---

921

cross-linking methods: peroxides, silane, and high-energy irradiation.[1,2] Polymers obtained by peroxide crosslinking reaction are classified as PE-Xa (or P--XLPE), by silane linkage as PE-Xb (or Si-XLPE), and by high irradiation linkage as PE-Xc (or I-XLPE), and crosslinking degree is 75, 65 and 60 %, respectively.[3,4] Cross-linked polyethylene are used in the wire and pipe industries, in healthcare prosthetics, primarily in cable industry, as they have excellent power insulation, good heat resistance, dimensional stability and resistance to environmental stress cracking due to cross-links.[5] A feasible and successful method has not yet been developed for the recovery of defective products that do not comply with the reaction conditions during the production of cross-linked polyethylene.[5] The scrap cross-linked polyethylene cables consist of cables that are replaced during the periodic maintenance of electrical distribution lines or cables that cannot be used as a result of faulty production. Since XLPE is a thermosetting polymer, it hardens irreversibly.[6] For this reason, it makes it impossible to recover by melting it to be reshaped and used again. Mechanical recovery is also not possible, as it inhibits flow at high temperatures.[6] While producing *HDPE* in subcritical and supercritical methanol and water is somewhat promising, the cleavage of the main chain and the selectivity of removal of crosslinks still remains to be studied.[6] Although recently, experiments on thermoplasticization by selective degradation of the cross-linked structure, using supercritical fluids, have been successfully carried out, it has not yet been put into practice on an industrial scale.[6,7]

Wang *et al.*[8] succeeded in producing fuel by hydrogenating polyethylene with a tungstated zirconia catalyst at low temperatures of 250 °C. Although the method was carried out under mild conditions than thermal and catalytic pyrolysis experiments, thermal or catalytic pyrolysis methods are still seen as more convenient processes since they are high-cost processes in terms of industrial application. Recycling of XLPE by thermal decomposition methods is a more satisfactory method as it will provide alternative contributions to energy production.[6]

Catalysts play an important role in the pyrolysis of hydrocarbons and olefins.[9] The catalyst lowers the pyrolysis temperature by reducing the activation energy required to break the carbon bonds, thus shortening the pyrolysis time.[9] In addition, the catalyst is effective in the selectivity of pyrolytic products according to their molecular weight distribution. During the catalytic pyrolysis process, carbocationic decomposition of volatile molecules, isomerization, oligomerization, cyclization and aromatization reactions occur.[9] Homogeneous catalysts such as AlCl$_3$, heterogeneous catalysts such as zeolite solid acid catalyst and *FCC* are used in the pyrolysis of polymers.[9] Heterogeneous catalysts are more preferred over homogeneous catalysts because of the difficulty in separating the catalyst from the products after pyrolysis. The most commonly used solid acid

catalysts in polymer pyrolysis are heterogeneous catalysts such as ZSM-5, HZSM-5, Y-zeolite and MCM-41.[9,10,11] The acid content, pore structure and shape of zeolites plays an important role in diffusion and cracking of molecules into the acid region of the catalyst during pyrolysis. As the diffusion rate of molecules into the pores of the catalyst increases, the retention time and cracking rate decrease and more liquid product is obtained. Increasing the residence time of molecules in the pores of the catalyst increases secondary reactions and therefore gas formation.[9–11] ZSM-5 with a micro pore diameter of 0.55 nm and HZSM-5 with a medium pore diameter of 0.9 nm catalyse the conversion of hydrocarbons and olefins into low molecular weight components.[10,11] The catalytic activity of ZSM-5 with smaller pore diameter is higher than HZSM-5. In the pyrolysis of plastics, small molecules such as gasoline are formed with ZSM-5, while larger molecules such as diesel oil or jet fuel are formed with HZSM-5.[10,11] Due to the high catalytic activity of ZSM-5, more gas is produced in the pyrolysis of plastics than other zeolites. Eze *et al.*[12] investigated the pyrolysis of different plastics with various catalysts and catalyst mixtures. They observed that the highest degradation rate was obtained with zeolite catalysts, and the highest liquid yield was obtained in 1:1 ratio MCM-41 and ZSM-5 catalyst mixtures. They stated that since pyrolytic liquids contain high amounts of aromatic compounds, pyrolytic liquids are a product similar to gasoline. Eze *et al.*[12] also obtained 76, 77, 58 and 63 % liquid product from the pyrolysis of LDPE, LLDPE, HDPE and XLPE, respectively at 430 °C with silica-alumina catalyst. They stated that the reason for obtaining a lower rate of liquid product from HDPE and XLPE was due to wax formation. Santos *et al.*[13] stated that HDPE cracked 48.3 % with ZSM-5, 88.4 % with HZSM-5 at 450 °C, and <16.3 % without catalyst. Ratnasari *et al.*[14] investigated the effect of MCM-41 and ZSM-5 catalysts on the thermal degradation of HDPE, using a two-stage pyrolysis method. Approximately 65 % pyrolytic oil was obtained with MCM-41 alone, the amount of non-condensable gas increased with ZSM-5 alone. They stated that the thermal cracking rate of ZSM-5 is much faster than MCM-41, because ZSM--5 has a higher Si:Al ratio and more acidic character than MCM-41.

During cracking, the surface activity of the catalyst decreases rapidly as the catalyst surface is covered with carbonaceous residues formed by secondary reactions. When transition metals such as Zn, Cu or alkali metals are immobilized on the catalyst surface, secondary reactions that cause coke formation are reduced. As the acidity and surface activity of the metal-loaded catalyst increases, wax formation decreases and the formation of gasoline and kerosene-like molecules increases.[10,11,15] One of the most important features of metal-loaded zeolites is that they reduce the sulphur value of the fuel. Mesoporous molecular sieves (MCM-41), mesoporous aluminosilicate (MAS) and *Y*-type zeolite (NaY) were used for the desulphurization of hydrotreated naphtha.[16–18] Amorphous

inner walls leading to poor stability and weak acidity reduce the catalytic powers of mesoporous molecular sieves. To improve the stability and acidity of the mesoporous molecules, the amorphous matrix is modified with aluminum and silica and partially converted into the nano-sized zeolite phase. The desulfurization activity of MAS, MCM-41 and NaY in hydrotreated diesel sample containing 207 and 315 ppm sulphur was compared. MAS showed a higher activity than MCM-41 and NaY, and sulphur values were found to decrease to 53 and 109 ppm, respectively.[16,17] Although the pore diameter (3.51 nm) and the surface area (940 m^2 g^{-1}) of MAS were lower than MCM-41, MAS showed higher activity against sulphur because it was more acidic than MCM-41. Li *et al*. reduced sulphur value of diesel from 315 to 54 ppm with Cu-MAS.[17]

In this study, the thermochemical transformation of XLPE was carried out without catalyst, using mesoporous MCM-41 heterogeneous catalyst in the polymer phase, Cu-MAS catalyst in the gas phase and catalysts in both phases, with a heating rate of 5 and 10°C min^{-1}. Since it is aimed to produce diesel equivalent fuel, microporous catalysts (ZSM-5 and HZSM-5) with high acidic and catalytic activity were not preferred. To obtain products in the boiling point range of diesel, mesoporous MCM-41 polymer phase, which has a larger pore diameter and lower catalytic activity and acidity than microporous catalysts, was used. To reduce coking and desulphurization, Cu-MAS, which has higher catalytic activity, was used as a catalyst in the gas phase. In multiphase catalytic cracking experiments performed with low heating rate, the highest amount of fuel and the least amount of gas and wax were obtained.

EXPERIMENTAL

The cross-linked polyethylene was obtained from a local power cable manufacturer's copper recovery department in shreds <10 mm. The composition of waste plastic is given in Table I. Cetyltrimethylammonium bromide (*CTMAB*, 98 %), sodium aluminate (NaAlO$_2$) were obtained from Sigma-Aldrich, Aluminium sulphate (Al$_2$(SO$_4$)$_3$·18H$_2$O), sodium silicate solution (8 % Na$_2$O, 27 % SiO$_2$), K$_2$CO$_3$, H$_2$SO$_4$ (97 %), NaOH, Cu(NO$_3$)$_2$, γ-Al$_2$O$_3$ (particle size 63–200 μm, pore size 9 nm) and silica gel (particle size: 63–200 μm, pore size: 60 A, pore volume: 0.7–0.85 cm^3 g^{-1}, surface area: ≥ 480 m^2 g^{-1}) was obtained from Merck.

Table I. Waste XLPE composition

Ultimate analysis		Proximate analysis	
Element	Content, wt. %	Component	Content, wt. %
C	85.94	Volatiles	98.43
H	13.21	Fixed carbon	0.16
N	0.07	Ash	0.54
S	0.24	Moistures	0.87
		Croslinked degree	84.00

Thermal cracking experiments were carried out in a two-stage fixed bed reactor. The first reactor is 50 cm long, 30 cm high, made of 4 mm 316Ti stainless steel and is designed to melt the polymer. The empty volume of the reactor is 35 L. During the melting of the polymer, a 80 cm length and 14 cm diameter column was connected to the reactor for volumetric expansion and removal of gases. The reactor is heated with a 7.5 kW electrical resistance. The second fixed bed reactor with a diameter of 20 cm, a length of 30 cm and an empty volume of 10 L (Fig. 1), was used in the pyrolysis experiments. The amount of polymer melt fed into the cracking reactor is controlled by the overflow pipe connecting the two reactors. A column with a diameter of 14 cm and a length of 160 cm, consisting of 3 sections, was connected to the steam outlet of the reactor. The first section, the upper part of the column, is the reflux part. The gas phase catalytic reactions were carried out with the catalyst in pellet form, which was charged to the second section of the column. The column also acts as a reflux column to separate waxes and liquids from the gas phase that escape the gas phase as a result of sudden expansions. In the last section of the column, gases are discharged from the reactor and polymer melt is fed into the reactor from the first reactor. The reactor is heated with a 7.5 kW electrical resistance. The column is connected on a single pass condenser column with a length of 1,5 m, a diameter of 16 cm and a 1/2-in tube bundle. Two collection vessels are connected to the condenser outlet to separate the light and heavy distillate phases. The uncondensed gases were burned after desulphurization by passing through sodium hydroxide solution.
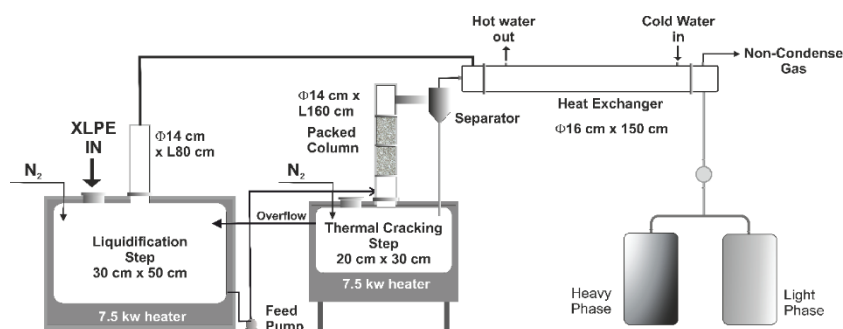
Fig. 1. Apparatus to experimental set-up.

The temperature values measured by the pt100 sensors placed inside the reactors and on the column, the heating rate was realized with a computer-controlled K-type thermocouple. The pyrolysis process was carried out at atmospheric pressure using inert N_2 carrier gas (a flow rate of 200 cm^3 min^{-1}). LECO, CHNS-932 elemental analyser was used for C, H, N and S analysis in fuel. Viscosities were measured according to the ASTM D445 method by the Ostwald viscometer at 40 °C. The calorific value of the pyrolysis oil samples was measured using a U-Therm YX-ZR model semi-automatic calorimeter. Densities of pyrolytic oils were measured with Anton Paar DMA 38N densimeter according to the ASTM D7777 method. The flash point of the pyrolytic oil samples was determined using the PMA 500 model Pensky––Martens device according to the ASTM D93 method. In order to find the amounts of diesel and gasoline-like fractions, distillation of pyrolytic oils was carried out according to ASTM D-93. Sunflow brand, 1440 rpm, 5 L min^{-1}, SF-025 model, 0.2 kW, 220 V hot oil transfer pump was used for the transfer of the polymer melt. The cetane number was calculated according to the ASTM D'4737-03 method.

Determination of croslinging degree of waste XLPE

Polyvinyl chloride (PVC) and metallic impurities in the sample are separated in water by density difference and dried at room temperature. Crosslinking degree of XLPE sample was determined by gel content according to ASTM 10147:2004. To determine the gel content of XLPE, approximately 0.30 g of sample was placed in a xylene weighing flask and extracted by heating at 110 °C for 8 h. It was then dried under vacuum at 150 °C for 30 min. The gel content of the XLPE was determined by weighing the weight of the remaining cross-linked fraction. Cross-linking degree was determined as 84 %.

Mesoporous MCM-41 Synthesis

MCM-41 was synthesized according to the method in the literature.[16,19] 72 g of CTMAB was dissolved in 1000 cm^3 distilled water under stirring 265 g of sodium silicate and was then introduced into the mixture. H_2SO_4 was added dropwise to give a solution with a pH of 11. The mixture was allowed to heat in an oven at 100 °C for 24 h. The precipitate was filtered, washed, and dried at 55 °C under a vacuum, before calcination. Then, the dried precipitate was calcined under airflow at 550 °C for 6 h.

Mesoporous aluminosilicate (MAS) synthesis

MAS was synthesized by a two-step method.[16,17] Nanoclustered zeolite Y seeds were prepared by reacting NaOH (0.088 mol) and $NaAlO_2$ (0.10 mol) in H_2O (8.5 mol) with silicate anions (0.90 mol) in the form of a sodium silicate solution containing 27 % SiO_2 and 14 % NaOH under vigorous stirring at 100 °C overnight. The addition of cetyltrimethylammonium bromide (0.20 mol), sulphuric acid (0.52 mol) and water (127 mol) to the seeds solution, followed by an additional stirring period of 20 h at 100 °C afforded a hexagonal alumina-silicate mesostructure, which we denote as *MAS*. The synthesized *MAS* was calcinated under a nitrogen atmosphere at 550 °C for 1 h, and then in the air at the same temperature for 6 h.

Cu(I)-MAS synthesis

Ion exchange was performed by mixing MAS with 0.5 M $Cu(NO_3)_2$ solution for 24 h.[16,17] Then, the filtered adsorbent was dried at 100 °C for 24 h. Finally, Cu^{2+} was reduced to Cu^+ by calcining in nitrogen atmosphere at 450 °C for 3 h.

Pellet synthesis

Pellets were synthesized by the literature method.[16] 20 wt. % < 2 mm of γ-Al_2O_3 was added onto the synthesized zeolites. Deionized water was carefully added until the mixture became mushy. The mixture, which came to the consistency of dough, was cut in the dimensions of 3 mm×10 mm by passing through a laboratory-type extruder. Wet pellets were kept at room temperature overnight and then dried in an oven at 120 °C for 4 h. Dried pellets were calcined at 550 °C for 6 h.

Two-stage thermal and catalytic cracking of XLPE

12 kg of XLPE was added to the reactor, and melting of polymer was carried out in an inert nitrogen atmosphere. In the first stage reactor, the heating rate was kept low (2 °C) to prevent sudden volumetric expansion and heated until all of the polymer was liquefied. In the second step, 12 kg melted polymer was added to the second reactor (cracking reactor, Fig. 2). The thermal cracking process was completed by keeping the heating rate at 5 and 10 °C min^{-1}. The experiments were repeated by adding 120 g of catalyst to the molten polymer alone, adding catalyst to the column only, and adding catalyst to both the polymer and the column. MCM-41 as polymer phase catalyst was added to the liquefied polymer in the second stage,

and Cu(I)-MAS was added as gas phase catalyst to the catalytic column connected to the steam outlet.
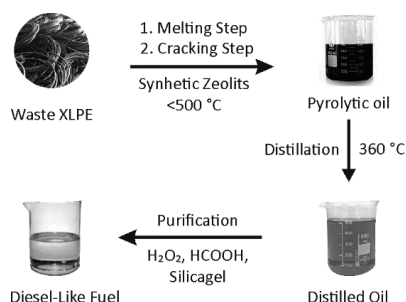

Fig. 2. The conversion of waste XLPE cables to diesel-like fuel.

Pretreatment and setting of sludge

Before the distillation process, impurities such as polymeric substances, asphaltenes and water must be separated from the pyrolytic oil. Thus, coking is minimized during the distillation process. A flocculent/coagulant containing 0.2 wt. % polyacrylamide and 0.5 wt. % sodium silicate was added to pyrolytic oil and mixed with an air compressor at 60 °C for 2 h, then left for 6 h to settling of the precipitate. Thus, the residue and water were separated from the pyrolytic oil.

Distillation

To purify the pyrolytic liquids obtained from the pyrolysis of XLPE, the pyrolytic liquids were first catalytic distilled, then treated with active silica gel and filtered. 600 cm^3 of the supernatant was placed in a catalyst-filled packed column-mounted distillation kettle. Ceramic wool was placed at the bottom of second column section and Cu(1)-MAS in pellet form was filled on the column. The distillates were collected in the collection vessels between 55 and 360 °C. The non-condensed gases were burned in the burner after desulphurization by passing through the 4 M NaOH solution. Distillates up to 180 °C were deposited in the light distillate vessel, and those between 180–360 °C were collected in the heavy distillate vessel.

Desulfurization and decolourization process

100 mL of distilled pyrolytic oil and 12 mL of formic acid was added to a 250 mL three-necked flask and mixed with a magnetic stirrer in a thermostatic water bath at 50 °C for 30 min. Then, 7 ml (30 %) H_2O_2 was added to the mixture and the solution was stirred for additional 180 min. Air was passed through the balloon during mixing. The mixture was transferred to a separatory funnel, after 45 min the oxidized pyrolytic oil and oxidant phase were separated. The sulphur containing components were extracted by mixing the oxidized pyrolytic oil with a 1:1 ratio of 50 % aqueous methanol solution.

Purification step

To decolorize and remove impurities in the distilled and desulfurized pyrolytic oil, 1 % silica gel was added to the solution and stirred at 60 °C and 80 rpm for 45 min, then filtered. The process steps are given in Fig. 2 until a diesel equivalent product is obtained from XLPE.

Calculations

After the pyrolysis and distillation experiments, the liquid product volume and density were measured, and the liquid product amount was calculated by weight. The residue remaining in the reactor was weighed to measure the amount of non-pyrolysis XLPE (char). The

amount of uncondensed gas was measured by subtracting the amount of liquid and solid phase from the amount of XLPE added to the reactor. The pyrolytic liquid was settled for 8 h and the wax formed was separated from the liquid product by separatory funnel. The amount of wax in solid form at room temperature was weighed and its ratio in the pyrolytic liquid product was determined.

RESULTS AND DISCUSSIONS

The biggest difference between polyethylene and XLPE is that polyethylene melts above its melting point temperature, while XLPE softens by acting like rubber. Crosslinking reduces melt index and elongation at break, improves creep resistance, impact strength, environmental stress crack resistance (ESCR) and resistance to slow crack growth. The density and tensile strength of polyethylene are not affected by crosslinking. The crosslinking of polyethylene takes place in four stages: initiation, propagation, branching and termination.[4] Cross-linking changes the physical properties of the polymer such as density, flexibility, hardness and viscosity. Crosslinking occurs between carbon atoms or other chain branches in adjacent chain molecules or between chains branches joined to the same polymer chain (Fig. 3).[20]
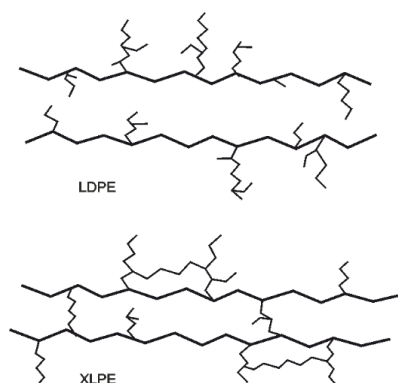
Fig. 3. The view of polyethylene and crosslinked polyethylene.[20]

According to Chen *et al.*,[21] three types of radical chain reactions occur between volatile compounds during pyrolysis: initiation, propagation and termination. These radical reaction mechanisms are: 1) cracking of molecules to form alkanes and alkenes by the Rice-Kossiakoff mechanism, 2) adding alkenes to radicals to increase carbon chain growth and radical scattering and 3) adding radicals to each other to form larger molecules (Eqs. (1)–(3)). Radical scattering and interrelationships are more dominant at low temperatures, leading to an increase in carbon chain length and thus a decrease in non-condensable gas yield. These results show that the reactions between the volatile components occurring during the pyrolysis of hydrocarbons are not stable in the cracking process. The reactions between the volatile components are dependent on the pressure, heating rate and temperature, as well as the varying residence time. Since cracking is

more dominant at high temperatures, the carbon chain of the molecules will shorten, so the oil yield decreases and the amount of non-condensed gas increases:

$$\text{Cracking: R-CH}_2\text{–CH}_2\text{–C}\dot{\text{H}}\text{–R' } \rightarrow \text{R–CH}_2{}^{\bullet} + \text{CH}_2\text{=CH–R'} \qquad (1)$$

$$\text{Propagation: R}^{\bullet} + \text{CH}_2\text{=CH–R' } \rightarrow \text{R–CH}_2\text{–C}\dot{\text{H}}\text{–R'} \qquad (2)$$

$$\text{Coupling: R–CH}_2{}^{\bullet} + \text{R'–CH}_2{}^{\bullet} \rightarrow \text{R–CH}_2\text{–CH}_2\text{–R'} \qquad (3)$$
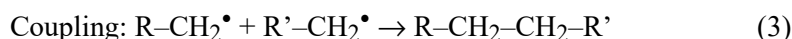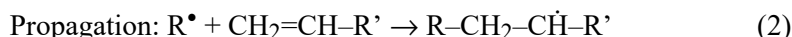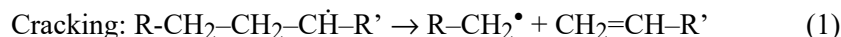
The two stage pyrolysis processes of XLPE obtained from scrap cables were carried out catalyst-free thermal pyrolysis (T-Pyr), polymer phase catalytic pyrolysis (PPC-Pyr), gas-phase catalytic pyrolysis (GPC-Pyr), multi-phase catalytic pyrolysis (MPC-Pyr) at different heating rates. MCM-41 was chosen to obtain higher liquid products in the polymer phase with boiling points in the range of diesel fuel. MCM-41 has a larger pore diameter than other synthetic zeolites, which is weaker than microporous catalysts, also reduces the amount of non-condensable gas.[10,11] Its only disadvantage is that the catalyst efficiency decreases due to rapid clogging of the catalyst pores. Since the catalyst will be added again in each experiment, the disadvantage of catalyst poisoning will be eliminated. Strongly acidic and microporous catalysts such as ZSM-5 and HZSM-5 were not preferred in this study because they increased the amount of non-condensable gas and gasoline was obtained as the main product. In the gas phase, Cu(I)-MAS was used as a catalyst. Cu(I)-MAS in the gas phase, it ensures the re-cracking of large molecules formed as a result of secondary reactions, thus reducing the amount of wax and sulphur amount in the liquid product.[17,18]

As seen in Table II, 83.84 and 91.40 % diesel equivalent fuel was obtained in gas phase and multi-phase catalytic pyrolysis of XLPE with a heating rate of 5 °C min^{-1}, respectively. These values appear to be close to the 83.15 % gasoline value obtained from the two-stage catalytic pyrolysis of HDPE by Ratnasari *et al.*[14] The amount of fuel obtained from single-stage catalytic pyrolysis of XLPE (63 %) by Eze *et al.*[12] is much lower than that obtained in our study. Single-stage pyrolysis is insufficient to completely crack high-density plastics such as HDPE and XLPE.

Mo *et al.*[22] investigated the pyrolysis characteristics of cross-linked polyethylene cables by thermogravimetric method. As seen in Fig. 4, in the study carried out from room temperature to 800 °C, at 40 °C, 20 mL min^{-1} in air, 98.83 % weight loss is observed between 400–500 °C, which is the pyrolysis stage of the polymer. The peak of the DTG curve showing the endothermic reaction is 484.96 °C, and it merges with the DSC curves. In our study, in two-stage multi--phase catalytic pyrolysis experiments, the pyrolysis temperature was found to be 448 °C at 5 °C heating rate and 441 °C at 10 °C min^{-1} heating rate. The pyrolysis temperature at both heating rates is lower than the temperature found by Mo *et al.*[22] It is clear from these results that the two-stage catalytic pyrolysis method of

XLPE has reduced the pyrolysis temperature, so that less energy will be consumed to complete pyrolysis in industrial processes.

TABLE II. The experimental results of XLPE pyrolysis at 5 and 10 °C min⁻¹; T-Pyr: thermal pyrolysis, PPC-Pyr: polymer phase catalytic pyrolysis, GPC-Pyr: gas phase catalytic pyrolysis, MPC-Pyr: multiphase catalytic pyrolysis

Pyrolysis method	Liquid wt. %	Gas wt. %	Residue[a] wt. %	Wax[b] wt. %	Liquefaction temp., °C	Pyrolysis temp., °C
Heating rate, 5 °C/min						
T-Pyr	46.59	5.52	9.26	38.63	237	482
SPC-Pyr	72.83	4.78	6.18	16.21	218	467
GPC-Pyr	83.84	4.11	5.42	6.63	–	458
MPC-Pyr	91.40	3.21	3.56	1.83	–	448
Heating rate, 10 °C/min						
T-Pyr	27.83	7.23	8.43	56.51	216	473
SPC-Pyr	44.60	6.42	7.12	41.86	207	461
GPC-Pyr	59.17	5.76	6.73	28.34	–	452
MPC-Pyr	72.07	5.11	5.56	17.26	–	441

[a]Remaining char in the reactor; [b]the waxes were separated by settling the pyrolytic liquid for 8 h
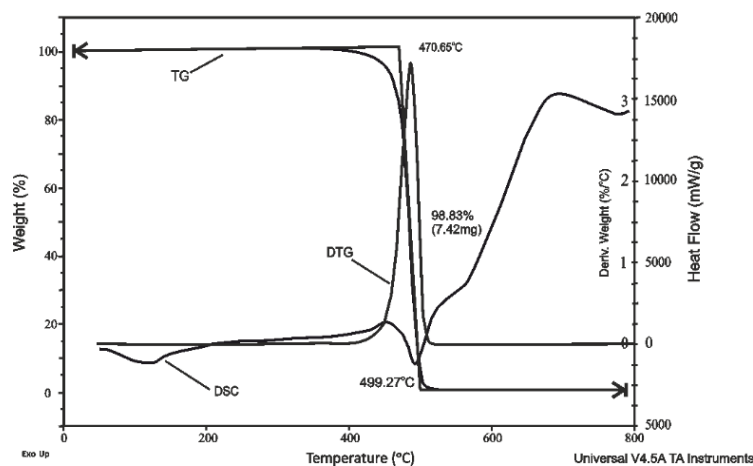
Fig. 4. TGA-DSC curve on XLPE cable material.[22]

Due to the low heat conductivity of the polymer in the first stage of pyrolysis, no significant increase was observed in the pyrolysis temperature in the first 45 min, the temperature rice slowly between the 45th and 60th min, and the temperature increase suddenly accelerated after the 60th min. From these results, it was understood that the melting of the polymer started at the 45th min, completed at the 60th min, and thermal degradation started after the 60th min. The conversion of the polymer via time at 5 °C min⁻¹ is shown in Fig. 5. As can be seen from Fig. 5, the liquid product yield is low in the first 60 min. The thermal

degradation started to accelerate after 60 min, as the heat given to the system up to the liquefaction temperature was spent on loosening the crosslinks and phase change in the polymer. The pyrolysis process was completed in the 105th min..

Fig. 5. Conversion of XLPE to liquid products at a 5 °C min^{-1} heating rate.

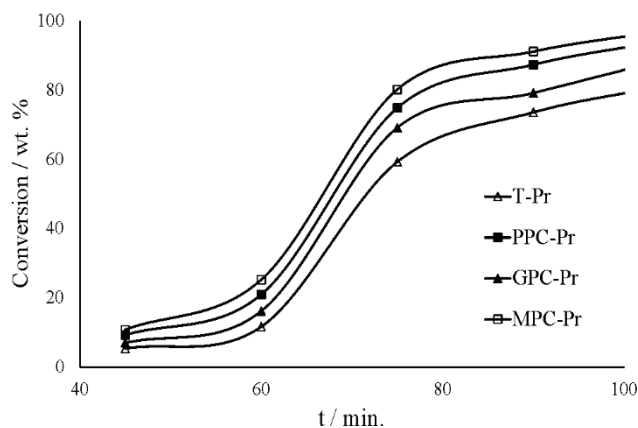In Table II, the highest amount of liquid product was determined as 91.40 % in multi-phase catalytic experiments. At the same time, the amounts of uncondensed gas and residue remaining in the reactor are lowest in the multi-phase catalytic pyrolysis experiment. At high heating rate, the amount of liquid decreases, and the amount of uncondensed gas and residue is found to be slightly higher. At high heating rate, the rate of cracking and the speed of cracked gas molecules increased, thus the catalytic interaction decreased. By the increase of coking at high heating rate, the amount of residue remaining in the reactor increased slightly. These results show that the retention time decreases depending on the heating rate, thus the evaporation rate increases, and the secondary reactions decrease. Therefore, the amount of uncondensed gas increased, and larger molecules were obtained in the form of wax without cracking.

Table II shows that the liquefaction temperature and pyrolysis temperature in the pyrolysis experiments of XLPE decreased depending on the increase in the heating rate. With the increase in heating rate, the intermolecular cross-links loosened faster and the polymer passed into liquid form before the bonds started to break. This was observed during pyrolysis as the temperature remained constant throughout liquefaction and started to rise with the start of cracking. In Table II, it can also be seen that the liquefaction and pyrolysis temperatures in catalyst-free pyrolysis experiments are higher than in catalytic pyrolysis. It is clearly seen that the catalyst reduces the activation energy required to break intermolecular bonds. The temperature of gas phase catalytic pyrolysis is lower than that of polymer phase catalytic pyrolysis. The catalytic interaction in the gas phase is

faster than in the solid phase, and the catalyst minimizes secondary reactions. In both polymer phase and gas phase catalytic experiments, the pyrolysis temperature and liquefaction temperature are the lowest. Using catalysts in both phases accelerates the faster degradation of the polymer.

As a result of thermal cracking of PE plastic types, molecules that have not completed the full cracking reaction form waxes with a boiling point higher than 500 °C. In order to obtain high amounts of fuel in the pyrolysis of plastics, it is desired that the amount of wax is at a minimum level. Al-Salem *et al.*[23] obtained 32 % and 64.5 % wax in the pyrolysis of HDPE and LDPE at 500 °C, respectively. Arabiourrutia *et al.*[24] obtained wax in the range of 70–80 % from the pyrolysis of HDPE, LDPE and PP at 450–600 °C. They found that the amount of wax decreased due to the decrease in secondary reactions at high heating rate and pyrolysis temperature. As can be seen from Table II, the liquid yield was increased, and the amount of wax was reduced because of the correct catalyst determination strategy in the gas phase and polymer phase. The catalyst used in the polymer phase increased the cracking rate, on the one hand, large molecules continued to be cracked in the gas phase, and on the other hand, the amount of uncondensed gas decreased due to catalytic radical reactions. The packed column also acts as a molecular sieve and thus prevents the escape of non-condensed gases, while large molecules such as waxes continue to break down into smaller molecules in the gas phase. Parameters such as retention time of cracked molecules, pyrolysis temperature and heating rate affect the amount of fuel, gas and wax. While no wax is observed in the catalytic pyrolysis of plastics at high heating rates, the amount of gas increases and the amount of fuel decreases. As the retention time of cracked gases increases at low pyrolysis temperatures, coking and wax formation increases. For this reason, thermal and catalytic pyrolysis experiments were carried out under mild conditions, below 500 °C. It is aimed to increase fuel efficiency rather than completely preventing wax formation. As seen in Table II, the lowest amount of wax and the highest amount of fuel were obtained in multiphase catalytic cracking experiments at a heating rate of 5 °C. In thermal cracking experiments, the highest wax and lowest fuel amount were obtained.

In Table III, the carbon, hydrogen and nitrogen content of the fuel were found to be close to diesel fuel. The reason why the carbon content of the fuel obtained by multi-phase catalytic cracking is slightly higher than the others may be due to the higher amount of cracked low molecular weight hydrocarbons. The ash content of fuels is in the negligible range.

As seen in Table III, the sulphur value of the fuel obtained from multi-phase catalytic cracking experiments was reduced from 0.24 to 0.052 ppm. The desulphurization efficiency was calculated as 78.4 %. In catalytic pyrolysis experiments of XLPE, the sulphur removal efficiency was found to be less than the

hydrotreated diesel sample, since the factors such as steric hindrance of large molecules, coking and wax reduce the catalytic activity of Cu(I)-MAS. As it can be seen in Table III, the desulfurization efficiency is listed as MPC-pyr > GPC--pyr > PPC-pyr > T-pyr. Cu(I)-MAS showed higher catalytic activity than MCM--41 in sulphur removal. Pyrolytic oil samples were distilled and treated with formic acid-hydrogen peroxide and finally silica gel to remove impurities, thus a light transparent lemon-yellow coloured diesel quality fuel was obtained.

As can be seen in Table III, the density values obtained in the vapour phase catalytic experiments were found to be closer to diesel fuel due to the higher degradation of the polymer in the multiphase catalytic cracking process. The density value of the fuel obtained from thermal pyrolysis and polymer phase catalytic pyrolysis experiments is lower than that obtained in the gas phase and multi-phase. The reason for this may be repolymerisation or isomerization reactions that occur by catalysing secondary reactions in the gas phase. The density value of the fuel formed by multi-phase catalytic cracking is the lowest, as expected. Some of the small molecules formed as a result of cracking in the polymer phase cracked again in the gas phase, reducing the density values of the fuel. The density of liquid from the gas-phase catalytic pyrolysis was found to be equivalent to diesel fuel in Table III.

TABLE III. Physicochemical properties of liquid products according to pyrolysis method with 5 °C min^{-1} of heating rate; v: kinematic viscosity, GCV: gross calorific value

Parameter	T-Pyr	PPC-Pyr	GPC-Pyr	MPC-Pyr	DF
C	84.56	84.60	84.89	85.38	86.43
H	13.72	14.76	13.98	13.78	13.99
N	0.56	0.62	0.58	0.61	0.13
S	0.17	0.11	0.059	0.052	Nd
Ashes, wt. %	0.02	0.04	0.03	0.02	Nd
GCV / MJ kg^{-1}	44.56	46.12	45.34	45.97	44.79
Density, kg/m^3	811.24	810.16	832.54	796.67	830.00
v / cSt at 40 °C	2.69	2.32	2.72	2.17	2.43
Flash point, °C	56	53	57	52	56
Yield, wt. %	53.92	70.12	86.48	89.56	
Cetane number	55	54	59	53	57
Distillation temperature, °C					
IBP	168	164	174	147	165
10 % recovery	201	197	221	187	209
50 % recovery	247	244	287	234	281
90 % recovery	344	342	352	339	344
FBP	366	364	370	358	368

The gross calorific value (GCV) of the fuels obtained from catalytic and thermal pyrolysis of XLPE compared with diesel fuel (DF) was found to be close to each other (Table III). The calorific value of the fuel obtained from polymer

phase catalytic pyrolysis was found to be slightly higher than the others (46.12 MJ/kg). This may be because more olefinic molecules are formed by catalytic reactions in the polymer phase. The diesel product used in the comparison was obtained from local companies, and there may be differences between the calorific values of diesel products of different companies. In general, it has been observed that the calorific values of the fuel obtained from the catalytic pyrolysis of XLPE are at the same level as the diesel supplied from the market.

The kinematic viscosity values are between 2.17 and 2.72 cSt and correspond to the kinematic viscosity value of diesel fuel (2.43 cSt). It is understood that the ratio of olefin and aromatic compounds in pyrolytic fuels is higher than in paraffinic compounds. Thus, it has been observed that the high wax ratio seen in the single-stage pyrolysis experiments is eliminated by the cascade pyrolysis method in Table III.

As can be seen in Table III, the flashpoint of the fuels obtained from polymer phase catalytic pyrolysis is lower (52 °C). The flashpoint of the fuel obtained as a result of catalytic pyrolysis in the gas phase is 57 °C, slightly higher than the flashpoint of diesel fuel at 56 °C. From this, it was understood that the paraffinic structure of the molecules formed because of the thermal decomposition in the gas phase is higher than that of diesel fuel. In a way, this shows that the fuel obtained as a result of gas-phase catalytic pyrolysis is comparable to diesel fuel. The cetane number was found to be 57 in the gas phase catalytic pyrolysis process (Table III). This value is close to the cetane number (56) of the diesel fuel used in the comparisons. The number of paraffinic molecules in fuels can be explained as more regular burning of the fuel.

The cetane number of the fuel was found at the desired value due to the paraffinic molecules formed because of the pyrolysis of XLPE in Table III. Since the best cetane number and other physical properties are obtained from the gas phase catalytic pyrolysis, the fuel obtained from the gas phase catalytic pyrolysis of XLPE can be used as a diesel equivalent fuel by adding fuel additives without the need to blend with other fuels, or it can be directly blended with diesel in any ratio, can reduce consumption costs. It was observed that the distillation data (10, 50 and 90 % recovery values) obtained from gas phase catalytic pyrolysis were compatible with diesel fuel. The distillation range of the fuel obtained in the gas phase coincides with that of diesel.

CONCLUSIONS

Scrap XLPE is the most economical potential raw material source in obtaining fuel by pyrolysis method as free waste. In industrial applications, the pyrolysis of XLPE is not preferred because it produces a high amount of wax. Also, wax causes major problems as it clogs the process lines. In this study, the formation of wax was minimized by the two-stage heating method and the diesel

equivalent pyrolytic fuel was obtained at the maximum ratio. To obtain the highest fuel efficiency in the catalytic or thermal pyrolysis process, it has been determined that the polymer should be melted at a low heating rate up to 207––214 °C, and then the pyrolysis should be completed by increasing the heating rate not exceeding 10 °C min^{-1}. In addition, the successful applicability of the column-filled distillation method has been observed for the purification of the obtained pyrolytic fuels. The thermal catalysis, polymer phase catalysis and gas phase catalysis methods were compared, and it was understood that the most suitable method in terms of fuel properties was the multi-phase catalytic pyrolysis method. The most widely known thermal cracking catalyst, synthetic zeolites, was used in the experiments in order to determine the difference between thermal cracking and catalytic cracking.

The main purpose of the study is to reveal a decisive method in industrial applications by decreasing the wax ratio with the gradual heating rate and increasing the fuel efficiency. The type and amount of catalyst, reactor types, the pyrolysis of XLPE with scrap tires, waste mineral oil, or waste vegetable oil, and changes in the chemical structure of the products in these application differences are planned as the subject of further studies. The waste XLPE is still collected in nature as garbage or directly incinerated. The recovery of waste XLPE polymers as an energy source rather than mechanical recovery is a work that should be considered in waste management plans. It will take its place in the recycling sector as an alternative method for the disposal of such wastes with high energy value in a way that will minimize environmental problems.

ИЗВОД

ДВОФАЗНА ТЕРМОКАТАЛИТИЧКА КОНВЕРЗИЈА ОТПАДНОГ XLPE У ГОРИВО СЛИЧНО ДИЗЕЛУ

UFUK SANCAR VURAL[1], ABDULLAH YINANC[2] и HUSEYIN CAHIT SEVINDIR[3]

[1]Pasabayir Mh. Mehmetcik Cd. 77/18, Bandirma, Balikesir, Turkey, [2]Tekirdag Namik Kemal University, Corlu Vocational School of Technical Sciences, Tekirdag, Turkey u [3]Suleyman Demirel University, Department of Environmental Engineering, Faculty of Engineering, Isparta, Turkey

Умрежени полиетилени (XLPE) нису пожељни у индустријским применама пиролизе и методама механичког рециклирања због велике термохемијске отпорности на топлоту и деформације. Студије о пиролизи XLPE до 600 °C за добијање горива генерално су дале велику количину воска и нису биле од интереса за енергетски сектор. У овој студији, двостепена пиролиза XLPE изведена је у присуству катализатора и без катализатора (термално, T-pyr) на 500 °C, са брзинама загревања од 5 и 10 °C min^{-1}. Изведене су три различите каталитичке студије додавањем смеше катализатора (MCM-41 + HZSM-5) само у полимерну фазу (PPC--pyr), пуњењем излазне колоне гаса смешом катализатора (Cu(I)-MAS + HZSM-5) (GPC-Pyr) и додавањем смеше катализатора у полимерну и гасну фазу (MPC-pyr).

Највећа количина дизел горива (91,40 %) добијена је у експериментима више-фазне каталитичке пиролизе на 460 °C са брзином загревања од 5 °C min^{-1}. Утвр-ђено је да калоријска вредност, кинематичка вискозност, густина, тачка паљења и цетански број горива износе 45,97 MJ kg^{-1}, 2,72 cSt, 832,5 kg m^{-3}, 57 и 59 °C, редом. Резултати двостепеног каталитичког крекинга и профил брзине загревања биће водич за индустријску примену пиролизе. Једноставна изводљивост указује да би то била веома исплатива инвестиција за индустријску примену.

REFERENCES

1. N. D. Sarkari, P. Ayar, M. H. Oskouei, F. K. Khosrowshahi, M. Mohseni, *Constr. Build. Mater.* **287** (2021) 122999 (https://doi.org/10.1016/j.conbuildmat.2021.122999)
2. A. K. Sen, B. Mukherjee, A. S. Bhattacharyya, P. P. De, A. K. Bhowmick, *Poly. Degrad. Stab*. **36** (1992) 281 (https://doi.org/10.1016/0141-3910(92)90068-G)
3. D. Manas, M. Manas, A. Mizera, P. Stoklasek, J. Navratil, S. Sehnalek, P. Drabek, *Polymers* **10** (2018) 1361 (https://doi.org/10.3390/polym10121361)
4. S. M. Tamboli, S. T. Mhaske, D. D. Kale, *Indian J. Chem. Technol.* **11** (2004) 853 (http://nopr.niscpr.res.in/handle/123456789/9558)
5. C. Meola, G. M. Carlomagno, G. Giorleo, in: *Encyclopedia of Chemical Processing*, Vol. 1, S. Lee, Ed., Taylor & Francis, Abingdon-on-Thames, 2005
6. P. Singh, N. Déparrois, K. G. Burra, S. Bhattacharya, A. K. Gupta, *Appl. Energy* **254** (2019) 113722 (https://doi.org/10.1016/j.apenergy.2019.113722)
7. H. Lee, J. H. Jeong, H. Cho, C. M. Koo, S. M. Hong, H. Kim, Y. Lee, *Polym. Degrad. Stab*. **93** (2008) 2084 (https://doi.org/10.1016/j.polymdegradstab.2008.09.006)
8. C. Wang, T. Xie, P. A. Kots, B. C. Vance, K. Yu, P. Kumar, J. Fu, S. Liu, G. Tsilomelekis, E. A. Stach, W. Zheng, D. G. Vlachos, *JACS Au* **1** (2021) 1422 (https://doi.org/10.1021/jacsau.1c00200)
9. C. Kassargya, S. Awada, G. Burnensa, K. Kahine, M. Tazerout, *Fuel* **224** (2018) 764 (https://doi.org/10.1016/j.fuel.2018.03.113)
10. L. Yu, A. Farinmade, O. Ajumobi, Y. Su, V. T. John, J. A. Valla, *Appl. Catal., A* **602** (2020) 117727 (https://doi.org/10.1016/j.apcata.2020.117727)
11. T. Liu, Y. Li, Y. Zhou, S. Deng, H. Zhang, *Catalysts* **13** (2023) 382 (https://doi.org/10.3390/catal13020382)
12. W. U. Eze, R. Umunakwe, H. C. Obasi, M. I. Ugbaja, C. C. Uche, I. C. Madufor, *Clean Tech. Recycl.* **1** (2021) 50 (https://doi.org/10.3934/ctr.2021003)
13. E. Santos, B. Rijo, F. Lemos, M. A. N. D. A. Lemos, *Chem. Eng. J.* **278** (2019) 122077 (https://doi.org/10.1016/j.cej.2019.122077)
14. D. K. Ratnasari, M. A. Nahil, P. T. Williams, *J. Anal. App. Pyr.* **224** (2017) 631 (https://doi.org/10.1016/j.jaap.2016.12.027)
15. J. Yu, S. Liu, A. Cardoso, Y. Han, K. Bikane, L. Sun, *Energy* **188** (2019) 116117 (https://doi.org/10.1016/j.energy.2019.116117)
16. U. S. Vural, S. Uysal, A. Yinanc, *J. Serb. Chem. Soc.* **87** (2022) 1219 (https://doi.org/10.2298/JSC211108048V)
17. W. Li, Q. Liu, J. Xing, H. Gao, X. Xiong, Y. Li, X. Li, H. Liu, *Environ. Energy Eng.* **53** (2007) 3263 (https://doi.org/10.1002/aic.11319)

18. H. Tang, W. Li, W. Liu, L. Guan, J. Q. Song, J. M. Xing, H. Z. Liu, *Sci. China, Ser. B-Chem.* **52** (2009) 276 (https://doi.org/10.1007/s11426-009-0061-8)
19. T. F. Parangi, R. M. Patel, U. V. Chudasama. *Bull. Mat. Sci*. **37** (2014) 609 (https://doi.org/10.1007/s12034-014-0709-7)
20. H. Ahmad, D. Rodrigue, *Polym. Eng. Sci.* **62** (2022) 2376 (https://doi.org/10.1002/pen.26049)
21. Z. Chen, X. Zhang, L. Che, H. Peng, S. Zhu, F. Yang, X. Zhang, *Fuel* **271** (2020) 117308 (https://doi.org/10.1016/j.fuel.2020.117308)
22. S. Mo, J. Zhang, D. Liang, H. Chen, *Proced. Eng.* **52** (2013) 588 (https://doi.org/10.1016/j.proeng.2013.02.190)
23. S. M. Al-Salem, A. Dutta, *Ind. Eng. Chem. Res.* **60** (2021) 8301 (https://doi.org/10.1021/acs.iecr.1c01176)
24. M. Arabiourrutia, G. Elordi, G. Lopez, E. Borsella, J. Bilbao, M. Olazar, *J. Anal. Appl. Pyr.* **94** (2012) 230 (https://doi.org/10.1016/j.jaap.2011.12.012).